



University of Kentucky
UKnowledge

Theses and Dissertations--Chemical and
Materials Engineering

Chemical and Materials Engineering

2015

FUNDAMENTAL STUDIES OF SURFACTANT TEMPLATED METAL OXIDE MATERIALS SYNTHESIS AND TRANSFORMATION FOR ADSORPTION AND ENERGY APPLICATIONS

Saikat Das

University of Kentucky, saikat39@gmail.com

[Right click to open a feedback form in a new tab to let us know how this document benefits you.](#)

Recommended Citation

Das, Saikat, "FUNDAMENTAL STUDIES OF SURFACTANT TEMPLATED METAL OXIDE MATERIALS SYNTHESIS AND TRANSFORMATION FOR ADSORPTION AND ENERGY APPLICATIONS" (2015). *Theses and Dissertations--Chemical and Materials Engineering*. 48.

https://uknowledge.uky.edu/cme_etds/48

This Doctoral Dissertation is brought to you for free and open access by the Chemical and Materials Engineering at UKnowledge. It has been accepted for inclusion in Theses and Dissertations--Chemical and Materials Engineering by an authorized administrator of UKnowledge. For more information, please contact UKnowledge@lsv.uky.edu.

STUDENT AGREEMENT:

I represent that my thesis or dissertation and abstract are my original work. Proper attribution has been given to all outside sources. I understand that I am solely responsible for obtaining any needed copyright permissions. I have obtained needed written permission statement(s) from the owner(s) of each third-party copyrighted matter to be included in my work, allowing electronic distribution (if such use is not permitted by the fair use doctrine) which will be submitted to UKnowledge as Additional File.

I hereby grant to The University of Kentucky and its agents the irrevocable, non-exclusive, and royalty-free license to archive and make accessible my work in whole or in part in all forms of media, now or hereafter known. I agree that the document mentioned above may be made available immediately for worldwide access unless an embargo applies.

I retain all other ownership rights to the copyright of my work. I also retain the right to use in future works (such as articles or books) all or part of my work. I understand that I am free to register the copyright to my work.

REVIEW, APPROVAL AND ACCEPTANCE

The document mentioned above has been reviewed and accepted by the student's advisor, on behalf of the advisory committee, and by the Director of Graduate Studies (DGS), on behalf of the program; we verify that this is the final, approved version of the student's thesis including all changes required by the advisory committee. The undersigned agree to abide by the statements above.

Saikat Das, Student

Dr. Stephen E. Rankin, Major Professor

Dr. Thomas Dziubla, Director of Graduate Studies

FUNDAMENTAL STUDIES OF SURFACTANT TEMPLATED METAL
OXIDE MATERIALS SYNTHESIS AND TRANSFORMATION FOR
ADSORPTION AND ENERGY APPLICATIONS

DISSERTATION

A dissertation submitted in partial fulfillment of the
requirements for the degree of Doctor of Philosophy in the
College of Engineering
at the University of Kentucky

By

Saikat Das

Lexington, Kentucky

Director: Dr. Stephen E Rankin, Professor of Chemical Engineering

Lexington, Kentucky

2015

Copyright © Saikat Das 2015

ABSTRACT OF DISSERTATION

FUNDAMENTAL STUDIES OF SURFACTANT TEMPLATED METAL OXIDE MATERIALS SYNTHESIS AND TRANSFORMATION FOR ADSORPTION AND ENERGY APPLICATIONS

This work addresses fundamental aspects of designing templates and curing conditions for the synthesis of mesoporous metal oxide thin films. The first section addresses selection of cationic-carbohydrate surfactant mixtures to synthesize templated silica thin films for selective adsorption of simple carbohydrates based on molecular imprinting. Nuclear magnetic resonance and fluorescence spectroscopy results suggest a novel structure for mixtures of alkyl glucopyranosides or xylopyranosides with cationic (trimethylammonium) surfactants. Despite thermodynamically favorable mixing, the carbohydrate headgroups in the mixed micelle adopt an inverted configuration with their headgroups in the micelle core, and therefore are inaccessible for molecular imprinting. This orientation occurs even when the alkyl tail length of the carbohydrate surfactant is greater than that of the cationic surfactant, but this limitation can be overcome by introducing a triazole linker to the carbohydrate surfactant. The next section addresses the effects of aging conditions on the structural and chemical evolution of surfactant templated silica thin films. The third section describes the synthesis of carbohydrate/cationic surfactant imprinted silica thin films with orthogonally oriented cylindrical pores by modifying the glass surface with a random copolymer.

The last part of the dissertation addresses the effect of pore orientation on the transformation mechanism of block copolymer templated titania thin films during high temperature curing. Mesoporous titania thin films can be used for photochemical and solar cell applications, but doing so requires addressing the tradeoff between loss of mesostructural order and growth of crystallinity during thermal treatment. By using advanced x-ray scattering techniques it has been shown that the titania films with vertically oriented pores can better withstand the anisotropic stress that develops during thermal treatment compared to titania films with mixed pore orientation. For instance, films with parallel or mixed pores can only be heated at 400 °C for a brief time (~10 min) without loss of order, while orthogonally oriented films can be heated at 550

°C or greater for extended time periods (on the order of hours) without significant loss of long-range mesopore structure. Detailed kinetic modeling was applied to enable the comparison of activation energy for mesostructure loss in films as a function of pore orientation and thickness.

KEYWORDS: mixed surfactant, silica, titania, separation, solar cells

Saikat Das
07/30/2015

FUNDAMENTAL STUDIES OF SURFACTANT TEMPLATED METAL
OXIDE MATERIALS SYNTHESIS AND TRANSFORMATION FOR
ADSORPTION AND ENERGY APPLICATIONS

By
Saikat Das

Dr. Stephen E Rankin
Director of Dissertation

Dr. Thomas Dziubla
Director of Graduate Studies

07/30/2015

To, Salil Kanta Das

“This is for you dad, I am very happy that I have accomplished your unfulfilled dream, Love You”

ACKNOWLEDGEMENTS

I would like to thank Dr. Stephen E. Rankin for his continuous support and guidance throughout my PhD. He has always encourage me to think independently on my project and always welcome any new idea. During my research I failed several occasions but he never lost his patience and always advised me to find the solution. I would also like to thank Dr. Anne-Frances Miller for her valuable time and advice during my PhD. A major part of my research is become successful due to her advice and active involvement. I would like to thank my committee members Dr. Barbara L. Knutson and Dr. Thomas Dziubla for their valuable advice and encouragement for the completion of my dissertation. I would like to thank Dr. Hans-Joachim Lehmler and his research group for synthesizing different novel surfactants for my research. I would also like to thank Dr. Chiranjib Bhattacharjee and Dr. Dwaipayan Sen from Jadavpur University and Prof. Purushottam Chakraborty from Saha Institute of Nuclear Physics to grind the research interest in me during my undergraduate studies and inspire my to pursue PhD.

I was also very fortunate to get the scientific and technical advice from John Layton from NMR facility and Joseph Strzalka from Argonne National Lab during my research. Their excellent technical expertise really facilitated my work. I would also like to thank all my previous and current lab members; specially Dr. Qingliu Wu, Dr. Suvid Joshi, Dr. Janet Mohandas, Ravinder Garlapalli, Suraj Nagpure and Syed Zahadul Islam; for their continuous support. Their presence in the lab made a very friendly work culture.

I would also like to thank all my friends in Lexington specially Utshab Chakravorty, Dr. Sourik Ganguly, Dr. Daipayan Banerjee, Swagata Banerjee, Dr. Barunava Patra, Soma

Chakraborty Patra, Suvamay Jana and Aindrila Jana. They made me feel Lexington as my second home. Thanks all.

Lastly I would like to acknowledge the four most important person in my life, they consist my family. First person is my father Salil Kanta Das, my inspiration. He is the reason behind my PhD. He had to leave his PhD research due to financial crisis in a join family. I always used to see that pain in his eyes. That really motivated me to pursue my PhD. I hope now I can bring smile to his face. The second person is my mother Rita Das. She gives me the courage to face every difficult situation in my life. Every time I fell down she is the one who holds my hand and lift me up. Because of her sacrifice I am here. I also like to thank my mother-in-law Swapna Nath for believe in me and giving me the blessings to become successful in my life. Last but not the least I want to thank my wife Barsha Nath. In last two years she has changed me completely. Due to her my life has become really wonderful. Thank you so much for standing beside me in every ups and downs in the last two years and the uncountable days to follow.

TABLE OF CONTENTS

ACKNOWLEDGMENTS.....	iii
TABLE OF CONTENTS.....	v
LIST OF TABLES.....	vii
LIST OF FIGURES.....	viii
1. OVERVIEW.....	1
1.1. Research hypotheses.....	7
1.2. Overview of dissertation.....	9
2. BACKGROUND.....	12
2.1. Summary.....	12
2.2. Surfactant.....	13
2.3. Mixed surfactant system.....	15
2.4. Mesoporous silica and titania thin films.....	18
2.5. Spectroscopy techniques.....	23
2.5.1. Nuclear magnetic resonance spectroscopy.....	23
2.5.2. Fluorescence spectroscopy.....	34
2.5.3. Fourier transform infrared spectroscopy.....	36
2.6. Materials characterization.....	37
2.6.1. X-ray diffraction.....	37
2.6.2. Grazing incidence small angle x-ray scattering.....	39
3. NMR STUDIES SUGGEST AN INVERTED MICELLE-IN-MICELLE CONFIGARATION IN CATIONIC/CARBOHYDRATE SURFACTANT MIXTURES	54
3.1. Summary.....	54
3.2. Introduction.....	55
3.3. Experimental.....	57
3.4. Results & Discussion.....	59
3.5. Conclusions.....	72
4. TUNING THE POSITION OF HEAD GROUPS BY SURFACTANT DESIGN IN MIXED MICELLES OF CATIONIC AND CARBOHYDRATE SURFACTANTS.....	80
4.1. Summary.....	80
4.2. Introduction.....	81
4.3. Experimental.....	85
4.4. Results & Discussion.....	87
4.5. Conclusions.....	103
5. ORIENTING THE PORES OF CATIONIC-CARBOHYDRATE MIXED SMALL MOLECULE SURFACTANT TEMPLATED SILICA THIN FILMS BY TUNING SURFACE CHEMISTRY.....	119

5.1.	Summary.....	119
5.2.	Introduction.....	120
5.3.	Experimental.....	123
5.4.	Results & Discussion.....	125
5.5.	Conclusions.....	128
6.	STRUCTURAL AND CHEMICAL EVOLUTION OF MIXED CATIONIC/CARBOHYDRATE SURFACTANT TEMPLATED SILICA THIN FILMS DURING LONG-TIME AGING.....	132
6.1.	Summary.....	132
6.2.	Introduction.....	133
6.3.	Experimental.....	135
6.4.	Results & Discussion.....	137
6.5.	Conclusions.....	144
7.	IN-SITU GISAXS INVESTIGATION OF PORE ORIENTATION EFFECTS ON THE THERMAL TRANSFORMATION MECHANISM IN MESOPOROUS TITANIA THIN FILMS.....	155
7.1.	Summary.....	155
7.2.	Introduction.....	156
7.3.	Experimental.....	159
7.4.	Results & Discussion.....	161
7.5.	Conclusions.....	170
8.	PORE ORIENTATION EFFECTS ON THE KINETICS OF MESOSTRUCTURE LOSS IN SURFACTANT TEMPLATED TITANIA THIN FILMS.....	181
8.1.	Summary.....	181
8.2.	Introduction.....	182
8.3.	Experimental.....	186
8.4.	Results & Discussion.....	188
8.5.	Conclusions.....	197
9.	CONCLUSIONS & FUTURE WORKS.....	211
9.1.	Conclusions.....	211
9.2.	Future works.....	216
	APPEXDIX A.....	220
	APPENDIX B.....	233
	APPENDIX C.....	242
	APPENDIX D.....	262
	APPENDIX E.....	269
	APPENDIX F.....	273
	REFERENCES.....	276
	VITA.....	304

LIST OF TABLES

Table 3.1. Comparison of T_1 values of headgroup protons in $C_{16}TAB/C8X1$ and pure $C8X1$ micelles.....	74
Table 4.1. Values of mixed critical micelle concentration (cmc) from pyrene solvatochromism, overall mole fraction of $C_{16}TAB$ (α_1) in mixed solution, mole fraction of $C_{16}TAB$ (X_1) in mixed micelle at cmc and at 30 mM total surfactant concentration, interaction parameter (β) and aggregation number (N_{agg}) from pyrene quenching for $C_{16}TAB/C12G1$, $C_{12}TAB/C12G1$ and $C_{10}TAB/C12G1$ mixtures.....	106
Table 4.2. Comparison of T_1 and T_2 values of headgroup protons in $C_{16}TAB/C12G1$, $DTAB/C1G1$ and $DeTAB/C12G1$ mixed micellar systems.....	106
Table 8.1. Avrami parameters n and k determined using the linearized Avrami equation at different isothermal conditions for titania thin films (60 nm thick) on both unmodified and modified borosilicate glass substrates.....	200
Table 8.2. Avrami parameters n and k determined using the linearized Avrami equation at different isothermal conditions for titania thick films (250 nm thick) on modified substrate.....	200
Table 8.3. Avrami parameters n and k determined using the linearized Avrami equation for different ramp rates to reach the final calcination temperature of 500 °C for titania thick films (250 nm thick) on modified substrate.....	200

LIST OF FIGURES

- Figure 2.1. 1D ^1H NMR spectrum of 1:1 $\text{C}_{16}\text{TAB}/\text{C8G1}$ in D_2O at $50\text{ }^\circ\text{C}$ (total surfactant concentration 30 mM).....41
- Figure 2.2. COSY spectrum of 1:1 $\text{C}_{16}\text{TAB}/\text{C8G1}$ in D_2O at $50\text{ }^\circ\text{C}$ (total surfactant concentration 30 mM). Cross peaks indicating coupling between protons are numbered and will be discussed in Chapter 3.....42
- Figure 2.3. HSQC spectrum of 1:1 $\text{C}_{16}\text{TAB}/\text{C8G1}$ in D_2O at $50\text{ }^\circ\text{C}$ (total surfactant concentration 30 mM). Numbered peaks represent directly bonded ^1H - ^{13}C pairs and their assignment will be discussed in Chapter 3.....43
- Figure 2.4. 2D NOESY spectrum of 1:1 $\text{C}_{16}\text{TAB}/\text{C8G1}$ in D_2O at $50\text{ }^\circ\text{C}$ (total surfactant concentration 30 mM). Numbered cross peaks indicate NOE correlations and will be discussed further in Chapter 3.....44
- Figure 2.5. 1D NOE spectrum of 1:1 $\text{C}_{16}\text{TAB}/\text{C8G1}$ in D_2O at $50\text{ }^\circ\text{C}$ (total surfactant concentration 30 mM). The ammonium methyl protons (N_{CH_3}) were irradiated to give the NOE spectrum (top) which can be compared to the regular 1D spectrum (bottom) to identify correlated protons. In this case, only $\alpha'_{a,b}$ protons are correlated with N_{CH_3} protons (see Chapter 3 for details).....45
- Figure 2.6. Pyrene fluorescence emission intensity ratio I_1/I_3 vs. total surfactant concentration for DeTAB/C12G1 at $50\text{ }^\circ\text{C}$. 1:1 overall ratio of surfactants was used. Arrows denote the mixed cmc value.....46
- Figure 2.7. Fluorescence emission spectra of pyrene in DeTAB/C12G1 1:1 mixture in water with different hexadecylpyridinium chloride quencher concentrations (indicated in the legend).....47
- Figure 2.8. Determination of aggregation number: Linear fitting of $\ln(I_0/I)$ vs. $[\text{Q}]$ for DeTAB/C12G1 1:1 mixture at $50\text{ }^\circ\text{C}$ where I_0 and I are the fluorescence intensities in the absence and presence of the quencher respectively. $[\text{Q}]$ is the quencher concentration which was varied from 0 mM to 0.8 mM.....48
- Figure 2.9. Representative FT-IR absorbance spectrum of a silica thin film on a silicon wafer which is templated with a 10:1 ratio of C_{16}TAB to C8G1. The film was aged for 7 days at $20\text{ }^\circ\text{C}$ under a relative humidity of 45% prior to measuring this spectrum.....49
- Figure 2.10. Schematic of x-ray diffraction. The diffracted rays from two planes exhibit constructive interference when the extra distance traveled by incident photons along the two illustrated vectors is equal to an integer of the x-ray wavelength used.....50

Figure 2.11. XRD pattern of C ₁₆ TAB templated silica films (after extraction) aged at room temperature (23 °C) and 45 %RH for 7 days.....	51
Figure 2.12. Schematic of the GISAXS experiment geometry.....	52
Figure 2.13. GISAXS pattern of unsandwiched titania thin film after aging at 4 °C for 2 h and just after reaching final calcination temperature 500 °C. The films are oriented horizontally (in the xy plane) relative to the incident beam for this experiment.....	53
Figure 3.1. 1D ¹ H NMR spectrum of 1:1 (A) C ₁₆ TAB/C8G1 and (B) C ₁₆ TAB/C8X1 in D ₂ O at 50 °C (total surfactant concentration 30 mM), with Molecular structures of (A) C ₁₆ TA ⁺ and C8G1 (B) C ₁₆ TA ⁺ and C8X1, determined by geometry optimization using the PM3 semiempirical molecular orbital method. The labeling of the protons in these structures will be used in the discussion of the nmr spectra.....	75
Figure 3.2. Schematic diagram showing relative position of head groups in three possible mixed micelles of C ₁₆ TAB and C8G1: (A) ideal mixed headgroup configuration based on the 3D geometry of the micelles and favorable interactions between headgroups, (B) segregated model where glucoside groups cluster in the corona, and(C) inverted carbohydrate model where the glucoside groups cluster in the core of the micelle.....	76
Figure 3.3. 2D NOESY spectrum of 1:1 C ₁₆ TAB/C8G1 in D ₂ O at 50 °C (total surfactant concentration 30 mM). Cross peaks indicate the NOE correlations between the associated protons and are symmetric along the diagonal. Fig. 3A indicates several sugar-sugar or cationic-cationic surfactant NOE correlations using 600 ms mixing time (cross peak 1) H6 _A & H6 _B proton; 2) α'' _A & α'' _B proton; 3) H3/H4 & H6 _{A,B} proton; 4) H3/H4 & H2 proton; 5) H1 & H2; 6) α' _{a,b} & β' _{a,b} ; 7) α'' _B & β'' _{A,B} ; 8) α'' _A & β'' _{A,B} ; 9) β'' _{A,B} & (CH ₂) _{m+n} ; 10) α' _{a,b} & (CH ₂) _{m+n} ; 11) (CH ₂) _{m+n} & ω'/ω''; 12) α' _{a,b} ,H5 & H3/H4 proton; 13) α' _{a,b} ,H5 & H6 _{A,B} proton; and 14) α'a,b,H5 & H1 proton). Fig. 3B indicates several alkyl tail correlations with the H1 proton of C8G1 using a 1000 ms mixing time (cross peak 15) H1 & α'' _A ; 16) H1 & α'' _B ; 17) H1 & β'' _{A,B} ; 18) H1 & (CH ₂) _{m+n} ; 19) H1 & ω'/ ω'' proton.....	77
Figure 3.4. ¹ H- ¹ H NOESY plane for the C5 carbon of C8G1 taken from the 3D HSQC-C13-NOESY spectrum of 1:1 C ₁₆ TAB/C8G1 in D ₂ O at 50 °C (total surfactant concentration 30 mM). The spectrum shows two cross peaks (circled in blue) below the diagonal peak (H5 proton of C8G1, red contours), indicating sugar—sugar NOE correlations between (cross peak 1) H5 & H6 _{A,B} protons and (cross peak 2) H5 & H1 protons.....	78

Figure 3.5. Fluorescence emission spectra of 2-naphthylboronic acid in glucose and different surfactant solution. Fluorescence intensity reduces in the order of glucose> C8G1> C₁₆TAB> C₁₆TAB/C8G1. Total surfactant or glucose concentration was fixed to 30 mM.....79

Figure 4.1. Molecular structures of (a) C₁₆TA⁺ [TA⁺ denotes a trimethylammonium headgroup] (b) C₁₂TA⁺ (c) C₁₀TA⁺ and (d) C12G1 determined by geometry optimization using the PM3 semiempirical molecular orbital method as implemented in the program Avogadro. The labeling of the protons in these structures will be used in the discussion of the NMR spectra..... 107

Figure 4.2. Pyrene fluorescence emission intensity ratio I₁/I₃ vs. total surfactant concentration for (a) C₁₆TAB/C12G1, (b) C₁₂TAB/C12G1 and (c) C₁₀TAB/C12G1 at 50 °C. In all cases a 1:1 overall ratio of surfactants was used. Arrows denote the mixed cmc values.....108

Figure 4.3. 1D ¹H NMR spectrum of 1:1 (a) C₁₆TAB/C12G1 (b) C₁₂TAB/C12G1 and (c) C₁₀TAB/C12G1 in D₂O at 50 °C (total surfactant concentration 30 mM).....109

Figure 4.4. 2D NOESY spectrum of 1:1 C₁₆TAB/C12G1 in D₂O at 50 °C (total surfactant concentration 30 mM). Cross peaks indicate the NOE correlations between the associated protons and are symmetric along the diagonal. The spectrum indicates several sugar-sugar or cationic-cationic surfactant NOE correlations (cross peak 1) α^{''}_A/H6_A & α^{''}_B proton; 2) H3/H4 & H6_A proton 3) H3/H4 & H2 proton; 4) α^{''}_B & H1 proton; 5) H3/H4 & H1 proton; 6) H1 & H2 proton; 7) α[']_{a,b}/H5 & H3/H4 proton; 8) α[']_{a,b}/H5 & H6_B proton; 9) α[']_{a,b}/H5 & H1 proton; 10) α^{''}_A/H6_A & β^{''}_{A,B} proton; 11) α^{''}_B & β^{''}_{A,B} proton; 12) α[']_{a,b}/H5 & β[']_{a,b} proton; 13) α^{''}_A/H6_A & (CH₂)_{m+n} proton; 14) H6_B & (CH₂)_{m+n} proton; 15) α[']_{a,b}/H5 & (CH₂)_{m+n} proton; 16) β[']_{a,b} & (CH₂)_{m+n} proton; 17) β^{''}_{A,B} & (CH₂)_{m+n} proton; 18) (CH₂)_{m+n} & ω'/ω'' proton).....110

Figure 4.5. 1D NOE spectrum of 1:1 C₁₆TAB/C12G1 in D₂O at 50 °C (total surfactant concentration 30 mM). The only correlation that is seen with the N_{CH₃} protons (in the upper spectrum) is from the α[']_{a,b} protons of C₁₆TAB. The lower 1D NMR spectrum of the mixture is provided for reference.....111

Figure 4.6. 2D NOESY spectrum of 1:1 C₁₀TAB/C12G1 in D₂O at 50 °C (total surfactant concentration 30 mM). Cross peaks indicate the NOE correlations between the associated protons and are symmetric along the diagonal. The spectrum indicates several sugar-sugar or cationic-cationic surfactant NOE correlations (cross peak 1) α^{''}_A/H6_A & α^{''}_B proton; 2) α^{''}_B & H3/H4 proton; 3) α^{''}_A/H6_A & H3/H4 proton; 4) H2 & H3/H4 proton; 5) H3/H4 & α[']_{a,b}/H5 proton; 6) H2 & H6_B proton; 7) α^{''}_A/H6_A & H1 proton; 8) α^{''}_B & H1 proton; 9) H3/H4 & H1 proton; 10) β[']_{a,b} & (CH₂)_{m+n} proton; 11) β^{''}_{A,B} &

(CH₂)_{m+n} proton; 12) ω'/ω" & (CH₂)_{m+n} proton; 13) H₂ & β"_{A,B} proton; 14) α'_{a,b}/H₅ & β'_{a,b} proton; 15) H₁ & (CH₂)_{m+n} proton; 16) α"_A/H_{6A} & (CH₂)_{m+n} proton; 17) α"_B & (CH₂)_{m+n} proton; 18) H₃/H₄ & (CH₂)_{m+n} proton; and 19) α'_{a,b}/H₅ & (CH₂)_{m+n} proton).....112

Figure 4.7. Schematic diagram showing relative position of head groups in ideal mixed micelle of C₁₀TAB and C12G1 based on the 3D geometry of the micelles and favorable interactions between headgroups.....113

Figure 4.8. Molecular structures of (a) C₁₆TA⁺ and (b) C8XT1 determined by geometry optimization using the PM3 semiempirical molecular orbital method as implemented in the program Avogadro. The labeling of the protons in these structures will be used in the discussion of the NMR spectra.....114

Figure 4.9. 1D ¹H NMR spectrum of 1:1 C₁₆TAB/C8XT1 in D₂O at 50 °C (total surfactant concentration 30 mM).....115

Figure 4.10. 2D NOESY spectrum of 1:1 C₁₆TAB/C8XT1 in D₂O at 50 °C (total surfactant concentration 30 mM). Cross peaks indicate the NOE correlations between the associated protons and are symmetric along the diagonal. The spectrum indicates several sugar-sugar or cationic-cationic surfactant NOE correlations (cross peak 1) H₃ & H₄ proton; 2) H₃ & α'_{a,b}/H₂/H_{5B} proton; 3) H₄ & α'_{a,b}/H₂/H_{5B} proton; 4) H_{5A} & α'_{a,b}/H₂/H_{5B} proton; 5) H₁ & α'_{a,b}/H₂/H_{5B} proton; 6) H_N & α"_{A,B} proton; 7) H_{N-1} & H_{N-1'} proton; 8) β"_{A,B} & α'_{a,b}/H₂/H_{5B} proton). In also indicates one sugar-cationic correlation between β'_{a,b} protons of C₁₆TAB with α"_{A,B} protons of C8XT1.....116

Figure 4.11. 1D NOE spectrum of 1:1 C₁₆TAB/C8XT1 in D₂O at 50 °C (total surfactant concentration 30 mM). The spectrum indicates several sugar-cationic NOE correlations (H_N, H_{N-1}, H_{N-1'}, H₁, H₅ and H₄ proton of C8XT1) with the N_{CH₃} protons of C₁₆TAB. There is also a cationic-cationic correlation between α'_{a,b} protons and N_{CH₃} protons of C₁₆TAB. The lower spectrum is the 1D spectrum of the system over the same chemical shift range, for reference.....117

Figure 4.12. Schematic diagram showing relative position of head groups in mixed micelle of C₁₆TAB and C8XT1 based on the 3D geometry of the micelles and favorable interactions between headgroups.....118

Figure 5.1. XRD patterns of C₁₆TAB/C8XT1 templated silica thin films on both modified and PVA-r-PE unmodified substrate after aging at 20±1 °C and 45±5% RH for 2 days.....129

Figure 5.2. TEM images of C₁₆TAB/C8XT1 templated silica thin films at (a) low magnification and (b) high magnification scraped from unmodified substrate after aging at room temperature (23±1 °C) and 45±5% RH for 2 days followed by calcination at 550 °C with a heating at a rate of 0.5 °C/min.....130

Figure 5.3. TEM images of C ₁₆ TAB/C8XT1 templated silica thin films at (a) low magnification and (b) high magnification scraped from modified substrate after aged at room temperature (23±1 °C) and 45±5% RH for 2 days followed by calcination at 550 °C with a heating at a rate of 0.5 °C/min. The inset shows a fast Fourier transform of the upper image.....	131
Figure 6.1. (a) XRD pattern collected in Bragg-Brentano geometry and (b) GISAXS pattern of C ₁₆ TAB templated silica films (after extraction) aged at room temperature (23±1 °C) and 45±5 %RH for 7 days.....	146
Figure 6.2. Representative FT-IR absorbance spectrum of a silica thin film on a silicon wafer templated with a 10:1 ratio of C ₁₆ TAB to C8G1. The film was aged for 7 days at 20±1 °C under a relative humidity of 45±5% prior to measuring this spectrum. The uncoated silicon wafer was used as the background for FT-IR spectra to allow direct transmission measurements to be made.....	147
Figure 6.3. Change in order, as measured by PRI, of C ₁₆ TAB/C8G1 templated silica thin films by varying C8G1 mass fraction after aging at 20±1 °C and 25±5% RH for 10 days.....	148
Figure 6.4. Change in (a) d-spacing and (b) long range order (PRI) with time measured from XRD patterns of 10:1 C ₁₆ TAB/C8G1 templated silica thin films during aging at 20±1 °C and 45±5 %RH.....	149
Figure 6.5. Change in condensation (the ratio of FT-IR intensities of Si-O-Si and Si-OH bands) of 10:1 C ₁₆ TAB/C8G1 templated silica thin films during aging at 20±1 °C and 45±5% RH over a total time scale of 4 days.....	150
Figure 6.6. Change in (a) d-spacing and (b) long range order (PRI) for 10:1 C ₁₆ TAB/C8G1 templated silica thin films after aging at different temperatures at 45±5% RH for 7 days.....	151
Figure 6.7. Change in condensation (from FT-IR bands) of 10:1 C ₁₆ TAB/C8G1 templated silica thin films after aging at different temperatures at 45±5% RH for 7 days.....	152
Figure 6.8. Change in (a) d-spacing and (b) long range order (PRI) of 10:1 C ₁₆ TAB/C8G1 templated silica thin films after aging at different relative humidity at 20±1 °C for 7 days.....	153
Figure 6.9. Change in condensation (from FT-IR) of 10:1 C ₁₆ TAB/C8G1 templated silica thin films after aging at different relative humidity at 20±1 °C for 7 days.....	154

Figure 7.1. SEM images of (a) unsandwiched (b) sandwiched titania films aged at 4 °C and calcined at 400 °C for 10 min after heating at a rate of 40 °C/min. The scale bar in both images is 250 nm wide.....172

Figure 7.2.(a) SEM (scale bar 250 nm) and (b) TEM images (scale bar 100 nm) of unsandwiched titania films prepared by dip coating from sols aged at 4 °C and calcined at 500 °C after heating at a rate of 40 °C/min. Insets are fast Fourier transforms (FFTs) of the images provided to emphasize the lack of long-range order.....173

Figure 7.3. GISAXS patterns of (a) unsandwiched and (b) sandwiched titania thin films after aging at 4 °C for 2 h and just before calcination at room temperature (22.5°C). The films are oriented horizontally (in the xy plane) relative to the incident beam for this experiment.....174

Figure 7.4. GISAXS patterns of (a) unsandwiched and (b) sandwiched titania thin films after aging at 4 °C for 2 h and just after reaching final calcination temperature 500 °C. The films are oriented horizontally (in the xy plane) relative to the incident beam for this experiment.....175

Figure 7.5. GISAXS pattern of (a) unsandwiched and (b) sandwiched titania thin films after heating at 40 °C/min to 500 °C and holding at that temperature for 500 sec. The film is oriented horizontally (in the xy plane) relative to the incident beam for this experiment.....176

Figure 7.6. Evolution of the (100) diffraction peak in the q_y direction for (a) unsandwiched and (b) sandwiched titania thin films during isothermal heat treatment at 500 °C. The plots were generated by integrating slices from the 2D GISAXS patterns for q_z values from 0.06 to 0.07 for times starting after the 40 °C/min ramp to the final temperature.....177

Figure 7.7. Intensity of the (100) reflection vs. time at 500 °C expressed as a ratio to the initial intensity at the end of the 40 °C/min ramp. Data are shown for unsandwiched (filled symbol and solid curve) and sandwiched (open symbols and dashed curve) films. The curves are fits of an exponential function to the initial 5 min (unsandwiched) and 3 min (sandwiched) of data.....178

Figure 7.8.(a) SEM (scale bar 250 nm) and (b) TEM images (scale bar 100 nm) of sandwiched titania thin films on modified glass slides aged at 4 °C for 2 h and calcined at 500 °C. The insets of fast Fourier transforms (FFTs) of the images.....179

Figure 7.9.(a) HRTEM image and (b) Selected area electron diffraction (SAED) pattern and of sandwiched titania thin films on modified glass slides aged at 4 °C for 2 h and calcined at 500 °C.....180

Figure 8.1. SEM images of the top surface of titania films on (a) unmodified (b) modified borosilicate glass slides aged for 2 h at 4 °C and immediately calcined at 500 °C for 60 min after heating at a rate of 40 °C/min.....201

Figure 8.2. GISAXS patterns at room temperature (22.5 °C) of titania thin films (60 nm thick) on (a) unmodified and (b) modified substrate after aging at 4 °C for 2 h but before calcination. The films are oriented horizontally (in the xy plane) relative to the incident beam for this experiment.....202

Figure 8.3. GISAXS patterns of titania thin films (60 nm thick) on (a) unmodified and (b) modified substrate after aging at 4 °C for 2 h and just after reaching final calcination temperature 600 °C with a 40 °C/min ramp rate. The films are oriented horizontally (in the xy plane) relative to the incident beam for this experiment.....203

Figure 8.4. GISAXS pattern of titania thin films (60 nm thick) on (a) unmodified and (b) modified substrate after heating at 40 °C/min to 600 °C and holding at that temperature for 60 min. The film is oriented horizontally (in the xy plane) relative to the incident beam for this experiment.....204

Figure 8.5. SEM images of titania films on (a) unmodified (b) modified substrate titania aged at 4 °C for 2 h and calcined at 600 °C for (a) 60 min and (b) 90 min after heating at a rate of 40 °C/min.....205

Figure 8.6. Normalized (100) diffraction peak height measured from line cuts over q_z values from 0.06-0.07 Å⁻¹ from *in situ* GISXAS data for titania thin films during isothermal treatment at 600 °C after heating at a ramp of 40 °C/min.....206

Figure 8.7. Avrami equation plots based on (100) peak height data for thin titania films on (a) unmodified and (b) modified substrate at different isothermal conditions after ramping at 40 °C/min.....207

Figure 8.8. Arrhenius plot for HCP mesostructure loss of thin (~60 nm thick) titania films on modified and unmodified borosilicate glass substrates.....208

Figure 8.9. Evolution of the normalized (100) diffraction peak height from linecuts taken over q_z from 0.06-0.07 Å⁻¹ from *in situ* GISXAS data of titania thick films on modified borosilicate glass slides during isothermal treatment at 600 °C after heating at 25 °C/min.....209

Figure 8.10. Plot of the (a) linearized Avrami equation (b) Arrhenius equation for thick (~250 nm) titania films on modified borosilicate glass slides at different isothermal conditions after heating at a ramp rate of 25 °C/min.....210

CHAPTER 1

OVERVIEW

Carbohydrates have drawn significant attention in cell and molecular biology due to their pivotal roles in molecular transport,^{1, 2} interaction with proteins,^{3, 4} and responsibility for disease transmission.^{5, 6} As a result, significant advances are being made based on glycobiology in the fields of biointerface engineering,^{7, 8} glycomics,^{9, 10} saccharide sensors,^{11, 12} carbohydrate drug discovery and refinement,^{13, 14} enzyme mimics^{15, 16} etc. These fields would benefit from technologies to recognize and separate specific carbohydrates from mixtures of similar compounds. Also, many carbohydrates (like glucose and xylose) are of growing interest for separation and purification in biofuels production systems and in the production of commodity chemicals from lignocellulosic biomass.¹⁷⁻²⁰ With these applications in mind, it would be invaluable to build an efficient, inexpensive, robust technique to selectively separate valuable carbohydrates generated from breakdown of the large amounts of biomass that are produced every year.

Among all the approaches reported in the literature for high selectivity adsorption, molecular imprinting is possibly the most interesting and promising approach to separate valuable carbohydrates from biomass due to its ability to generate adsorbents with high affinity and selectivity towards the target molecules comparable to natural receptors.²¹⁻²⁶ The first conceptual description of molecular imprinting came from Emil Fischer with his “lock and key” concept in 1894.²⁷ By molecular imprinting we strive to

create molecular binding sites in a stable framework with specific size, shape and functional group arrangement complementary to the target molecule. The binding sites can be formed due to different types of complementary interactions like hydrogen bonds, van der Waals forces, electrostatic interactions and hydrophobic interactions between the targeted moiety and the framework.²⁸⁻³⁰ Molecular imprinting has numerous applications in drug separations,³¹⁻³³ bio-sensors,^{34, 35} catalysis,³⁶⁻³⁸ and antibody mimics.^{39, 40}

In general cross-linked polymers are used to form the network around the templates for molecular imprinting.⁴¹⁻⁴³ However, due to the low thermal, chemical and mechanical stability of many organic polymers it becomes very problematic to build a robust framework for many applications.⁴⁴ Also, the tendency of many polymers to lose imprinted site fidelity due to heating over their glass transition temperature and their non-porous nature provide incentive to better understand the use of inorganic oxide frameworks for molecular imprinting. Metal oxides turn out to be the ideal choice to build the framework due to a combination of (1) high thermal and chemical stability that prevents the loss of imprinted sites and (2) flexibility to tune the binding sites using different organometallic chemistry.⁴⁵⁻⁵⁰

The pioneering work on surfactant templating of ordered silica thin films by Brinker's group⁵¹ drew a significant amount of attention from researchers in the porous materials area due to the potential applications of these templated silica materials based on their large surface area combined with tunable pore size distribution.⁵²⁻⁵⁴

Applications of these templated silica materials are numerous and include sensors,^{55, 56} membranes,^{57, 58} and drug delivery systems.^{59, 60} These surfactant templated silica thin films are also a perfect candidate for molecular imprinting application.^{61, 62} Templated silica thin films are usually synthesized by building the metal oxide frame work around the surfactant templates by evaporation-induced self-assembly (EISA) using dip or spin-coating.^{63, 64}

Carbohydrate surfactants can be used for molecular imprinting as the headgroup complementary to the targeted carbohydrate would create the imprinted sites on the silica network. After forming the material and allowing it to fully cure, we expect to be able to extract all of the surfactants to leave behind imprinted sites complementary to the sugar of interest. The main problem for this synthetic procedure is that many monosaccharide surfactants such as n-octyl- β -D-glucopyranoside (C8G1) favor lamellar phases and are difficult to use to template stable mesophases such as hexagonal phases.⁶⁵ Silica films with well defined hexagonal pores are beneficial for carbohydrate adsorption using molecular imprinting due to their well defined diffusion path and very high surface area.⁶⁶ To overcome their limitations, carbohydrate surfactants are often mixed with cationic surfactants to favor the formation of a hexagonal phase.⁶⁷ The cationic surfactant is introduced to provide electrostatic interactions with the metal oxide structure (and therefore a basis for forming well-defined and well-ordered pores) and the carbohydrate headgroup is present to facilitate molecular imprinting of sites on the metal oxide surface specific to the sugar headgroup. In this way we would be able to build a highly selective, robust technique to separate carbohydrates having similar

structures. Xylose and glucose are a good representative pairs found in plant-derived biomass, as they differ only by one hydroxyl methyl group but otherwise have identical stereochemistry.

Selection of a proper cationic-carbohydrate surfactant mixture is crucial for molecular imprinting because in order to create molecular imprinted sites in mixed surfactant-templated metal oxides it is necessary to have the carbohydrate head group slightly “pushed” outside of the corona region of the mixed micelle in order to have a significant interaction with the metal oxides to create binding sites for molecular imprinting. The interactions and structure of the mixed micelle can be influenced by the choice of tail lengths of the component surfactants and the linkers between the head and tail groups of the surfactants. To know the accessibility of the carbohydrate head group in cationic/carbohydrate micelles, a detailed understanding of the nature of the interactions between the headgroups in the mixed micelles is needed. Although there have been several reports on the interactions between mixed surfactants based on the regular solution theory interaction parameter (β), the interaction parameter only gives information about the bulk interaction energy associated with the mixed surfactants.⁶⁸
⁶⁹ The relative positions of the surfactants in the mixed micelle or the interaction sites between the cationic and nonionic surfactants have not been thoroughly investigated. In this dissertation, a detailed fundamental study was done using nuclear magnetic resonance (NMR) spectroscopy and fluorescence spectroscopy to select a suitable cationic-carbohydrate surfactant combination where the sugar headgroup is slightly

pushed outside of micelles to promote favorable interactions with the silica framework for molecular imprinting.

In addition to the selection of a proper surfactant combination, the pore orientation in the imprinted silica thin films is also important for selective adsorption of carbohydrates. Conventional techniques to synthesize cationic-nonionic surfactant templated silica thin films with 2D HCP well-ordered channels on ordinary substrates (glass slides or silicon wafers) leads to cylindrical channels parallel to the substrate due to the preferential interaction between the polar head groups of surfactants and the hydrophilic substrate.⁵¹ These parallel pores are expected to be inaccessible to the majority of solutes. Cubic bi-continuous structures are a possible way to avoid this problem but are problematic because lateral diffusion can occur as the accessible pores are not isolated from each other.^{58, 70} They also require high surfactant concentrations for their formation, which can cause them to be difficult to stabilize. As a result, templated silica thin film with 2D HCP channels oriented orthogonally to the substrate would be desirable to provide accessible pores with a well-defined short diffusion path into the film. In this dissertation, the surface chemistry of the substrate will be tuned using a random-co-polymer to test the hypothesis that this modification will create orthogonally oriented 2D HCP channels in the imprinted silica thin films.

Apart from synthesizing orthogonally oriented and molecularly imprinted silica thin films, it is also important to stabilize the silica structure during the aging period after film deposition.^{71, 72} The long-time effects of different aging conditions on mixed

surfactant templated silica thin films have not been thoroughly studied although an aging period from hours to days is often used to stabilize silica thin films. Also, the effects of different aging conditions on the long range order of these thin films have not been studied in great detail. In order to achieve the overall goal of demonstrating surfactant-based molecular imprinting on silica films, we need both stability and consistency in the structural properties of the films. Stability in the silica framework is important to eliminate the risk of pore shrinkage and collapse during extraction of surfactant templates, and to provide consistency in the structural properties such as long range order and d-spacing in order to reproduce desirable results regarding molecular imprinting. In this dissertation the effect of different aging parameters including temperature and humidity will be thoroughly investigated using x-ray diffraction (XRD) and Fourier transform infrared spectroscopy (FT-IR) to determine the optimum aging condition to stabilize these imprinted silica films for the specific adsorption of carbohydrates using molecular imprinting.

The last part of the dissertation addresses the effect of pore orientation on the transformation mechanism of polymer templated titania thin films during high temperature curing. Mesoporous titania thin films can be used for energy applications such as solar cells and batteries.⁷³⁻⁷⁶ The geometry and morphology of these metal oxide thin films can be controlled by tuning the surface chemistry of the substrate and templates.⁷⁷⁻⁸⁰ In our study, Pluronic P123 block copolymer was used to tune the pore geometry and the pore orientation. For all mesoporous titania films, controlling the crystallization of the titania after the initial synthesis is both necessary and challenging.

The necessity comes due to the importance of titania crystallinity in controlling the band gap and charge carrier mobilities.^{81, 82} Controlling crystallization is challenging due to the loss of mesostructural order during high temperature crystallization⁸³. The optimization between the mesostructural order and crystallinity must be achieved during curing to have better solar cell efficiency. In this dissertation, we have used in-situ Grazing incidence small angle x-ray scattering (GISAXS) technique in Advanced Photon Source (APS) at Argonne National Lab (ANL) to study the effect of pore orientation on mesostructural order and crystallinity during high temperature curing. The dramatic importance of pore orientation on thermal stability and crystallization mechanism of the ceramic structure will be presented in this part along with mathematical modeling.

1.1. Research Hypotheses

Four hypotheses will be tested in this dissertation. First, to create the mixed surfactant templated silica thin films for specific adsorption of carbohydrates using molecular imprinting, it is hypothesized that a perfect cationic-carbohydrate mixed surfactant system can be selected where the carbohydrate head group is “pushed out” of the mixed micelle to become accessible for molecular imprinting. It is also hypothesized that the hydrophilicity of the surfactant head group, the polarity of the linker, and the tail length of the both surfactants may play a important roles in the relative position of sugar headgroup in mixed micelles. Different nuclear magnetic resonance (NMR) and fluorescence spectroscopy techniques will be used to develop a molecular level understanding of the relative positions of the carbohydrate headgroup in mixed micelles

in response to changes in the structure of cationic and carbohydrate cosurfactants. The results will dictate the selection of a surfactant combination based on surfactant chain lengths and the nature of the linker.

The second hypothesis is that the surface chemistry of the substrate can be selected to make it chemically neutral with respect to the polar head group and tails of the templating surfactants for cationic-carbohydrate templated silica thin films so that pores become orthogonally oriented to the substrate. For that purpose, a random copolymer will be used to modify the substrate chemistry before the cationic-carbohydrate templated silica film deposition and the film structure will be evaluated using x-ray diffraction (XRD) and transmission electron microscopy (TEM). Consistent results with both XRD and TEM will give evidence for orthogonally oriented pores in these mesoporous silica thin films.

Initial study on surfactant templated silica thin films in our group has shown batch to batch variations in long range order and structural stability for a given synthesis procedure. This structural inconsistency leads to the third hypothesis that the evolution of surfactant templated silica structure is not only limited to the initial few minutes after film deposition but also continues for at least several days. It is also hypothesized that the aging temperature and humidity significantly affect the mesostructural order and polycondensation of the templated silica thin films during this longtime aging. Both x-ray diffraction (XRD) and Fourier transform infrared spectroscopy

(FT-IR) will be used to determine the long range order and the polycondensation extent in these cationic-carbohydrate templated silica films.

The fourth and the final hypothesis is that the pore orientation on the P123 templated titania thin films can have a dramatic impact on the transformation mechanism during high temperature curing / crystallization. Pore orientation can dictate both the mesostructural order and the crystallinity of mesoporous titania thin films after high-temperature thermal treatment. To study the transformation kinetics of titania thin films, *in situ* grazing incidence small angle x-ray scattering (GISAXS) will be presented based on measurements at the Advanced Photon Source (APS) at Argonne National Lab (ANL). The *in situ* results will be fit with a kinetic model for phase transformation to compare the rate constant and activation energy for mesostructural deterioration based on the pore orientation. The *in situ* results will be complemented by *ex situ* transmission electron microscopy (TEM) and scanning electron microscopy (SEM) data where the TEM/SEM will provide the direct images of the mesostructures. All these results will help us to select optimum curing condition of these mesoporous titania thin films for energy applications.

1.2. Overview of Dissertation

This dissertation has nine chapters. Chapter 1 gives a general idea about the motivation behind the work presented in the dissertation. It states the hypothesis and the procedures to test them. Chapter 2 presents a brief overview on the different techniques used in the work. It also gives a description of problems faced during the use of these techniques and the possible troubleshooting solutions. Chapter 3 describes an

investigation of the relative positions and interactions between trimethylammonium-based cationic and nonionic carbohydrate-based surfactants in mixed micelles with D₂O as the solvent. This is accomplished using nuclear magnetic Resonance (NMR) spectroscopy and fluorescence spectroscopy. This study focuses on the effects of the structure of the carbohydrate headgroup (glucopyranoside vs. xylopyranoside) of carbohydrate surfactants with fixed hydrocarbon chain length (octyl) on interactions with a cationic surfactant (hexadecyltrimethylammonium bromide, or C₁₆TAB). From this study for the first time an inverted micelle-in-micelle structure was proposed. Chapter 4 continues the search for cationic-carbohydrate surfactant combinations where the carbohydrate head is pushed outside of the mixed micelle. From this study it is shown that even matching surfactant tail lengths is not sufficient to push the carbohydrate headgroup out of the mixed micelle. It is shown that this problem can be overcome by introducing an additional dipolar force to the carbohydrate surfactant using a triazole linker. Chapter 5 describes a simple procedure to prepare carbohydrate/cationic surfactant imprinted silica thin films with orthogonally oriented close-packed cylindrical pores by using a surface modification technique. This is accomplished by using a random copolymer to modify the substrate and neutralize preferential interactions between the headgroup and tail of the surfactants with the hydrophilic substrate so that the pores become vertically oriented and accessible for adsorption. Chapter 6 addresses the effects of aging conditions on the structural and chemical evolution of mixed cationic-carbohydrate surfactant templated silica thin films. The results suggest that the high temperature aging at 50±1 °C in low humid (45±5% RH)

condition is the most suitable condition for well-ordered silica thin films. Chapter 7 demonstrates the pore orientation effect on the transformation mechanism of the pluronic P123 block copolymer templated titania thin films during high temperature curing. The result shows how the pore orientation can dramatically affect both the mesostructural order and crystallization mechanism of these templated titania thin films during high temperature curing. Chapter 8 continues with a detailed kinetic study of the transformation mechanism of the P123 templated thin films. The data are fit with the Avrami equation followed by the Arrhenius equation to compare the rate constants and activation energies for mesostructural deterioration as a function of pore orientation and film thickness. Chapter 9 summarizes the results from this dissertation work and discusses possible future direction to apply these research outcomes for separation and energy applications.

CHAPTER 2

BACKGROUND

2.1. Summary

This chapter briefly reviews prior literatures relevant to our work and several characterization techniques used in this dissertation. It will first give general background information about surfactants, mixed surfactant systems and mesoporous thin films. Then it will introduce the basic procedures to use different instruments used in this thesis and highlight the steps required to interpret the data with an emphasis on methods specific to this work. This part will begin with a discussion of nuclear magnetic resonance (NMR) spectroscopy techniques. Several advanced NMR techniques will be used in Chapters 3 and 4 to measure properties of mixed cationic-carbohydrate surfactant micelles with the goal of giving accessible sugar headgroups for materials synthesis. The chapter then will provide a discussion of fluorescence spectroscopy techniques used to measure different micellar parameters (such as aggregation number) in Chapters 3 and 4. Following this will be a discussion of Fourier transform infrared (FT-IR) spectroscopy and x-ray diffraction (XRD) techniques, which will be used in Chapter 5 to measure change in condensation rate and long range order in silica thin films under different aging conditions. Finally, the chapter will discuss materials characterization techniques starting with grazing incidence small angle x-ray scattering (GISAXS), which is used for ex-situ and in-situ experiments in Chapters 7 and 8 to investigate the transformation mechanism of templated titania thin films during high temperature

curing. The chapter concludes with a brief discussion of transmission electron microscopy (TEM) and scanning electron microscopy (SEM) techniques used to image mesoporous silica and titania thin films in Chapter 5-7.

2.2. Surfactant

The term surfactant is a contraction of “surface active agent” used to describe amphiphilic molecules consisting of covalently bound hydrophilic head groups and hydrophobic tails. These surfactants reduce the surface tension by orienting themselves at the air/solution interface.⁸⁴⁻⁸⁶ Based on the nature of the head group, surfactants can be classified cationic, anionic and nonionic. Cationic surfactants have positively charged head groups and are often used for their softening, antistatic, soil repellent and antibacterial properties.^{87, 88} Examples of cationic surfactants are quaternary ammonium or amine salts with different alkyl chains.⁸⁹ Anionic surfactants have negatively charged head group that helps to interact with the fibers and solid particles, which makes them the most commonly used surfactants for cleaning purposes..^{90, 91} Alkyl sulfates and alkyl-ether sulfates are examples of anionic surfactants.^{92, 93} Nonionic surfactants have drawn attention and market share in the last three decades due to their biocompatibility in many commercial products. The lack of charge in the headgroups of nonionic surfactants makes them capable of forming different complex mixtures for application purposes.^{94, 95} Common examples of nonionic surfactant are fatty acid esters, ethoxylated compounds, and amine, or amide derivatives.⁸⁸ Another important subgroup of nonionic surfactant is alkylpolyglucoside or carbohydrate surfactants.^{65, 96} Carbohydrate surfactants are derived from various carbohydrates

(sugars) and as such have polar, nonionic headgroups. Carbohydrate surfactants are of sustained interest in many industries and research fields due to their biocompatibility and environment friendly synthesis routes from renewable sources.^{97, 98}

All surfactants have the ability under the right conditions to form large organized aggregates, or micelles, beyond a certain concentration known as the critical micelle concentration (cmc).^{99, 100} The cmc is a very important parameter of a surfactant and can be affected by different parameters including temperature, pressure and additives such as salts.¹⁰¹⁻¹⁰³ Hara et al. has reported the pressure dependence of the cmcs of the nonionic surfactant Triton-X-100 (TX100).¹⁰⁴ In their study the cmc of TX100 was found to first increase at low pressures and then to increase with pressure at high pressure (> 100 MPa). In other words the cmc goes through a maximum with increasing pressure. In their study the change in cmc as a function of pressure is related to the partial molar volume change involved in the formation of micelles from monomers. In micelles the compressibility is higher compared to the molecularly disperse state due to the open structure in micelles. As a result of that, the partial molar volume in the micellar state decrease faster than the partial volume in the monomeric state with increasing pressure. At 100 MPa the difference between these two partial volume changes sign and that corresponds to the maximum cmc for that surfactant. Similar trends were also observed for anionic surfactant sodium dodecylsulfate (SDS) and cationic surfactant decyltrimethylammonium bromide (DeTAB) by other groups.¹⁰⁵⁻¹⁰⁷

Mohajeri et al. has reported the effect of temperature on the cmc of nonionic polyoxyethylene sorbitan fatty acid esters.¹⁰⁸ In their study, the cmc decreases initially

and then increases with an increase in temperature. The cmc goes through a minimum at 42 °C for this nonionic surfactant. To form micelle a minimum temperature is required where the solubility is high enough to allow enough surfactant to dissolve to form micelles. This point is called the critical micelle temperature or the Krafft temperature.^{109, 110} Krafft temperature can vary from surfactant to surfactant based on the nature of the head group and tail of the surfactants.^{111, 112} Aggregation number is also an important parameter which indicates the average number of surfactant monomers in micelles. Based on the packing behavior of the head groups and tails, different miceller shapes are also possible including spherical, cylindrical and ellipsoidal, each of which would have different ranges of aggregation numbers.^{113, 114}

2.3. Mixed surfactant system

Mixture of surfactants are often preferred over individual surfactants due to different synergistic effects and comparatively low production costs.^{115, 116} As a result of that, mixed surfactant systems are used widely in different industrial applications including pharmacology, cosmetics and coatings.¹¹⁷⁻¹¹⁹ Mixed surfactant system do not behave the same as individual surfactants in forming micelles. Even ideal systems show variations in partitioning of surfactants between the bulk solution (monomers) and micelles as a function of concentration. This is analogous to vapor-liquid transitions where boiling of a pure substance occurs at a single temperature but for mixtures vapor-liquid coexistence occurs over a range of temperatures and compositions. In addition, many mixed surfactants exhibit nonideal mixing behavior and the properties of these mixed surfactant systems depend on the interactions between the head groups

and also on the interactions between chains.^{87, 120, 121} The composition of mixed surfactant micelles is not the same as the overall composition and is dependent on the surfactant concentration as well.

Several thermodynamic models have been developed for mixed micelles and different micellar properties, such as the composition of the mixed micelle and the mixed cmc, can be calculated based on the interaction parameters in the model. A common model used to interpret mixed micelle cmc values based on regular solution theory has been described by Holland and Rubingh, and this same approach can be extended to Clint's pseudo-phase separation model of micellization.^{68, 122, 123} In the pseudophase approximation, micelles are treated as a separate phase than the bulk phase and chemical potential models can be applied to model nonideal mixing. Clint originally applied the pseudo-phase separation concept to ideal mixed surfactants to develop expressions for cmc (Eq. 1) and micelle composition (Eq. 2).

$$\frac{1}{cmc} = \frac{\alpha_1}{cmc_1} + \frac{1 - \alpha_1}{cmc_2} \quad (1)$$

$$X_1 = \frac{\alpha_1 C - C_1^m}{C - C_1^m - C_2^m} \quad (2)$$

where cmc = mixed cmc, cmc_1 = cmc of first pure surfactant, cmc_2 = cmc of second pure surfactant, α_1 = bulk mole fraction of the first surfactant, X_1 = mole fraction of the first surfactant in the micelle, C = total surfactant concentration in solution, C_1^m = monomeric concentration of first pure surfactant in bulk solution and C_2^m = monomeric concentration of second pure surfactant in bulk solution.

Using regular solution theory model, Clint's model can be extended to describe the mole fraction of each pure component the mixed micelle at the cmc. According to regular solution theory, the micellar mole fraction of the first surfactant component (X_1) in a binary mixture at the cmc can be calculated from the mixed cmc using Eq. 3, and the interaction parameter (β) can be found using Eq. 4.

$$\frac{X_1^2 \ln\left(\frac{\alpha_1 cmc}{X_1 cmc_1}\right)}{(1-X_1)^2 \ln\left(\frac{(1-\alpha_1)cmc}{(1-X_1)cmc_2}\right)} = 1 \quad (3)$$

$$\beta = \frac{\ln\left(\frac{\alpha_1 cmc}{X_1 cmc_1}\right)}{(1-X_1)^2} \quad (4)$$

The interaction parameter β , as the name implies, describes the degree of interaction between two surfactants. This β value can be represented in terms of excess Gibbs free energy if the excess entropy of mixing is assumed to be zero.¹²⁴ As a result of that, a negative β value indicates a synergistic effect or favorable mixing between two surfactants. In contrast, a positive β value indicates antagonistic behavior of the mixture and a β value close to zero indicates almost ideal mixing.¹²⁵ Several studies have reported the effects of different parameters such as tail length, nature of the head group and solvent on the interaction parameter β . According to Sierra et al. the interactions between nonionic alkylglucoside (β -C₁₀G)/alkylmaltoside (β -C₁₀M) surfactants and anionic sodium dodecyl sulfate (SDS) becomes stronger (more negative β value) when the hydrocarbon chain length is shorter and the hydrophilic head group

of the non-ionic surfactant is larger.¹²⁶ They also have shown favorable interactions between two non-ionic surfactants (β -C₁₀G/ β -C₁₀M) which may be related to the packing arrangement of the nonionic head groups in the mixed micelle shown by the MM2 force field molecular mechanics calculation. The most preferred configuration is suggested by this calculation when the sugar head group of β -C₁₀G is located between the two glucose units of maltose headgroup of β -C₁₀M. Wydro et al. has also reported strong interaction ($\beta=-1.28$) between the cationic surfactant hexadecyltrimethylammonium bromide (CTAB) and nonionic surfactant n-dedecyl- β -D-glucoside.¹²⁷ This suggests that the mixing of an ionic surfactant with a nonionic surfactant can result in more favorable interactions between the two headgroups than are seen for each pure species on its own.

Clint's model can be extended using RST to estimate the mole fraction of each pure component in a mixture above the cmc value of the mixture.¹²⁸ The mole fraction (X_1) can be calculated at a total surfactant concentration C by solving equation 5 using a nonlinear equation solver.

$$X_1^2(e^{\beta X_1^2} cmc_2 - e^{\beta(1-X_1)^2} cmc_1) + X_1(C + e^{\beta(1-X_1)^2} cmc_1 - e^{\beta X_1^2} cmc_2) - \alpha_1 C = 0 \quad (5)$$

2.4. Mesoporous silica and titania thin films

Surfactant templated mesostructured silica materials were first reported by kresge et al. by using the evaporation induced self-assembly (EISA) process.¹²⁹ In this process, surfactants act as templates and silica forms the structure around the template by hydrolysis and polycondensation reactions. After formation of a stable structure the

surfactants are removed to form an ordered mesoporous silica material. This technique has several advantages including simple synthesis procedure and excellent control over the mesophase and pore size.^{53, 130, 131} As a result, mesoporous silica materials may be considered to be ideal candidates for high-value materials applications such as low dielectrics, adsorbents, optical materials and membranes.¹³²⁻¹³⁵

In the last three decades several detailed studies have been reported addressing the fundamentals of the sol gel synthesis process of these mesoporous materials along with different characterization procedures and potential applications.¹³⁶⁻¹³⁸ several in situ studies of thin film formation have been done by Brinker's group and Innocenzi's group describing the mesostructural formation and evolution during film synthesis by using in-situ grazing incidence x-ray scattering (GISAXS) and Fourier transform infrared (FTIR) spectroscopy. Brinker's group has shown the composition-structure relationships during the sol-gel synthesis process.¹³⁹⁻¹⁴¹ From their study the effect of solvent evaporation during EISA process on the surfactant aggregates, surfactant-silica interaction and film thickness were established. According to their study, the solvent evaporation rate is directly related to the concentration gradient of solvents in the film. Fast evaporation introduces large concentration gradient whereas slow evaporation introduces homogeneous solution. Based on the concentration gradient, the location at which different phases nucleate in the film and their evolution can be controlled. Also, they have shown that a higher degree of orientation (within the plane of the film) is favored by a slow evaporation rate. Therefore, the evaporation rate can be controlled to form different mesostructures or to change the long range order. Although their studies have

shown the importance of the initial few minutes during film deposition for dictating phase or long range order, they do not describe the evolution of mesostructural changes over the time scale typically used for film aging.

Innocenzi's group has investigated the various stages during film formation and also the order-disorder transitions during the thermal annealing procedure.¹⁴² Babonneau and coworkers have shown the ability to form different mesophases such as cubic, 2D hexagonal and 3D hexagonal by introducing slight change in the synthesis procedure during EISA.¹⁴³ Grosso et al. has shown the effect of condensation rate on the orientational order of the pores in the silica thin films.¹⁴⁴ Their work also suggests the importance of controlling different parameters including humidity, coating sol pH and ethanol vapor pressure.^{63, 145} For example the variation of relative humidity from 20% to 70% can transform the mesostructure from poorly ordered to 2D hexagonal and then 3D cubic during film deposition for CTAB templated silica thin films. According to their study, the humidity can change the solvent vapor pressure just after film deposition and can introduce film composition change that influence the final organization of the mesostructure. All of these studies contribute to better understand the EISA procedure for well-ordered mesoporous silica films formation. However, the long-time effect of process parameters on evolution of films after deposition was not studied and needs further investigation.

Mesoporous titania thin films have drawn a significant amount of attention due to their high surface area, tunable pore size, thermal stability, and unique optical and electronic properties.¹⁴⁶⁻¹⁵⁰ As a result, there are numerous applications of mesoporous titania thin

films in the field of catalysis, photovoltaic and membrane applications.¹⁵¹⁻¹⁵⁴ Coakley et al. has shown a simple synthesis technique to apply mesoporous titania thin films for organic-inorganic photovoltaics where 33% of the total volume of the thin films can be filled with semiconducting polymer¹⁵⁵. Achieving this level of polymer loading is challenging because of the loss of conformational entropy of polymers upon confinement in pores whose radius is less than the radius of gyration of the polymers. This loss of conformational entropy inhibits infiltration into the pores and reduces the efficiency of the photovoltaics due to limited contact between the polymer and oxide semiconductor. In a different approach, Zukalova et al. showed that organized mesoporous titania films exhibit greatly enhanced solar conversion efficiency (by about 50%) in dye-sensitized solar cells compared to traditional films of the same film thickness made from randomly oriented anatase nanocrystals.⁷⁴ According to Choi et al. mesoporous photocatalytic titania films can be used as membranes for different environmental applications.¹⁵⁶ Mesoporous titania materials can also be used to prepare anode materials in lithium ion batteries due to several advantages including excellent cycle stability, small volume expansion during intercalation-extraction of Li ions, and high discharge voltage plateau.¹⁵⁷⁻¹⁵⁹ Titania thin films can be produced by the surfactant templated EISA process using either spin or dip coating. Several reports have shown the tunability of this EISA process to prepare mesoporous titania thin films with different mesophases. For example Alberius et al. has shown a general predictive synthesis route to prepare cubic, hexagonal and lamellar mesostructured titania films.¹³⁸

One of the unique property of titania is the phase transformation of titania during high temperature curing. Titania is amorphous at room temperature but forms anatase crystallites above 400 °C. Further heating leads to the anatase-rutile phase transformation around 700 °C.¹⁶⁰ The crystallization of titania controls the energy band gap and electron mobility of the material. These factors dictate the light absorption and electronic properties of the materials and therefore their photochemical and photovoltaic performance. Several studies have been done to follow the kinetics of titania crystallization. Zhang et al. described the crystallization kinetics of nanometer-sized titania as a four step process.¹⁶¹ According to their study, the process begins with interfacial nucleation of anatase at contact areas between amorphous particles followed by crystal growth of anatase by redistribution of atoms from smaller anatase crystals or amorphous particles onto the nanocrystal surfaces. Finally, the oriented attachment of adjacent anatase particles which are in favorable orientation occurs. They have measured activation energies associated with each step. Kirsch et al. reported the activation energy for crystallization of mesoporous titania thin films by using the Avrami equation to model kinetics of structural transitions and the Arrhenius equation to describe the temperature dependence of rate coefficients.¹⁶² The Avrami equation is often applied to model the kinetics of phase transformation of solid materials at isothermal condition.^{163, 164} It is also known as Johnson-Mehl-Avrami-Kolmogorov or

JMAK equation and is given by Eq. 6:

$$-\ln(1 - \alpha) = (kt)^n \quad (6)$$

where α = amount of transformed material, t = time, k = temperature dependent rate constant and n = transformation propagation parameter.

The value of n dictates the nature of transformation or the mechanism of crystal growth.^{164, 165} For example if the value of $n=1$, one-dimensional surface-nucleation dominated crystallite growth is indicated. All of these studies help us to better understand the kinetics of crystallization of titania.

2.5. Spectroscopy techniques

2.5.1. Nuclear Magnetic Resonance (NMR) Spectroscopy

NMR is a very powerful technique that gives several modes to directly characterize molecular interactions between different nuclei¹⁶⁶⁻¹⁶⁹. It is based on the magnetic spin of the nucleus and only applicable for the molecules those have non-zero overall nuclear spin (including ¹H, ¹³C, ³¹P and ²⁹Si)¹⁷⁰⁻¹⁷³. Here, different types of NMR techniques will be used to investigate the proximity of the carbohydrate and cationic surfactant headgroups in cationic-carbohydrate surfactant mixed micellar systems. For all NMR experiments the samples were prepared by dissolving the surfactant mixtures in D₂O (deuterium oxide), which not only reduces interfering peaks that would be generated by H₂O but also provides a ²H signal that can be used to shim and lock the magnetic field of the sample. The total surfactant concentration was fixed to 30 mM, which (as we will discuss) is above the critical micelle concentration (cmc) of the surfactant in the mixture,

and well above the cmc of the mixed surfactant systems employed. Samples were prepared in 5 mm borosilicate glass NMR tubes sealed with a plastic caps. Both 400 MHz and 600 MHz varian NMR spectrometers were used for our experiments, and for consistency of interpretation the sample temperature was fixed at 50 °C with a variable temperature (VT) controller. This temperature was chosen because it is above the highest Krafft temperature of surfactants employed (n-octyl- β -D-xylopyranoside) and is consistent with temperatures used in synthesis of templated materials by nanocasting⁶⁷. The following sections will briefly describe the procedure employed for different NMR techniques.

1D proton (¹H) NMR

1D proton NMR is a standard technique based on measuring the spectrum of ¹H nuclei (always available on NMR instruments because of the high natural abundance of this nucleus), and provides information about the local chemical environments of the different types of hydrogen and their relative number in a given sample¹⁷⁴⁻¹⁷⁶. To collect a proton NMR spectrum, an NMR tube containing the desired surfactant mixture was first loaded into the NMR spectrometer and a standard proton NMR experiment was selected from the instrument software. The temperature was raised to 50 °C and 5 minutes after reaching the final temperature (50 °C) the sample was locked and shimmed (which refers to the process of adjusting the magnetic field in the probe to give an optimal field around the sample) using standard procedures. The rate of spinning the sample was set to 20 Hz to avoid artifacts due to subtle imperfections in the NMR tube. After this setup, a preliminary proton NMR spectrum was collected using

16 scans. To improve the quality of the spectrum the pw90 (the pulse width that rotate the magnetization from the direction of the magnetic field (the z axis) to the xy plane to produce the largest signal in a single scan) was calibrated at fixed transmitter power (tpwr) by collecting spectra with an array of values of the 'pw' parameter. After calibrating the value of pw90, its value was used as the pulse width in the standard proton NMR pulse sequence and the experiment was repeated with 64 scans. Finally the spectrum was referenced (to set the chemical shift scale) by using the partially hydrogenated D₂O peak as the reference. This and all other data were saved on machines in the Chemistry Department NMR facility for future reference. Figure 2.1 shows a representative proton NMR spectrum of a 30 mM C₁₆TAB/C8G1 1:1 mixture in D₂O. 1D spectra are interpreted based on standard ranges of chemical shifts encountered for nuclei of interest and splitting patterns caused by coupling among nuclei. However, the spectrum exhibits significant complexity due to coupling among ¹H nuclei in the carbohydrate headgroups, and peaks were assigned to different protons in the two surfactants using 2D techniques as discussed in Chapter 3. Note that some peaks are relatively broad (such as the (CH₂)_{n+m} peak) due to the wide variety of local chemical environments found in a micellar system. The narrow carbohydrate peaks (such as the H1 peaks) are more typical of the resolution provided by ¹H NMR.

Spin-lattice (T₁) and spin-spin (T₂) relaxation measurements

It is common to measure rates of relaxation of various nuclei in the field of the spectrometer while performing NMR experiments. Knowing these parameters not only allows one to choose conditions to give meaningful results (such as selecting a delay

between pulses that will give quantitative results) but also provides insight into the local molecular environments of the nuclei. T_1 is the relaxation time constant of the nuclear magnetization vector in the direction parallel to the magnetic field due to the transfer of energy from a nucleus to the surrounding medium by tumbling, whereas T_2 is proportional to the time required for nuclear magnetization vector to relax in the plane perpendicular to the magnetic field due to interactions with other spins in the mixture^{177, 178}. From an instrumental point of view, T_1 is important because it dictates the fastest rate of repeating pulses without introducing artifacts and T_2 determines the rate at which signal decays in the plane perpendicular to the main field, which is inversely related to the width of NMR peaks.

Generally, T_2 decreases as a nucleus enters into an environment with a higher local density of spins, or if the lifetime of interactions with neighboring spins increases (for instance, in a more viscous environment). For small molecules with rapid tumbling, the dependence of T_1 and T_2 on molecular mobility is the same, but for low molecular mobilities, T_1 follows the opposite trend from T_2 ; as the local density surrounding a nucleus increases or the mobility decreases, T_1 is expected to *increase* due to slow tumbling while T_2 decreases.¹⁷⁹⁻¹⁸¹ Thus, comparing these two parameters is a good way to learn about the local environment experienced by parts of a molecule in a micellar environment.

For T_1 measurement experiments, the procedure begins with the same setup as for a 1D proton spectrum using the calibrated pw90 value. Then the experiment parameters were moved to another experiment using the inversion recovery (INVREC) pulse

sequence for T_1 measurements. In this experiment, a 180° pulse is applied to flip the magnetization of a nucleus followed by a delay and a 90° pulse and signal measurement. The delay time is varied to allow relaxation to occur to varying degrees. An exponential recovery is observed with a time constant equal to T_1 . The following parameters were used: recycling delay (d_1) = 15 sec, number of transient (nt) = 8 and number of points (np) = 8192. The parameter d_2 (the delay between the pw180 pulse and pw90 pulse) was arrayed from 0.05 to 6.07 sec with 25 values and with exponential increment. The pulse sequence was checked again to make sure the right pw90 and d_1 values were entered into the pulse sequence. The required timing for this experiment was checked and then the experiment was run. After completing the experiment the threshold value was set on the 1D proton NMR spectra and then the T_1 analysis tab was pressed from control panel to get the T_1 values for each peak (by fitting exponentials to the recovery intensities) with standard error. The experiment was saved for future reference. From this T_1 values and standard errors of the T_1 values for each peak with 95% confidence interval were calculated.

For T_2 experiments a proton NMR spectrum was first collected with calibrated pw90 and then the parameters were moved to a new experiment. In the new experiment the Carr-Purcell Meiboom-Gill (CPMG2) pulse sequence was selected for T_2 analysis. In this spin echo pulse sequence, a 90° pulse is first applied to move magnetization into the xy plane. A delay is applied followed by a 180° pulse to flip the magnetization vector followed by a second delay equal to the value of the first. The two delays allow magnetization vectors to refocus so that signal can be performed, and by increasing the

duration of the delay, greater relaxation in the xy plane occurs before measurement. Basic NMR parameters were $d_1 = 40$ sec, $nt = 4$ and $np = 32768$. The parameter 'bigtau' (which defines the delays between pulses) was arrayed from 0.001 to 2.44 sec with 40 values and exponential increments. Then the pulse sequence and the required time for the experiment were checked. After verifying the pulse sequence, data acquisition was started for the T_2 experiment. After completing the experiment the threshold value was fixed and the intensity vs. τ values were collected for each peak. The experiment was saved for future reference. Fitting was done using a single exponential using the following equation:

$$I = A * e^{-\tau/T_2}$$

where I = intensity, τ = spin echo delay and T_2 = spin-spin relaxation time. Sigmaplot software was used to calculate the T_2 parameter and standard error. These standard errors were used to calculate the 95% confidence interval of T_2 values for each peak.

Correlation spectroscopy (COSY)

COSY allows one to identify the proximity of the homonuclear spins which are correlated by through-bond coupling generally over up to 3 or 4 bonds^{182, 183}. It is the simplest and most widely used NMR experiment to analyze bonding configurations in chemical structures.¹⁸⁴⁻¹⁸⁶ This technique is very useful when multiplets overlap or excessive coupling complicates the 1D spectrum. It is mostly used for analyzing coupling relationship between protons but it can also be used for other highly abundant homonuclear spins including ^{19}F , ^{31}P and ^{11}B .¹⁸⁷⁻¹⁹⁰

To run this experiment, a 1D proton NMR spectrum was first collected with calibrated pw90. Then the spectral width (sw) of the spectra was selected according to the desired chemical shift range. The parameters were moved to a new experiment and the gDQcosy pulse sequence was selected for a gradient enhanced double quantum filtered COSY experiment. The following parameters were used: $d_1 = 6$ sec, number of transients to reach steady state (ss) = 32, nt = 4 and np=ni=576. The pulse sequence and estimated time were checked before acquiring the data. After completing the experiment the 2D data were collected and the experiment was saved for future reference. Figure 2.2 shows a representative COSY spectrum of C₁₆TAB/C8G1 1:1 mixture. In the 2D COSY spectrum, the cross peaks appear when there is a correlation due to spin-spin coupling through bonds between the associated protons and are symmetric along the diagonal. The “sequential walking” procedure is normally used to identify different correlations in COSY spectra.¹⁹¹ The first step for this procedure is to match the diagonal peaks to the equivalent resonances in the 1D spectrum. Then one can start from a diagonal peak and draw a horizontal line to the nearest cross peak then from the cross peak draw a vertical line and see which diagonal peak it intersects. This cross peak will indicate the correlation between the two associated diagonal peaks. For example in Figure 2.2 a horizontal line is drawn from the diagonal peak of the H1 proton of C8G1 which hits the number 4 cross peak. From the number 4 cross peak another vertical line is drawn which hits the diagonal peak of the H2 proton. Therefore, cross peak 4 correlates the H1 and H2 protons in Figure 2. The rest of the assignments from this spectrum will be discussed in Chapter 3.

Heteronuclear correlation spectroscopy (HSQC)

HSQC is a NMR technique that correlates coupled heteronuclear spins across single bonds^{192, 193}. This technique is highly effective to identify directly attached nuclei such as ^1H - ^{13}C correlations in hydrocarbon molecules. To run this experiment, first 1D proton and 1D carbon NMR spectra were collected. The calibrated pw90 (for both ^1H and ^{13}C), spectral width (sw) and transmitter offset frequency (tof) were noted. Then in a new experiment, the gradient enhanced heteronuclear single quantum coherence (gHSQC) pulse sequence was opened and the parameters collected from the previous ^1H and ^{13}C NMR experiments were used. The following parameters were also used: $d_1 = 5$ sec and $np = ni = 576$. The pulse sequence and estimated time were checked and the data acquisition was started. After completing the experiment the 2D data were collected and was saved for future reference. Figure 2.3 shows a representative HSQC spectrum of $\text{C}_{16}\text{TAB}/\text{C8G1}$ 1:1 mixture. In the HSQC experiment there are two types of correlations that can be seen. Those with dark spots indicate the correlation of carbon that are directly attached to an odd number of proton(s) (called a positive correlation). The other correlation presented by white spots indicates carbons that are directly attached to an even number of protons (i.e. a negative correlation). By correlating these spots with the associate peaks in the 1D spectra we can identify the directly attached carbon and hydrogens nuclei in our molecules to make definitive assignments of the identify of peaks. For example in Figure 2.3 vertical and horizontal lines (in blue) drawn from dark spot 1 correlates the C1 carbon and H1 proton of C8G1, respectively. This indicates that the H1 proton is directly attached to the C1 carbon and the cross-peak is dark because a

single proton is attached. Similarly, vertical and horizontal line (in red) drawn from white spot 9 correlates the C6 carbon with the H_{6A,B} protons. Because two protons are involved in the correlation, the cross-peak is light in color. The rest of the peak assignments from this spectrum will be discussed in Chapter 3.

Nuclear Overhauser effect spectroscopy (NOESY)

NOESY is a very useful NMR technique to identify the interaction between the spins which are directly correlated by through-space dipolar coupling^{191, 194, 195}. The NOE is a cross-relaxation process occurring between protons that are less than 5 Å apart. In our mixed surfactant system this technique is a very useful tool because it can directly give us information about the relative position of the carbohydrate headgroup in mixed micelles by correlating protons in close proximity from the carbohydrate and cationic surfactant. To run the 2D NOESY experiment, a 1D proton NMR spectrum was first collected with calibrated pw90. Then the spectral width (sw) was selected according to the desired chemical shift range and the proton spectrum was rerun. Then the referencing of the spectrum (using peaks from partially protonated D₂O) and integration of the peaks were done, and the data was saved for future reference. Then the parameters were moved to another experiment and the NOESY pulse sequence was opened. The following parameters were used: d₁= 3 sec, nt=8, ni=np=512 and ss=128.

The mixing time (mixN) is a very important parameter because in this mixing time period the NOE grows and then decays. If we select a very small mixing time, then some NOEs may not develop in that time. If, on the other hand, we select a very long mixing time then some NOEs may decay to zero and cannot be detected. The proper mixing time can

be selected by considering the spin-lattice (T_1) relaxation values for the protons because the NOE reaches its maximum when the mixing time is on the order of the T_1 relaxation value. For molecules having protons with different T_1 values it is best to first fix the mixing time equal to the shortest T_1 value and then to vary the mixing time up to the longest T_1 value. In our case we first fix the mixing time to 600 ms and then vary it up to 1700 ms. After setting all the parameters the data were acquired. After completing the data acquisition the 2D data was collected and saved for future reference. Figure 2.4 shows a representative 2D NOESY spectrum of the $C_{16}TAB/C8G1$ 1:1 mixture. In this figure we can see several cross peaks. These cross peaks are symmetric across the diagonal and indicate protons correlated through space via NOE interactions.

There are generally two types of NOE correlations that we can expect in this spectrum. One is between protons from the same types of surfactants and other one is between protons from two different surfactants. Both of these NOEs are caused by through-space correlations. One can determine the correlated protons by drawing vertical and horizontal lines from a particular cross peak. For example, in Figure 2.4 vertical and horizontal lines are drawn from cross peak 5 which intersect the diagonal peaks of the H2 proton and H1 protons, respectively. Therefore, cross peak 14 represents the NOE correlation between the H2 proton and H1 proton. The assignment of the rest of the cross peaks will be discussed in Chapter 3.

For a 1D NOE experiment, a calibrated 1D proton NMR spectrum was first acquired. Then the 'cyclenoe' pulse sequence was used with the following parameters: d_1 (relaxation delay) = 6 sec; nt (number of transient) = 32; np (number of points) = 8192;

satpwr (saturation power)=-16; sattime (saturation time)= 4 sec and MixN (mixing time)=600 ms. In this pulse sequence, radiation is done from protons of interest so peaks associated with the irradiated proton through NOEs are observed. The protons of interest were subject to saturation in half the transients collected, whereas an off-resonance position was subjected to saturation in the other half of the transients. The spectrum resulting from off-resonance saturation was subtracted from the one obtained with saturation of protons of interest to yield a difference spectrum in which only resonances affected by cross-relaxation with protons of interest appear. After setting all the parameters the data acquisition was done. The 1D NOE data was collected and saved for future reference.

Figure 2.5 shows a representative 1D NOE spectrum of a C16TAB/C8G1 1:1 mixture. The lower part of the 1D NOE spectrum is the normal 1D proton spectrum whereas the upper part denotes the spectrum after subtraction. In the subtracted part, two types of peaks can be seen. The first is the radiated peak, which normally appears in negative phase, and the second are NOE peaks that appear in positive phase. From the NOE peak one can draw a vertical line which intersects the related peak in the proton spectrum to allow the protons correlated to the irradiated peak to be identified. For example, in Figure 2.5 one vertical line is drawn from the NOE peak to show the correlation between the radiated peak of N_{CH_3} (negative phase) and the correlated $\alpha'_{a,b}$ protons. More 1D NOE experiments and their interpretation will be discussed further in Chapter 3.

2.5.2. Fluorescence spectroscopy

Fluorescence spectroscopy is a very important tool to characterize different micellar parameters such as critical micelle concentration (cmc) and aggregation number¹⁹⁶⁻¹⁹⁹. It is based on the energy emission of a probe molecule due to the transfer of electron from an excited state to another excited state or the ground state^{200, 201}. It has many advantages: first, high sensitivity so that a very small amount of the probe molecule can be added to avoid perturbing the configuration of our original system. Second, many probe molecules are available that are solvatochromic, meaning that their emission characteristics vary with respect to the local solvation environment. Third, energy transfer between excited probe molecules and other molecules in close proximity so that experiments can be designed that take advantage of fluorescence quenching phenomena. In the following paragraphs we will briefly describe the procedures to calculate different micellar parameters.

Critical micelle concentration (cmc) determination:

Fluorescence measurements using pyrene as a probe were used to measure the critical micelle concentration (cmc) of surfactant mixtures.^{99, 202} Fluorescence experiments were performed with a Varian Cary Eclipse fluorescence spectrophotometer (Walnut Creek, CA) at room temperature. Emission spectra were collected using an excitation wavelength of 335 nm. An aliquot solution of pyrene dissolved in ethanol was transferred from stock solution to a beaker and the solvent was evaporated with dry nitrogen. Surfactant mixtures dissolved in water were added according to the required concentrations. The pyrene concentration (0.001 mM) was kept constant for every

experiment. For mixed cmc measurements, the total surfactant concentration was varied from 0.9 mM to 2.5 mM. Figure 2.6 shows the ratio of two pyrene fluorescence emission bands appearing at 374 nm (I_1) and 387 nm (I_3) vs. total surfactant concentration curve for DeTAB/C12G1 1:1 mixed cmc calculation. This ratio is a measure of polarity near pyrene, where a lower value indicates a less polar microenvironment.^{203, 204} The break point in each plot is considered to be the cmc of the mixture²⁰² because pyrene is able to partition from the polar aqueous environment into the more nonpolar environment provided by micelles. We will discuss cmc values determined by pyrene solvatochromism in Chapter 5.

Aggregation number calculation

Steady state fluorescence quenching experiments allow the determination of the absolute concentration of micelles in solution based based on the effect of an added quencher on the intensity emitted from a probe molecule dissolved in the micelles. In aggregation number studies, the total surfactant concentration was fixed at 30 mM (the concentration used for all other measurements). Hexadecylpyridinium chloride was used as a quencher and its concentration was varied from 0 mM to 0.8 mM. The mean aggregation number (N_{agg}) of these surfactant mixtures was calculated using steady state quenching of solubilized pyrene by hexadecylpyridinium chloride. The mean

aggregation number was calculated using following equation ²⁰⁵:

$$\ln\left(\frac{I}{I_0}\right) = -\frac{(N_{agg}[Q])}{(c-cmc)}$$

where I = fluorescence intensity in the presence of quencher, I_0 = fluorescence intensity in the absence of quencher, $[Q]$ = concentration of quencher, and c = total surfactant concentration.

Figure 2.7 shows a representative figure of the raw pyrene emission spectra used for aggregation number calculation of a DeTAB/C12G1 1:1 mixture. We can see the effect of quencher concentration on the fluorescence intensity. From $\ln(I_0/I)$ vs $[Q]$ curve shown in Figure 2.8. The slope is found by linear regression and used to calculate the aggregation number. We will discuss more about these measurements in Chapter 4.

2.5.3. Fourier transform infrared spectroscopy (FT-IR)

FT-IR is a powerful spectroscopy technique for the chemical analysis of the sample materials based on the different vibrational modes of the material components ^{206, 207}. For this technique, an infrared beam is passed through the sample materials and during that time some the radiation is adsorbed and rest of it transmitted through. Due to the different vibrational modes of the chemical bonds, the adsorption and transmission characteristic of different species vary, which permits analysis the different chemical component in the materials. In our study, FT-IR was collected directly in transmission mode for films cast onto silicon wafers using a ThermoNicolet Nexus 470 instrument

with a MCT detector. The films needed to be thin (<200 μm thick) to transmit sufficient infrared intensity for the measurement to work well. Prior to film deposition, the spectrum of the bare silicon wafer was collected and used as the background of that particular sample throughout all subsequent measurements. It was important to be sure to reposition the wafer in exactly the same place in the transmission holder to avoid interference from background changes.

Figure 2.9 shows a representative FT-IR absorbance spectrum of surfactant templated silica thin films. We can identify different vibrational modes in this spectrum. First, in the 3200-3400 cm^{-1} range there, O-H stretching bands appear due to SiO-H dangling bonds and adsorbed water.²⁰⁸ In the 2800-3000 cm^{-1} range there are two bands, both are associated with the CH_2 stretching vibrations of the surfactant. At low wave numbers, two bands appear. The first one at 1160 cm^{-1} represents anti-symmetric stretching of the oxygen atom in Si-O-Si bonds and the second one at 950 cm^{-1} correspond to Si-OH stretching of silanols. These bond vibrations indicate the presence of different species in the materials. For example the CH_2 bands indicate the presence of surfactants in the material. Also, the relative intensities of the Si-OH stretching and Si-O-Si stretching bands can be taken as a measure of the extent of condensation in the material. FTIR spectra will be discussed in more detail in Chapter 5.

2.6. Materials Characterization

2.6.1 X-ray diffraction (XRD)

X-ray diffraction (XRD) is a very useful tool to get the information about the atomic-to-nm scale structure of the ordered or crystalline materials. It is based on the principle of

the interference of the diffracting monochromatic X-ray beams from any materials having well defined spatial arrangements^{209, 210}. The interference of the x-ray beams are governed by Bragg's law²¹¹ given

by:

$$n\lambda = 2d\sin(\theta)$$

where d is the interplanar distance or d -spacing, θ is the scattering angle, λ is the characteristic wave length and n is an integer. Figure 2.10 shows the schematic of the x-ray diffraction where the diffracted rays interfere. For conventional XRD we use diffractometer based on the Bragg-Brentano geometry²¹² in which both the incident angle (θ) and the detector angle (2θ) are varied normal to the thin film sample. Here, x-ray diffraction (XRD) was performed on thin films using a Bruker D8 Advance instrument. During XRD characterization a scan speed of 1 degree/min was accomplished by a lock coupled method.

Figure 2.11 shows a representative XRD pattern of a C₁₆TAB templated silica thin film. Diffraction peaks are obtained due to the periodic order in the mesostructure. If there is a long range order in the material then multiple peaks due to higher order reflections can be seen. From the relation between these peaks one can assign the different crystallographic structure for the materials. For example, in the case of 2D hexagonal phase, the d -spacing ratios for (100), (110), (200), (210) and (300) planes would be expected to follow the sequence 1: $1/\sqrt{3}$: $1/\sqrt{4}$: $1/\sqrt{7}$: $1/\sqrt{9}$. On the other hand, for the Ia3d cubic phase, the d -spacing ratios for the (211), (220), (321), (400), (420), (332) and (422) planes would be expected to follow the sequence $1/\sqrt{6}$: $1/\sqrt{8}$, $1/\sqrt{14}$: $1/\sqrt{16}$:

$1/\sqrt{18}$: $1/\sqrt{20}$.^{128, 213} Unfortunately, in Figure 2.11 we can see only two peaks due to the orientation of the mesophase in the thin film. These peaks can either be indexed as the (100) and (200) planes of the 2D hexagonal phase, or indexed as the (220) and (400) planes of the Ia3d cubic phase. To make a final assignment, other techniques such as grazing incidence small angle x-ray scattering or transmission electron microscopy are needed. XRD results will be discussed in more detail in Chapter 5.

2.6.2. Grazing incidence small angle x-ray scattering (GISAXS)

GISAXS is a very powerful technique to characterize the structure of the meso- or nanoscopic objects at surfaces or in thin films. It is based on the combination of small angle x-ray scattering and grazing incidence diffraction principles^{214, 215}. Figure 2.12 shows a schematic of the GISAXS experiment geometry in which α is the incidence angle, β is the exit angle, and ϕ is the scattering angle in the surface plane. q_y and q_z are the scattering vectors in the 2D detector. The incidence angle α is close to the critical angle (the angle at which total external reflection of the x-ray beam occurs) of the sample material and by varying the incidence angle we get the structure property information along the thickness of our materials. Because it is a nondestructive technique sensitive to orientation and structure changes, GISAXS was an important tool for in-situ studies the transformation mechanism of surfactant templated titania thin films in Chapters 7 and 8.

All of the *In-situ* GISAXS experiments were done at the Advanced Photon Source at Argonne National Laboratory on beamline 8-ID-E using a wave length of 1.687 Å and a sample-detector distance of 1040 mm. Aged samples were placed on a sample holder

which was connected with heating coils and then heated to a desired final calcination temperature with different ramp rates. After reaching the final calcination temperature, all samples were kept at that temperature during *in situ* GISAXS measurements. The heating device used was a stainless steel block with a temperature controller. The thermocouple used for temperature control was placed on the titania film as close as possible to the sampled area without interfering with the scattering. A GISAXS pattern was collected at room temperature before heat was turned on and again after the final temperature was attained, at which point the sample was realigned. *In-situ* data were collected with a Pilatus 1M pixel array detector using a 1 sec exposure time. Images were corrected for detector nonuniformity and converted to q-space using the GIXSGUI package for Matlab. Figure 2.13 shows the GISAXS pattern of the titania thin films with oriented pores. This particular sample shows Bragg rods on both sides of the beam stop consistent with vertically aligned columnar pores, but different diffraction patterns will be discussed in more detail in Chapters 7 and 8.

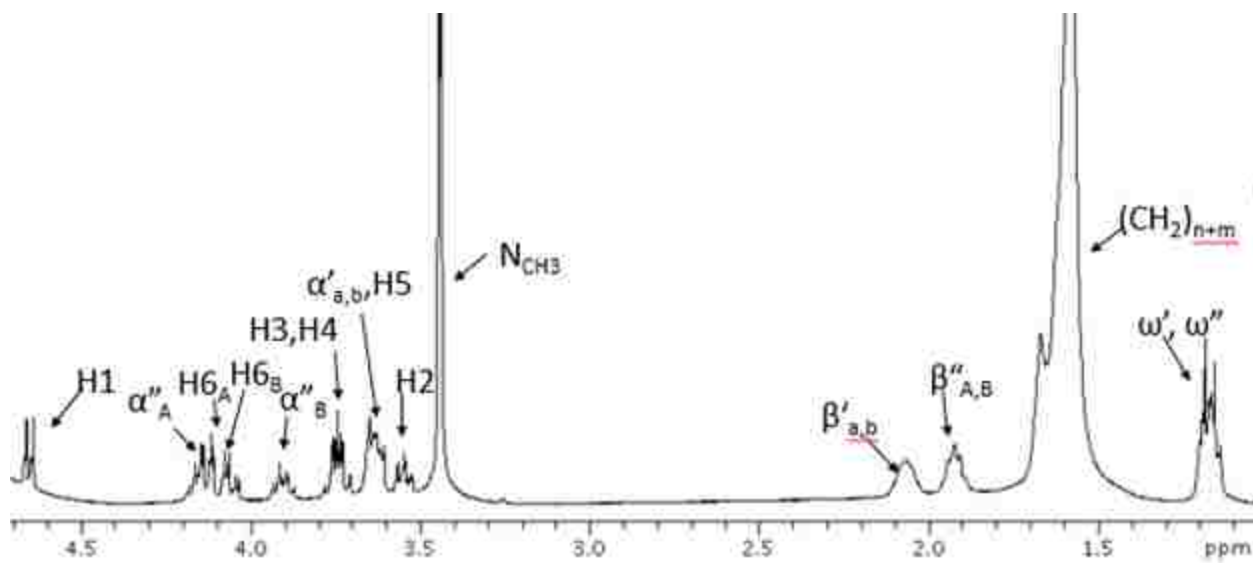


Figure 2.1. 1D ^1H NMR spectrum of 1:1 $\text{C}_{16}\text{TAB}/\text{C8G1}$ in D_2O at $50\text{ }^\circ\text{C}$ (total surfactant concentration 30 mM).

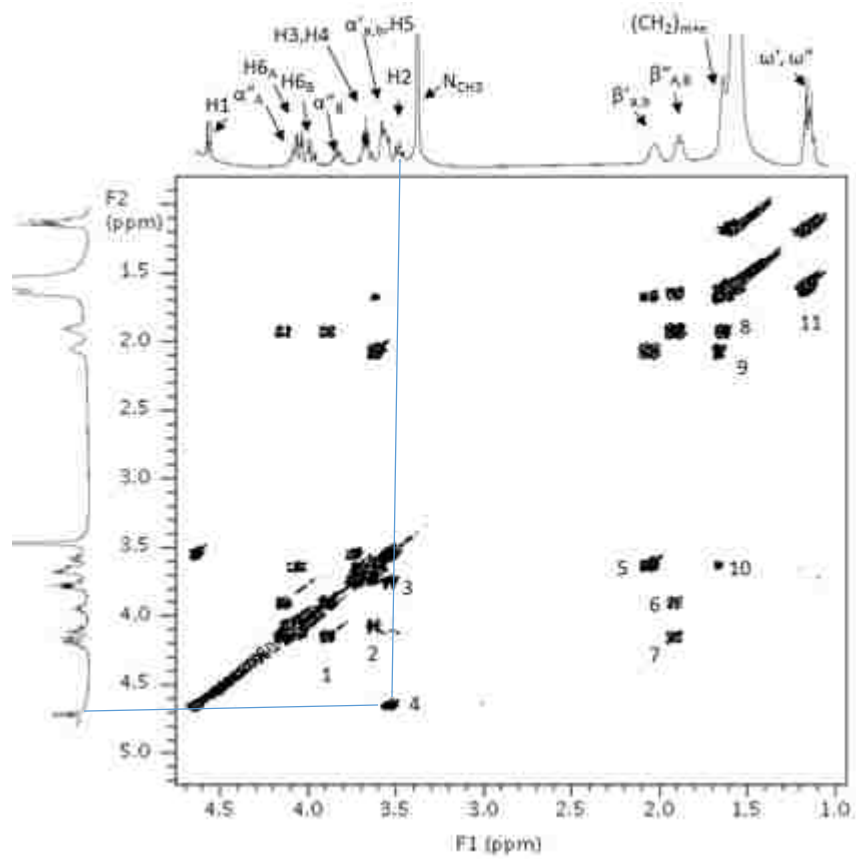


Figure 2.2. COSY spectrum of 1:1 C₁₆TAB/C8G1 in D₂O at 50 °C (total surfactant concentration 30 mM). Cross peaks indicating coupling between protons are numbered and will be discussed in Chapter 3.

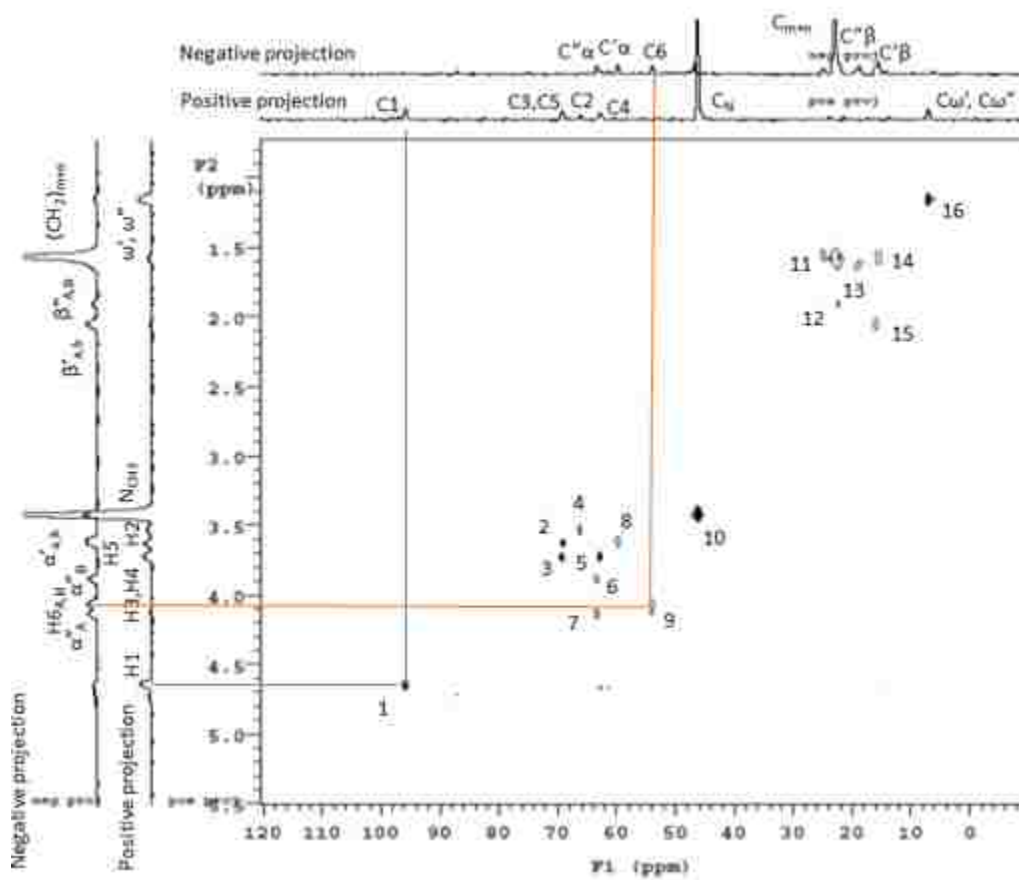


Figure 2.3. HSQC spectrum of 1:1 C₁₆TAB/C8G1 in D₂O at 50 °C (total surfactant concentration 30 mM). Numbered peaks represent directly bonded ¹H-¹³C pairs and their assignment will be discussed in Chapter 3.

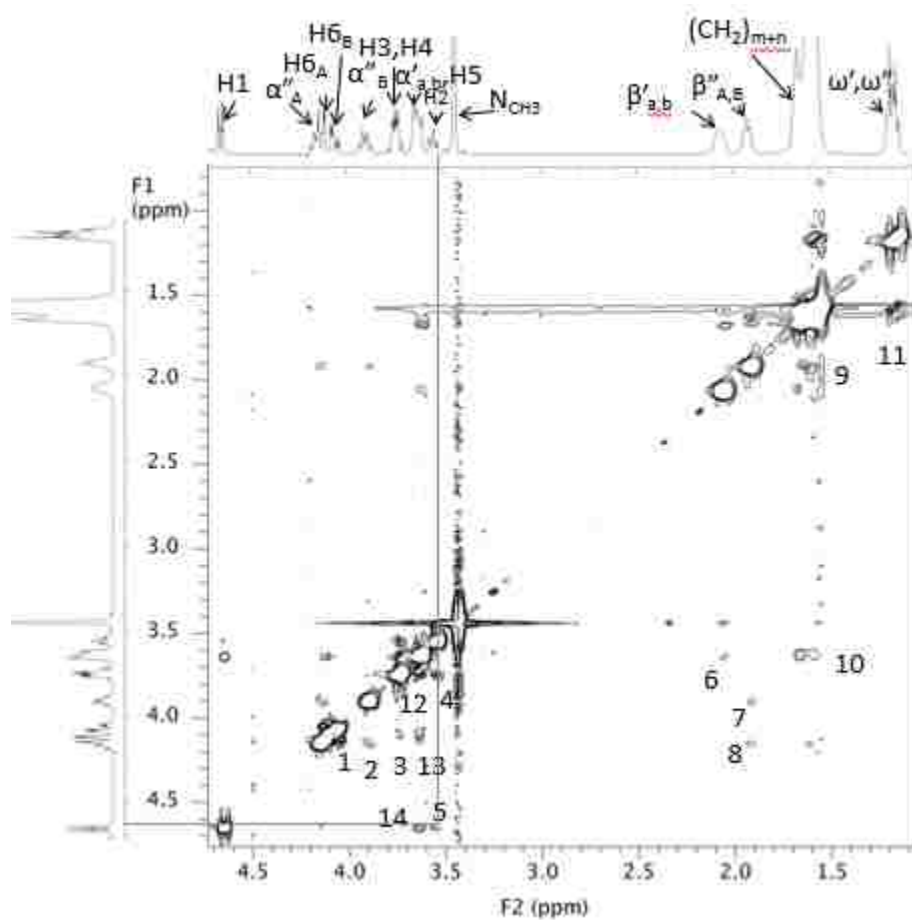


Figure 2.4. 2D NOESY spectrum of 1:1 C₁₆TAB/C8G1 in D₂O at 50 °C (total surfactant concentration 30 mM). Numbered cross peaks indicate NOE correlations and will be discussed further in Chapter 3.

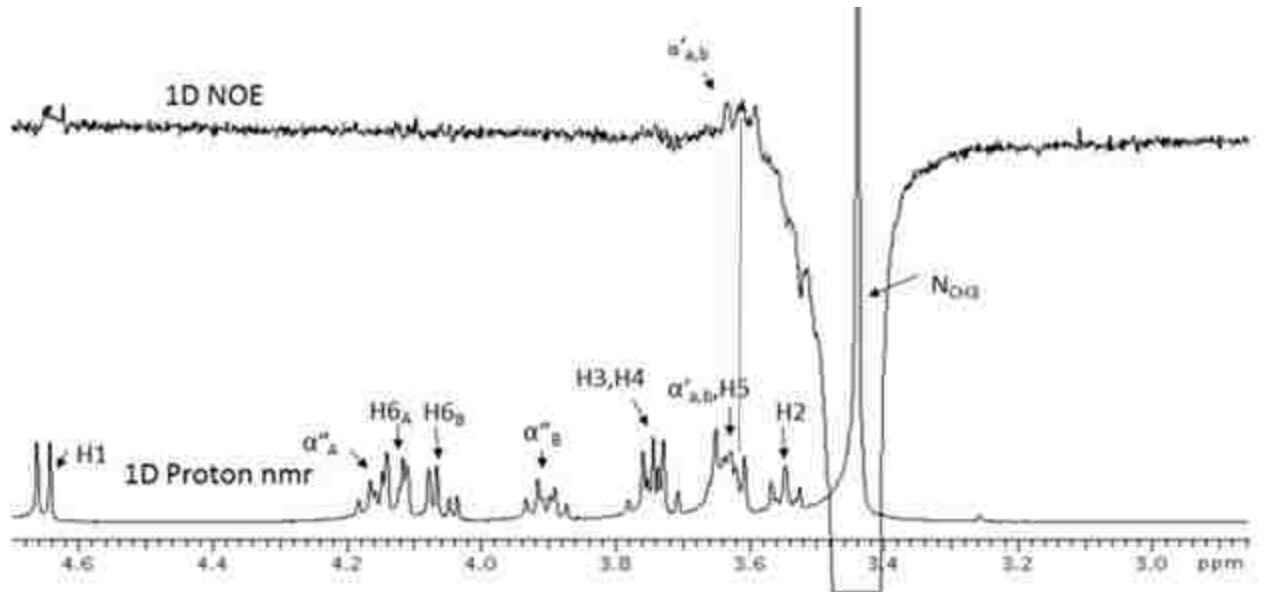


Figure 2.5. 1D NOE spectrum of 1:1 C₁₆TAB/C8G1 in D₂O at 50 °C (total surfactant concentration 30 mM). The ammonium methyl protons (N_{CH3}) were irradiated to give the NOE spectrum (top) which can be compared to the regular 1D spectrum (bottom) to identify correlated protons. In this case, only α'_{a,b} protons are correlated with N_{CH3} protons (see Chapter 3 for details).

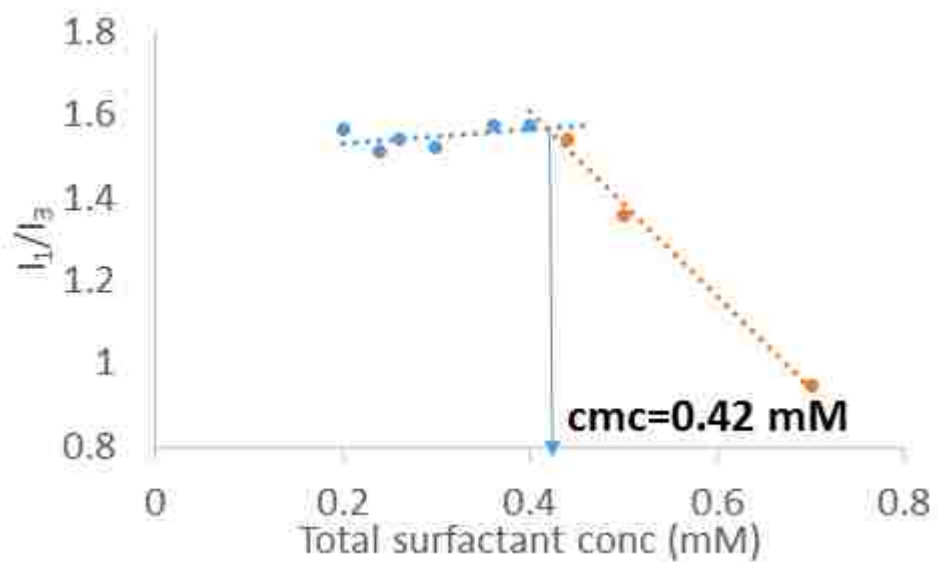


Figure 2.6. Pyrene fluorescence emission intensity ratio I_1/I_3 vs. total surfactant concentration for DeTAB/C12G1 at 50 °C. 1:1 overall ratio of surfactants was used. Arrows denote the mixed cmc value.

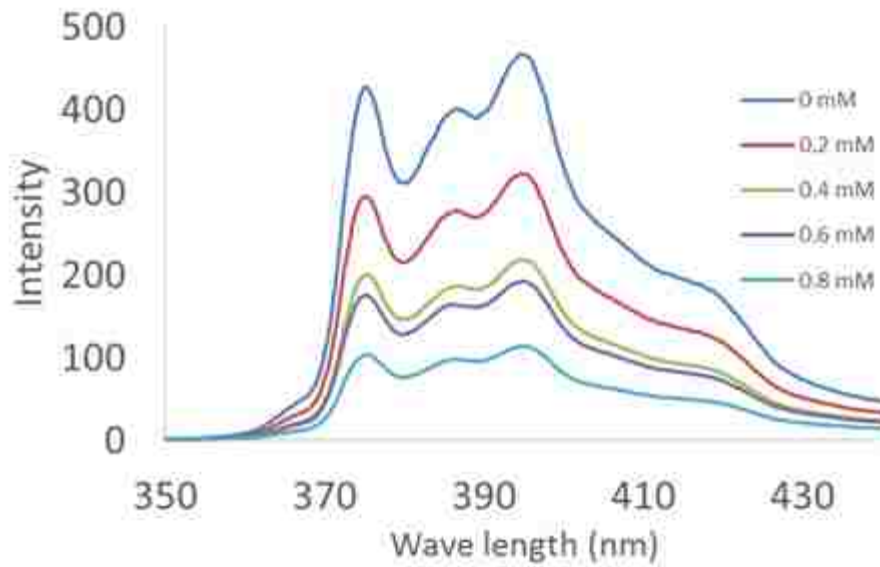


Figure 2.7. Fluorescence emission spectra of pyrene in DeTAB/C12G1 1:1 mixture in water with different hexadecylpyridinium chloride quencher concentrations (indicated in the legend).

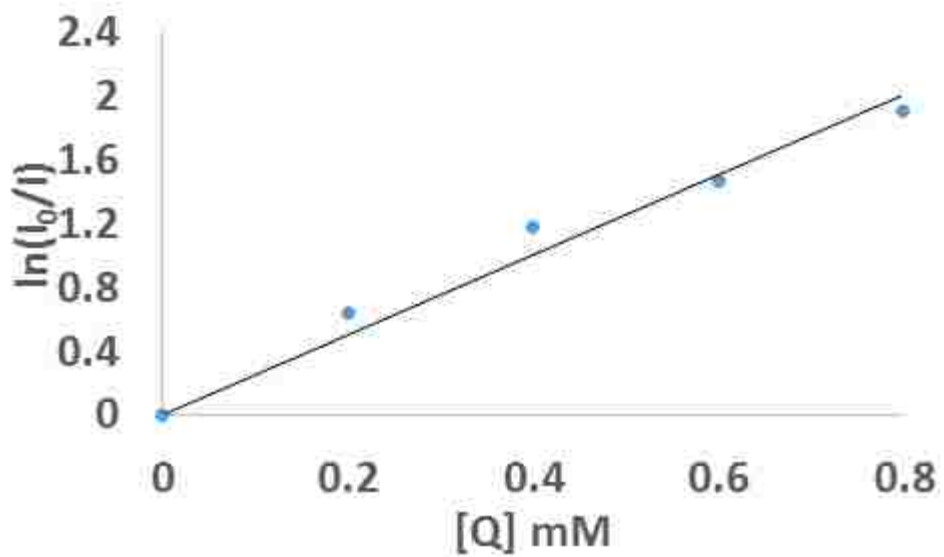


Figure 2.8. Determination of aggregation number: Linear fitting of $\ln(I_0/I)$ vs. $[Q]$ for DeTAB/C12G1 1:1 mixture at 50 °C where I_0 and I are the fluorescence intensities in the absence and presence of the quencher respectively. $[Q]$ is the quencher concentration which was varied from 0 mM to 0.8 mM.

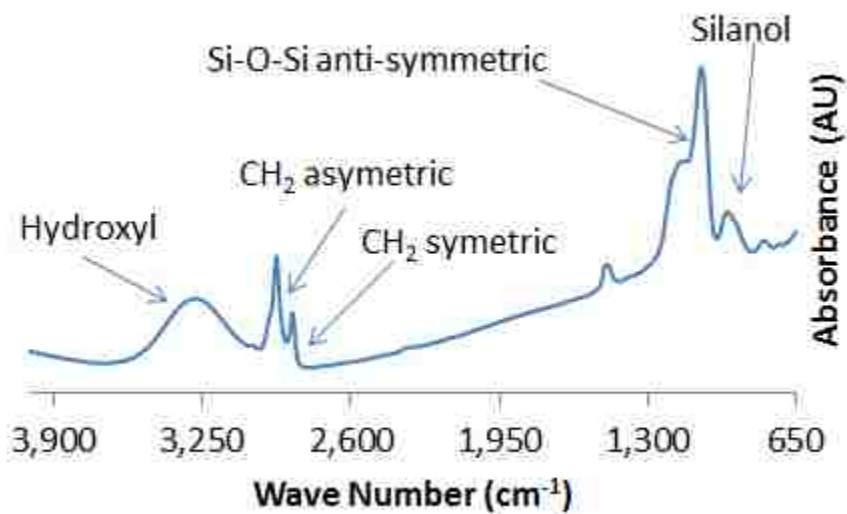


Figure 2.9. Representative FT-IR absorbance spectrum of a silica thin film on a silicon wafer which is templated with a 10:1 ratio of C₁₆TAB to C8G1. The film was aged for 7 days at 20 °C under a relative humidity of 45% prior to measuring this spectrum.

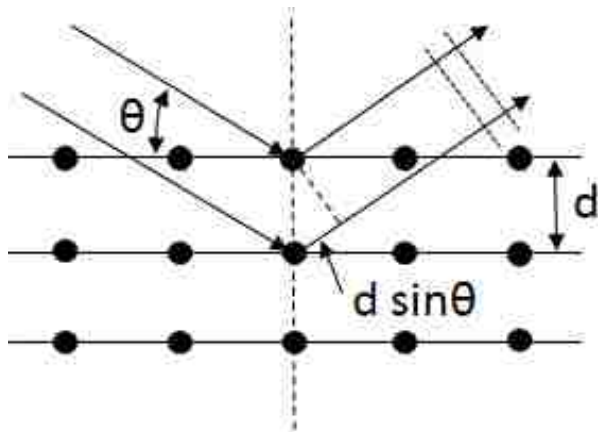


Figure 2.10. Schematic of x-ray diffraction. The diffracted rays from two planes exhibit constructive interference when the extra distance traveled by incident photons along the two illustrated vectors is equal to an integer of the x-ray wavelength used.

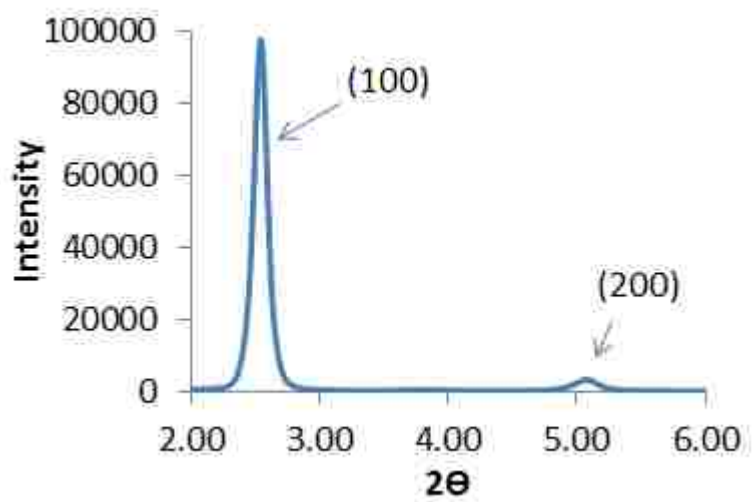


Figure 2.11. XRD pattern of C₁₆TAB templated silica films (after extraction) aged at room temperature (23 °C) and 45 %RH for 7 days.

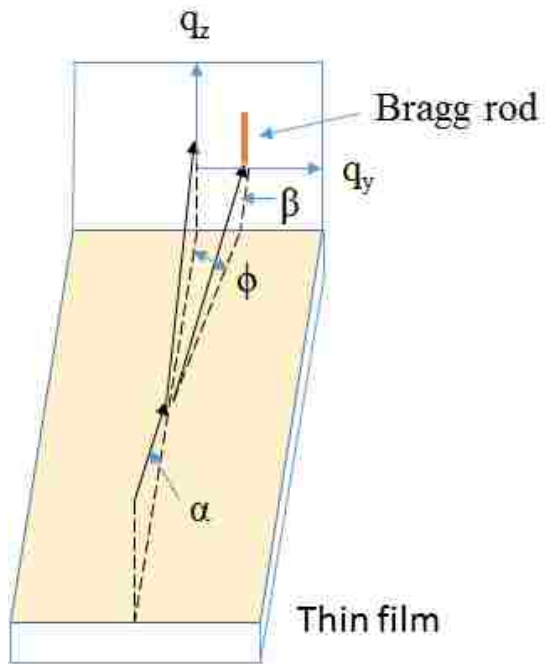


Figure 2.12. Schematic of the GISAXS experiment geometry.

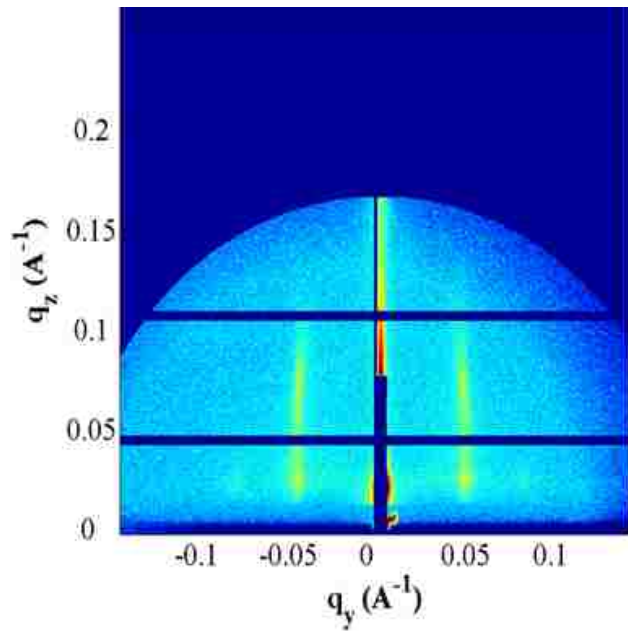


Figure 2.13. GISAXS pattern of unsandwiched titania thin film after aging at 4 °C for 2 h and just after reaching final calcination temperature 500 °C. The films are oriented horizontally (in the xy plane) relative to the incident beam for this experiment.

CHAPTER 3

NMR Studies Suggest an Inverted Micelle-in-Micelle Configuration in Cationic/Carbohydrate Surfactant Mixtures

3.1. Summary

Nuclear magnetic resonance is applied to investigate the relative positions and interactions between cationic and non-ionic carbohydrate-based surfactants in mixed micelles with D₂O as the solvent. This is accomplished using relaxation measurements (analysis of spin-lattice relaxation (T_1) and spin-spin relaxation (T_2) parameters) and nuclear Overhauser effect spectroscopy (NOESY). This study focuses on the effects of the structure of the carbohydrate headgroup (glucopyranoside vs. xylopyranoside (X)) of carbohydrate surfactants with fixed hydrocarbon chain length (octyl) on interactions with a cationic surfactant (hexadecyltrimethylammonium bromide, or C₁₆TAB). While the interactions between carbohydrate and cationic surfactants are thermodynamically favorable, the NOESY results suggest that both of the sugar head groups are located preferentially at the interior core of the mixed micelles, so that they are not directly exposed to the bulk solution. The more hydrophilic sugar headgroups of the glucopyranoside surfactant (C8G1) have more mobility than sugar heads of C8X1 due to increased hydration. Here for the first time an inverted carbohydrate configuration in mixed micelles is proposed and supported by fluorescence spectroscopy experiments. The invert carbohydrate configuration in mixed micelle would limit the use of these mixed surfactants when access to the carbohydrate headgroup is important, but may

present new opportunities where the carbohydrate-rich core of the micelles can be exploited.

3.2. Introduction

Carbohydrate-derived surfactants (also known as sugar surfactants) are of sustained interest because of their biocompatibility and applicability in the food and pharmaceutical industries ^{216, 217}. These surfactants also can be synthesized from renewable resources, and thus represent a green alternative to petroleum-based surfactants ²¹⁶ and a biodegradable value-added product in a biorefinery context ²¹⁸. Despite these advantages, intermolecular interactions among headgroups are strong relative to other nonionic surfactants. This gives rise to features that may not be desirable for some applications such as physicochemical properties (e.g. critical micelle concentration or cmc) that depend on headgroup structure and anomeric form ²¹⁹, clustering of headgroups at the micelle surface ²²⁰, and formation of limited types of lyotropic phases at room temperature ²²¹.

To overcome many of these limitations, mixtures of carbohydrate surfactants with other ionic and nonionic surfactants are frequently used. Carbohydrate/cationic surfactant mixtures have been investigated in some detail and often exhibit favorable headgroup interactions resulting in synergistic effects including cmc depression, enhanced adsorption on silica, and formation of mixed vesicle structures ²²². In addition to interfacial applications, carbohydrate surfactants have begun to be explored for templating of ordered mesoporous materials ²²³. However, many monosaccharide

surfactants such as n-octyl- β -D-glucopyranoside (C8G1) favor lamellar phases which are unstable as templates²²³. This problem can be overcome by adding a cationic surfactant to favor the formation of stable hexagonal and cubic phases⁶⁷.

In spite of progress in the use of mixed carbohydrate/cationic surfactants for interfacial and materials applications, further development requires detailed understanding of the nature of the interactions between the headgroups in the mixed micelles. Much of the current understanding of synergy and mixing in carbohydrate/cationic surfactant systems is derived from bulk studies of micellization²²². These studies are generally interpreted using a pseudo-phase separation model with an activity coefficient model such as regular solution theory (RST)⁶⁸. In RST, the interaction energy parameter β describes the enthalpic interaction between the surfactants in a mixed micelle relative to their interactions with themselves. β values of carbohydrate / cationic mixtures have been reported that indicate favorable mixing ($\beta < 0$) for several commercially available pairs of surfactants including C8G1 and hexadecyltrimethylammonium bromide (C₁₆TAB)²²⁴. However, these values do not provide direct insight into the structural origins of the interactions.

The current study uses NMR to determine molecular-level interactions between headgroups in mixed surfactants. NMR was first applied to the study of cationic/carbohydrate mixed surfactant systems by Somasundaran and coworkers²²⁵,²²⁶, who identified sites of interaction between n-dodecyl- β -D-maltoside and single-tailed and Gemini cationic surfactants. However, there has been no similar study

focused on the effects of varying surfactant headgroup structure on the relative positioning of surfactants in mixed micelles containing a simple single-tailed cationic surfactant. Here, NMR is used to study the relative position of sugar head groups in mixtures consisting of alkyl glucopyranoside (C_nG1 where n = the alkyl chain length) or alkyl xylopyranoside (C_nX1 where n = the alkyl chain length) surfactants mixed with cationic surfactant C₁₆TAB. The lyotropic phase behavior of C₈G1 and C₁₆TAB in water were studied previously and it was found that silica materials could be synthesized with similar long-range structure by a nanocasting approach ⁶⁷. However, being able to actually use the carbohydrate headgroup of the surfactant for complexation with precursors during materials synthesis requires understanding its relative position within mixed micelles. The molecular level positioning of surfactant headgroups in mixed micelles of these systems will be understood by measuring T₂ (spin-spin relaxation) parameters, T₁ (spin-lattice relaxation) parameters, and NOESY (nuclear Overhauser enhancement spectroscopy) spectra.

3.3. Experimental

Cetyltrimethylammonium bromide (C₁₆TAB) (technical grade, Acros Organics) and n-octyl-β-D-glucopyranoside (C₈G1) (99+%, Affymetrix) were used as received. n-Octyl-β-D-xylopyranoside (C₈X1) was synthesized in four steps from D-xylose by benzylation with benzoyl chloride, bromination with HBr / AcOH, glycosylation with octanol in the presence of Ag₂CO₃ and CaSO₄, and hydrolysis with sodium methoxide / Dowex 50W×8-100 ion exchange resin. The final product, C₈X1, was purified by recrystallization from

hexane / acetone. The full characterization and purity of C8X1 is described by Xu et al²²⁷. All of the NMR samples were prepared by dissolving surfactant mixtures at the desired concentration in D₂O (100 atom% D, Fischer Scientific). The total surfactant concentration was fixed at 30 mM in all samples. Pyrene, hexadecylpyridinium chloride and 2-naphthylboronic acid (Sigma-Aldrich) were used as received.

NMR experiments were conducted using a 400 MHz or 600 MHz Varian Inova NMR spectrometer at a fixed temperature of 50 °C maintained by a variable temperature (VT) controller. This temperature was chosen because it is relevant to prior synthetic work and because it is above the Krafft temperature of C8X1. Spin-lattice relaxation (T_1) measurements were performed using inversion recovery and spin-spin relaxation (T_2) measurements were performed using the CPMG spin-echo method. Nuclear Overhauser effect spectroscopy (NOESY) was performed using standard NOESY pulse sequence with 'Z' filter, and a 3D HSQC-C13-NOESY experiment for the C8G1 / C₁₆TAB system was performed using the gnoesyChsqc pulse sequence. Further details of the NMR experiments are described in the *SI* Appendix C.

Fluorescence experiments were performed with a Varian Cary Eclipse fluorescence spectrophotometer (Walnut Creek, CA) at room temperature. Pyrene was used as a fluorescence probe for mixed cmc and aggregation number calculations, and emission spectra were collected using an excitation wavelength of 335 nm. An aliquot solution of pyrene dissolved in ethanol was transferred from stock solution to a beaker and the solvent was evaporated with dry nitrogen. Surfactant mixtures dissolved in water were

added according to the required concentrations. The pyrene concentration (0.001 mM) was kept constant for every experiment. For mixed cmc measurements, the total surfactant concentration was varied from 0.9 mM to 2.5 mM. For aggregation number studies, the total surfactant concentration was fixed at 30 mM and hexadecylpyridinium chloride (0-0.8 mM) was used as a quencher. For carbohydrate fluorescence quenching experiments, 2-naphthylboronic acid was first dissolved in a water: DMSO 99:1 v/v solution and then added to surfactant solution to maintain the probe concentration of 3.35×10^{-3} mM and total surfactant concentration of 30 mM. Emission spectra were collected using an excitation wavelength of 268 nm.

Dynamic light scattering experiments were performed using a Zetasizer Nano-ZS (Malvern Instrument Inc.) instrument which is equipped with a He-Ne laser (4mW, 633 nm) as the light source. Samples were first filtered directly through a 0.2 μm syringe filter into a 1 mL cuvette and then directly placed in the instrument. The samples were at first equilibrated at 50 °C for 2 min before taking any measurements. The measurements were obtained in triplicate and the average number-weighted hydrodynamic radii were reported with standard deviations.

3.4. Results & Discussion

C8G1 and C8X1 were selected as sugar surfactants in this study because they have the same hydrocarbon tail (octyl), are the same type of enantiomer (D), and the same anomeric form (β). The only difference is that C8X1 has one less CH_2O group, which makes it less hydrophilic compared to C8G1 but otherwise structurally similar. To

compare the two mixed surfactant systems, a fixed 1:1 molar ratio of the carbohydrate surfactants with C₁₆TAB was employed. Figure 3.1 shows the 1D ¹H NMR spectra of C₁₆TAB / C8G1 and C₁₆TAB / C8X1 surfactant mixtures with the molecular structures of C₁₆TAB and both carbohydrate surfactants. The labeling of the protons in all surfactants is also provided. Because of the complexity of coupling interactions in carbohydrates, the peaks in the spectra were assigned using gradient double quantum filtered correlation spectroscopy (gDQFCOSY) and gradient heteronuclear single quantum coherence (gHSQC) experiments (Supporting Information *Appendix C*, Figures C.1-C.4). The assignments for C₁₆TAB / C8G1 mostly agree with the pure C₁₆TAB and C8G1 system^{228, 229} except that the resonance of the H5 proton of C8G1 and that of the α'_{a,b} proton of C₁₆TAB overlap in this mixture.

The cmc of C₁₆TAB is 0.9 mM²³⁰, that of C8G1 is 25 mM²³¹) while C8X1 has a lower cmc of 15 mM, measured at 50 °C via a spin-lattice relaxation (T₁) study (Supporting Information *Appendix C*, Figure C.5). Solvatochromic fluorescence measurements using pyrene as a probe were used to measure the mixed cmc for both C₁₆TAB/C8G1 and C₁₆TAB/C8X1 mixtures. The mixed cmc values were found to be 1.71 mM and 1.61 mM respectively for C₁₆TAB/C8G1 and C₁₆TAB/C8X1 1:1 mixtures (Supporting Information *Appendix C*, Figure C.6). The total surfactant concentration was selected to be 30 mM to stay well above the cmcs for each surfactant mixture so that the mixed micelle composition would be close to the bulk composition.

At the cmc, the mole fraction of each surfactant in mixed micelles and the interaction parameter (β) were calculated using Rubingh's implementation of regular solution theory (RST) ⁶⁸ and at 30 mM, the composition of micelles was estimated using an RST extension of Clint's micelle partitioning model (Supporting Information *Appendix C*, Eq. C1-C2 and associated discussion). The results are summarized in Appendix C, Table C.1. Thus the mole fraction of C₁₆TAB in the 1:1 C₁₆TAB/C8G1 mixture at the cmc is 0.96 and the β value is -2.6, which agrees well with the values reported previously for this mixture ($\beta = -2.5$ ²²⁴). For the C₁₆TAB/C8X1 1:1 mixture the mole fraction of C₁₆TAB and β value are 0.9 and -0.86, respectively. Thus, C8X1 has comparatively less favorable interaction with C₁₆TAB than C8G1. Although at the cmc the majority of the surfactant in the mixed micelle is C₁₆TAB in both cases, the composition of the micelles change as the concentration exceeds the cmc. The mole fraction of C₁₆TAB in both C₁₆TAB/C8G1 and C₁₆TAB/C8X1 mixtures is calculated to be ~ 0.58 at 30 mM total surfactant concentration, which is close to the bulk mole fraction in the surfactant mixture (0.5). Having a mole fraction in the micelles close to 1:1 should give the greatest likelihood of observing interactions between headgroups of the two surfactants.

The mean aggregation number (N_{agg}) of these surfactant mixtures was also measured using steady state quenching of solubilized pyrene by hexadecylpyridinium chloride (Supporting Information *Appendix C*, Figure C.7) and found to be 42 and 48 for C₁₆TAB/C8G1 and C₁₆TAB/C8X1 respectively (fits are shown Supporting Information *Appendix C*, Figure C.8). The hydrodynamic radii (R_h) of these surfactant mixtures was also measured using dynamic light scattering and were found to be 0.4 nm and 0.41 nm

for C₁₆TAB/C8G1 and C₁₆TAB/C8X1 respectively compared to 0.39 nm, 0.95 nm and 0.4 nm for pure C₁₆TAB, C8G1 and C8X1 at 50 °C, respectively. Thus, the micelle sizes of both surfactant mixtures are similar and consistent with their relatively small aggregation numbers. The similarity of the sizes of all micelles suggests that they have similar globular shapes. Interestingly, the sizes of the micelles measured for the pure surfactants are relatively small compare to literature but most of these previous studies were done at lower temperature or with salt additives.^{232, 233} Increasing the temperature and adding of salt have both been shown to decrease the size of micelles due to a reduction in the driving force for aggregation of surfactants.^{232, 234, 235}

Anyway, these micellization measurements together show that the cationic and sugar surfactants mix favorably with almost equimolar concentration in the mixed micelles at 30 mM. Based on the 3D structure of the surfactants, one might therefore expect an arrangement of surfactants in mixed micelles such as that shown schematically in Figure 3.2A where the sugar and cationic headgroups are located in the corona region and the tails mix together in the micelle core. However, neither the precise radial positioning of the sugar headgroups nor the validity of this structure are known, so NMR studies of interactions and dynamics in the mixed micelles were conducted.

To understand the positions of the sugar headgroups relative to the aliphatic tail of C₁₆TAB in the mixed systems, 2D NOESY measurements were made for both surfactant mixtures at 50 °C. Figure 3.3 shows the 2D NOESY pattern for a 1:1 C8G1 / C₁₆TAB mixture in D₂O with a total surfactant concentration of 30 mM. Figure 3.3A shows the

full NOESY spectrum with 600 ms mixing time whereas Figure 3.3B expands the region containing correlations to the H1 proton of C8G1 from a NOESY collected using a 1000 ms mixing time (the full spectrum is Supporting Information *Appendix C*, Figure C.9). The NOE mixing time was varied (from 900 to 1700 ms) to resolve discriminate among the cross peaks associated with the protons having higher T_1 values. All of the cross peaks are numbered in Figure 3.3, and can be categorized according to the nature of the interaction. In Figure 3.3A, we see several sugar-sugar and cationic-cationic NOE correlations (cross peaks 1-11) enumerated in the figure caption. In addition to these clear interactions among surfactants of the same type, there are another three cross peaks (cross peaks 12, 13 and 14) in Figure 3.3A that can be either sugar-cationic interactions or sugar-sugar interactions. The ambiguity arises because the chemical shift of the α proton of C₁₆TAB coincides with the chemical shift of the H5 proton of C8G1 (Figure 3.1). Cross peaks 12, 13 and 14 correlate the H3/H4 protons, H_{6A,B} proton, and H1 proton of C8G1 to the ambiguous α protons of C₁₆TAB or H5 proton of C8G1. To resolve this ambiguity, a 3D NOESY-¹³C-HSQC experiment was performed. This is an advanced technique to clearly assign homonuclear ¹H-¹H NOEs from a crowded region with the help of differences in carbon chemical shifts assigned in the HSQC spectrum. The carbon dimension of the HSQC permits identification of the nOes to Hs bonded to the carbon of interest, in the associated ¹H-¹H plane. As ¹³C the chemical shifts of the α C of C₁₆TAB and C5 of C8G1 are distinguishable, the 3D spectrum allows clear assignment of the HH cross-peak that cannot be resolved in the 2D spectrum.

Figure 3.4 shows the NOESY plane of Hs bonded to the ^{13}C H5 proton of C8G1, and the corresponding plane of Hs bonded to the α protons of C₁₆TAB is shown in Supporting Information *Appendix C*, Figure C.10. Both contain some t1 noise, but no clear NOE cross peaks associated with the α protons of C₁₆TAB are seen in Figure C.10, whereas two clear NOE cross peaks can be seen for the H5 protons of C8G1 in Figure 3.4. Cross peak 1 and 2 correlate the H5 proton of C8G1 to the H_{6A,B} protons of C8G1 and H1 of C8G1, respectively. These serve as positive controls indicating that our NMR experiment succeeds in identifying Hs nearby. In fact, no correlations between sugar Hs and cationic surfactant headgroup Hs could be detected although there are many sugar-sugar correlations evident in the NOESY patterns for the C₁₆TAB/C8G1 mixture. One remaining possible correlation between the two types of surfactants would be between the N_{CH3} protons of C₁₆TAB with the sugar headgroup protons. A vertical steak appears at the position of the N_{CH3} protons in Figure 3.3A due to t1 noise. To reveal possible correlations, a 1D NOE spectrum was measured using excitation from the N_{CH3} protons of C₁₆TAB (Supporting Information *Appendix C*, Figure C.11 and associated discussion) but no correlations with C8G1 headgroups were observed.

Additional correlations were revealed by adjusting the mixing time for NOESY to 1000 ms (Figure 3.3B). Cross peaks 15 & 16 correlate the H1 proton of C8G1 with α'' protons of C8G1 whereas cross peak 17 correlates H1 proton of C8G1 with $\beta''_{A,B}$ protons of C8G1. Cross peak 18 correlates the H1 proton of C8G1 with the rest of the alkyl chain protons (after the β position) of C₁₆TAB or C8G1 while cross peak 19 correlates the H1 proton of C8G1 with ω protons of C₁₆TAB or C8G1. Taken together, the NOESY results

suggest that the headgroups of C8G1 are not associated with any C₁₆TAB protons near the headgroup, but instead are most strongly associated with other sugar headgroups and tail protons. Thus despite synergistic mixing in the mixed micelles, some sort of segregation is occurring so that the headgroups are not close together.

Analogous results were obtained for the other non-ionic surfactant. Supporting Information *Appendix C*, Figure C.12 shows the 2D NOESY spectrum for the C8X1 / C₁₆TAB surfactant mixture using the same mixing time as for Figure 3.3. As with the C8G1 / C₁₆TAB system, Figure C.12 also does not indicate any sugar-cationic surfactant interactions between C₁₆TAB and C8X1 surfactant in micelles, although an increase in the intensities of sugar-sugar cross-peaks indicates interactions among C8X1 surfactant molecules (cross peaks 1-7, 9 and 10; cross peak 8 correlates the α and β protons of C₁₆TAB). A set of cross peaks (11-16) also correlates protons in the alkyl tails of C8X1 or C₁₆TAB with protons in or near the headgroups of the surfactants. The 1D NOEs resulting from inversion of the N_{CH3} protons (Supporting Information *Appendix C*, Figure S13 and associated discussion) also show no relaxation with sugar headgroups of C8X1 in the mixed system. Similar to the C₁₆TAB/C8G1 mixture, the NOE mixing time was also varied (900-1700 ms) to seek cross relaxation with protons having higher T₁ values, and several extra instances were found between the H1 proton of C8X1 with the alkyl chain of C8X1 or C₁₆TAB (Supporting Information *Appendix C*, Figure C.14 and associated discussion). Just as for C8G1, this is more consistent with sugar headgroups being segregated near the alkyl groups of the tails rather than being packed with the trimethylammonium headgroups. Hence, the representative schematic in Figure 3.2A is

not consistent with the NOESY data for either sugar surfactant, and different arrangements of the surfactants need to be considered.

Figure 3.2B shows an alternative configuration where the individual surfactant may exist in a segregated form in the mixed micelle. The headgroups are both located in the micelle corona, but demixing would be consistent with NOE correlations among sugars but not between sugars and trimethylammonium. To investigate this possibility, spin-lattice relaxation (T_1) studies were done for the C8X1/C₁₆TAB and pure C8X1 micelle. The hypothesis behind the measurements was that, if the micelle sizes were similar for pure C8X1 and C₁₆TAB/C8X1 mixtures and if the individual surfactants were segregated inside the mixed micelle, then the protons of the sugar headgroup would have a similar chemical environment to pure C8X1 micelles, and therefore similar mobility and T_1 values. Table 3.1 shows the comparison of T_1 values of C8X1 headgroup protons in a pure 30 mM C8X1 solution and a 1:1 C8X1 / C₁₆TAB mixture. The T_1 values for C8X1 headgroup protons are consistently larger in the pure micelle compared to the mixed surfactant system, which suggests reduced mobility in the former. This difference is due to close packing of the headgroups in pure C8X1 micelles and implies that C8X1 in the C₁₆TAB/C8X1 mixture is not segregated into clusters of xylopyranoside headgroups that behave the same as in a single-surfactant micelle. Since C8G1 shows more favorable mixing than C8X1 with C₁₆TAB, the simple segregation picture in Figure 3.2B model does not appear to be a reasonable structure for either system.

Instead, because the NOE data show correlations between sugar headgroups and tail protons, it is likely that the sugar headgroups aggregate together in *inverted* submicelles within the tails of the mixed micelle. Based on the spherical symmetry of the micelle, Figure 3.2C shows the most likely configuration where the sugar surfactants are inverted in the mixed micelle so that the sugar head groups are segregated at the core of the micelle. While it is initially not intuitive, this structure is consistent with all NOE observations. To test this hypothesized headgroup arrangement, fluorescence quenching experiments were done using 2-naphthylboronic acid as a probe. Glucose has been shown to quench this probe resulting reduction in fluorescence emission intensity²³⁶. Also the probe is nonpolar, so it is expected to be solubilized near the hydrophobic tails so quenching can indicate the position of the sugar head groups relative to the nonpolar micellar environment.

Figure 3.5 shows the emission spectra of naphthalene-2-boronic acid added to solutions containing pure glucose, pure C₁₆TAB, pure C8G1 and C₁₆TAB/C8G1 mixtures. For all of these conditions the total solute concentration was fixed to 30 mM to provide a basis for comparison. As expected, glucose quenches the probe to some extent, but unfortunately, C₁₆TAB also quenches the probe. Still, the degree of quenching decreases in the order C₁₆TAB/C8G1 > C₁₆TAB > C8G1 > Glucose. Since the total solute concentration was kept constant for all cases, the degree of quenching of the probe by the C₁₆TAB/C8G1 mixture would have been expected to fall between the quenching observed separately by C₁₆TAB and C8G1 if quenching were only caused by interactions between the probe and headgroups located at the corona of the micelles. Instead, the

C₁₆TAB/C8G1 mixture displays the greatest degree of quenching. Similar results were found as probe concentration was increased (Supporting Information *Appendix C*, Figure C.15 and associated discussion). This extra quenching in the C₁₆TAB/C8G1 mixture is consistent with the structure shown in Figure 3.2C, where partial solubilization of the probe in the tails of the micelles provides intimate contact with the headgroups of the inverted C8G1 surfactants, and therefore enhanced quenching. The same probe was used for experiments with xylose, but unfortunately no quenching was observed.

As an additional probe of the local microenvironment in which sugar head groups are located in C₁₆TAB/C8G1 and C₁₆TAB/C8X1 mixed micelles, spin-lattice (T_1) and spin-spin (T_2) relaxation measurements were done. For small molecules with rapid tumbling, the dependence of T_1 and T_2 on molecular mobility is the same, but for low rates of motion T_1 follows the opposite trend from T_2 : as the rate of motion decreases, T_1 is expected to *increase* due to slow tumbling while T_2 decreases²³⁷. Also, because C8G1 and C8X1 are compared at equal mixing ratios with C₁₆TAB and at the same concentration, the concentration of monomeric surfactants is expected to be approximately equal since all micelle parameters in Table 3.1 are similar. Therefore, observed differences in T_1 and T_2 are most likely due to differences in the micellar contribution that arises from differences in the location and hydration of the saccharide headgroup.

Table C.2 compares T_1 and T_2 values for select headgroup protons of C8G1 / C₁₆TAB and C8X1 / C₁₆TAB mixtures. The selected protons are in comparable positions in both sugar surfactants and free from any ambiguity due to contributions to the decay profile from

protons in different chemical environment. For the sugar surfactants, T_1 values are consistently smaller and T_2 values are consistently larger for the C8G1 mixture compared to the C8X1 mixture. T_2/T_1 ratios are considered to be a summative measure of “degree of restricted motion”, where small values indicate more restriction^{225, 226}. A greater value is found for sugar headgroup protons of C8G1 than C8X1. As examples, for H6 of C8G1, $T_2/T_1 = 0.118 \pm 0.016$ vs. 0.016 ± 0.006 for H5 of C8X1. For H1 protons, values of 0.027 ± 0.006 for C8G1 and 0.015 ± 0.003 for C8X1 are found. For H3/H4 of C8G1, $T_2/T_1 = 0.088 \pm 0.013$, while for H3 of C8X1 it is 0.065 ± 0.011 . All of these comparisons indicate greater mobility of sugar head groups inside of the micelle for C8G1 / C₁₆TAB compared to C8X1 / C₁₆TAB. Assuming that both systems have the inverted sugar surfactants illustrated in Figure 3.2C, this is best explained by differences in hydration of the sugar head groups. Because C8G1 is more hydrophilic than C8X1, it pulls more water into the inverted core of the micelle, thus giving greater mobility to the headgroups than for C8X1.

While the hypothesized C8G1-in-CTAB micellar configuration in Figure 3.2C has not been proposed previously for mixed sugar / cationic surfactant systems, there is some literature precedent that supports this concept, and it may actually help to explain prior observations in the biophysics literature. First, Warner et al. reported an octanol-water partition coefficient K_{ow} ²³⁸ corresponding to a free energy for transfer from water to octanol at 298 K of $-RT \ln(K_{ow}) = -11.1$ kJ/mol. For comparison, the free energy for micellization of C8G1 is $RT \ln(cmc) = -9.1$ kJ/mol. Therefore, transfer of C8G1 completely

into a nonpolar environment is thermodynamically preferable to forming micelles, which is consistent with partitioning into the nonpolar core of CTAB-based micelles.

In the context of biophysics, C8G1 is a common detergent for dispersion of proteins and lipids, and Wenk et al. reported that C8G1 readily partitions into lipid bilayers and is able to access both inner and outer leaflets²³⁹. These and similar results from the Seelig group are consistent with the concept of partitioning of C8G1 into micelles or bilayers formed by a host surfactant with highly polar headgroups²⁴⁰, so the novel suggestion here is that glucoside headgroups are “buried” in a sugar-rich core rather than being mixed with the headgroups of the host surfactant. Observations of C8G1 / lipid structure support this idea. ²H NMR measurements showed that C8G1 disrupts lipid tail segments without disrupting lipid headgroup interactions²³⁹, which is more consistent with Figure 3.2C than the more conventional picture in Figure 3.2A. Structural studies have shown that addition of C8G1 favors the formation and stabilization of lamellar / bilayer structures over lipid mesophases with greater curvature such as hexagonal and bicontinuous cubic²⁴¹. If C8G1 partitions near the corona of the lipids, the packing parameter should be *reduced*, which would favor higher-curvature mesophases²⁴². The actual effect can be rationalized by a secondary effect of C8G1 on the packing of lipid tails²⁴¹, but a more direct explanation is that C8G1 partitions near the tails and therefore increases the packing parameter to favor lamellae. In addition, C8G1 in lyotropic mesophases has been shown to be hydrated by only 1.6-1.7 water molecules per sugar headgroup, suggesting strong hydrogen bonding interactions among headgroups rather than with water²⁴³. Thus, a reasonable driving force for the

headgroups to retreat to the interior of micelles would be to facilitate hydrogen bonding among sugar headgroups. Thus, while the micelle-in-micelle picture proposed here is new, both the tendency of C8G1 to partition into bilayers and the strong hydrogen bonding among headgroups support the picture, and suggest that these interactions may help C8G1 to favor lipid bilayers at low concentrations.

Finally, the segregation of headgroups between the interior and exterior of surfactant aggregates is a familiar concept in asymmetric lipid vesicles and several synthetic strategies have been developed to prepare such asymmetric structures ^{244, 245}. Computational studies of mixed micelles have focused on differences in structure for synergistic vs. antagonistic interactions between headgroups, and have shown the possibility that headgroup-headgroup interactions can lead to headgroup segregation within micelles, or complete micelle phase separation ^{246, 247}. However, the structure in Figure 3.2C is most likely driven not by antagonistic headgroup-headgroup interactions but a preference of trimethylammonium headgroups for water compared to glucopyranoside, and the tendency for hydrogen bonding among the glucopyranoside headgroups. When one headgroups favors the bulk solvent more than the other, segregation between inner and outer leaflets of vesicles and quasi-vesicles has been predicted computationally ^{248, 249}. Thus, spontaneous assembly due to differences in solvent headgroups and inter-headgroup interactions may drive the formation of the structure in Figure 3.2C, which is like a very small asymmetric vesicle or quasi-vesicle.

3.5. Conclusions

A detailed study of headgroup interactions in mixed cationic and sugar-based surfactants was performed using fluorescence probe measurements and NMR experiments including spin-lattice (T_1) relaxation, spin-spin (T_2) relaxation and 2D NOESY measurements. The results suggest a new type of mixed micelle structure in which the carbohydrate surfactant is inverted with its head towards the core of the micelle in a structure similar to a very small asymmetric vesicle. While it is clear that both octyl glucoside (C8G1) and xyloside (C8X1) surfactants mix favorably with C₁₆TAB as indicated by a negative apparent interaction parameters (β), no protons of the sugar and cationic head groups were located close enough together to induce detectable nuclear Overhauser effect (NOE). Instead of interacting with the cationic head group, sugar head groups were found to interact with other sugars and with the surfactant tails. After ruling out phase separation among headgroups based on relaxation measurements, the most consistent model of these mixed micellar systems has the sugar surfactants in an inverted configuration in the core of the mixed micelles. The hypothesized was further tested using fluorescence quenching experiments where enhanced quenching of a boronic acid fluorescent probe was observed due to the confinement of the sugar heads near the micelle core. The inverted mixed micelle structure is driven by the difference in interaction forces between the surfactant heads and the polar surrounding may contribute to this inverted carbohydrate configuration. Because the columbic interaction force between the cationic heads with the surrounding water is stronger than the hydrogen bonding forces between the non-ionic sugar head and the

surrounding water, the carbohydrate heads prefer to stay near the core of the mixed micelle. While studies of C12G2 with a variety of cationic surfactants have been reported and show that the two glucose groups “straddle” the cationic headgroup²²⁶, a completely different architecture is shown to be active in this case. We also have shown the mobility of the sugar head of C8G1 has increased significantly compare of sugar head of C8X1 in mixed micelle due to differences in hydration in the core. Prior investigations of solubilization and structure of C8G1 mixtures with lipids are consistent with the hypothesized structure and it is hoped that this investigation will inspire new studies that investigate this possibility in lipid-based systems.

This study has provided new insights into the 3D structure of synergistic cationic / sugar surfactant micelles, and suggests that the hydroxyl groups of C8G1 and C8X1 should not be directly accessible for interaction with the bulk solution. This has negative implications for applications that rely on interactions with the sugar headgroups at the micelle surface (such as complexation with functional groups during materials synthesis) and suggests that new approaches will be needed to tune surfactant structures so that sugar surfactants are accessible at the micelle surface. However, work is underway to understand how the structure of pairs of cationic and sugar surfactants can be tuned to encourage the sugars to move to the exterior of the micelle, and this will be submitted in the near future.

Table 3.1. Comparison of T_1 values of headgroup protons in C_{16} TAB/C8X1 and pure C8X1 micelles.

Surfactants	Protons	T_1 (ms)*
C_{16} TAB/C8X1	H5 _A	695±18
Pure C8X1	H5 _A	1120±50
C_{16} TAB/C8X1	H2,H5 _B	1000±60
Pure C8X1	H2,H5 _B	2780±10
C_{16} TAB/C8X1	H1	1110±40
Pure C8X1	H1	1490±38
C_{16} TAB/C8X1	H3	1730±31
Pure C8X1	H3	2700±110

*Intervals are ± the 95% confidence interval calculated using the standard error for the parameter.

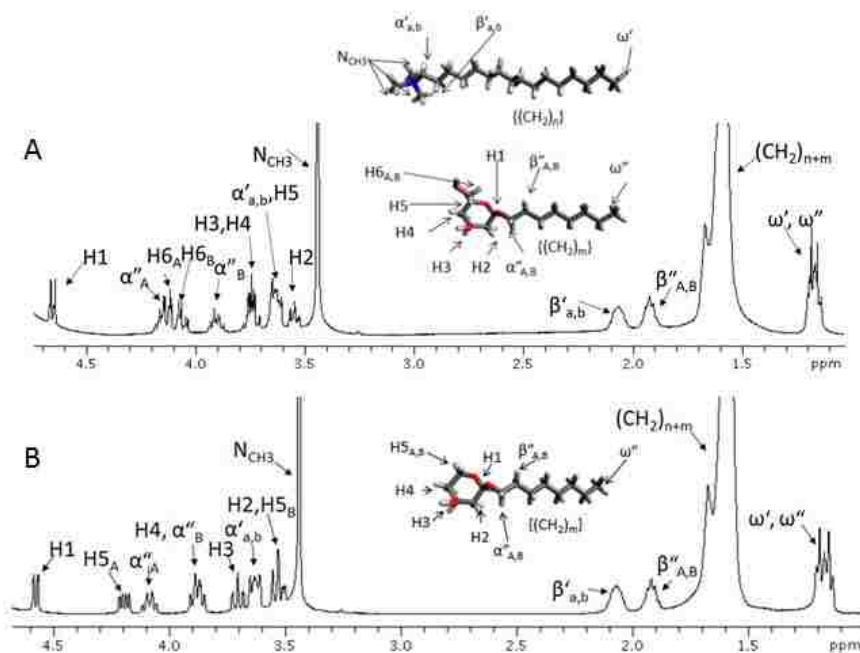


Figure 3.1. 1D ¹H NMR spectrum of 1:1 (A) C₁₆TAB/C8G1 and (B) C₁₆TAB/C8X1 in D₂O at 50 °C (total surfactant concentration 30 mM), with Molecular structures of (A) C₁₆TA⁺ and C8G1 (B) C₁₆TA⁺ and C8X1, determined by geometry optimization using the PM3 semiempirical molecular orbital method. The labeling of the protons in these structures will be used in the discussion of the NMR spectra.

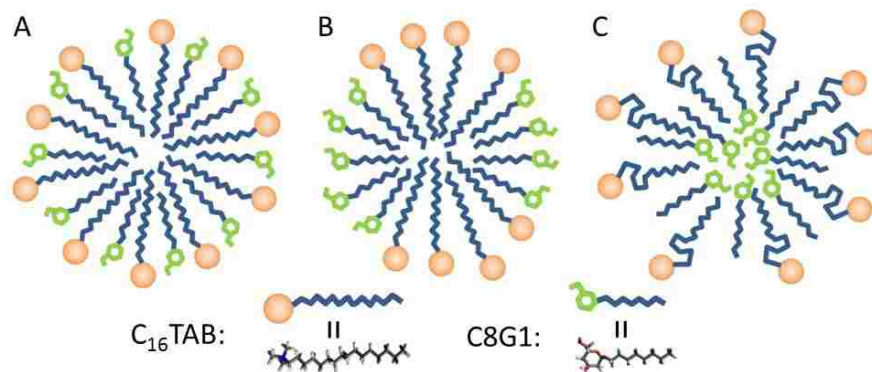


Figure 3.2. Schematic diagram showing relative position of head groups in three possible mixed micelles of $C_{16}TAB$ and $C8G1$: (A) ideal mixed headgroup configuration based on the 3D geometry of the micelles and favorable interactions between headgroups, (B) segregated model where glucoside groups cluster in the corona, and (C) inverted carbohydrate model where the glucoside groups cluster in the core of the micelle.

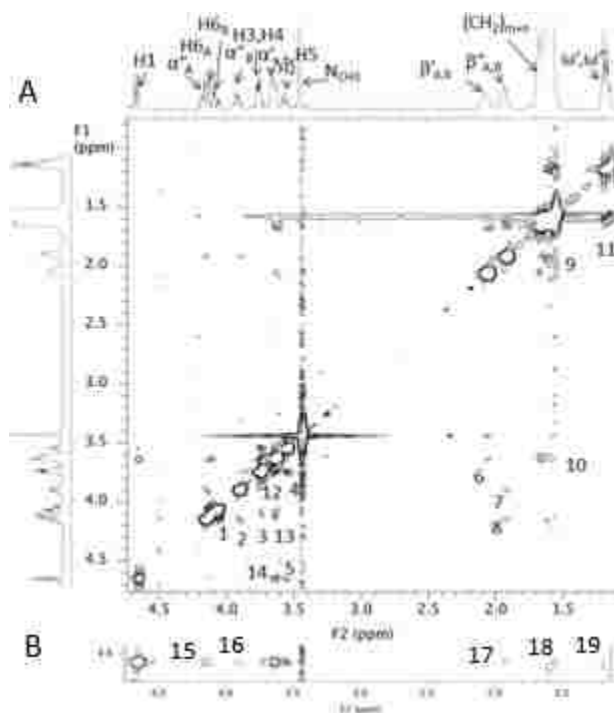


Figure 3.3. 2D NOESY spectrum of 1:1 C₁₆TAB/C8G1 in D₂O at 50 °C (total surfactant concentration 30 mM). Cross peaks indicate the NOE correlations between the associated protons and are symmetric along the diagonal. Fig. 3A indicates several sugar-sugar or cationic-cationic surfactant NOE correlations using 600 ms mixing time (cross peak 1) H_{6A} & H_{6B} proton; 2) α''_A & α''_B proton; 3) H₃/H₄ & H_{6A,B} proton; 4) H₃/H₄ & H₂ proton; 5) H₁ & H₂; 6) α'_{a,b} & β'_{a,b}; 7) α''_B & β''_{A,B}; 8) α''_A & β''_{A,B}; 9) β''_{A,B} & (CH₂)_{m+n}; 10) α'_{a,b} & (CH₂)_{m+n}; 11) (CH₂)_{m+n} & ω'/ω''; 12) α'_{a,b},H₅ & H₃/H₄ proton; 13) α'_{a,b},H₅ & H_{6A,B} proton; and 14) α'_{a,b},H₅ & H₁ proton). Fig. 3B indicates several alkyl tail correlations with the H₁ proton of C8G1 using a 1000 ms mixing time (cross peak 15) H₁ & α''_A; 16) H₁ & α''_B; 17) H₁ & β''_{A,B}; 18) H₁ & (CH₂)_{m+n}; 19) H₁ & ω'/ω'' proton.

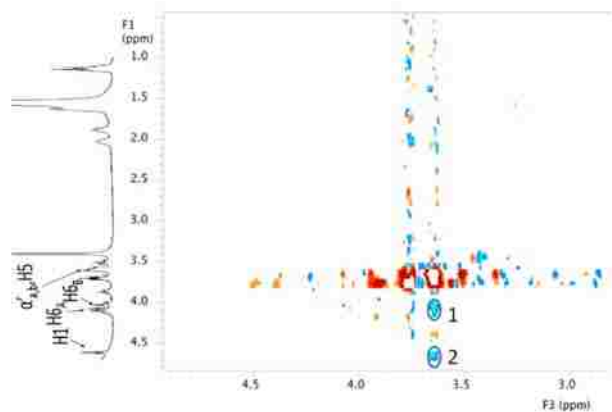


Figure 3.4. ^1H - ^1H NOESY plane for the C5 carbon of C8G1 taken from the 3D HSQC-C13-NOESY spectrum of 1:1 C₁₆TAB/C8G1 in D₂O at 50 °C (total surfactant concentration 30 mM). The spectrum shows two cross peaks (circled in blue) below the diagonal peak (H5 proton of C8G1, red contours), indicating sugar—sugar NOE correlations between (cross peak 1) H5 & H6_{A,B} protons and (cross peak 2) H5 & H1 protons.

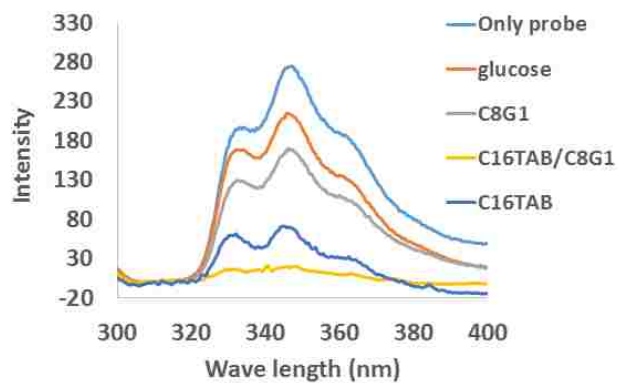


Figure 3.5. Fluorescence emission spectra of 2-naphthylboronic acid in glucose and different surfactant solution. Fluorescence intensity reduces in the order of glucose > C8G1 > C₁₆TAB > C₁₆TAB/C8G1. Total surfactant or glucose concentration was fixed to 30 mM.

CHAPTER 4

Tuning the position of head groups by surfactant design in mixed micelles of cationic and carbohydrate surfactants

4.1. Summary

The accessibility of the head group of carbohydrate surfactants within mixed micelles with trimethylammonium-based cationic surfactants in D₂O was investigated using nuclear magnetic resonance (NMR) spectroscopy. The dynamics of different parts of the surfactants were probed using relaxation measurements (analysis of spin-lattice relaxation (T_1) and spin-spin relaxation (T_2)), and relative positioning by nuclear Overhauser effect spectroscopy (NOESY). Additional micellar properties were determined using fluorescence spectroscopy with solvatochromic probes. The central question being studied was how to improve accessibility of the carbohydrate head group compared to mixtures of hexadecyltrimethylammonium bromide (C₁₆TAB) and octyl β -D-glucopyranoside (C8G1). Previous NMR measurements have shown that the glucose headgroups in this mixed micelle system are located in aggregates in the interior of the micelle rather than being accessible at the corona. Improving accessibility was attempted by designing surfactants either to “push out” the headgroup by adjusting the relative lengths of the alkyl tails of the cationic and carbohydrate surfactants, or to “pull out” the carbohydrate headgroup by varying the polarity of the linker between the carbohydrate and alkyl tail in the sugar-based surfactant. The results show that matching the surfactant chain lengths is not an effective strategy to “push

out” the carbohydrate head group due to a large mismatch in interaction forces between cationic headgroup vs. carbohydrate head groups with D₂O. In the most extreme example of this, when the cationic chain length (in C₁₀TAB) is less than the carbohydrate surfactant chain length (C₁₂G₁), slow relaxation dynamics are observed due to the headgroups being buried within very rigid micellar aggregates. However, tuning the headgroup polarity to “pull out” the carbohydrate is found to be effective. This is done by replacing the ester linkage (e.g. in n-octyl-β-d-xylopyranoside) with a triazole linkage formed using click chemistry. The polarity of the triazole linkage pulls the carbohydrate to the exterior of the micelle, as indicated by direct NOE correlations between triazole and carbohydrate protons and protons near the cationic headgroup. These findings will help to design new combinations of surfactants based on click chemistry in which the sugar headgroup is accessible to a polar medium in mixed micelles with cationic surfactants.

4.2. Introduction

In recent years, carbohydrate-based surfactants (a.k.a. sugar surfactants) have drawn attention in the interfacial science community due to their environmentally friendly properties including being derived from renewable sources²⁵⁰⁻²⁵³, low toxicity^{227, 254-256} and biodegradability^{257, 258}. Because of these properties, sugar surfactants have tremendous potential for food²⁵⁹, alternative fuel²⁶⁰ and pharmaceutical applications²⁶¹. Despite these advantages, the application of these carbohydrate surfactants is often limited by their heavily hydrated non-ionic head groups which form clusters due to very strong intermolecular interactions among themselves²⁶². These

strong inter-headgroup interactions lead to high Krafft temperatures ⁶⁵, slow lateral diffusion in micelles ²⁶³, and the formation of limited types of lyotropic phases at room temperature²⁶⁴ which constrain their applications.

Limitations in interfacial properties are often addressed by mixing sugar surfactants with other ionic or nonionic surfactants ^{265, 266}. Mixtures of cationic and carbohydrate surfactants have been investigated extensively due to favorable synergistic effects such as decreased critical micelle concentration (cmc), surface tension and Krafft temperature; and increased colloidal stability relative to individual surfactants ²⁶⁷⁻²⁶⁹. In addition to the classic interfacial applications, an emerging application of carbohydrate surfactants is as templates for ordered mesoporous materials ²⁷⁰⁻²⁷². However, many carbohydrate surfactants such as n-octyl- β -D-glucopyranoside (C8G1) favor lamellar phases and are difficult to use to template stable mesophases such as the columnar hexagonal phase²⁷². This problem can also be overcome by adding cationic surfactant to combat strong hydrogen binding among carbohydrate headgroups to favor the formation of hexagonal and cubic phases ^{67, 273}.

Although mixing with cationic surfactant solves problems related to strong clustering of sugar surfactants, it also creates one big uncertainty: the accessibility of the carbohydrate head group. Having accessible carbohydrate head groups is crucial in several applications including molecular imprinting ²⁷⁴. The process of molecular imprinting creates molecular binding sites in a stable framework (such as a metal oxide) with specific size, shape and functional group arrangement complementary to the target

molecule ²⁷⁵⁻²⁷⁸. In order to create molecular imprinted sites in mixed surfactant-templated metal oxides, it is necessary to have the carbohydrate head group located slightly outside of the corona region of mixed micelles in order to interact with metal oxide precursors to create binding sites for molecular imprinting. For this and other mixed surfactant applications, a detailed understanding of the nature of the interactions between the headgroups in mixed micelles is needed.

Previous studies of mixed micelles, including carbohydrate/cationic mixtures, focused primarily on bulk thermodynamic measurements. Different models have been used to describe the mixed micellization, most commonly the pseudo-phase separation model in which micelles are treated as a separate phase that remains in dynamic equilibrium with the solvated monomer phase ²⁷⁹. Nonideal mixing in micelles can be explained in this context by the regular solution theory (RST) model ^{69, 280}. According to RST, the interaction energy parameter β describes the interaction between the ionic and non-ionic surfactants in mixed micelles ^{68, 95} where more negative values of β signify more favorable interaction between the two surfactants ^{265, 281}. These parameters can be estimated from bulk micellization experiments for mixed micelle systems, but they do not provide direct information about the interaction sites between the surfactants.

Structural characterization of mixed micelles has been performed using a variety of techniques including nuclear magnetic resonance (NMR), small-angle neutron scattering (SANS) and fluorescence spectroscopy to determine the size, shape, aggregation number and interaction sites in mixed micelles ^{122, 282-285}. Among these, NMR has the

unique ability to give molecular level information about the interactions between headgroups in mixed surfactants. NMR was first applied to the study of cationic/carbohydrate mixed surfactant systems by Somasundaran and coworkers, who identified sites of interaction between n-dodecyl- β -D-maltoside and single-tailed and Gemini cationic surfactants ^{286, 287}. Our previous study shows that when monosaccharide surfactants such as n-octyl- β -D-glucopyranoside (C8G1) or n-octyl- β -D-xylopyranoside are mixed with cetyltrimethylammonium bromide (C₁₆TAB), the carbohydrate head groups aggregate into clusters within the micelles, and most likely point toward the core of the mixed micelle. This makes the carbohydrate head totally inaccessible for molecular imprinting. To make the glucose or xylose head group accessible we propose two hypotheses: first, that matching the cationic and carbohydrate surfactant tail lengths can “push out” the sugar headgroup to the exterior of the mixed micelle. The second hypothesis is that matching the interaction forces of carbohydrate and cationic head groups with the polar medium can be used to “pull out” the sugar head group. To test the latter, a carbohydrate surfactant with a triazole linker will be mixed with a cationic surfactant and compared to a carbohydrate surfactant with an ester linker. The triazole linker is expected to provide dipolar interactions between the carbohydrate head and cationic surfactants or the surrounding polar medium.

Here, the relative position of sugar head groups in cationic-carbohydrate mixed micellar systems will be investigated using NMR as a function of structural parameters selected with the intention of moving the sugar headgroups out of the core of the micelle. Additional micellar properties (cmc and aggregation number) will be studied using

fluorescence spectroscopy. The carbohydrate surfactant n-dodecyl- β -D-glucopyranoside (C12G1) (with an ester linkage) will be mixed with cationic surfactants of varying tail chain length including cetyltrimethylammonium bromide (C₁₆TAB), dodecyltrimethylammonium bromide (C₁₂TAB), and decyltrimethylammonium bromide (C₁₀TAB). The accessibility of the sugar head will also be studied in the case of carbohydrate surfactant n-octyl- β -D-triazole-xylopyranoside (C8XT1) mixed with C₁₆TAB. The molecular level interactions between the surfactants in mixed micelles of these systems will be understood by measuring T₂ (spin-spin relaxation) parameters, T₁ (spin-lattice relaxation) parameters, and NOESY (nuclear Overhauser enhancement spectroscopy) spectra with the goal of testing hypotheses about the effects of sugar surfactant architecture on headgroup location.

4.3. Experimental

Cetyltrimethylammonium bromide (C₁₆TAB), dodecyltrimethylammonium bromide (C₁₂TAB) and decyltrimethylammonium bromide (C₁₀TAB) (all technical grade, Acros Organics) and n-dodecyl- β -D-glucopyranoside (C12G1) (99+%, Affymetrix) were used as received. n-octyl- β -D-triazole-xylopyranoside (C8XT1) was synthesized using click chemistry according to the procedure described by Oldham et al.²⁸⁸. All of the NMR samples were prepared by dissolving surfactant mixtures at the desired concentration in D₂O (100 atom% D, Fischer Scientific). The total surfactant concentration was fixed at 30 mM in all samples. Pyrene and hexadecylpyridinium chloride (C₁₆PyCl, Sigma-Aldrich) were used as received.

NMR experiments were conducted using a 400 MHz spectrometer at a fixed temperature of 50 °C maintained by a variable temperature (VT) controller. One-dimensional ^1H NMR spectra were acquired using the Varian *s2pul* pulse sequence with 32 scans and 3 sec delay (d_1) between pulse sequences for each sample. Spin-lattice relaxation (T_1) measurements were performed using the INVREC (inversion recovery) pulse sequence with 15 sec delay (d_1) between pulse sequences. Spin-spin relaxation (T_2) measurements were performed using the CPMGT2 (Carr-Purcell-Meiboom-Gill ²⁸⁹, ²⁹⁰) pulse sequence with a 40 sec delay (d_1) between pulse sequences. Nuclear Overhauser effect spectroscopy (NOESY) was performed using standard NOESY pulse sequence with 'Z' filter ²⁹¹ (to remove artifacts due to through bond magnetization transfer mechanism). Unless otherwise indicated, a mixing time of 600 ms was chosen by matching with the shortest T_1 value among all protons to observe every possible NOE correlation. A delay of 3 sec (d_1) between pulse sequences and, for 2D spectra, a resolution of 512×512 pixels were chosen. Fitting to determine T_2 parameters in some experiments was done using nonlinear regression with Sigma Plot 11.

Fluorescence experiments were performed using a Varian Cary Eclipse fluorescence spectrophotometer (Walnut Creek, CA) at room temperature. Pyrene was used as a fluorescence probe for mixed cmc and aggregation number calculations, and emission spectra were collected at an excitation wavelength of 335 nm. An aliquot solution of pyrene dissolved in ethanol was transferred from stock solution to a beaker and the solvent was evaporated with dry nitrogen. Surfactant mixtures dissolved in water were added according to require amount. The pyrene concentration (0.001 mM) was kept

constant for every experiment (both cmc and aggregation number measurements). For mixed cmc measurements, the total surfactant concentration was varied from 0.9 mM to 2.5 mM. For aggregation number studies, the total surfactant concentration was fixed at 30 mM. C₁₆PyCl was used as a quencher for aggregation number studies and its concentration was varied from 0 mM to 0.8 mM.

4.4. Results & Discussion

Figure 4.1 compares the molecular structures of C_nTAB (n = 16, 12 or 10) and C12G1 as determined by geometry optimization using the PM3 semiempirical molecular orbital method. The labeling of the protons in all surfactants is also provided in Figure 4.1. To check the accessibility of the sugar head in the three mixed surfactant systems, a fixed 1:1 molar ratio of the cationic surfactants with C12G1 was employed at a temperature of 50 °C (for comparison to prior mixing measurements with C₁₆TAB and C8G1). The cmc of C₁₆TAB, C₁₂TAB and C₁₀TAB are 0.9 mM²³⁰, 15 mM²⁸⁵ and 65 mM²⁹² respectively whereas the cmc of C12G1 is 0.13 mM²²⁴. Fluorescence measurements using pyrene as a probe were used to measure the mixed cmc for C_nTAB/C12G1 mixtures. Figure 4.2 shows the ratio of two pyrene fluorescence emission bands appearing at 374 nm (I₁) and 387 nm (I₃) vs. the total surfactant concentration where the change in slope suggests micelle formation. The break point in each plot is considered to be the cmc of the mixture, which is 0.19 mM, 0.26 mM and 0.42 mM for C₁₆TAB/C12G1, C₁₂TAB/C12G1 and C₁₀TAB/C12G1 respectively. The total surfactant concentration was selected to be 30 mM to stay well above the mixed cmc for each surfactant mixture so that the mixed micelle composition would be close to the bulk composition.

At the cmc, the mole fraction of each surfactant in mixed micelles and the interaction parameter (β) can be calculated using Rubingh's implementation of regular solution theory (RST) ⁶⁸. These are found by first solving Eq. (1) for X_1 (the mole fraction of cationic surfactant in the mixed micelle) and then using this value to calculate β using Eq. (2):

$$\frac{X_1^2 \ln\left(\frac{\alpha_1 cmc}{X_1 cmc_1}\right)}{(1-X_1)^2 \ln\left(\frac{(1-\alpha_1) cmc}{(1-X_1) cmc_2}\right)} = 1 \quad (1)$$

$$\beta = \frac{\ln\left(\frac{\alpha_1 cmc}{X_1 cmc_1}\right)}{(1-X_1)^2} \quad (2)$$

where α_1 = mole fraction of cationic surfactant in overall solution, cmc_1 = critical micelle concentration of the cationic surfactant, cmc_2 = critical micelle concentration of C12G1 and cmc = critical micelle concentration of the C12G1/cationic surfactant mixture.

Using Eq. 1 and 2 with the values from Figure 4.2, the mole fraction of C₁₆TAB in the 1:1 C₁₆TAB/C12G1 mixture at the cmc is 0.22 and the β value is -1.2, which is somewhat low compared to the value reported previously for this mixture ($\beta = 0.5$) ²²⁴. Negative β value means there is a favorable interaction between the two surfactants, and the increase in the value relative to C₁₆TAB/C8G1 suggests less favorable interactions ²⁹³. For C₁₂TAB/C12G1 and C₁₀TAB/C12G1 mixtures, Rubingh's method is difficult to apply because the cmc of the mixture is greater than cmc_2/α_2 which makes Eq. (1) very sensitive to X_1 . Little precision is expected, but for both systems X_1 is significantly less than 0.01, which gives $\beta > 100$ for C₁₂TAB/C12G1 and >1000 for C₁₀TAB/C12G1. The

huge variation in cmc between the surfactants makes these numbers difficult to measure with any precision, but the results suggest that mixing with C12G1 becomes less favorable as the cationic chain length decreases. Because of the breakdown of Rubingh's model, the model-independent approach described by Bergström et al.²⁹⁴ was used to calculate the synergistic parameter $\beta_{\text{Bergström}} = 4\ln(a_1+a_2)$ where $a_1 = \alpha_1*\text{cmc}/\text{cmc}_1$ and $a_2 = (1-\alpha_1)*\text{cmc}/\text{cmc}_2$. These values are reported in Table 1 as well and, while they do not agree with literature results calculated using Rubingh's model, they do show that the system moves from synergism ($\beta_{\text{Bergström}} = -0.71$) to antagonism ($\beta_{\text{Bergström}} = +1.93$) upon going from $n = 16$ to $n = 10$ without exceeding the value where micellar phase separation would be expected ($\beta_{\text{Bergström}} = +2.77$ ²⁹⁴).

Although at the cmc the majority of the surfactant in the mixed micelles is C12G1, the composition changes as the concentration exceeds the cmc. The mole fraction of individual surfactants in mixed micelles above the cmc can be calculated by solving nonlinear Eq. (3) based on an expansion of Clint's mixed micelle model using RST¹²⁸.

$$X_1^2(e^{\beta X_1^2}\text{cmc}_2 - e^{\beta(1-X_1)^2}\text{cmc}_1) + X_1(c + e^{\beta(1-X_1)^2}\text{cmc}_1 - e^{\beta X_1^2}\text{cmc}_2) - \alpha_1 c = 0 \quad (3)$$

here c = the total surfactant concentration and all other variables are defined above. With Eq. (3), the mole fraction of C₁₆TAB in C₁₆TAB/C12G1 mixtures is calculated to be ~0.42 at 30 mM total surfactant concentration, almost equal to the bulk composition. However, the composition of the other two systems cannot be calculated since β cannot be estimated.

The mean aggregation number (N_{agg}) of these surfactant mixtures was also calculated using steady state quenching of solubilized pyrene by hexadecylpyridinium chloride. (see supporting information, *Appendix D*, Figure D.1). The mean aggregation number was calculated using Eq. (4)²⁰⁵:

$$\ln\left(\frac{I}{I_0}\right) = -\frac{(N_{agg}[Q])}{(c-cmc)} \quad (4)$$

where I = fluorescence intensity in the presence of quencher, I_0 = fluorescence intensity in the absence of quencher, $[Q]$ = concentration of quencher, and c = total surfactant concentration.

Using Eq. (4), the mean aggregation numbers (N_{agg}) of C_n TAB/ $C12G1$ mixtures were determined to be 54, 54 and 74 for $n = 16, 12$ and 10 , respectively (fits are shown in supporting information, *Appendix D*, Figure D.2). The higher aggregation number for C_{10} TAB/ $C12G1$ may indicate larger micelle size or more close packed micelle for C_{10} TAB/ $C12G1$ compare to other mixtures, but the precise implications of the bulk measurements of micelle properties summarized in Table 4.1 needs more detailed interpretation. The precise radial positioning of the sugar headgroup can be understood using detailed NMR studies of interactions and dynamics in the mixed micelles.

Figures 4.3 shows the stack plot of 1D 1H NMR spectra C_n TAB / $C12G1$ surfactant mixtures. The peaks in the spectra were assigned by comparing to the previous study by Das et al. on the C_{16} TAB/ $C8G1$ system²⁹³. As the head group for both cationic and sugar surfactants are the same as for C_{16} TAB/ $C8G1$, only small shifts in the relative position of

peaks would be expected due to the varying chain lengths. The proton labels are indicated in Figure 4.1 and assignments for all three mixtures remain the same, except the relative position change of the H2 proton of C12G1. As the cationic tail chain length decreases from $n = 16$ to 12 to 10 in C_n TAB, the proton chemical shift of the H2 proton of C12G1 moves downfield. This suggests a change in chemical environment which will be explored in more detail by NOESY below. Also for the C_{10} TAB/C12G1 mixture, line broadening of the proton spectrum is observed, which is normally associated with shorter spin-spin relaxation (T_2) due to less mobility of molecules. This will be quantified by spin-echo measurements below.

To investigate the mobility of the sugar head group in mixed micelles, spin-lattice relaxation (T_1) and spin-spin relaxation (T_2) measurements were done for 30 mM C_n TAB/C12G1 mixtures at 50 °C. Before discussing the results of relaxation measurements, it is beneficial to introduce what is expected for micellar solutions. T_1 is the relaxation time constant in the direction parallel to the magnetic field due to the exchange of energy between a nucleus and the surrounding medium by tumbling, whereas T_2 is the spin-spin relaxation time constant, and is proportional to the time required for nuclei to relax in the plane perpendicular to the magnetic field due to interactions with other spins in the mixture. Generally, T_2 decreases as a nucleus enters into an environment with a higher local density of spins, or if the lifetime of interactions with neighboring spins increases (for instance, in a more viscous environment). For small molecules with rapid tumbling, the dependence of T_1 and T_2 on molecular mobility is the same, but for low molecular mobilities, T_1 follows the opposite trend of T_2 ; as the

local density surrounding a nucleus increases or the mobility decreases, T_1 is expected to increase due to slow tumbling. Thus, comparing these two parameters is a good way to learn about the local environment experienced by parts of a molecule in a micellar environment.

In micellar solutions, surfactants experience two (micro)phases, one being the bulk solution in which surfactant monomers are dispersed with solvent in close proximity, and the other being the interior of micelles where molecules are more tightly packed and less mobile. The high-density / low mobility core of the micelles is expected to give rise to the shortest T_2 values and longest T_1 values while for free monomers in solution, significantly less density of protons and rapid tumbling of the molecules should give rise to the longest T_2 and shortest T_1 values. The T_2/T_1 ratio is also considered to be a measurement of “degree of restricted motion” as established by Somasundaran’s group^{286, 287}.

Measurement of relaxation parameters may be complicated by the presence of two microenvironments in micellar solutions. If exchange of surfactants between micelles and the bulk solution is slow (on the timescale of the pulse sequences used for relaxation measurements), the decay of signal would be expected to follow a weighted sum of exponentials corresponding to the relaxation of the population in each environment. If exchange is fast, signal will decay with a single exponential with the weighted average of the relevant parameters (T_1 or T_2) for monomer and micellar microenvironments. When $C_{16}TAB$, $C_{12}TAB$ and $C_{10}TAB$ are compared at equal mixing

ratios with C12G1 and at the same concentration, the concentration of monomeric surfactants is expected to be approximately equal. Therefore, observed differences in T_1 and T_2 are most likely due to differences in the micellar contribution that arises from differences in the mobility of the sugar head group.

Table 4.2 lists T_1 and T_2 values for selected headgroup protons of C_n TAB/C12G1 mixtures. The selected protons are free from any ambiguity due to contributions to the decay profile from protons in different chemical environments. For C_{16} TAB/C12G1 and C_{12} TAB/C12G1 mixtures, T_1 and T_2 values are comparable for all selected protons. This suggests a similar chemical environment around the sugar headgroups that gives almost the same level of mobility for the sugar head groups in these two mixtures. In contrast, the C_{10} TAB/C12G1 mixture consistently has larger T_1 values and smaller T_2 for the sugar headgroup protons of C12G1 in than in C_{16} TAB/C12G1 or C_{12} TAB/C12G1 mixture. The T_2/T_1 values listed in table 4.2 shows also indicate a higher degree of restricted motions of sugar head group of C12G1 in the C_{10} TAB/C12G1 mixture compare to other mixtures. This would be consistent with close association of the C12G1 headgroups in micellar aggregates, leading to less molecular tumbling and therefore more solid-like NMR relaxation characteristics.

Although T_1 and T_2 analysis give indirect information about the local environment around the carbohydrate head groups in mixed micelles, the proximity of protons in sugar head groups to other species in mixed micelle was measured using 2D Nuclear Overhauser effect spectroscopy (NOESY) for all three mixtures. Figure 4.4 shows the

2D NOESY pattern for a 1:1 C₁₆TAB/C12G1 mixture in D₂O at 50 °C with a total surfactant concentration of 30 mM. All of the cross peaks are numbered in Figure 4.4, and can be categorized according to the nature of the interaction. Several sugar-sugar NOE correlations (cross peaks 1-6) are found among the headgroup protons of C12G1. Cross peak 1 correlates the α''_B proton of C12G1 with the α''_A /H6_A proton of C12G1, while cross peak 2 correlates the H3/H4 proton of C12G1 with the H6_A proton of C12G1. Cross peak 3 correlates the H2 proton of C12G1 with neighboring H3/H4 protons of C12G1. Cross peak 4 represents a correlation between the α''_B proton of C12G1 and the H1 proton of C12G1. Cross peak 5 correlates the H3/H4 proton of C12G1 with the H1 proton of C12G1 whereas cross peak 6 correlates the H1 and H2 protons of C12G1.

In addition to these clear interactions among headgroups of the same type, there are three cross peaks (cross peaks 7, 8 and 9) in Figure 4.4 that can be either sugar-cationic interactions or sugar-sugar interactions. The ambiguity arises because the chemical shift of the α' proton of C₁₆TAB coincides with the chemical shift of the H5 proton of C12G1 (Figure 4.3). Cross peak 7-9 correlate this ambiguous α' proton of C₁₆TAB or H5 proton of C12G1 with the H3/H4 proton, H6_B proton and H1 proton of the C12G1 sugar headgroup, respectively. In previous study with C₁₆TAB/C8G1 mixtures, the same types of correlations were seen between the same protons and 3D NOESY-¹³C-HSQC was used to show that correlations were only with the H5 proton of C8G1. There were no sugar-cationic correlations. Due to the similarity with the correlation patterns in Figure 4.4 and the headgroups of the surfactants, cross peaks 7-9 are assigned to sugar-sugar correlation for the C₁₆TAB/C12G1 mixture. Apart from these correlations there are

several others sugar-sugar and cationic-cationic correlations (cross peaks 10-18) between sugar head group protons with the alkyl chain protons of C12G1 or C₁₆TAB. Cross peak 10 and 11 correlate the $\alpha''_A/H6_A$ and α''_B protons of C12G1 with $\beta''_{A,B}$ protons of C12G1, respectively. Cross peak 12 correlates $\alpha'_{a,b}$ protons of C₁₆TAB or H5 proton of C12G1, respectively. Cross peak 13-18 correlates the rest of the alkyl chain methylene protons (after the β position) of C₁₆TAB or C12G1 with the (13) $\alpha''_A/H6_A$ proton of C12G1, (14) H6_B proton of C12G1, (15) $\alpha'_{a,b}$ proton of C₁₆TAB or H5 proton of C12G1, (16) $\beta'_{a,b}$ proton of C₁₆TAB, (17) $\beta''_{A,B}$ protons of C12G1, and (18) ω protons of C₁₆TAB or C12G1.

One remaining possible correlation between the heads of the two surfactants would be between the N_{CH3} protons of C₁₆TAB with the sugar headgroup protons. A vertical streak appears at the position of the N_{CH3} protons in Figure 4.4 due to t₁ noise. This noise is caused by unavoidable instrument or temperature control instability and is most prominent for higher intensity peaks. This may be resolved by using a symmetrization method²⁹⁵ but this technique is capable of introducing artificial cross peaks for uncoupled signals with excessive t₁ signals, so this method was not used here to resolve the N_{CH3} cross peaks. Instead, the NOE correlations of N_{CH3} protons of C₁₆TAB were measured using 1D NOE.

Figure 4.5 shows the 1D NOE spectrum for the C₁₆TAB/C12G1 1:1 surfactant mixture at 50 °C with a total surfactant concentration of 30 mM. In Figure 4.5, spectrum radiation was done from the N_{CH3} protons of C₁₆TAB head group. In 1D NOE every radiated

spectrum is subtracted from a reference spectrum so that only peaks having NOE correlations with the radiated peak appear after spectrum processing. In Figure 4.5 by comparing the subtracted spectrum (upper part of the figure) with the 1D proton NMR spectrum (lower part of the figure) the only correlation that is seen with the N_{CH_3} proton is the α proton of $C_{16}TAB$. No correlations with the sugar headgroup protons were found. The 2D and 1D NOE spectrum results therefore indicate that there is no evidence of correlations between sugar and cationic headgroups in the $C_{16}TAB/C12G1$ system.

2D NOESY experiment was also done for the 30 mM $C_{12}TAB/C12G1$ 1:1 surfactant mixture followed by a 1D NOE experiment radiated from the N_{CH_3} peak of $C_{12}TAB$ (see Supporting Information, *Appendix D*, Figure D.3 and D.4 along with associated discussion). The results for the $C_{12}TAB/C12G1$ mixture were similar to $C_{16}TAB/C12G1$ and indicate no sugar-cationic correlations. In both systems, correlations were found among carbohydrate protons and between carbohydrate head and alkyl chains, which are consistent with our previous study of the $C_{16}TAB/C8G1$ mixture. There we had concluded that the sugar heads are solubilized as clusters, most likely with their headgroups pointing towards the core of the mixed micelle in an inverted micelle-within-micelle configuration. The NOE results (Figures 4.4 and 4.5) show that increasing the carbohydrate surfactant alkyl tail length from C8 to C12 did not result in “pushing” the glucopyranoside headgroup to the exterior of the micelle. Matching the lengths of the two alkyl tails in the $C_{12}TAB/C12G1$ system (Figures D.3 and D.4) also did not provide enough of a driving force to cause the alkyl surfactant to reorient with its headgroup in the corona or exterior of the micelle. Therefore, as one last attempt to use relative

lengths of tails to promote accessibility of the sugar headgroup, a cationic surfactant with a shorter tail than the sugar surfactant was investigated (the C₁₀TAB/C12G1 system).

Figure 4.6 shows the 2D NOESY spectrum for the C₁₀TAB/C12G1 surfactant mixture under the same conditions as Figure 4.4. As for the other two mixtures of C12G1 with cationic surfactants, Figure 4.6 does not indicate any sugar-cationic headgroup NOE interactions between C₁₆TAB and C12G1 surfactants in the micelle, although we can see an increase in interactions among sugar headgroup protons and between sugar headgroup and alkyl chain protons. Cross peaks 1-9 all indicate sugar-sugar headgroup correlations. Cross peaks 1 and 2 correlate the α''_B proton of C12G1 with $\alpha''_A/H6_A$ and H3/H4 protons of C12G1, respectively, while cross peaks 3 and 4 correlate the H3/H4 proton with $\alpha''_A/H6_A$ and H2 protons of C12G1, respectively. Cross peak 5 correlates the H3/H4 proton of C12G1 with the H5 proton of C12G1 or $\alpha'_{a,b}$ proton of C₁₀TAB, but by analogy with C₁₆TAB/C12G1 the former (sugar-sugar) correlation is more likely. Cross peak 6 correlates the H2 and H6_B protons of C12G1 while cross peak 7 correlates the $\alpha''_A/H6_A$ and H1 protons of C12G1. Cross peak 8 and 9 correlate H1 proton of C12G1 with the α''_B and H3/H4 protons of C12G1, respectively.

Apart from sugar-sugar correlations, there are some correlations among the alkyl chain protons of C₁₀TAB or C12G1. Cross peak 10 and 11 correlate methylene protons (beyond β) in alkyl chains of C12G1 or C₁₀TAB with $\beta'_{a,b}$ proton of C₁₀TAB and $\beta''_{A,B}$ protons of C12G1, respectively. Cross peak 12 correlates ω protons of C₁₀TAB or C12G1 with alkyl

methylene protons (beyond β) of C₁₀TAB or C12G1. There are also several explicit correlations (cross peaks 13-19) between the sugar head group and the alkyl chains of C₁₀TAB or C12G1. Cross peak 13 correlates H2 and $\beta''_{A,B}$ protons of C12G1 while cross peak 14 correlates $\alpha'_{a,b}$ protons of C₁₀TAB or H5 proton of C12G1 with $\beta'_{a,b}$ protons of C₁₀TAB. Cross peak 15-18 correlate alkyl chain methylene protons (beyond β) of C12G1 or C₁₀TAB with (15) H1, (16) $\alpha''_A/H6_A$, (17) α''_B and (18) H3/H4 protons of the C12G1 head group, respectively. Cross peak 19 correlates methylene protons of the alkyl chains (beyond β) of C12G1 or C₁₀TAB with the $\alpha'_{a,b}$ proton of C₁₀TAB or H5 proton of C12G1.

1D NOE experiments (see Supporting Information, *Appendix D*, Figure D.5 with associated discussion) were also done to see the correlations between the N_{CH3} protons of C₁₀TAB with the sugar head group but, similar to other two surfactant mixtures here, also showed no correlation between the N_{CH3} protons of C₁₀TAB and the sugar head of C12G1. All of these NOE measurements show that even if the carbohydrate chain lengths are adjusted to the point that the cationic surfactant tail is shorter than in the carbohydrate surfactant, no evidence for direct mixing between cationic and sugar headgroups in the corona of the micelle can be found. This suggests a structural model similar to that of C₁₆TAB/C8G1²⁹³ in which sugar headgroups point towards the core of the mixed micelle. The NOE results actually suggest that trying to tune tail lengths to “push out” the headgroup strengthened interactions among sugar headgroups and between sugar headgroups and the alkyl chains of the both surfactants. In C₁₀TAB/C12G1, this leads to a high degree of confinement of sugar headgroups within the micelle as suggested by T₁ / T₂ analysis (Table 4.2), but the entropic penalty

associated with this confinement is still not enough to cause the micelle to adopt a configuration with accessible sugar headgroups. Figure 4.7 schematically shows the arrangement of the sugar heads near the core of the mixed micelle for the C₁₀TAB/C12G1 mixture. Sugar heads are not at all accessible for this and the other C_nTAB/C12G1 mixtures studied.

The mechanism of “pushing out” sugar headgroups by matching the surfactant chain length is most likely unsuccessful because of the huge mismatch of interaction forces between the two different types of headgroups with the polar surroundings. The trimethylammonium headgroup of the cationic surfactants interacts very strongly with the surrounding polar environment by ionic hydration forces, while the carbohydrate surfactants interact by hydrogen bonding in a manner similar to water itself. This difference is exemplified in the much higher cmc value for a cationic surfactant with the same tail: 15 mM for C₁₂TAB vs. 0.13 mM for C12G1, which indicates that C12G1 is more hydrophobic and susceptible to separation from the aqueous phase. At the same time, C12G1 has an even greater driving force to separate into a nonpolar medium if possible. The octanol-water partition coefficient can be extrapolated from a study of surfactants of varying tail length to be given by $\log(K_{ow}) \sim 4.3$ ²³⁸. This corresponds to a free energy of transfer from water to octanol of -24.5 kJ/mol at 298 K, whereas the free energy of micellization of C12G1 is -22.2 kJ/mol at the same temperature. As a result, C12G1 is solubilized by C_nTAB surfactants at concentrations much lower than the cmc of the cationic surfactant even when RST models suggest that synergistic interactions are not operative.

To make the carbohydrate head accessible near the exterior of the mixed micelle, an alternative approach is to introduce a functional group into the carbohydrate surfactant to provide an additional molecular force to “pull” the sugar head toward the polar exterior of the mixed micelle. To make this possible without altering the sugar headgroup, the linker between the sugar and alkyl tail was replaced with a triazole group. Figure 4.8 compares the molecular structures of C8XT1 with C₁₆TAB as determined by geometry optimization using the PM3 semiempirical molecular orbital method. Our hypothesis is that due to an extra dipolar interaction between the triazole linker and cationic headgroups or polar surrounding, the carbohydrate head group will be “pulled out” of the mixed micelle. For that reason we mixed n-octyl-β-D-triazole-xylopyranoside (C8XT1) with C₁₆TAB under the same conditions as the other mixed micelle studies.

Due to readily availability of C8XT1²⁸⁸, it was selected instead of a glucose-based surfactant with triazole linker. However, C8X1 (octyl-β-D-xylopyranoside) shows evidence of also having its sugar headgroup “buried” in the core of mixed micelles with C₁₆TAB²⁹³, and presumably if the xylosehead group is drawn to the exterior of a mixed micelle, glucose headgroups also can be due to the more hydrophilic nature of the glucoside compared to xyloside headgroups. The individual cmc as well as mixed cmc of the C₁₆TAB/C8XT1 mixture was calculated by a spin lattice relaxation study and fluorescence probe experiments. The cmc values are 11 mM and 1.42 mM for pure C8XT1 and C₁₆TAB/C8XT1 mixture respectively (see Supporting Information, *Appendix D*, Figure D.6 and D.7 with associated discussion). The mole fraction of C₁₆TAB in the mixed

micelle at the cmc and the β value for C₁₆TAB/C8XT1 were calculated with Rubingh's model to be 0.83 and -1.47, respectively. The negative β value suggests a synergistic interaction between the two surfactants and is less than β for C₁₆TAB/C8X1 (-0.86)²⁹³. Although the majority of the surfactant in mixed micelles is C₁₆TAB at the cmc (due to its lower cmc), at 30 mM the C₁₆TAB mole fraction is calculated using Eq. (3) to be 0.55, almost equal to the bulk composition.

Figure 4.9 shows the 1D ¹H NMR spectrum of the C₁₆TAB/C8XT1 1:1 mixture. The peaks in the spectra were assigned by comparing to the previous study by Das et al. on the C₁₆TAB/C8X1 system and including the unique linker protons. To investigate the proximity of the carbohydrate headgroup with other protons in the C₁₆TAB/C8XT1 mixture, a 2D NOESY pattern was collected. Figure 4.10 shows the 2D NOESY spectrum for the C₁₆TAB / C8XT1 surfactant mixture under the same conditions as Figure 4.4 and Figure 4.6. Figure 4.10 shows relatively fewer sugar-sugar correlations (peaks 1-8) compare to the C_nTAB/C12G1 mixtures. Cross peak 1 correlates the H3 and H4 protons of C8XT1 while cross peak 2 correlates the H3 proton of C8XT1 with the H2/H5_B proton of C8XT1 or $\alpha'_{a,b}$ protons of C₁₆TAB. Cross peak 3- 5 correlate the H4, H5_A and H1 protons with the H2/H5_B proton of C8XT1 or $\alpha'_{a,b}$ proton of C₁₆TAB, respectively. Cross peak 6 correlates the H_N proton of C8XT1 from the triazole linker with the $\alpha''_{A,B}$ proton of C8XT1 while cross peak 7 correlates the H_{N-1} and H_{N-1'} protons of C8XT1. Cross peak 8 correlates the $\beta''_{A,B}$ proton of C8XT1 with the H2/H5_B proton of C8XT1 or $\alpha'_{a,b}$ protons of C₁₆TAB. In addition to these sugar-sugar correlations, one sugar-cationic correlation (cross peak 9) is found between the $\alpha''_{A,B}$ proton of C8XT1 and the $\beta'_{a,b}$ protons of

C₁₆TAB. This direct interaction between cationic and carbohydrate surfactants was absent for other alkyl esters of sugars mixed with trimethylammonium surfactants such as C₁₂G1/C₁₆TAB (Figure 4.4) or C8X1/C₁₆TAB²⁹³. Fewer sugar-sugar headgroup correlations and a new direct sugar-cationic correlation indicate a significant change in the arrangement of the sugar head group in mixed micelle of C₁₆TAB/C8XT1 mixture compared to the other systems studied here. Also, no correlations between sugar headgroups and alkyl tail protons are found in Figure 4.10, also supporting the idea that the sugar headgroups have moved out of the core of the mixed micelle.

To see the correlations between the N_{CH3} head group of C₁₆TAB with sugar headgroups of C8XT1, a 1D NOE experiment was also done (Figure 4.11). Radiation was done from N_{CH3} protons of C₁₆TAB. In contrast to Figure 4.5, several sugar head correlations with the NH₃ proton are found in Figure 4.11. Specifically, the NH₃ protons of C₁₆TAB correlate with the H_N, H_{N-1}, H_{N-1'}, H1, H5 and H4 proton of C8XT1. There is also one cationic-cationic surfactant correlation between the α'_{a,b} and N_{CH3} protons of C₁₆TAB similar to the C₁₆TAB/C₁₂G1 mixture. All of these direct correlations between the sugar and cationic head indicate that as hypothesized, the sugar head has been “pulled” to the exterior of the mixed micelle by interactions between the polar triazole linker and the ionic headgroups and water in the corona region.

Figure 4.12 illustrates schematically where the sugar and cationic head are located in the mixed micelle. The change in the carbohydrate head group orientation in the mixed micelle contrasts with Figure 4.7 and suggests that the strategy of introducing more

polar linker than an ester linkage not only has synthetic advantages for easy use of natural products to produce sugar surfactants^{288, 296} but can also make the sugar headgroups accessible to the exterior of the micelle for applications such as molecular imprinting of polymeric and metal oxide matrices. This helps to explain why previous attempts to imprint silica using mixtures of C₁₆TAB and C8G1 or C8X1 were only successful when mixed monolayers, rather than micelles, were used to present the sugars to the oxide surface. These results suggest that sugar surfactants with triazole linkers should be promising candidates when mixed with cationic surfactants for generating high surface area, mesoporous molecular sieves with selective sugar binding sites.

4.5. Conclusions

In this study, the accessibility of the head groups of carbohydrate surfactant in a mixed micelles with cationic surfactant was studied in detail using different NMR techniques including spin-lattice (T_1) relaxation, spin-spin (T_2) relaxation and 2D NOESY measurements. Additional micellar parameters were measured by fluorescence probe measurements. The results suggest that matching of cationic and carbohydrate surfactant tail lengths is not sufficient to “push out” the carbohydrate head group to the exterior of the micelle. Consistent with our previous study of the C₁₆TAB/C8G1 mixture, there is no detectable nuclear Overhauser effect (NOE) correlation between the headgroup of dodecyl glucoside (C12G1) and the head group of C₁₆TAB. Instead, the sugar headgroups interact among themselves or with the tails of the surfactants. These correlations indicate that sugar headgroups aggregate at the interior of the micelle,

most likely pointing towards the core of the mixed micelle consistent with previous study of C₁₆TAB/C8G1 mixture. The situation does not change after replacing the hexadecyl chain of C₁₆TAB with a dodecyl chain in C₁₂TAB, and the inverted orientation of the carbohydrate heads becomes more extreme when the cationic chain is reduced to decyl (C₁₀TAB). For C₁₀TAB/C12G1 mixture, stronger NOE interactions between the sugar heads and surfactant tails are seen, indicating greater confinement of the sugar head in the core compare to C₁₆TAB/C12G1 and C₁₂TAB/C12G1. Restricted motion is supported by line broadening in the proton spectrum along with spin-lattice relaxation (T₁) and spin-spin relaxation (T₂) analysis.

Tuning relative tail lengths may not be able to change the headgroup accessibility because of the large difference in molecular interactions between sugar headgroups (which interact as well or better with each other as with water) and cationic headgroups with a polar medium. The large difference in favorability of interactions with water is not overcome by entropic penalties associated with confinement of sugar headgroups in the core of the micelle. Therefore, a second hypothesis was tested that adding a more polar linker to the sugar surfactant would “pull” the sugar headgroup near the exterior of the mixed micelle. To investigate this hypothesis C₁₆TAB, was mixed with n-octyl-β-D-triazole-xylopyranoside (C8XT1), a new carbohydrate surfactant with a triazole linker. Successive 2D NOESY and 1D NOE measurements for C₁₆TAB/C8XT1 show several NOE correlations between the sugar and cationic headgroups in the mixed system, which proves the hypothesis that tuning interactions with a polar linker is a viable strategy to create mixed micelles with accessible headgroups.

This study has provided new insights into the 3D structure of synergistic cationic / sugar surfactant micelles, and suggests that merely knowing that mixing is thermodynamically favorable does not guarantee that sugar headgroups are accessible to the bulk polar medium. For instance, C₁₆TAB and C8G1 have good synergy ($\beta = -2.5$) but the glucoside headgroups are not accessible²⁹³. Increasing the sugar surfactant tail to C12G1 worsens the bulk synergy, and decreasing the cationic tail length creates more antagonistic interactions, none of which help to drive the sugar headgroup out of the micelles. This prevents the use of carbohydrate alkyl ester / cationic surfactant mixtures for applications such as molecular imprinting. However, this problem is solved by tailoring the linker with a triazole linker in the carbohydrate surfactant to make the carbohydrate headgroup accessible without changing its structure.

Table 4.1. Values of mixed critical micelle concentration (cmc) from pyrene solvatochromism, overall mole fraction of C₁₆TAB (α_1) in mixed solution, mole fraction of C₁₆TAB (X₁) in mixed micelle at cmc and at 30 mM total surfactant concentration, interaction parameter (β) and aggregation number (N_{agg}) from pyrene quenching for C₁₆TAB/C12G1, C₁₂TAB/C12G1 and C₁₀TAB/C12G1 mixtures.

Surfactant	cmc	α_1	X ₁ (at cmc)	X ₁ (at 30 mM)	β	$\beta_{\text{Bergström}}$	N _{agg}
CTAB/C12G1	.19	0.5	0.22	0.42	-1.2	-0.71	54
C ₁₂ TAB/C12G1	.26	0.5	<0.01	X	>0	0.03	54
C ₁₀ TAB/C12G1	0.42	0.5	<0.01	X	>0	1.92	74

Table 4.2. Comparison of T₁ and T₂ values of headgroup protons in C₁₆TAB/C12G1, DTAB/C1G1 and DeTAB/C12G1 mixed micellar systems.

Surfactants	Protons	T ₁ (ms)	T ₂ (ms)	T ₂ /T ₁ (ms)
C ₁₆ TAB/C12G1	H1	746±14	21±5	.028±.006
C ₁₂ TAB/C12G1	H1	735±20	19±4	.026±.005
C ₁₀ TAB/C12G1	H1	1063±40	10±5	.009±.004
C ₁₆ TAB/C12G1	6B	450±26	74±7	.164±.018
C ₁₂ TAB/C12G1	6B	482±4	72±7	.149±.014
C ₁₀ TAB/C12G1	6B	497±12	14±3	.028±.006
C ₁₆ TAB/C12G1	H3,H4	794±20	76±12	.096±.015
C ₁₂ TAB/C12G1	H3,H4	542±12	88±17	.162±.031
C ₁₀ TAB/C12G1	H3,H4	893±24	43±6	.049±.006

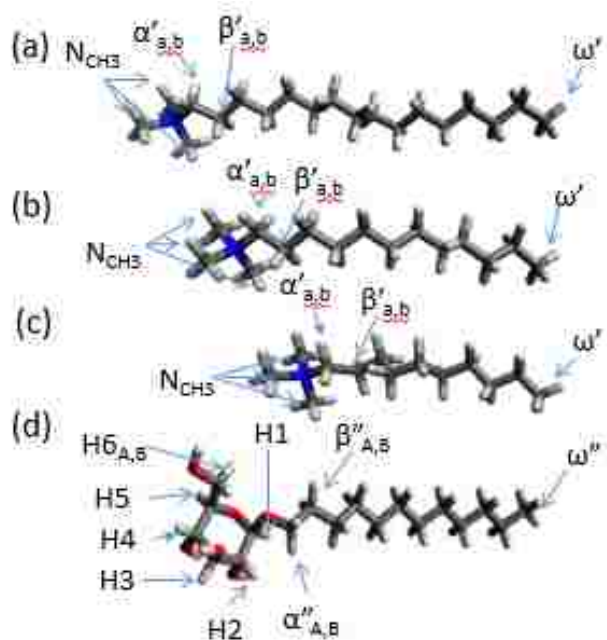


Figure 4.1. Molecular structures of (a) C₁₆TA⁺ [TA⁺ denotes a trimethylammonium headgroup] (b) C₁₂TA⁺ (c) C₁₀TA⁺ and (d) C₁₂G1 determined by geometry optimization using the PM3 semiempirical molecular orbital method as implemented in the program Avogadro. The labeling of the protons in these structures will be used in the discussion of the NMR spectra.

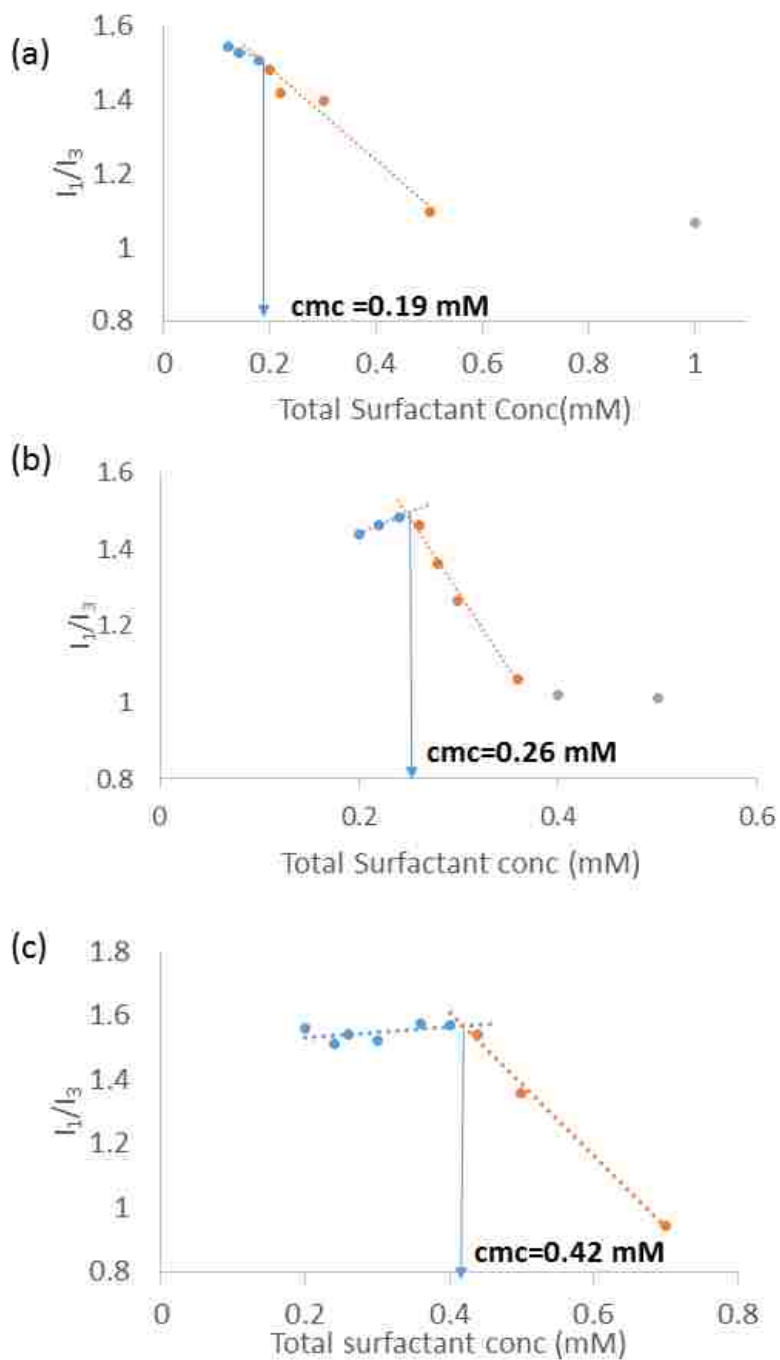


Figure 4.2. Pyrene fluorescence emission intensity ratio I_1/I_3 vs. total surfactant concentration for (a) $C_{16}TAB/C_{12}G1$, (b) $C_{12}TAB/C_{12}G1$ and (c) $C_{10}TAB/C_{12}G1$ at 50 °C. In all cases a 1:1 overall ratio of surfactants was used. Arrows denote the mixed cmc values.

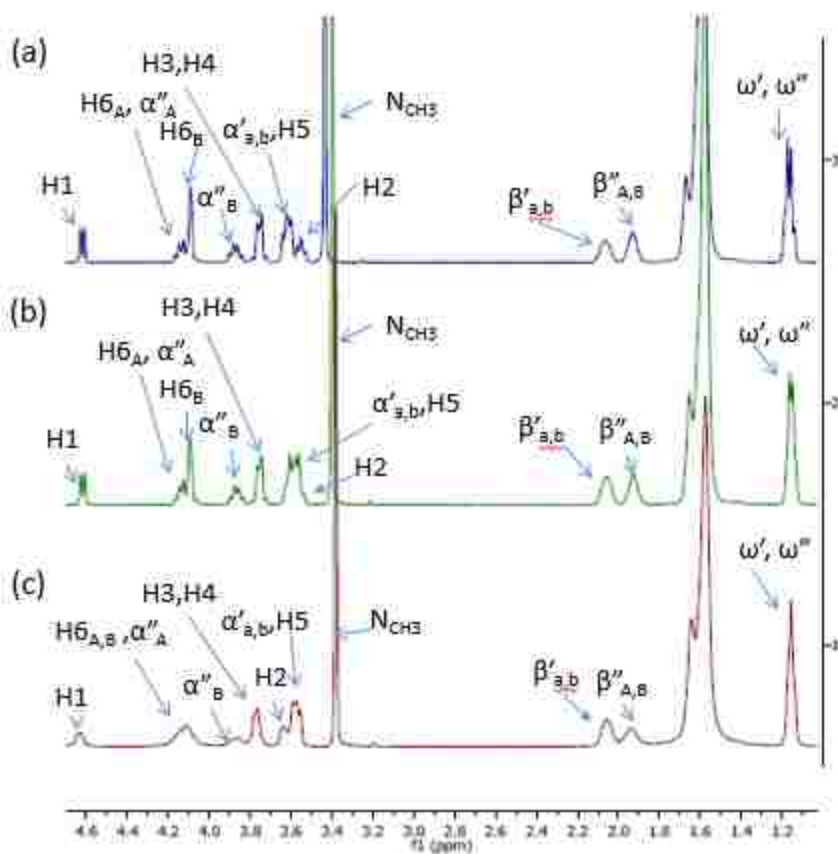


Figure 4.3. 1D ^1H NMR spectrum of 1:1 (a) $\text{C}_{16}\text{TAB}/\text{C}_{12}\text{G1}$ (b) $\text{C}_{12}\text{TAB}/\text{C}_{12}\text{G1}$ and (c) $\text{C}_{10}\text{TAB}/\text{C}_{12}\text{G1}$ in D_2O at $50\text{ }^\circ\text{C}$ (total surfactant concentration 30 mM).

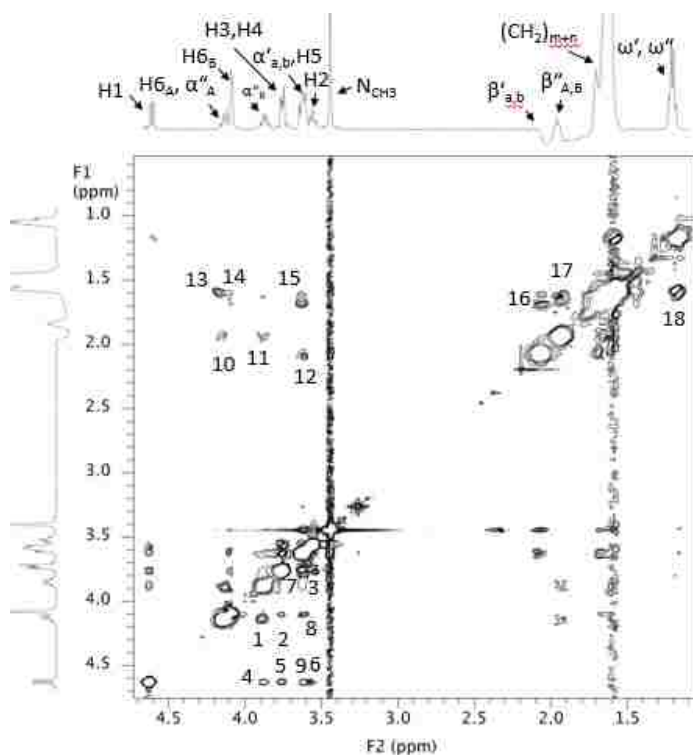


Figure 4.4. 2D NOESY spectrum of 1:1 C₁₆TAB/C₁₂G1 in D₂O at 50 °C (total surfactant concentration 30 mM). Cross peaks indicate the NOE correlations between the associated protons and are symmetric along the diagonal. The spectrum indicates several sugar-sugar or cationic-cationic surfactant NOE correlations (cross peak 1) $\alpha''_A/H6_A$ & α''_B proton; 2) H3/H4 & H6_A proton 3) H3/H4 & H2 proton; 4) α''_B & H1 proton; 5) H3/H4 & H1 proton; 6) H1 & H2 proton; 7) $\alpha'_{a,b}/H5$ & H3/H4 proton; 8) $\alpha'_{a,b}/H5$ & H6_B proton; 9) $\alpha'_{a,b}/H5$ & H1 proton; 10) $\alpha''_A/H6_A$ & $\beta''_{A,B}$ proton; 11) α''_B & $\beta''_{A,B}$ proton; 12) $\alpha'_{a,b}/H5$ & $\beta'_{a,b}$ proton; 13) $\alpha''_A/H6_A$ & (CH₂)_{m+n} proton; 14) H6_B & (CH₂)_{m+n} proton; 15) $\alpha'_{a,b}/H5$ & (CH₂)_{m+n} proton; 16) $\beta'_{a,b}$ & (CH₂)_{m+n} proton; 17) $\beta''_{A,B}$ & (CH₂)_{m+n} proton; 18) (CH₂)_{m+n} & ω'/ω'' proton).

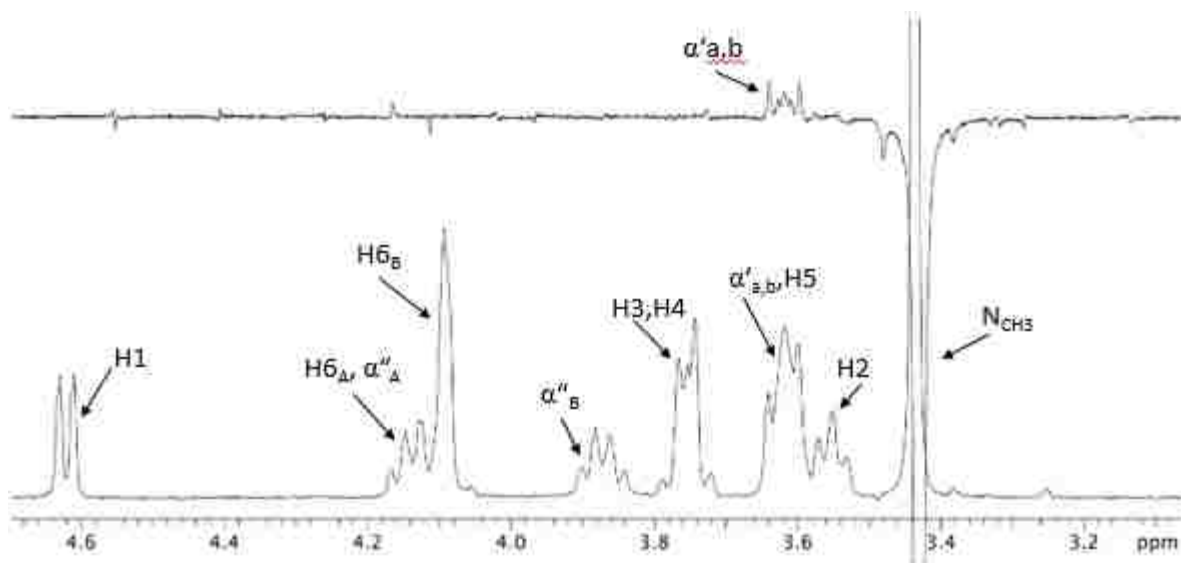


Figure 4.5. 1D NOE spectrum of 1:1 C₁₆TAB/C12G1 in D₂O at 50 °C (total surfactant concentration 30 mM). The only correlation that is seen with the N_{CH3} protons (in the upper spectrum) is from the α'_{a,b} protons of C₁₆TAB. The lower 1D NMR spectrum of the mixture is provided for reference.

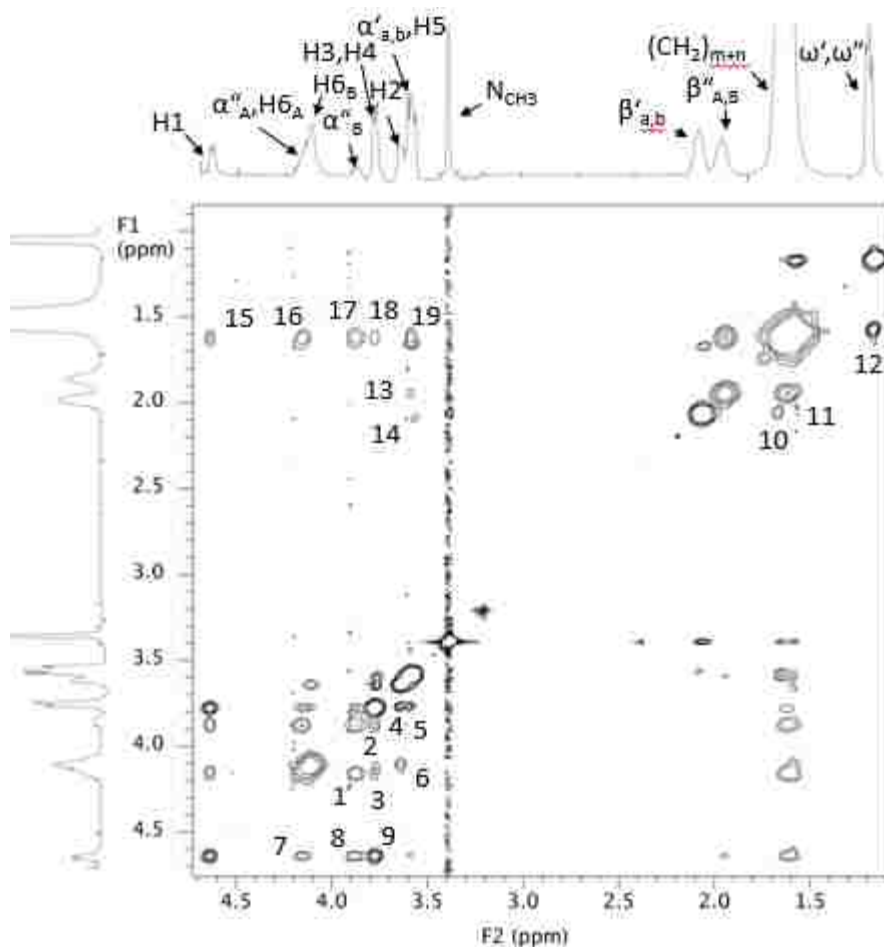


Figure 4.6. 2D NOESY spectrum of 1:1 C₁₀TAB/C₁₂G1 in D₂O at 50 °C (total surfactant concentration 30 mM). Cross peaks indicate the NOE correlations between the associated protons and are symmetric along the diagonal. The spectrum indicates several sugar-sugar or cationic-cationic surfactant NOE correlations (cross peak 1) $\alpha''_A/H6_A$ & α''_B proton; 2) α''_B & H3/H4 proton; 3) $\alpha''_A/H6_A$ & H3/H4 proton; 4) H2 & H3/H4 proton; 5) H3/H4 & $\alpha'_{a,b}/H5$ proton; 6) H2 & H6_B proton; 7) $\alpha''_A/H6_A$ & H1 proton; 8) α''_B & H1 proton; 9) H3/H4 & H1 proton; 10) $\beta'_{a,b}$ & (CH₂)_{m+n} proton; 11) $\beta''_{A,B}$ & (CH₂)_{m+n} proton; 12) ω'/ω'' & (CH₂)_{m+n} proton; 13) H2 & $\beta''_{A,B}$ proton; 14) $\alpha'_{a,b}/H5$ & $\beta'_{a,b}$ proton; 15) H1 & (CH₂)_{m+n} proton; 16) $\alpha''_A/H6_A$ & (CH₂)_{m+n} proton; 17) α''_B & (CH₂)_{m+n} proton; 18) H3/H4 & (CH₂)_{m+n} proton; and 19) $\alpha'_{a,b}/H5$ & (CH₂)_{m+n} proton).

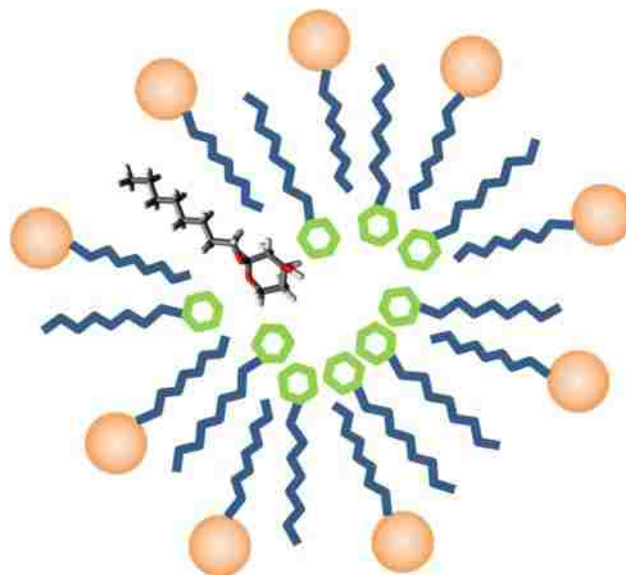


Figure 4.7. Schematic diagram showing relative position of head groups in ideal mixed micelle of C₁₀TAB and C₁₂G1 based on the 3D geometry of the micelles and favorable interactions between headgroups.

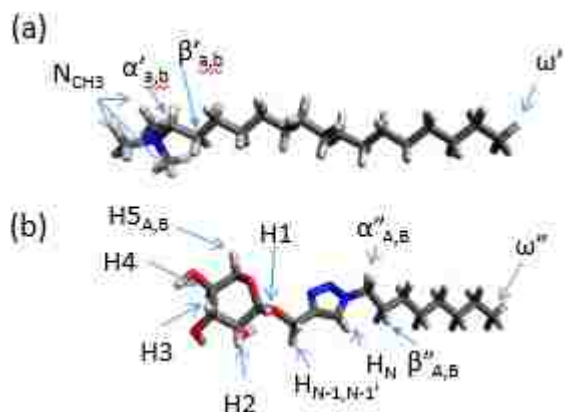


Figure 4.8. Molecular structures of (a) $C_{16}TA^+$ and (b) C_8XT1 determined by geometry optimization using the PM3 semiempirical molecular orbital method as implemented in the program Avogadro. The labeling of the protons in these structures will be used in the discussion of the NMR spectra.

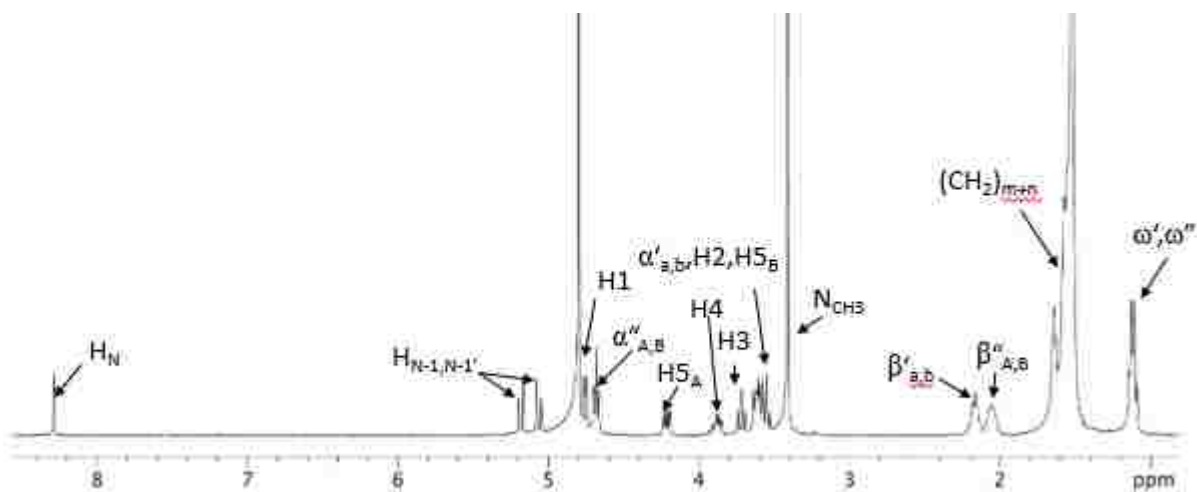


Figure 4.9. 1D ^1H NMR spectrum of 1:1 $\text{C}_{16}\text{TAB}/\text{C8XT1}$ in D_2O at $50\text{ }^\circ\text{C}$ (total surfactant concentration 30 mM).

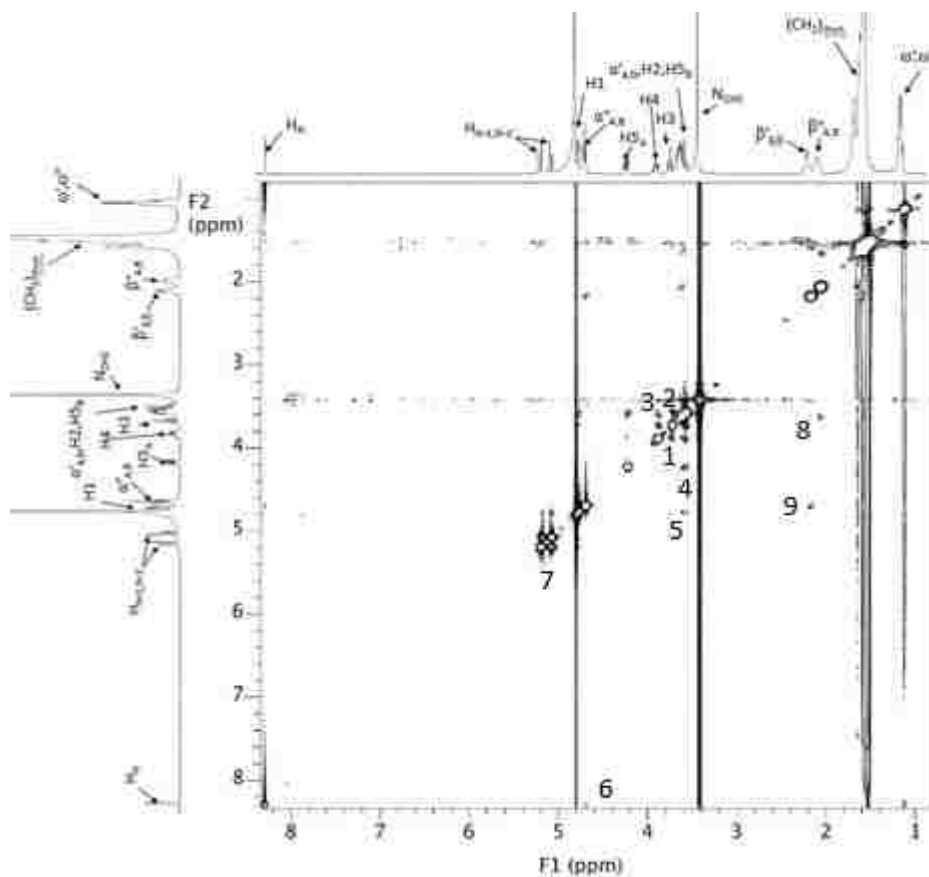


Figure 4.10. 2D NOESY spectrum of 1:1 C₁₆TAB/C8XT1 in D₂O at 50 °C (total surfactant concentration 30 mM). Cross peaks indicate the NOE correlations between the associated protons and are symmetric along the diagonal. The spectrum indicates several sugar-sugar or cationic-cationic surfactant NOE correlations (cross peak 1) H3 & H4 proton; 2) H3 & $\alpha'_{a,b}/H2/H5_B$ proton; 3) H4 & $\alpha'_{a,b}/H2/H5_B$ proton; 4) H5_A & $\alpha'_{a,b}/H2/H5_B$ proton; 5) H1 & $\alpha'_{a,b}/H2/H5_B$ proton; 6) H_N & $\alpha''_{A,B}$ proton; 7) H_{N-1} & H_{N-1'} proton; 8) $\beta''_{A,B}$ & $\alpha'_{a,b}/H2/H5_B$ proton). In also indicates one sugar-cationic correlation between $\beta'_{a,b}$ protons of C₁₆TAB with $\alpha''_{A,B}$ protons of C8XT1.

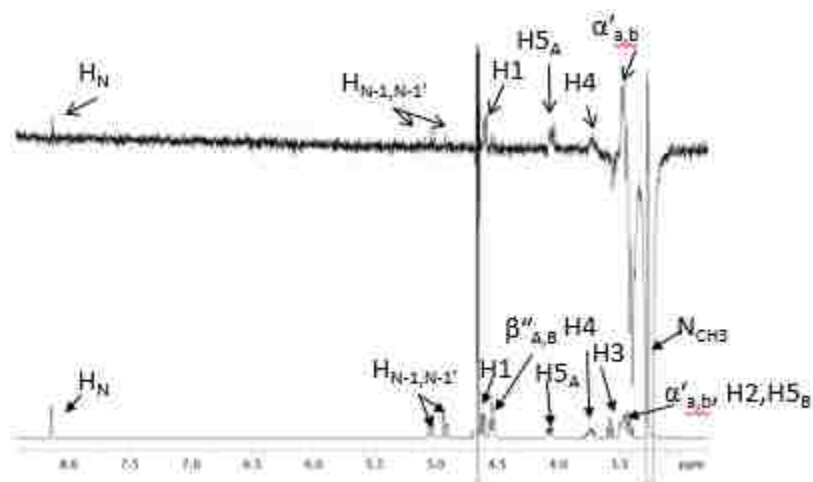


Figure 4.11. 1D NOE spectrum of 1:1 C₁₆TAB/C8XT1 in D₂O at 50 °C (total surfactant concentration 30 mM). The spectrum indicates several sugar-cationic NOE correlations (H_N, H_{N-1}, H_{N-1'}, H1, H5 and H4 proton of C8XT1) with the N_{CH3} protons of C₁₆TAB. There is also a cationic-cationic correlation between $\alpha'_{a,b}$ protons and N_{CH3} protons of C₁₆TAB. The lower spectrum is the 1D spectrum of the system over the same chemical shift range, for reference.

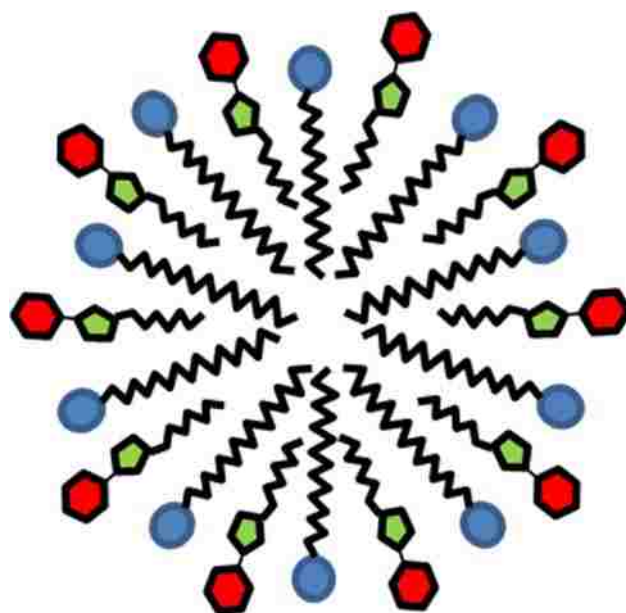


Figure 4.12: Schematic diagram showing relative position of head groups in mixed micelle of C_{16} TAB and C8XT1 based on the 3D geometry of the micelles and favorable interactions between headgroups.

CHAPTER 5

Orienting the Pores of Cationic-Carbohydrate Mixed Small Molecule Surfactant Templated Silica Thin Films by Tuning Surface Chemistry

5.1. Summary

This study addresses the synthesis of mixed cationic-carbohydrate surfactant templated silica thin films with orthogonally oriented pores by modifying the surface chemistry of a commercially available hydrophilic substrate (glass slide or silicon wafer) using a random copolymer with a mix of polar and nonpolar functionality. Hexadecyltrimethylammonium bromide ($C_{16}TAB$) mixed with n-octyl- β -D-triazolexylopyranoside ($C8XT1$) used as a template system, and poly(vinyl alcohol-r-ethylene) is used as a surface modifying agent. The hypothesis is that thin films of the random copolymer will provide a surface equally attractive to the polar heads and hydrophobic tails of the surfactants, and therefore should induce orthogonal orientation of the 2D hexagonal close packed mesostructured composite film. Templated silica films both on modified and unmodified substrate were characterized by x-ray diffraction (XRD) and transmission electron microscopy (TEM) techniques. On unmodified slides, XRD and TEM are consistent with a 2D hexagonal pore structure with columnar pores oriented parallel to the substrate. On modified substrates, loss of XRD intensity indicates that the pores oriented vertically relative to the substrate. TEM indicates that the 2D hexagonal structure is maintained, indicating that the complete loss of XRD intensity is due only to reorienting the mesostructure. These films are the first example of

vertically orienting small-molecule micellar templates using surface chemistry to create films with small mesopores (on the order of 2-3 nm after surfactant removal). These films are promising for applications requiring extremely high surface area, accessible, uniform channels including small molecule separations, (bio) chemical sensing and catalysis.

5.2. Introduction

Mixed cationic-nonionic surfactant templated silica thin films draw significant amount of attention due to their capability to form finely tunable mesostructures including lamellar, cubic, and 2D hexagonal close packed mesophases^{273, 297-301}. Among these, 2D hexagonal close packed cylindrical mesopores are potentially very useful for applications including catalysis, sensors and separations due to their well define diffusion path through the pores, high surface area, and ability to separate macromolecules by size exclusion^{137, 302-304}. Despite these advantages, conventional techniques to synthesize cationic-nonionic surfactant templated silica thin films with 2D HCP well-ordered channels on ordinary substrates (glass slides or silicon wafers) lead to cylindrical channels parallel to the substrate due to preferential interactions between the polar head groups of surfactants and the hydrophilic substrate⁵¹. These parallel pores are expected to be inaccessible to the majority of solutes. Cubic bi-continuous structures are a possible way to avoid this problem but are problematic because lateral diffusion can occur since the accessible pores are not isolated from each other^{58, 70}. They also require high surfactant concentrations for their formation, which can cause them to be difficult to stabilize. As a result, templated silica thin film with orthogonally oriented 2D

HCP channels to the substrate would be desirable to provide accessible mesopores with well-defined short diffusion path into the film. These orthogonally oriented thin films, especially if imparted with specific functional sites, would have several applications in the field of separations, sensors, and catalysis.

There are several methods reported in literature to form thin films with orthogonally oriented pores including epitaxial growth atop cubic films⁶⁶, electrical or magnetic field-induced orientation^{305, 306}, dimensional confinement by exo-template membranes³⁰⁷, and pattern supported growth (within the pores of anodized alumina)³⁰⁸. However, all of these techniques are limited by high production cost, technical complexity, unpredictable nature and difficult scalability. Our group has already established a well-defined, inexpensive, simple technique to build surfactant templated silica and titania thin films with orthogonally aligned 2D hexagonal mesophase based on Pluronic P123 surfactant templating on P123 or poly(ethylene oxide)(PEO)-*r*-poly(propylene oxide)(PPO) modified neutral surfaces⁷⁹. Our group has demonstrated via Monte Carlo simulations that the orthogonal alignment of lyotropic 2D hexagonal surfactant/solvent systems is possible using chemically neutral surface as the substrate³⁰⁹. However, the “neutrality” of the substrate (meaning not charge but equal interactions with heads and tails of surfactants) depends on the type of surfactant used and needs to provide domains small enough for the system to be neutral on the length scale of the micelles. For instance, it has been shown experimentally by our group that oriented channels are obtained for P123 templated films on P123 modified neutral substrate, but that the same conditions and P123 modification do not provide orthogonal orientation for Brij-

56 (primarily decaethylene glycol hexadecyl ether) surfactants⁸⁰. The short, alkyl tails of Brij-56 in comparison to the relatively large domains found in crosslinked P123 are the likely reason behind the dependence of mesophase orientation on surfactant structure.

Most of the prior studies on the synthesis of orthogonally aligned mesoporous films are based on templating with high molecular weight block copolymer templates (such as P123). There are very few reports in which small molecule surfactants were used as templates for orthogonally aligned mesophase films³¹⁰. Small-molecule surfactants are widely used in thin film synthesis and provide good control over pore size (in the size range < 10 nm) based on tail length and surface functionality based on headgroup selection. Therefore, new investigations are needed to develop surface modification techniques so that modified substrates do not have a strong preferential interaction with the polar head groups of cationic surfactants or the alkyl tails of either surfactant. Either interaction would lead to pores oriented parallel to the film which would be expected to have limited, difficult to reproduce, accessibility to solutes.

Here we report the first example of a simple method to orient a 2D hexagonal mesophase based on small molecule surfactants using surface modification with a polar-nonpolar random copolymer coating. The templating system selected is a cationic / carbohydrate surfactant mixture of interest for imprinting the surface of the pores³¹¹ or introducing transition metals via complexation³¹². The polar/nonpolar random copolymer is hypothesized to provide a chemically neutral surface to induce vertical orientation of the micelles of the 2D hexagonal mesophase formed by

cetyltrimethylammonium bromide and n-octyl- β -D-glucopyranoside. Our group has already shown the effectiveness of using a random co-polymer containing a mix of monomers from the surfactant (poly(propylene oxide-co-ethylene oxide)) to form neutral surfaces for mesostructure orientation in P123-templated silica films⁸⁰. In this study poly (vinyl alcohol-co-ethylene) is used as the surface modifying agent where the vinyl alcohol mers provide polar functionality and ethylene mers provide nonpolar functionality. Assuming that the polymer is a well-mixed random copolymer, a uniform distribution of functional groups should be presented at the surface of the film that would make the surface neutral with respect to the coating sol, which will lead to orthogonal orientation of cylindrical micelles.

5.3. Experimental

Cetyltrimethylammonium bromide (C₁₆TAB) (technical grade, Acros Organics), tetraethyl orthosilicate (TEOS) (98 % reagent grade, Sigma-aldrich), poly(vinyl alcohol-co-ethylene) (56 % PVA w/w%, Sigma-Aldrich) and dimethyl sulfoxide (DMSO) (Fisher Scientific) were used as received. n-octyl- β -D-triazole-xylopyranoside (C8XT1) was synthesized using the procedure described by Oldham et al²⁸⁸. Before any coating was performed, all of the glass slides and silicon wafers were cleaned using deionized ultrafiltered (DI-UF) water (Fisher Scientific), acetone and a UV-ozone cleaner. Surface modification, 1 g of poly(vinyl alcohol-co-ethylene) was dissolved in 30 ml of DMSO (dimethyl sulfoxide) and cast onto cleaned substrates by spin coating using a Laurell spin coater operating at 2200 rpm for 45 s. After coating, modified substrates were placed in a vacuum oven for 4 days at 120 °C to totally remove the DMSO. The surfactant templated silica thin films

were prepared by using TEOS as the silica precursor, which was first hydrolyzed by mixing it with water, hydrochloric acid and ethanol (mole ratio TEOS: ethanol: water: HCl = 1:3.8:1:5×10⁻³) and refluxing the mixture for 90 minutes. After that, more hydrochloric acid and water (mole ratio water: HCl = 1:0.001) were added and the mixture is stirred vigorously for 30 minutes at 50 °C to hydrolyze the remaining precursor. Subsequently, 60 ml of ethanol was added to the sol to dilute it and the required amount of surfactants (total surfactant mass 1.34 gm) were added to this mixture and it was stirred until all of the surfactants were dissolved. The required amount of surfactants was determined by using the ternary diagram of the mixed surfactants with water and replacing the volume of water in that phase with an equivalent volume of silica ⁶⁷. Following sol preparation, clean unmodified glass slides and the modified glass slides were coated by the spin coating technique using a Laurell spin coater. 100 µl of the sol was placed at the center of the substrate and coating was accomplished by spinning at 2200 rpm for 45 sec. After film deposition slides were aged at room temperature (~23 °C) and 45% RH for 2 days.

X-ray diffraction (XRD) was performed ex situ using a Bruker D8 Advance instrument. During XRD characterization a scan speed of 1 degree/min was accomplished using a lock coupled method. To perform transmission electron microscopy (TEM) the C₁₆TAB/C8XT1 templated silica thin films were first calcined in a closed oven at 550 °C with a heating at a rate of 0.5 °C/min to remove all polymers and surfactants. The mesoporous structures of the silica films were examined using a high resolution transmission electron microscope (TEM - 2010F JEOL) at a voltage of 200 kV. The TEM

samples were prepared by removing the film from the substrate with a razor blade and dispersing the resulting powder in ethanol. A drop of the resulting dispersion was placed onto a lacey carbon grid and dried before analysis.

5.4. Result & Discussion

Figure 5.1 shows the x-ray diffraction pattern of C₁₆TAB/C8XT1 templated silica thin films coated on both unmodified and modified glass slides and after aging at 20±1 °C and 45±5% RH for 2 days. The film thickness was found to be 60 nm using ellipsometry. For the films on unmodified substrate an intense (100) peak and a weaker higher order (200) peak are observed consistent with the 2D Hexagonal close packed (HCP) structure⁸⁰. The corresponding d-spacing for (100) peak is 2.8 nm. For the silica film on poly (vinyl alcohol-co-ethylene) modified substrate no diffraction peak was observed, which is consistent with having created a vertically oriented mesostructure. As summarized by Hillhouse et al. when the pores are oriented perpendicular to the substrate, due to the absence of scattering in the plane of the sample in conventional Bragg-Brentano geometry, we do not expect any diffraction peak in conventional XRD with 1D detector³¹³. Therefore, the absence of any diffraction peak for the silica films on poly (vinyl alcohol-co-ethylene) modified substrate is consistent with the 2D hexagonal mesophase being oriented vertically without any significant parallel orientation.

The absence of diffraction peak for C₁₆TAB/C8XT1 templated silica thin films coated on poly(vinyl alcohol-co-ethylene) modified substrate could also be caused by the loss of long range order of the mesostructure. For example, if the random polymer was able to dissolve into the silica sol during films deposition, the mixed templated material may

have little or no long range mesostructural order. To determine whether the absence of diffraction peak for C₁₆TAB/C8XT1 templated silica thin films coated on poly (vinyl alcohol-co-ethylene) was due to vertically orientation of the mesophase or due the loss of mesostructural order, TEM was used for the C₁₆TAB/C8XT1 templated silica thin films. Figure 5.2 shows the TEM images of materials scraped from unmodified substrate after calcination. The silica films on unmodified substrate clearly exhibit parallel strips suggesting close packed cylindrical channels of 2D HCP pores. The spacing between the parallel channels in TEM image is 2.8 nm, which is consistent with the d-spacing obtained from XRD for the (100) peak. That means well ordered 2D HCP pores were formed on the unmodified substrate. Figure 5.3 shows the TEM images of the films scraped from the poly (vinyl alcohol-co-ethylene) modified substrate after calcination. As the scraped material shown in Figure 5.3 has dimensions in the order of 200 nm and the film thickness of our film was determined by ellipsometry to be 60 nm so, the TEM images represent the top view of the silica film not the portion along film thickness. In Figure 5.3 instead of parallel cylindrical channels we can see the pore openings. Absence of parallel strips and the presence of pore openings on the top view of the films (Figure 5.3) indicate vertical oriented pores. Although the pores are not uniformly well ordered, they should be accessible.

Vertical pores could be disordered during calcination of the samples before TEM sample preparation. During calcination the intermediate poly (vinyl alcohol-co-ethylene) layer between the film and the substrate and also the templating C₁₆TAB/C8XT1 surfactant mixture were oxidized and removed. During this process the polymer diffuses out

through the pores of the silica films. That process may induce anisotropic stress on the silica wall of the pores. As a result of that vertical pores lost some of their long range order. For TEM characterization the intermediate polymer layer should be totally removed before TEM sample preparation to see the oriented pores. Another way to prepare the TEM sample is by dissolving the intermediate polymer layer and then net out the film on the TEM grid. This produce was tried using DMSO as a solvent without any luck. The reason may be the intermediate polymer layer was too thick to be removed by this process or it would need significant amount of time to remove the polymer completely. Also in contact with the solvent for longer time may also effect the silica film. In future the amount of polymer could be reduced and this procedure could be tried again. The best technique to characterize the pore orientation is to use some non-destructive techniques. Grazing incidence small angle x-ray scattering (GISAXS) could be the ideal choice.

By combining the XRD data with the TEM data it is cleared that for C₁₆TAB/C8XT1 templated silica thin films on poly (vinyl alcohol-co-ethylene) modified substrate, the mesophase oriented vertically to the substrate. As a result of that after removing the templates we get mesoporous silica thin films with orthogonally oriented pores. These orthogonally oriented pores should be highly accessible for the reactants compare to the pores with parallel orientation and will be very useful in future for the specific adsorption studies of carbohydrates using molecular imprinting. To demonstrate the importance of the equal molecular ratio of copolymers on the pore orientation, random-co-polymer with varying composition will be use in future to modify the

substrate. By comparing the XRD peak intensity between silica films on modified substrate, the dependence of co-polymer composition on surface neutrality will be demonstrated.

5.5. Conclusions

In summary, we have presented a simple inexpensive technique to prepare mesoporous silica films with small vertically oriented accessible mesopores by modifying the surface chemistry of the substrate using a polar/non-polar random-co-polymer poly (vinyl alcohol-co-ethylene). This represents the first example (that the authors are aware of) in which a small molecule has been used for this type of templating. No diffraction peak in XRD data combine with ordered oriented pores from TEM data suggest vertically oriented mesophase for the C₁₆TAB/C8XT1 templated silica thin films on poly (vinyl alcohol-co-ethylene) modified substrate. The random copolymer provides a uniform distribution of polar hydroxyl and non-polar methyl functionally on the substrate and due to that similar interactions with both heads and tails of small-molecule surfactants were obtained with the substrate. As a result of that hexagonal mesophase became oriented vertically to the substrate. Further future characterization is needed to understand the reason behind the lack of uniform long range order of the oriented pores. These films are promising for different applications including specific adsorption studies of carbohydrates using molecular imprinting.

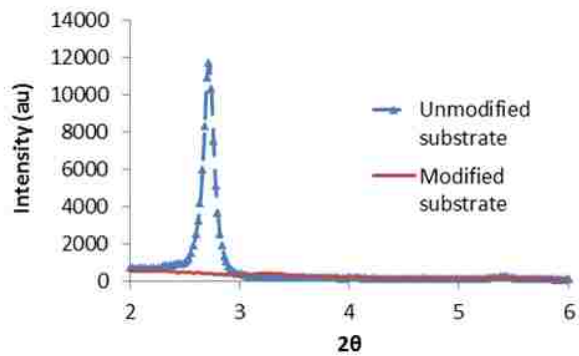


Figure 5.1. XRD patterns of C₁₆TAB/C8XT1 templated silica thin films on both modified and PVA-r-PE unmodified substrate after aging at 20±1 °C and 45±5% RH for 2 days.

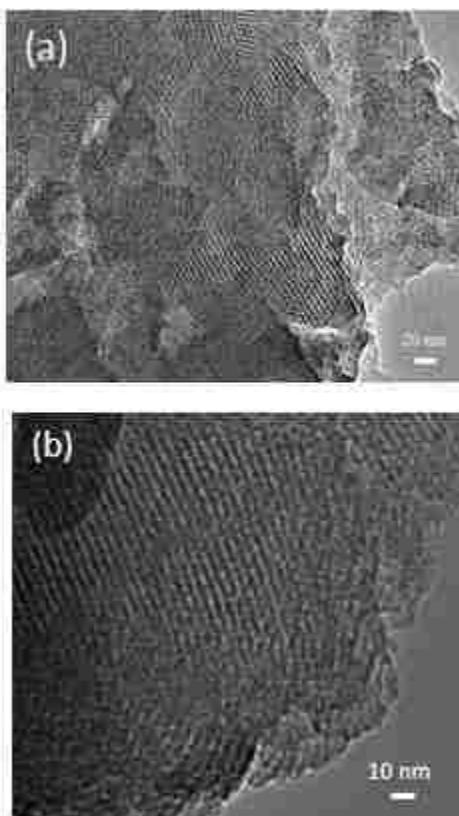


Figure 5.2. TEM images of C₁₆TAB/C8XT1 templated silica thin films at (a) low magnification and (b) high magnification scraped from unmodified substrate after aging at room temperature (23±1 °C) and 45±5% RH for 2 days followed by calcination at 550 °C with a heating at a rate of 0.5 °C/min.

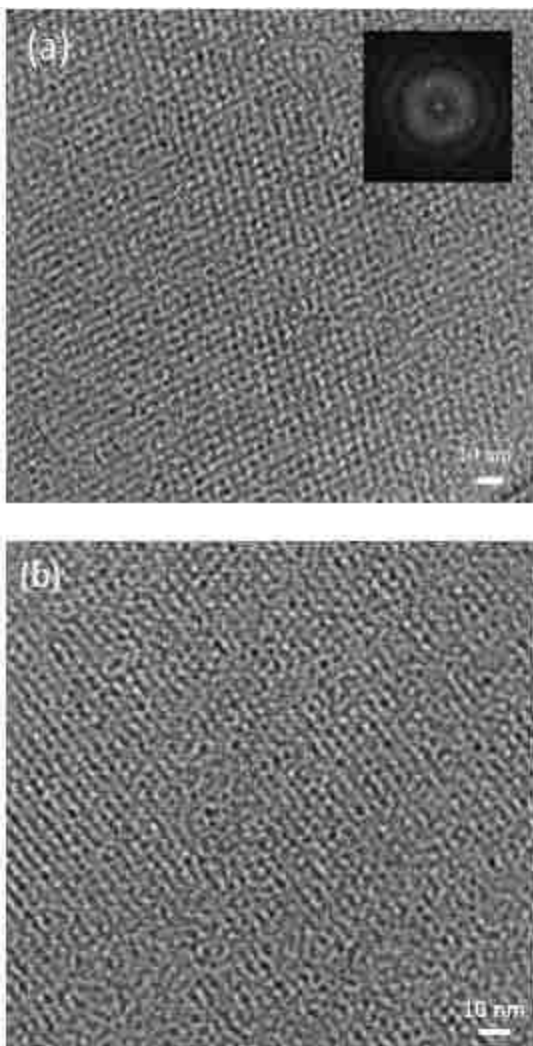


Figure 5.3. TEM images of $C_{16}TAB/C8XT1$ templated silica thin films at (a) low magnification and (b) high magnification scraped from modified substrate after aged at room temperature (23 ± 1 °C) and $45\pm 5\%$ RH for 2 days followed by calcination at 550 °C with a heating at a rate of 0.5 °C/min. The inset shows a fast Fourier transform of the upper image.

CHAPTER 6

Structural and chemical evolution of mixed cationic/ carbohydrate surfactant templated silica thin films during long- time aging

6.1. Summary

A detailed study on the effect of different aging parameters on the structural and chemical evolution of mixed surfactant templated silica films was done using a combination of x-ray diffraction (XRD) and Fourier transform infrared spectroscopy (FT-IR). XRD was used to measure mesostructural order in the templated films and FT-IR to provide insight into the polycondensation kinetics of the silica network. The templates for the silica thin films were mixtures of nonionic carbohydrate surfactant n-octyl- β -D-glucopyranoside mixed with cationic surfactant hexadecyltrimethylammonium bromide. After deposition, films were cured under varying process parameters including temperature and humidity, and studied over a period of several days. The evolution of long-range mesostructure order in the surfactant templated silica films was found not to be limited to the initial few minutes after film deposition, but instead to continue evolving for at least two weeks under fixed temperature and humidity conditions. Film contraction plays a significant role during that time which may be due to the slow removal of water and ethanol from the thin films. This work also shows the importance of the aging temperature and humidity, which significantly affect the mesostructural order and polycondensation of the templated silica thin films during longtime aging. Increasing temperature and humidity were both found to decrease the mesostructural

order while promoting polycondensation of the silica network. The insights into aging provided by this study will help to develop optimal conditions for long-term curing of surfactant templated silica films to balance competing needs for mesostructural order and a highly cured network.

6.2. Introduction

The pioneering work on surfactant templating of mesostructurally ordered silica thin films by Brinker's group ⁵¹ has drawn much interest from researchers in the porous materials community due to the potential applications of these materials based on their large surface area combined with tunable pore size distribution and structure ³¹⁴⁻³¹⁸. Applications of these templated silica materials are numerous and include sensors ³¹⁸⁻³²⁰, membranes ^{314, 321, 322}, drug delivery systems ³²³⁻³²⁵ and catalysts ^{312, 326, 327}. Templated silica thin films are often synthesized by co-assembling the metal oxide frame with surfactant templates by evaporation-induced self-assembly (EISA) ³²⁸⁻³³⁰ using dip or spin coating ^{56, 137, 331}. Despite the success of this approach and insights into the kinetics reported over the past two decades, proper control over the structural properties of these templated thin films is not always achieved ^{138, 145, 332, 333}. The variability in the templated metal oxide structure comes from the influence of the surrounding environment, which has a direct impact on the kinetics of thin film formation ^{137, 334-337}. Because of rapid heat and mass transfer with the surrounding environment, process conditions affect both the silica structure and assembly of the templating micelles. Changing the temperature and gas-phase environment near the film influence both the kinetics of the hydrolysis/polycondensation reactions of the silica

precursors and micelle size, shape and degree of ordering^{141, 142, 338, 339}. The influence of the film curing environment plays a significant role not only during the thin film deposition process but also during the aging of these thin films due to the flexibility of the silica structure and the susceptibility of the template micelles to environmental factors during aging. Aging time, temperature and humidity all play important roles in determining the final film structure and properties.

Several investigations of the kinetics of surfactant-templated thin film formation have been performed using in-situ GISAXS (grazing incidence small-angle x-ray scattering)^{308, 335}, NMR (nuclear magnetic resonance spectroscopy)^{340, 341}, and FT-IR (Fourier transform infrared spectroscopy)^{142, 342} but the primary focus of this work has been on the time scale of the film formation process itself. The long time effects of aging variables on mixed surfactant templated silica thin films have not been thoroughly studied, even though an aging period is usually included in the synthetic process to stabilize the silica thin films. By better understanding the quantitative evolution of long-range order and precursor reactions during this aging period, it will be possible to more rationally select conditions to efficiently achieve the best balance of promoting both long-range mesostructural order and silica polycondensation.

To control the film synthesis process, it is very important to isolate the effects of different aging process variables (including aging time, aging temperature, and aging humidity) and to study the effects of these individual factors on the structural and chemical properties of templated thin films during aging. Here we investigate the effect

of different aging conditions on alkyl glucopyranoside (C_nG1 where n = the alkyl chain length) and cationic (trimethylammonium) surfactant templated silica thin films. We study both the changes in structural properties (long range order and d-spacing) and the reaction kinetics (hydrolysis and polycondensation of the silica precursors) during aging in different environments.

6.3. Experimental

Cetyltrimethylammonium bromide (C₁₆TAB) (technical grade, Acros Organics), n-octyl-β-D-glucopyranoside (C8G1) (99+%, Affymetrix) and tetraethyl orthosilicate (TEOS) (98 % reagent grade, Sigma-aldrich) were used as received. The surfactant templated silica thin films were prepared by using TEOS as the silica precursor, which was first hydrolyzed by mixing it with water, hydrochloric acid and ethanol (mole ratio TEOS: ethanol: water: HCl = 1:3.8:1:5×10⁻³) and refluxing the mixture for 90 minutes. After that, more hydrochloric acid and water (mole ratio water: HCl = 1:0.001) were added and the mixture was stirred vigorously for 30 minutes at 50 °C to hydrolyze the remaining precursor. Subsequently, 24 ml of ethanol was added to the sol to dilute it and the required amount of surfactants (total surfactant mass 1.34 gm) were added to this mixture and it was stirred until all of the surfactants were dissolved. The required 1.34 gm of total surfactant amount (10:1 w/w% for C₁₆TAB and C8G1 mixture) was determined by using the ternary diagram of the mixed surfactants with water and replacing the volume of water in that phase with an equivalent volume of silica^{67, 138}. Prior to depositing any material the borosilicate glass slides and silicon wafers were cleaned by washing them with water followed by acetone and then by UV-Ozone

treatment for 10 minutes. Following sol preparation, clean glass slides and silicon wafers were coated by the spin coating technique using a Laurell spin coater. 100 μl of the sol was placed at the center of the substrate and coating was accomplished by spinning at 2200 rpm for 45 sec. After deposition, the films were aged in an oven or refrigerator in closed containers that were large enough to hold several slides, a beaker containing a solution to control water activity (if necessary), and a temperature/humidity sensor pen. To control humidity, different saturated salt solutions (K_2CO_3 for $\sim 45\%$ RH and NaCl for $\sim 75\%$ RH), dry nitrogen (for $\sim 10\%$ RH), or pure deionized water (for $\sim 97\%$ RH) were placed in the closed containers during aging. All measurements were performed in quadruplet to determine mean and standard deviation values for all samples.

X-ray diffraction (XRD) was performed *ex situ* for samples removed from the closed containers at varying times using a Bruker D8 Advance instrument. During XRD characterization a scan speed of 1 degree/min was accomplished by a lock coupled method. FT-IR spectra were collected directly in transmission mode for films cast onto thin silicon wafers using a ThermoNicolet Nexus 470 instrument with an MCT detector. Prior to film deposition, the spectrum of the bare silicon wafer was collected and used as the background of that particular sample throughout all subsequent measurements. It was important to be sure to reposition the wafer in exactly the same place in the transmission holder to avoid interference from background changes. GISAXS experiments were done at the Advanced Photon Source at Argonne National Laboratory on beamline 8-ID-E using a wave length of 1.687 \AA and a sample-detector distance of 1040 mm. Data were collected with a Pilatus 1M pixel array detector using a 1 sec

exposure time. Images were corrected for detector nonuniformity and converted to q-space using the GIXSGUI package for Matlab.

6.4. Results & Discussion

Mixed surfactant templated silica thin films were characterized by x-ray diffraction to study the evolution of long range order of the mesostructure. Figure 6.1 shows a representative example of the XRD pattern of a C₁₆TAB templated thin film after aging at 23±1 °C and 45± 5 %RH for 7 days. Figure 6.1(a) shows the conventional XRD pattern measured in the Bragg-Brentano geometry. The pattern consists of one intense peak (100) and one weak peak (200) which is consistent with a well-ordered 2D hexagonal columnar structure oriented parallel to the glass substrate onto which it is cast³⁴³. The 2D hexagonal structure and orientation is also confirmed by the 2D GISAXS pattern in Figure 6.1(b). The spots in Figure 6.1(b) represent the (100) peak seen in the XRD pattern (the vertical spot) and two (110) peaks consistent with the 2D HCP structure³⁴⁴. The d-spacing from Fig. 1(a) is 3.5 nm, which agrees with the d-spacing from the position of the (100) spot in Figure 6.1(b). While there is no way to directly measure mesophase crystallinity from a single x-ray pattern, the relative intensity between the two peaks in Figure 6.1(a) gives one quantitative measurement of the degree of long-range order in the structure, and will be calculated as PRI according to Eq. (1).

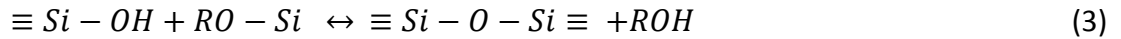
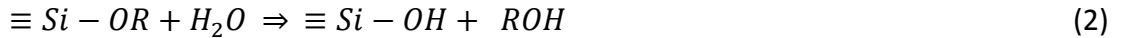
$$\text{Percentage relative intensity (PRI)} = \left(\frac{\text{Intensity of (200) peak}}{\text{Intensity of (100) peak}} \right) * 100\% \quad (1)$$

Some mesostructured materials only exhibit one x-ray reflection (usually the (100) peak), in which case they have a PRI of zero and would be defined to be relatively

weakly ordered, whereas larger values are associated with better long-range order. We compare PRI values for different aging conditions to understand the evolution of mesostructure in films subjected to different aging conditions. We also compare the d-spacing of the (100) peak to study the shrinkage or expansion behavior of these mesostructures due to different aging conditions.

The surfactant templated silica thin films were also characterized by FT-IR to understand the effect of different aging conditions on the condensation of the silica structure. Figure 6.2 shows a representative FT-IR absorbance spectrum of a silica film prepared with a 10:1 ratio of C₁₆TAB to C8G1 after aging at 20± 1 °C and 45± 5% RH for 7 days. All of the vibrational modes in this type of film have been assigned and discussed in existing literature ²⁰⁸. Among all the bands present in the spectrum, we label in Figure 6.2 the most relevant ones for this study. In the higher wavenumber range around (3350-3000 cm⁻¹) we see a broad peak due to the stretching of O-H in Si-OH groups and adsorbed water. We also can see two very sharp peaks around (3000-2800 cm⁻¹) which correspond to the CH₂ stretching of the surfactants. In the lower wavenumber range we see one very intense peak at ~1069 cm⁻¹) which is due to the anti-symmetric stretching of Si-O-Si. Another important peak for this study is found at 960-940 cm⁻¹ and is attributed to silanol (Si-OH) stretching in the silica structure. The reactions that occur during formation of a silica film from an alkoxy silane are hydrolysis (Eq. (2)) and

polycondensation (Eq. (3)).



First the ethoxy groups of the silica precursor (TEOS) are hydrolyzed to generate silanol groups and then silanols react with unhydrolyzed groups or other silanols to generate siloxane bonds by polycondensation reactions. Both hydrolysis and polycondensation are reversible reactions and the relative amount of Si-O-Si to Si-OH present in the structure indicates the degree of condensation. If the reaction were to go to completion, the product would be silica (SiO₂), although a fairly large number of residual SiOH groups are expected in a porous material. To study the change in condensation due to different aging conditions the ratio of the intensities of the primary Si-O-Si peak and the Si-OH stretching peak were used as a quantitative indicator of the progress of condensation. Calibration standards are not available for either band (since silanols are intermediate functional groups, compounds containing only SiOH groups are difficult to measure), but the ratio of the two bands provides an indication of the loss of SiOH to form Si-O-Si groups. Peak intensities were estimated by selecting a suitable local baseline for each of these two peaks and integrating over a fixed wavenumber range for each one.

Effect of surfactant composition

To investigate the effect of surfactant composition on the mesostructural order of the surfactant templated silica thin films the mass fraction of C8G1 in the surfactant mixture used to prepare silica films was varied from 0 to 0.2. All the films were aged at 20 ± 1 °C and 25 ± 5 % relative humidity (RH) for 10 days. Figure 6.3 shows the PRI vs. C8G1 mass fraction relation in the aged films. Pure C₁₆TAB templated silica thin films are found to have the highest mesostructural order (indicated by PRI) relative to mixtures with C8G1. The PRI decreases upon addition of C8G1 (0.05 mass fraction C8G1) increases again up to 0.09 mass fraction C8G1 before decreasing again (e.g. for 0.2 mass fraction C8G1). Further increase in mass fraction of C8G1 in the surfactant mixture ultimately leads to total mesostructural loss (observed with 0.5 mass fraction C8G1, data not shown). These observations are consistent with the general trend of decreasing order with increasing C8G1 content in powders prepared by nanocasting⁶⁷.

The reason behind the change in the mesostructural order with composition may be the relative arrangement of cationic and carbohydrate surfactants in the mixed micelle. For silica thin films templated with only C₁₆TAB, strong columbic interaction between the C₁₆TAB headgroup and the silica structure lead to highly ordered thin films. Addition of a small amount of C8G1 in the surfactant mixture may reduce the micelle surface charge to some extent, which has been speculated to be the reason that nematic phases are able to form as aggregates of rod-like micelles upon addition of a small amount of C8G1 to C₁₆TAB³⁴⁵. Further addition of C8G1 should continue to decrease the surface charge

density, which surprisingly leads to an optimal composition of 0.09 mass fraction C8G1 for a well-ordered mesostructured mixed surfactant composite. An optimal synergistic parameter has been predicted for mixtures of nonionic surfactant added to ionic surfactant on the basis of Poisson-Boltzmann theory ²⁹⁴. This synergism between surfactants may play a role, although specific structural factors may also contribute to the well-ordered structure at 0.09 mass fraction C8G1. Further addition of C8G1 leads to decreased synergism, and greater fluctuations in the structure of the micelles which leads to a rapid decrease in mesostructural order. Due to the highly ordered structure formation for films with 0.09 C8G1 mass fraction (10:1 C₁₆TAB/C8G1) this combination was used for further aging studies.

Evolution of films with time

To investigate the time evolution of surfactant-templated films, C₁₆TAB / C8G1 templated silica with a 10:1 ratio of C₁₆TAB to C8G1 were coated onto glass slides and silicon wafers and aged at controlled humidity (45±5% RH) and controlled temperature (20±1 °C) for up to 15 days, and XRD and FT-IR characterization was done to study changes in d-spacing, long-range order and condensation of the structure. As Figure 6.4(a) shows, the d-spacing of the samples decreases according to an exponential with respect to aging time, which indicates the shrinkage of the structure normal to the film surface. The main contribution to this shrinkage is likely to be slow condensation or rearrangement of the silicate species and some loss of water and ethanol as time proceeds, which reduces the local distance between the silicon atoms and thus induces

contraction of the films. However, Figure 6.5 shows that the clearest change in condensation extent within these thin films occurs over a short time; it seems that the majority of the change in condensation observable by FTIR takes place within the initial two hours of film curing. Therefore, the shrinkage of the structure after two hours of aging (which continues almost up to 7 days at 20 ± 1 °C) is not due the change in condensation of the silica structure observable by a change in the Si-O-Si : Si-OH band intensities. However, siloxane stretching bands are complex and multiple contributions can be found upon deconvolution of the bands, it is possible that condensation occurs that is not visible by FT-IR. Another contribution may come from the loss of water or solvent from the corona region of the micelles (near the interface between the surfactant head group and the frame works) with time, which also would induce shrinkage in the silica structure. Along with shrinkage, Figure 6.4(b) shows that there is a slight increase in long-range order with aging time which is most likely caused by internal compressive stress induced by shrinkage of the films during aging.

Effects of temperature during aging

To investigate the effects of temperature on aging, a set of C₁₆TAB / C8G1 templated silica coated glass sides and silicon wafers deposited from a single batch of sol were divided into four parts and were aged at four different temperatures (0 ± 1 °C, 20 ± 1 °C, 50 ± 1 °C and 100 ± 1 °C) under controlled humidity ($45\pm 5\%$ RH) for 7 days. XRD and FT-IR characterization was then performed to observe the changes in d-spacing, long-range order and degree of condensation of the films. Figures 6.6 and 6.7 show the d-spacing,

long-range order and Si-O-Si/Si-OH intensity ratio, respectively, for different aging temperatures. The effects of temperature are expected to be complex because, while increasing temperature accelerates activated processes, it also can introduce more defects into the long-range order of the structure and drive solvents out of the film more quickly.

The results show first that the d-spacing of the templated silica structures decreases with an increase in aging temperature (Figure 6.6(a)) which can be directly correlated with the increase in condensation from FT-IR shown in Figure 6.7. Accelerated polycondensation and enhanced drying due to the elevated temperature may contribute to this effect. Despite the evidence for faster curing in films aged at higher temperature, Figure 6.6(b) shows that the order of the structure decreases with increase in aging temperature. This may seem to contradict the study of aging time, which showed a correlation between contraction of the films and an increase in long-range order. However, the observed loss of long range order indicates that the net effect of aging at higher temperature is to introduce a higher number of defects into the long-range structure of the films, which leads to a decrease in PRI despite indications of greater condensation and contraction in the films.

Effect of humidity during aging

To study the effects of relative humidity, a set of C₁₆TAB / C8G1 templated silica coated glass slides and silicon wafers were divided into four parts and were aged closed boxes with four different relative humidity values (16± 5%, 45± 5%, 75± 5% and 96± 5% RH) in

closed chambers for 7 days at 20 ± 1 °C. XRD and FT-IR characterization were done at the end of this period. As Figure 6.8(a) the d-spacing increases with an increase in humidity, indicating an *expansion* of the silica mesostructure. However, from figure 9 the change in condensation is minor and is somewhat negative. This suggests that swelling of the mesostructure (most likely, absorption of water in the corona region of the micelles) is responsible for the expansion of the mesostructures. Consistent with this explanation, Figure 6.8(b) shows that increasing the relative humidity during aging leads to a decrease in the degree of long-range order of the structure. Overall, there is no indication that absorption of excessive water in the films reverses the condensation reaction; high humidity helps to cure the films more effectively. However, the mesostructure can be swollen by absorbed moisture and if this is nonuniform, poor long-range order may be the outcome.

6.5. Conclusions

In summary, XRD and FT-IR measurements were used to develop a clearer understanding of the effects of process parameters during aging on structure and chemistry in mixed surfactant templated silica thin films. For 10:1 C₁₆TAB/C8G1 templated silica films aged at constant humidity ($45 \pm 5\%$ RH) and temperature (20 ± 1 °C) the structure shrinks and the long range order increases as aging proceeds. The loss of water or solvent from the corona region of the micelles may be the reason for contraction, as significant changes in condensation (the other factor most likely to be responsible for shrinkage), after the initial two hours of aging. The internal compressive

stress induced by shrinkage of the films during aging may be the reason behind improved ordering of the films.

Increase in aging temperature for 10:1 C₁₆TAB/C8G1 templated silica films at constant humidity (45± 5% RH) for 7 days increases the extent of condensation and shrinkage of the mesostructure, but is accompanied with a decrease in the final long-range order of the films. The loss of long range order at higher temperature can be explained by an increase in the number of defects introduced into the mesostructure. Therefore, there is likely to be an optimal temperature that gives an adequate degree of condensation without excessive loss of long-range order. For this study, 50 °C seems to be a reasonable value. Increase in aging humidity for 10:1 C₁₆TAB/C8G1 templated silica films at constant temperature (20± 1 °C) for 7 days expands the mesostructure and decreases long-range order. At the same time, the condensation extent increases, so again there is likely to be an optimal relative humidity that assists with condensation without decreasing long-range order. This also suggests that, as other groups have suggested³⁴⁶, relative humidity can be used as a variable to tune the final pore characteristics of mesoporous silica thin films.

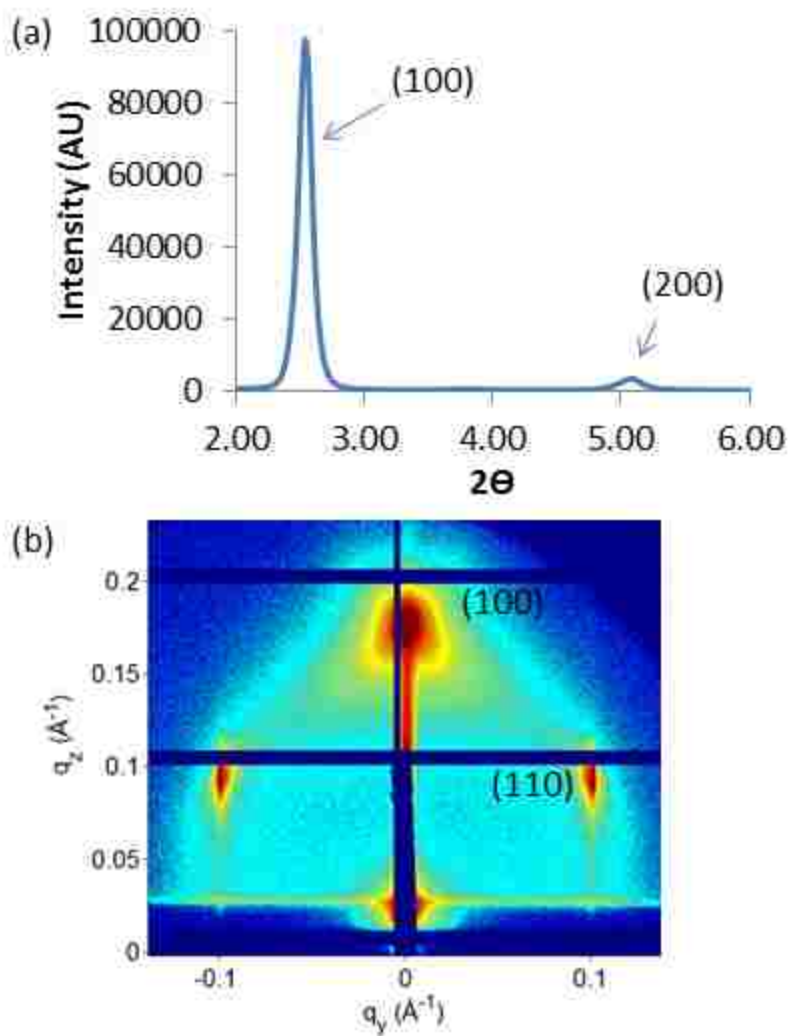


Figure 6.1. (a) XRD pattern collected in Bragg-Brentano geometry and (b) GISAXS pattern of C_{16} TAB templated silica films (after extraction) aged at room temperature (23 ± 1 °C) and 45 ± 5 %RH for 7 days.

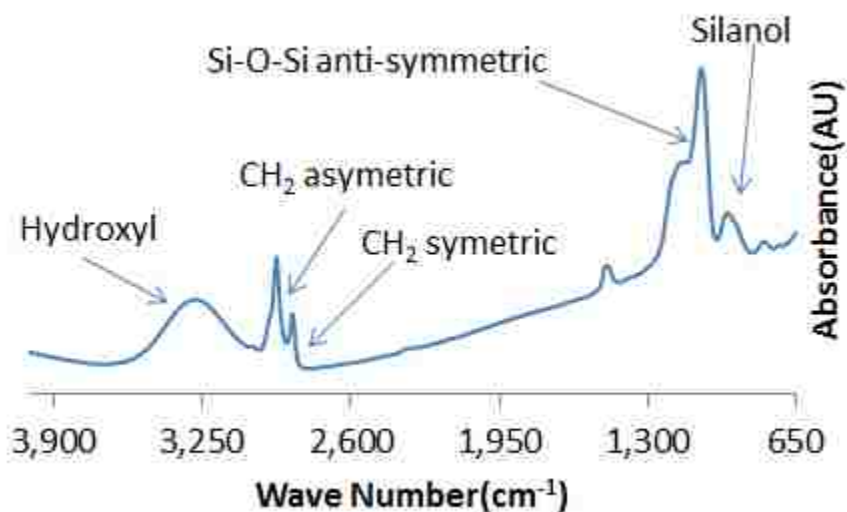


Figure 6.2. Representative FT-IR absorbance spectrum of a silica thin film on a silicon wafer templated with a 10:1 ratio of C₁₆TAB to C8G1. The film was aged for 7 days at 20±1 °C under a relative humidity of 45±5% prior to measuring this spectrum. The uncoated silicon wafer was used as the background for FT-IR spectra to allow direct transmission measurements to be made.

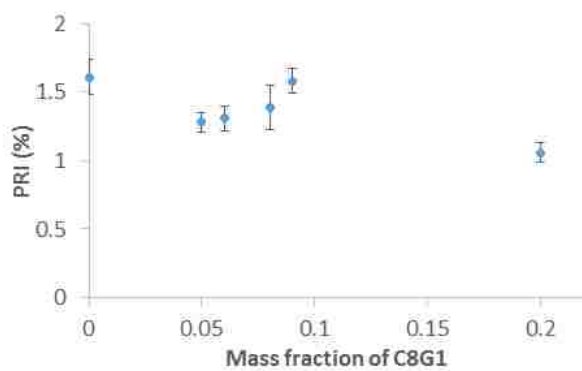


Figure 6.3. Change in order, as measured by PRI, of C₁₆TAB/C8G1 templated silica thin films by varying C8G1 mass fraction after aging at 20±1 °C and 25±5% RH for 10 days.

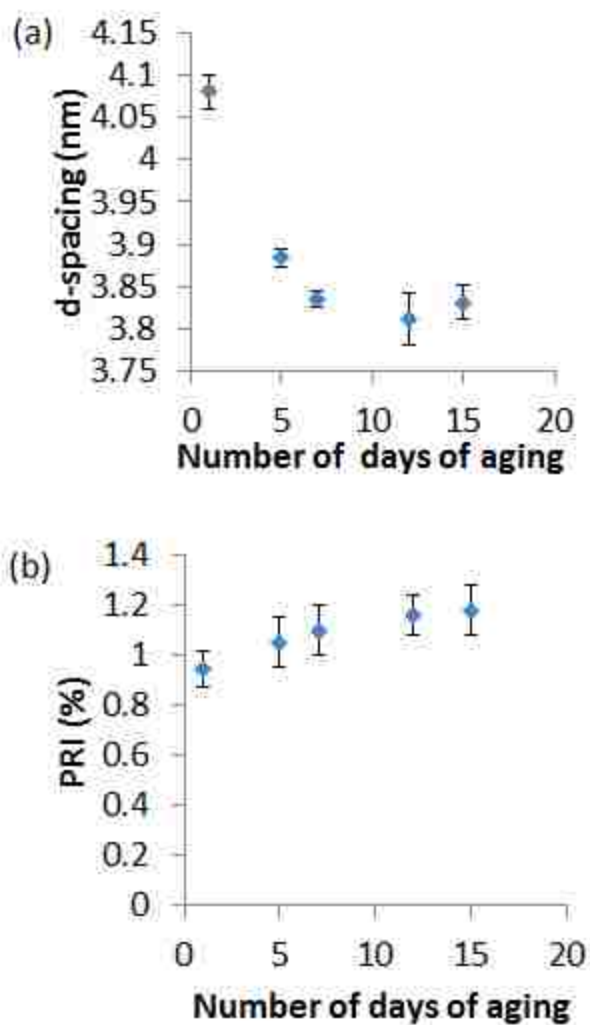


Figure 6.4. Change in (a) d-spacing and (b) long range order (PRI) with time measured from XRD patterns of 10:1 C₁₆TAB/C8G1 templated silica thin films during aging at 20±1 °C and 45±5 %RH.

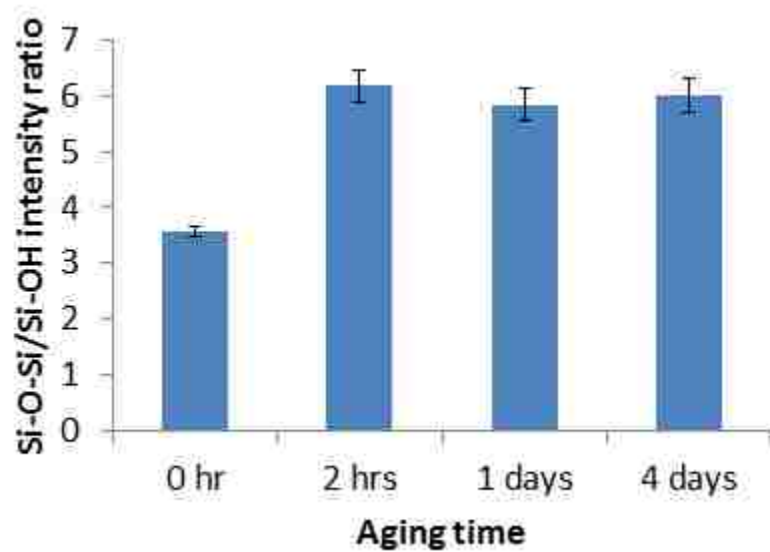


Figure 6.5. Change in condensation (the ratio of FT-IR intensities of Si-O-Si and Si-OH bands) of 10:1 C₁₆TAB/C8G1 templated silica thin films during aging at 20±1 °C and 45±5% RH over a total time scale of 4 days.

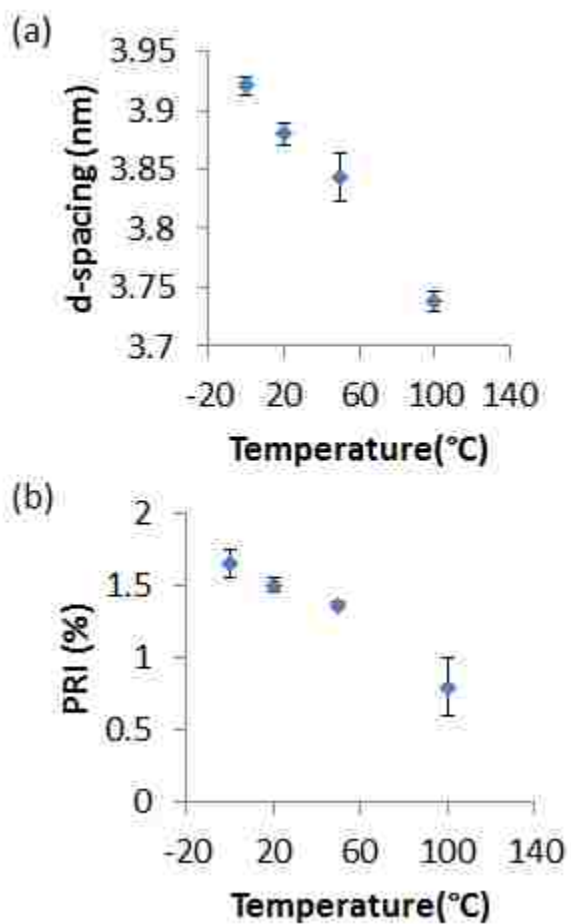


Figure 6.6. Change in (a) d-spacing and (b) long range order (PRI) for 10:1 C₁₆TAB/C8G1 templated silica thin films after aging at different temperatures at 45±5% RH for 7 days.

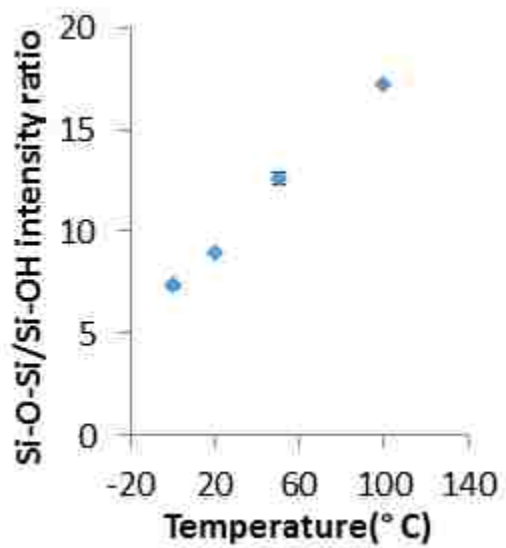


Figure 6.7. Change in condensation (from FT-IR bands) of 10:1 C₁₆TAB/C8G1 templated silica thin films after aging at different temperatures at 45±5% RH for 7 days.

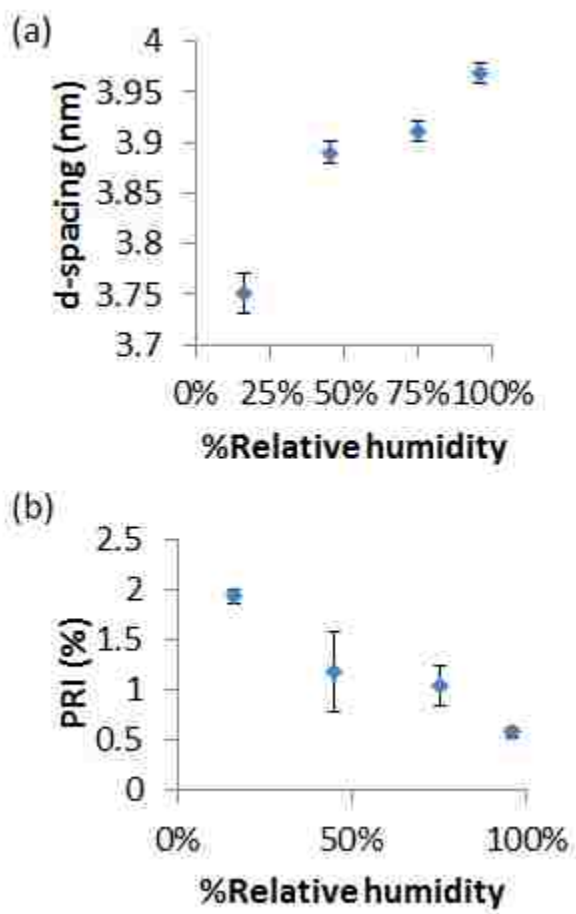


Figure 6.8. Change in (a) d-spacing and (b) long range order (PRI) of 10:1 C₁₆TAB/C8G1 templated silica thin films after aging at different relative humidity at 20±1 °C for 7 days.

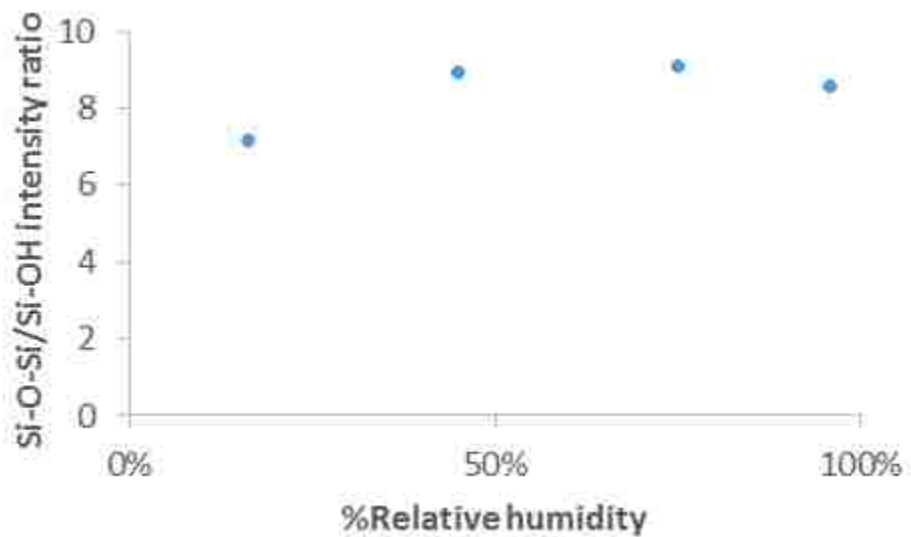


Figure 6.9. Change in condensation (from FT-IR) of 10:1 C₁₆TAB/C8G1 templated silica thin films after aging at different relative humidity at 20±1 °C for 7 days.

CHAPTER 7

In-Situ GISAXS Investigation of Pore Orientation Effects on the Thermal Transformation Mechanism in Mesoporous Titania Thin Films

This chapter is based on work published as:

Das, D.; Wu, Q.; Garlapalli, R.K.; Nagpure, S.; Strzalka, J.; Jiang, Z.; Rankin, S.E.; J. Phys. Chem. C, 2014, 118(2), pp 968-976.

7.1. Summary

This study addresses the effects of mesopore orientation on mesostructural stability and crystallization of titania thin films during calcination based on measurements with *in situ* grazing incidence small angle x-ray scattering (GISAXS). Complementary supporting information is provided by *ex situ* electron microscopy. Pluronic surfactant P123 (with average structure $(EO)_{20}(PO)_{70}(EO)_{20}$ where EO is an ethylene oxide unit and PO is a propylene oxide unit) serves as the template to synthesize titania thin films on P123-modified glass slides with 2D hexagonally close packed cylindrical mesopores. The orientation of the pores at the top surface is controlled by sandwiching another P123-modified glass slide on top of the titania thin film to completely orient the pores orthogonal to the films in some samples. This provides the opportunity to directly observe how pore orientation affects the evolution of pore order and crystallinity during calcination. The results show that when the pores are oriented parallel to the substrate at the top surface (for unsandwiched films), the pore structure is stable upon calcination at 400 °C, but that the structure is quickly lost due to crystallization throughout the film during calcination at 500 °C. The films with pores oriented orthogonal to the substrate

at the top surface (sandwiched films) retain their long-range pore order even after calcination at 500 °C. The reasons for this difference are ascribed to greater resistance to anisotropic stress during heating of the orthogonally oriented pores and to titania crystallization nucleation at the top surface of the films with orthogonally oriented pores.

7.2. Introduction

Titania thin films with ordered mesopore structures are of interest in numerous applications such as photovoltaics^{347, 348}, photocatalysis³⁴⁹⁻³⁵³ and sensing^{354, 355} due to their unique combination of optical / electronic properties³⁵⁶, high surface area, and uniform pore size³⁵⁷. One of the most promising techniques to prepare such thin films is via the evaporation-induced self-assembly (EISA) method^{358, 359} where the substrates are dip³⁶⁰ or spin coated³⁶¹ with a titania sol prepared using a templating agent (e.g. a small molecule surfactant³⁵⁰ or block copolymer³⁶²) present during hydrolytic polycondensation of a titania precursor such as a titanium alkoxide³⁶³ or titanium chloride³⁶⁴. By this approach, it is possible to generate films with a wide variety of well-ordered structures and mesophases^{78, 365-372} including 2D hexagonally close packed (HCP) cylindrical pores^{359, 373, 374}. While this phase is of interest because it provides a densely packed array of cylindrical pores for introduction of wires or for reaction with a contacting phase, its application is limited by the pores being oriented parallel to hydrophilic substrates (such as glass, ITO or silicon wafers) due to the preferential interactions of polar components (the titania precursor and PEO blocks) with the substrate³⁷⁵. Those parallel pores have very poor accessibility to reactants⁶⁶ and cannot

be used for applications such as inorganic-organic solar cells because of the limited availability of the pore space. Several years ago, Koganti et al. showed that this problem can be overcome by crosslinking a poly(ethylene-r-propylene) copolymer or P123 itself and then sandwiching the films to synthesize titania thin films with hexagonally ordered cylindrical mesopores tilted orthogonal to the substrate⁷⁹.

While the modification of the substrates with crosslinked copolymer allows orthogonally oriented HCP (o-HCP) titania films to be prepared, like all mesoporous titania films, controlling the crystallization of the titania after the initial synthesis is both necessary and challenging. The necessity comes due to the importance of titania crystallinity in controlling the band gap and charge carrier mobilities,³⁷⁶⁻³⁷⁸ which in turn determine the light absorption and electronic properties of the materials^{379, 380}. Controlling crystallization is challenging due to the loss of mesostructural order that can accompany the large amount of atomic movement that occurs during crystallization.^{381, 382} Kirsch et al. studied this problem previously and, based on a lower activation energy for mesostructure loss than for titania crystallization, suggested that the optimal strategy to preserve mesostructural order during crystallization is a rapid, high temperature crystallization.¹⁶² This strategy is consistent with a 10-minute calcination at 400 °C used in the initial work by Koganti et al. with o-HCP films.⁷⁹ However, calcination at this temperature leads to x-ray amorphous, nanocrystalline anatase walls in the resulting material. As we increase the temperature further, we expect greater crystallization to occur, but at the risk of losing mesostructural order.³⁸²⁻³⁸⁷ This is consistent with reports of mesostructural stability up to 400 °C^{373, 374}, and with coarsening reported for P123-

templated titania films upon calcination at 450 °C³⁸⁸. However, this is not a trivial optimization problem because the mechanism of crystallization differs significantly between bulk titania films and mesoporous films due to the possibilities of structure-dependent hindered or preferential nucleation and crystal growth, as discussed by other researchers^{383, 384, 389}.

Here we study the effect of the orientation of the pores of HCP columnar pores on the evolution of the mesostructural order and crystallinity during calcination at higher temperature than the nucleation temperature by in-situ grazing incidence small angle x-ray scattering (GISAXS). The importance of pore orientation was alluded to in a study of crystallization of mesostructured titania films by Bass et al., but was not directly addressed. Instead, they reported crystallization kinetics consistent with 1D diffusion-limited crystallization from a limited number of nucleation sites in well-ordered materials vs. 3D diffusion-limited crystallization in nonporous films.³⁸³ Disorder caused the films to crystallize more similarly to nonporous titania films. Consistent with this, Carreon et al. showed that cubic pores crystallize into anatase titania more readily than 2D hexagonal pores in P123-templated mesoporous titania films, and that this is related to greater photocatalytic activity in the former.³⁸⁸ Here, the orientation (and only the orientation) of the HCP pores at the air/film interface is controlled by either exposing the as-deposited films to air (to induce partial vertical alignment of the pores at the solid substrate but parallel pores at the air interface), or sandwiching the films with a second modified slide to induce full vertical alignment across the entire film. The sol and thermal history of the films are otherwise identical. This approach will allow us to

show that that the slight change in degree of pore orientation makes a huge impact on the evolution of mesostructural order and crystallinity during calcination. As we will show, for completely oriented films the crystallization appears to occur only on the top surface of the pores, which allows the films to retain their mesostructural order under conditions where the partially oriented (unsandwiched) titania films lose their mesostructural order due to crystallization of the titania throughout the film.

7.3. Experimental

Titania thin films were prepared based on the procedures of Koganti et al.⁷⁹ Prior to depositing any material, plain borosilicate glass slides were cleaned with a NoChromix glass cleaning solution (Godax Laboratories, Inc.). Cleaned glass slides were then modified by dip coating with an acetone solution containing equimolar amounts (0.415 mM) of Pluronic surfactant P123 (poly(ethylene glycol)-block-poly(propylene glycol)-block-poly(ethylene glycol) with Mn ~ 5800, Sigma-Aldrich) and 1,6-diisocyanatohexane (98%, Sigma Aldrich). To this solution, a single drop of glycerol was added to serve as a cross-linker so that the films would be stable. Slides with a modifying coating were aged at 120 °C overnight to drive the cross-linking reaction to completion. Titania sols were prepared by adding 2.1 g of titanium ethoxide (Technical grade, Sigma Aldrich) to 1.53 g concentrated HCl (36 wt%, EMD Chemicals), stirring for 10 min, and adding 0.65 g of P123 dissolved in 6 g of ethanol (200 Proof, Decon Laboratories). Films were dip coated at 7.6 cm/min withdrawal rate from the titania sol onto P123-modified glass slides and then aged in a highly humid environment (RH 95%) in a refrigerator (4 °C) for 2 h. The humid environment was achieved by placing two small beakers of deionized water in a

closed box along with the slides to allow vapor-phase equilibration of water. To achieve full orientation of the HCP phase vertical to the substrate, some of the freshly-deposited titania films were sandwiched with an identical P123-modified slide before starting the aging treatment. The superimposed modified substrate was removed before the substrate was subjected to heating. Both sandwiched and unsandwiched films were subjected to identical thermal treatment after aging.

In situ GISAXS experiments were done at the Advanced Photon Source at Argonne National Laboratory on beamline 8-ID-E³⁹⁰ using a wave length of 1.687 Å and a sample-detector distance of 2010 mm. Aged samples were placed on a sample holder which was connected with heating coils and then heated to a desired final calcination temperature with different ramp rates. After reaching the final calcination temperature, all samples were kept at that temperature during *in situ* GISAXS measurements. The heating device used was a stainless steel block with a temperature controller. The thermocouple used for temperature control was placed on the titania film as close as possible to the sampled area without interfering with the scattering. A GISAXS pattern was collected at room temperature before heat was turned on and again after the final temperature was attained, at which point the sample was realigned. *In situ* data were collected with a Pilatus 1M pixel array detector using a 10 s exposure time. Images were corrected for detector non-uniformity and converted to q-space using the GIXSGUI package for Matlab³⁹¹.

The mesoporous structure of the titania films were examined using a high resolution transmission electron microscope (TEM - 2010F JEOL) at a voltage of 200 kV. TEM samples were prepared by removing the film from the substrate with a razor blade and dispersing the resulting powder in ethanol. A drop of the resulting dispersion was placed onto a lacey carbon grid and dried before analysis. Scanning electron microscope imaging was carried out to examine the plan-view structure of the titania films using a Hitachi S-4300 instrument at 6 kV voltage. Samples were prepared for SEM by cutting a small piece of the titania film-coated substrate and attaching it onto a SEM stub with carbon tape.

7.4. Results & Discussion

Figure 7.1 shows the SEM images of unsandwiched and sandwiched HCP ordered titania thin films on P123 modified surface after calcination at the baseline temperature used to prepare ordered mesoporous films (400 °C). TGA measurement was performed to confirm that calcination at 400 °C leads to complete removal of the template (Supporting Information Appendix E, Figure E.1). In Figure 7.1a, parallel stripes can be observed indicating HCP pores oriented parallel to the substrate. The contrast of the image is poor because the pores are actually located underneath the top surface of the film, so the image is showing contrast due to differences in the thickness of the film below the top titania layer. Figure 7.1b shows the 2D HCP pattern of orthogonally oriented pores observed for sandwiched films after calcination at 400 °C. In both cases (whether the films are sandwiched or not), a very well-ordered 2D hexagonal structure forms and remains stable after calcination at 400 °C. The only effect of sandwiching the

films with a modified slide is to induce orientation of the pores orthogonal to the substrate at the top surface of the film. The thickness of these films, measured by ellipsometry, is on the order of 240 nm. The unit cell parameter is estimated by the average distance between pores in the SEM images to be approximately 14-15 nm.

When we increase the calcination temperature from 400 °C to 500 °C, the mesostructural order is totally lost after calcination in the unsandwiched films, as shown by (a) SEM and (b) TEM images in Figure 7.2. This loss of mesostructural order is caused by the non-uniform growth and sintering of anatase crystallites within the walls of the porous film, as indicated by the wavy, uniform array of titania rods at the top surface of the film in Figure 7.2a. Figure 7.2b shows that titania crystallites (which appear darker in bright-field TEM) are distributed throughout the film. The titania pore walls in films calcined at low temperature (<400 °C) are nanocrystalline but as the temperature increases, more extensive anatase crystallization takes place by growth and sintering of the existing nanocrystallites to give the coarse texture in Figure 7.2a. The grain growth due to crystallization most likely leads to anisotropic stress throughout the film caused by frustrated shrinkage at the substrate surface. This stress may contribute to deformation and loss of mesostructural order. Eventually, when the titania grain size in the pore wall becomes larger than the initial pore wall thickness, pores can collapse as has been reported by other researchers¹⁶². The bright features due to partial charging in the SEM image and the dark features due to high-density titania regions in the TEM image of Figure 7.2 are consistent with a nonuniform distribution of relatively large titania crystallites throughout the films. This mesostructure loss precludes utilizing the

pores of these films in applications such as photocatalysis and photovoltaics, so to better understand the rate and mechanism of mesostructure loss, a GISAXS study was also conducted.

Figure 7.3 compares the GISAXS patterns of unsandwiched and sandwiched titania films coated onto P123-modified glass slides after aging in the refrigerator (4 °C for 2 h) but before any heat treatment. The films are aligned horizontal relative to the incident X-ray beam. Identifying the starting phase and orientation prior to thermal treatment is important because this helps to rule out other possible interpretations of the observed data, such as apparent stripe patterns observed in “grid-like” structures in distorted cubic F127-templated titania films³⁹² and hexagonal patterns observed in (111) projections of cubic phases (e.g., Fm $\bar{3}$ m and Im $\bar{3}$ m) and distorted 3D hexagonal titania, previously observed for P123-templated TiO₂ with added butanol.^{368, 393} Soler-Illia et al. emphasized the importance of using complementary experimental techniques to assign structures of mesoporous materials.³⁹⁴ For the unsandwiched film (Figure 7.3a), a set of in-plane rods and out-of-plane spots is observed in the GISAXS pattern. Out-of-plane spots were indexed to distorted 2D HCP mesophase parallel to the substrate with rectangular symmetry (C2mm),³⁹⁵ and the inplane spots were indexed to an orthogonally oriented 2D HCP phase. Unit cell parameters for the rectangular pattern are $a = 14.9$ nm and $b = 19.3$ nm. A comparison of calculated and measured d-spacing values based on this structure is shown in Supporting Information *Appendix E*, Figure E.2. The ratio $b/a = 1.29$, which represents a 25% contraction normal to the plane of the film compared to an ideal hexagonal structure (which has $b/a = 1.73$). The unit cell

parameter for the vertically aligned hexagonal spots is $a = 15$ nm. Overall, the pattern is consistent with a mixed orientation HCP structure where the parallel domains (presumably present at the film–air interface in an unsandwiched film) are distorted due to contraction normal to the film during aging. In contrast, the sandwiched film shows a GISAXS pattern (Figure 7.3b) dominated by the orthogonal HCP mesopore pattern. There are faint hints of the parallel C2mm structure, most notably the (02) diffraction, but this blends into the intensity from the reflected beam. While the orthogonal alignment may not be 100% complete, Figure 7.3b indicates that sandwiching during aging gives a film with significantly more orthogonal HCP pores.

Figure 7.4 compares the GISAXS patterns of the TiO₂ films just after reaching the final calcination temperature 500 °C. At this point, no distinct out-of-plane diffraction spots are visible. Instead, two intense vertical rods located on both sides of the beam stop, at $q_y = \pm 0.048 \text{ \AA}^{-1}$, are indexed to the (100) plane of the HCP structure and indicate that orthogonally oriented HCP pores are present in both sandwiched and unsandwiched films.⁷⁹ Also consistent with this structure a very weak hemispherical out-of-plane diffraction ring are observed in both cases³⁹⁶. The intensity of the rods is reduced relative to Figure 7.3 (due to some loss of long-range order), and the spots from the parallel (C2mm) structure are lost in the unsandwiched film either because of a reduction in order within the parallel layer or because additional contraction caused the spots to move outside of the observed q-vector range. A similar trend (loss of out-of-plane diffraction spots) has been observed upon anisotropic contraction of cubic films in F127-templated materials during heating, but in that case the cubic phase was identified

prior to heating and elongation of inplane diffraction spots into rods was observed during curing.^{392, 394} Here, the elongated rod-like features were present prior to heating and thus are consistent with a layer of orthogonally aligned HCP pores at the substrate–film interface. In the unsandwiched films, this structure is accompanied by a thin layer of parallel distorted HCP pores at the vapor–film interface that may lose their order or become significantly compressed during heating to 500 °C.

Although the 2D GISAXS patterns of unsandwiched and sandwiched films look almost identical just after reaching final calcination temperature (500 °C), the patterns differ dramatically after holding the samples at calcination temperature (500 °C) for 500 sec. Figure 7.5 compares the 2D GISAXS pattern of unsandwiched and sandwiched titania films after calcination at this ramp rate and holding the samples at 500 °C for 500 seconds. The unsandwiched film (Figure 7.5a) has a low-intensity, diffuse pattern without vertical rods, suggesting loss of long-range mesostructural order, which is consistent with the SEM and TEM images in Figure 7.2. However, the mesostructural order remains stable for sandwiched films as indicated by the presence of intense vertical rods in Fig. 7.5b after calcination at 500 °C. The mesostructural order of sandwiched films remained stable not only for the 500 sec represented in Figure 7.5b, but for at least 25 additional minutes during the GISAXS experiment (data after 500 sec not shown). Note that the slide used for sandwiching was removed prior to heating the sample, so the difference between the two samples shown in Figure 7.5 is only due to the difference in initial pore orientation induced by sandwiching the film during low-temperature aging.

To further illustrate the stability of the mesostructural order in the films, time-resolved *in situ* GISAXS experiments were conducted. To best represent the evolution of the order, a slice of the 2D GISAXS patterns was taken at $q_z = (0.06-0.07) \text{ \AA}^{-1}$. Figure 7.6 shows the evolution of the resulting 1D scattering patterns for unsandwiched and sandwiched films over the course of the isothermal plateau at 500 °C. The (100) diffraction of the vertically oriented films is apparent at the start of the aging period at $q_y = \pm 0.048 \text{ \AA}^{-1}$ and to best visualize the results, time increases as the curves move forward in the waterfall plots. It is clear from Figure 7.6a that the unsandwiched films rapidly lose their mesostructural order. The intensity of the (100) peak from Figure 7.6a vs. time is plotted in Figure 7.7, and was fit with a first-order kinetic model for the first 5 minutes of treatment (the solid curve in Figure 7.7) to give a rate coefficient of $0.56 \pm 0.03 \text{ min}^{-1}$ for loss of mesostructural order in the unsandwiched films. In contrast, the sandwiched film shows almost no change in the intensity of the (100) peak over the 500 seconds illustrated in Figure 7.6b. Fitting the intensity vs. time results for this case (Figure 7.7) for the first 3 minutes (where the model matches well) leads to a lower limit on the rate coefficient of $0.047 \pm 0.07 \text{ min}^{-1}$ (dashed curve in Figure 7.7). Clearly, this represents an enormous improvement in the stability of the mesostructure towards being lost due to crystallization at this temperature. Also, the intensity becomes roughly constant at around 3 min for the sandwiched film which suggests that the majority of the mesostructure remains stable at 500 °C.

Two possible reasons could be responsible for the difference in mesostructure stability during crystallization for the sandwiched and unsandwiched films. The first is the

response of the films to the anisotropic stress that is likely to arise due to frustrated shrinkage of the film in the lateral direction. Adhesion of the film to the substrate gives rise to tensile stress in the plane of the film during crystallization³⁹⁷ and compressive stress normal to the substrate. This leads to deformation of 2D HCP structures to give films with rectangular symmetry when the material is able to withstand the stress,³⁹⁸⁻⁴⁰⁰ but when crystallization is occurring simultaneously, this stress most likely contributes to loss of long-range order. We speculate that one of the reasons that the sandwiched films are better able to withstand crystallization without loss of order is that the continuous matrix of TiO₂ in the lateral film direction of orthogonally oriented films better withstands tensile stress encountered during crystallization. The orthogonally oriented pores also are better able to withstand the compressive stress normal to the films rather than being “squeezed” to give a deformed structure that can lead to loss of order.

The second reason that the sandwiched films are more stable during crystallization could be a change in crystallization mechanism. To investigate this possibility, *ex situ* electron microscopy of the films following calcination at 500 °C after a 40 °C/min ramp was performed. Figure 7.8 shows the SEM and TEM images of the sandwiched titania films. These images show that, consistent with the GISAXS results, there is a considerable amount of mesostructural order retained in the films. Figure 7.8a shows that the top surface consists of a HCP array of cylindrical pores with minor defects but overall good retention of long-range order. The FFT (inset) confirms this order. The TEM image in Fig. 7.8b is a plan-view image of the same film (we can tell this because

the section of film being observed is much larger than the thickness of the film, so it must represent a piece of film that delaminated intact during sample preparation), and also shows fairly good retention of the orthogonal 2D HCP structure. In contrast, under the same condition the unsandwiched films totally lost their long-range mesostructural order, as observed by both SEM and TEM (Figure 7.2) and in GISAXS pattern in Figure 7.5a. At the top surface of the unsandwiched film (Figure 7.2a), remnants of aligned cylindrical pores can be observed, but the walls have coarsened relative to the original film due to sintering, and the uniformity of the pores has been lost. The net result is an undulating pattern with a net orientation but no long-range order. In the TEM image, a disordered array of pores orthogonal to the film can be seen (again, Figure 7.2b is a view of an oriented section of delaminated film). The appearance of the SEM and TEM images is different because the layer of parallel pores near the top surface (which gives rise to the SEM image) must have been thin, while the image through the film in TEM is consistent with disordered orthogonal HCP films that are present near the base of the film. This layered structure is consistent with the net orthogonal orientation observed by GISAXS prior to calcination.

In addition to the mesopore structure in the electron micrographs, additional features can be resolved. In SEM, regions are observed in Fig. 8a which appear bright because of charging. These are most likely crystallites of titania which are sitting on the top of the film. The top surface of the unsandwiched sample (Figure 7.2a), in contrast, has uniform brightness due to uniform crystallinity. This suggests that crystallization in the sandwiched film occurs preferentially at the film/air interface, rather than throughout

the film. Also in the TEM image of the unsandwiched film (Figure 7.2b), dark regions are observed throughout the entire film, which represent regions with higher electron density (higher crystallinity). In the sandwiched films (Figure 7.8b), there are fewer isolated particles of high contrast, which are consistent with the bright features observed by SEM. This again suggests that crystallization occurs throughout the unsandwiched film, while it occurs preferentially at the air/film interface in the sandwiched film.

To identify the crystalline phase present in the titania films, high-resolution TEM (HRTEM) and selected area electron diffraction (SAED) were performed for a sandwiched film after calcination at 500 °C (Figure 7.9). In a representative HRTEM image (Figure 7.9a) lattice fringes with a d spacing of 0.35 nm (corresponding to the (101) crystallographic plane of anatase TiO_2) can be clearly seen. Other HRTEM images were collected, all of which showed lattice fringes consistent with anatase, such as that in Supporting Information *Appendix E*, Figure E.3, which shows lattice fringes with a d spacing of 0.19 nm (corresponding to the (200) plane of anatase). No lattice fringes were observed with d spacings corresponding to rutile. In addition to direct visualization by HRTEM, the SAED pattern from the same sample (Figure 9b) has seven rings which were indexed to the anatase structure reported by Howard et al.⁴⁰¹ The d spacings from SAED have an average deviation of only 0.53% relative to literature values (complete comparison is provided in Supporting Information *Appendix E*, Table E.1). This shows that the crystallization process is an amorphous-to-anatase transition consistent with the phase diagram of bulk titania.

In well-ordered mesoporous materials, crystallization is thought to occur by a one-dimensional diffusion-controlled mechanism.^{383, 384} In the sandwiched films, the crystallization path along the walls is limited only by the thickness of the film, and preferential nucleation and growth of crystalline titania is able to occur at the film surface. This isolated crystallization on the top surface of the pore walls generates less stress throughout the pore walls and as a result the mesostructural order survives at a higher temperature for fully oriented sandwiched films. On the other hand, the unsandwiched films have a layer of parallel pores that “cap” the film and prevent the diffusion of titanium to the air/film interface. This leads to crystallization of the titania throughout the films, which gives rise to greater stress and a greater tendency to lose mesostructural order. Also, because of the change of orientation of the pores within the film, the mesostructure is more defective, and thus more likely to occur through more of a 3D diffusion-limited mechanism (as discussed by Bass et al. for mesoporous titania films with more defects³⁸³). This mechanism leads to crystallization throughout the sample and, because 3D crystallization has a lower activation energy than 1D crystallization in a well-ordered mesoporous structure³⁸³, occurs to a greater extent in the unsandwiched films. Thus, the unsandwiched films crystallize and lose their mesostructural order more quickly at 500 °C than the sandwiched films.

7.5. Conclusions

In summary, the effect of pore orientation on mesostructural stability and crystallization of titania thin films with 2D hexagonal close packed (HCP) columnar nanopores has been investigated using *in-situ* GISAXS and by ex-situ TEM and SEM imaging. From the results

it is clear that perfect orthogonal pore orientation in sandwiched films has a tremendous impact on mesostructural stability of the films. The electron microscopy suggests that this is not only due to differences in how the films respond to stress during crystallization; preferential crystallization at the top surface of the pores also occurs, which most likely leaves the interior of the pores less crystalline and helps to withstand the anisotropic stress that develops due to titania curing and crystallization. In unsandwiched films, the films contain more defects and do not have as many continuous pathways to the top surface of the film, so crystallization occurs in more of a 3D diffusion-limited manner throughout the film. While these observations are consistent with prior investigations of the crystallization mechanism in mesoporous and nonporous titania films,^{383, 384, 402} this is the first time that a surface-crystallization phenomenon has been observed in oriented mesoporous films and correlated with enhanced mesostructure stability. In the future, more detailed temperature-dependent studies are planned to further explore the kinetics of titania crystallization in confined pore walls that will ultimately lead to a better understanding of the optimal thermal treatment to use when preparing surfactant-templated, orthogonally oriented mesoporous titania films for photovoltaic and photocatalytic applications.

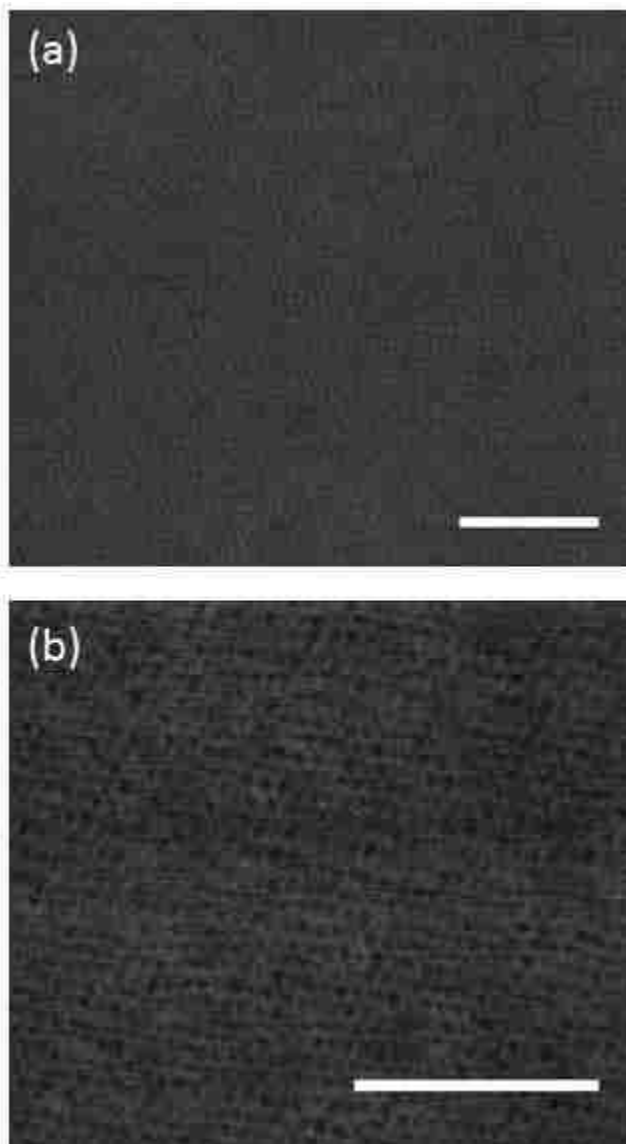


Figure 7.1. SEM images of (a) unsandwiched (b) sandwiched titania films aged at 4 °C and calcined at 400 °C for 10 min after heating at a rate of 40 °C/min. The scale bar in both images is 250 nm wide.

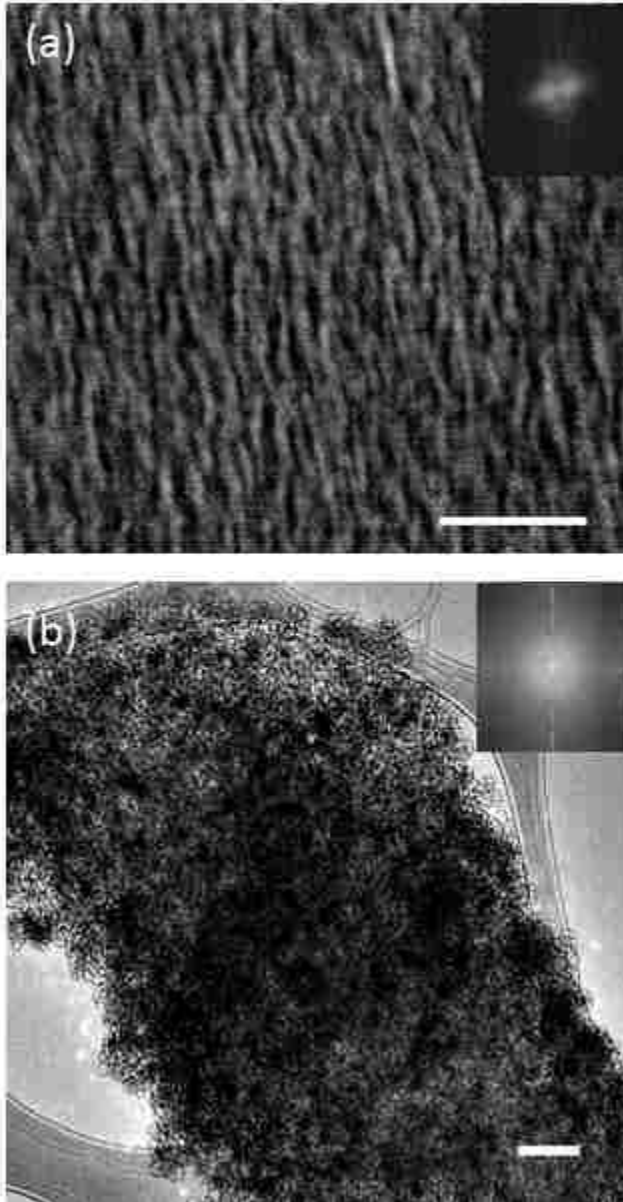


Figure 7.2. (a) SEM (scale bar 250 nm) and (b) TEM images (scale bar 100 nm) of unsandwiched titania films prepared by dip coating from sols aged at 4 °C and calcined at 500 °C after heating at a rate of 40 °C/min. Insets are fast Fourier transforms (FFTs) of the images provided to emphasize the lack of long-range order.

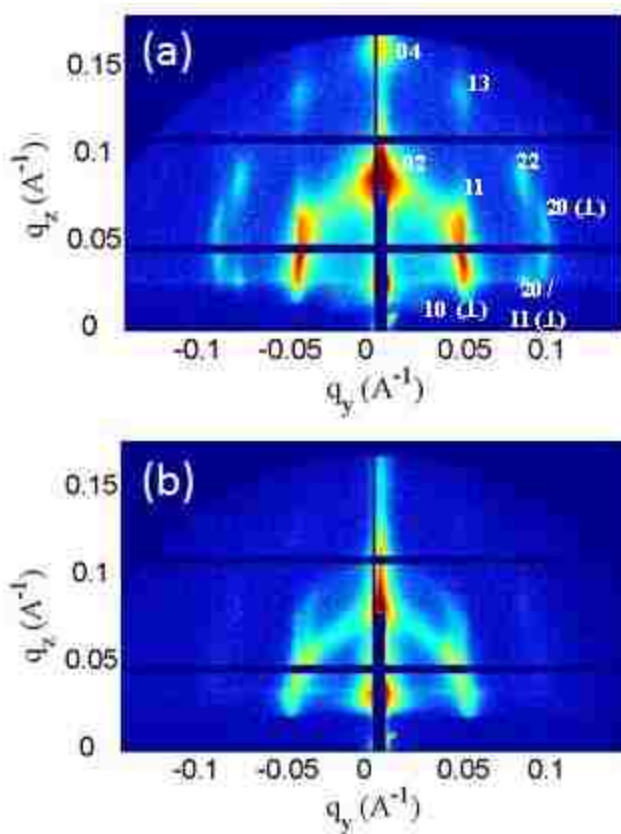


Figure 7.3. GISAXS patterns of (a) unsandwiched and (b) sandwiched titania thin films after aging at 4 °C for 2 h and just before calcination at room temperature (22.5°C). The films are oriented horizontally (in the xy plane) relative to the incident beam for this experiment.

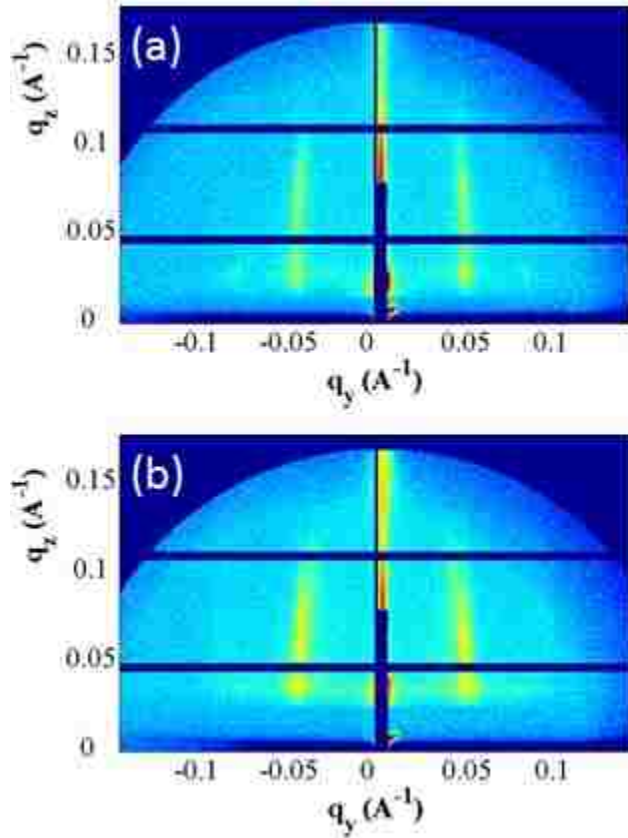


Figure 7.4. GISAXS patterns of (a) unsandwiched and (b) sandwiched titania thin films after aging at 4 °C for 2 h and just after reaching final calcination temperature 500 °C. The films are oriented horizontally (in the xy plane) relative to the incident beam for this experiment.

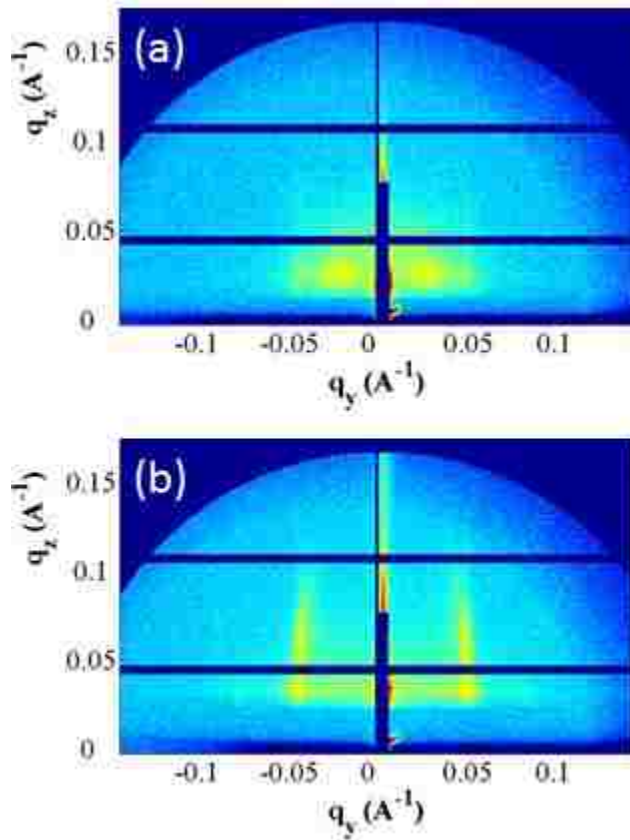


Figure 7.5. GISAXS pattern of (a) unsandwiched and (b) sandwiched titania thin films after heating at 40 °C/min to 500 °C and holding at that temperature for 500 sec. The film is oriented horizontally (in the xy plane) relative to the incident beam for this experiment.

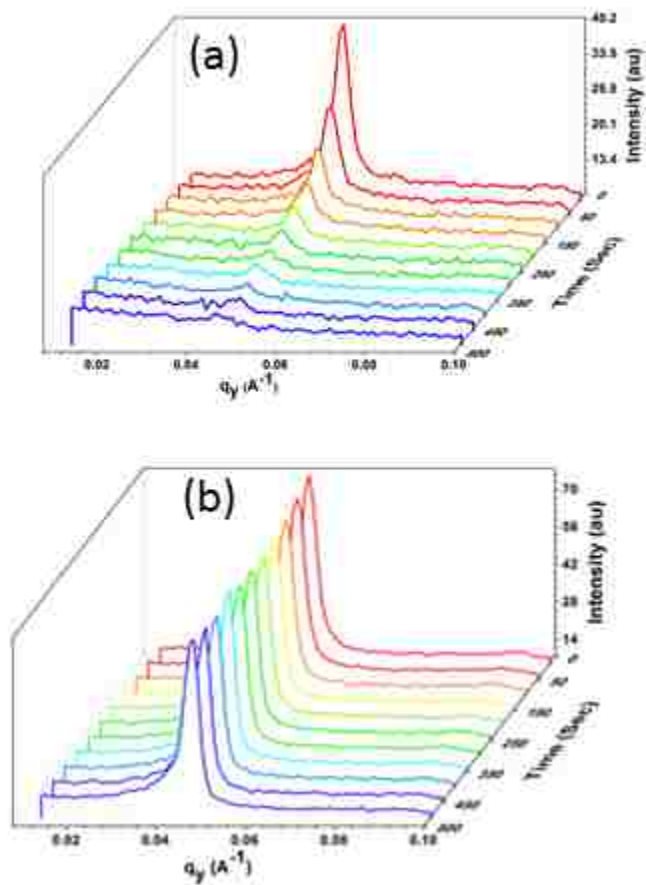


Figure 7.6. Evolution of the (100) diffraction peak in the q_y direction for (a) unsandwiched and (b) sandwiched titania thin films during isothermal heat treatment at 500 °C. The plots were generated by integrating slices from the 2D GISAXS patterns for q_z values from 0.06 to 0.07 for times starting after the 40 °C/min ramp to the final temperature.

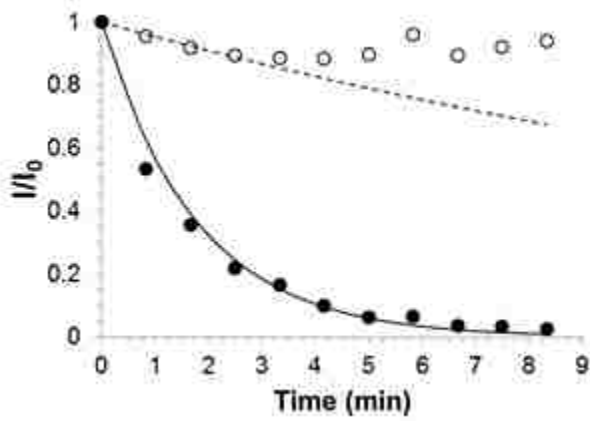


Figure 7.7. Intensity of the (100) reflection vs. time at 500 °C expressed as a ratio to the initial intensity at the end of the 40 °C/min ramp. Data are shown for unsandwiched (filled symbol and solid curve) and sandwiched (open symbols and dashed curve) films. The curves are fits of an exponential function to the initial 5 min (unsandwiched) and 3 min (sandwiched) of data.

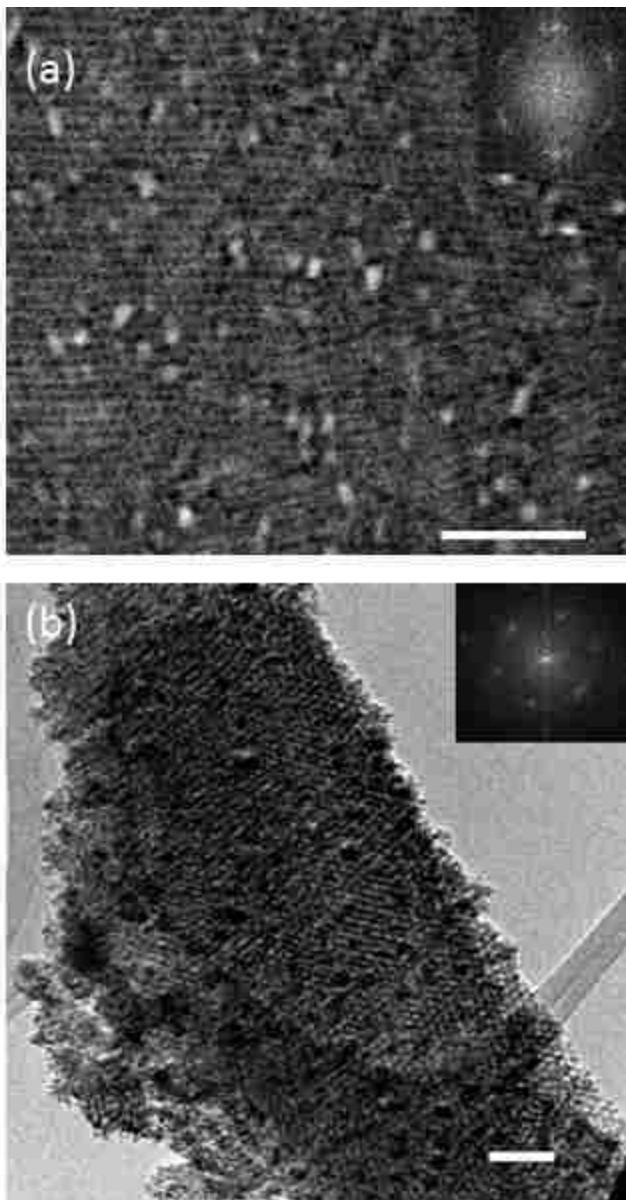


Figure 7.8. (a) SEM (scale bar 250 nm) and (b) TEM images (scale bar 100 nm) of sandwiched titania thin films on modified glass slides aged at 4 °C for 2 h and calcined at 500 °C. The insets of fast Fourier transforms (FFTs) of the images.

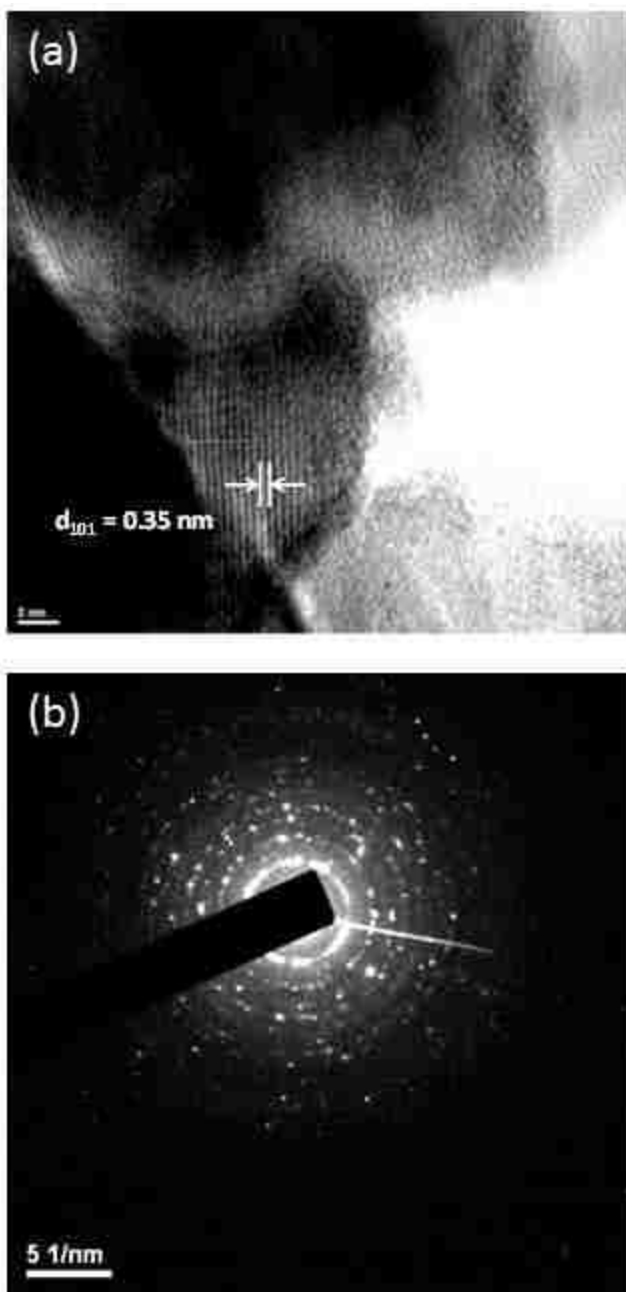


Figure 7.9. (a) HRTEM image and (b) Selected area electron diffraction (SAED) pattern of sandwiched titania thin films on modified glass slides aged at 4 °C for 2 h and calcined at 500 °C.

CHAPTER 8

Pore Orientation Effects on the Kinetics of Mesostructure Loss in Surfactant Templated Titania Thin Films

8.1. Summary

The mesostructure loss kinetics are measured as a function of the orientation of micelles in 2D hexagonal close packed (HCP) columnar titania thin films using in-situ grazing incidence small angle x-ray scattering (GISAXS). Complementary supporting information is provided by ex-situ scanning electron microscopy. Pluronic surfactant P123 acts as the template to synthesize HCP structured titania thin films. When the glass substrates are modified with crosslinked P123, the micelles of the HCP mesophase align orthogonal to the films, whereas a mix of parallel and orthogonal alignment is found on unmodified glass. The orthogonally oriented (o-HCP) thin (~60 nm thick) films prepared on modified substrate are more thermally stable toward mesostructure loss (activation energy ~155 kJ/mol) than the HCP films on unmodified substrates (activation energy ~126 kJ/mol). Nearly perfect orthogonal orientation of micelles on modified surfaces contributes to the larger activation energy by supporting the anisotropic stresses that develops orthogonal to the films during annealing. The effectiveness of orthogonal orientation and the corresponding thermal stabilization has a strong correlation with film thickness. Because the film thickness dictates the propagation of orientation throughout the films and the degree of confinement, thicker (~250 nm) films cast onto P123-modified substrates have a much lower activation energy for

mesostructure loss (89 kJ/mol) due to the mix of orientations found in the films. Thus we conclude that thin P123-templated o-HCP titania films are not only better able to achieve good orthogonal alignment of the mesophase relative to thicker films or films on unmodified substrates, but that confinement and alignment of the mesophase in the films synergistically stabilize the mesophase against thermally-induced mesostructure loss.

8.2. Introduction

Templated nanoporous titania thin films, prepared via evaporation-induced self-assembly (EISA),^{73, 403, 404} have attracted scientific interest for the last two decades in numerous applications such as photovoltaics,⁴⁰⁵⁻⁴⁰⁷ electronic devices,^{408, 409} photocatalysis^{350, 410} and sensors.^{354, 411} The well-ordered uniform titania pores, created after removal of a templating agent (surfactant⁴¹² or block copolymer⁴¹³), offer unique physicochemical properties such as high surface area, affinity towards certain ligands and electronic conductivity, that makes mesoporous titania thin films a perfect candidate for these above mentioned applications.^{153, 414} By varying the ratio of titania precursor to templating agent is possible to generate titania films with a wide variety of well-ordered mesostructures including lamellar, cubic and 2D hexagonally close packed (HCP).^{77, 78, 138, 146, 367, 368, 415} Among these phases 2D HCP cylindrical pores are of particular interest because they provide well defined short diffusion paths for reactants and charge carriers, ideal for introducing photoelectrochemistry or introducing wires for reaction with a contacting phase.^{74, 416, 417} However, a major barrier to the application of 2D HCP mesoporous titania is that the pores of the structure typically align parallel to

the coating substrate due to preferential interactions between hydrophilic substrates (such as glass, ITO or silicon wafers) and the polar components of the film (the titania precursor and polar parts of templating agent).⁵¹ Parallel pores are only poorly accessible to reactants, and thus are not usable in many of the applications of interest for titania.⁶⁶

The HCP pore orientation problem can be overcome by using a variety of approaches using fields, confinement, and surface modification techniques that makes the substrate neutral with respect to the polar and nonpolar parts of the templating agent.⁴¹⁸ Koganti et al. have shown for P123 templated titania thin films that it is possible to produce HCP mesopores aligned orthogonal to the substrate by first using a crosslinked layer of a surface modifier such as poly(ethylene oxide-r-propylene oxide) copolymer or P123 itself, and then by sandwiching the films.^{79, 80} The resulting films have accessible uniform cylindrical nanopores tilted so that they are accessible, and thus usable for applications analogous to anodized titanium films.⁴¹⁹⁻⁴²¹ The advantage of the surfactant templating approach, however, is that it allows for smaller pores to be produced more readily than anodization, and also as a coating process can be scaled up for large-area production and adapted for a variety of substrates and interfacial chemistries.

Along with the ordered mesostructure it is necessary to control titania crystallinity for (photo) electrochemical applications as it plays a significant role in tuning the band gap and charge carrier mobility.⁴²²⁻⁴²⁴ Sol-gel derived titania films generally are amorphous

after formation and crystallinity emerges with the formation of anatase during heat treatment above 400 °C.^{392, 425} Crystallization of titania by heat treatment comes with the potential sacrifice of mesostructural order due to the large amount of atomic movement during crystallization.^{147, 426} The tradeoff between maintaining mesopore structure and developing crystallinity during thermal treatment is a well-known challenge that has been addressed in prior studies. Kirsch et al. used a combination of wide- and small- angle x-ray scattering to measure activation energies for anatase formation vs. mesostructure loss in P123-templated $Im\bar{3}m$ cubic titania films. Because they observed a greater activation energy for crystallization, they recommended rapid, high temperature thermal treatments to promote crystallization with minimal mesostructure loss. Bass et al. studied the effects of mesostructure symmetry and concluded that disorder in the mesophase make the films crystallize similar to nonporous TiO_2 films,³⁸³ which is also consistent with the report of Carreon et al.³⁸⁸

A prior study by Das et al. showed that titania films with orthogonally oriented HCP (o-HCP) pores generated by sandwiching films between two modified substrate have better thermal stability than films with mixed pore orientation prepared from the same coating solution on a single modified substrate.⁴²⁷ The enhanced stability was attributed to differences in the ability of the o-HCP structure to withstand anisotropic stress during curing and a change in the mode of anatase nucleation. However, there are some limitations of using the sandwiching approach to controlling mesostructured orientation. It is a manual technique which is susceptible to variability in surface homogeneity, pressure during sandwiching, and time between film coating and

sandwiching. Also this technique may not be suitable for some applications where the top surface of the films needs to be modified just after coating.^{428, 429} Sandwiching also introduces the possibility that the differences observed in thermal stability were caused by a surface phenomenon such as heterogeneous nucleation of anatase. To overcome these limitations, Koganti et al. showed that the orthogonally oriented pores can also be created using only one modified substrate below a critical thickness (~100 nm).⁷⁹

Here we present a detailed study of the kinetics of the mesostructural transformation of thin (<100 nm thick) titania films using *in situ* grazing incidence small angle x-ray scattering (GISAXS) complemented by *ex situ* scanning electron microscopy (SEM). Transformation kinetics are studied as a function of pore orientation induced by modifying surface or by changing the film thickness. The *in situ* GISAXS data are gathered with sufficient temporal resolution to allow kinetics to be followed and are modeled using the Avrami equation at each temperature. Arrhenius temperature dependence is assumed to determine the activation energy for mesostructural deterioration for each case. The hypothesis to be tested is that thin films (~60 nm thick) prepared on a modified glass substrate with o-HCP structure will have higher activation energy for mesostructure loss than films with parallel or mixed HCP pores on unmodified substrates, which explains their greater thermal stability. A second part of the study will be to use thicker (~250 nm thick) films to address the effects of film thickness on the propagation of orientation throughout the films. It is expected that thicker films will have lower activation energy for mesostructure deterioration compare to thinner films on both unmodified and modified substrates, due to the mix of HCP

orientations in these films. The study also includes measurements of the effects of temperature ramp rate on mesostructural transformation of titania thin films to search for possible optimal conditions for heating.

8.3. Experimental

Titania thin films were prepared based on the procedures of Koganti et al.⁷⁹ Prior to depositing any material, plain borosilicate glass slides were cleaned with a NoChromix glass cleaning solution (Godax Laboratories, Inc.). Cleaned glass slides were then modified by dip coating with an acetone solution containing equimolar amounts (0.415 mM) of Pluronic surfactant P123 (poly(ethylene glycol)-block-poly(propylene glycol)-block-poly(ethylene glycol) with Mn ~ 5800, Sigma-Aldrich) and 1,6-diisocyanatohexane (98%, Sigma Aldrich). To this solution, a single drop of glycerol was added to serve as a cross-linker so that the films would be stable. The slides with a modifying coating were aged at 120 °C overnight to drive the cross-linking reaction to completion. Titania sols were prepared by adding 2.1 g of titanium ethoxide (technical grade, Sigma Aldrich) to 1.53 g of concentrated HCl (36 wt%, EMD Chemicals), stirring for 10 min and adding 0.65 g P123 dissolved in 36 g or 6 g of ethanol (200 Proof, Decon Laboratories) for thin or thick films respectively. Films were dip coated at 7.6 cm/min withdrawal rate from the titania sol onto P123-modified or unmodified glass slides and then were aged in a humid environment (RH 66%) in a refrigerator (4 °C) for 2 hr. The humid environment was achieved by placing two small beakers of potassium nitrate-saturated aqueous solution in a closed box along with the slides to allow vapor-phase equilibration of water.

In situ GISAXS experiments were done at the Advanced Photon Source at Argonne National Laboratory on beamline 8-ID-E⁴³⁰ using a wave length of 1.687 Å and a sample-detector distance of 1397.7 mm. Aged samples were placed on a sample holder which was connected with heating coils and then heated to a desired final calcination temperature with different ramp rates. After reaching the final calcination temperature, all samples were kept at that temperature during *in situ* GISAXS measurements. The heating device used was a stainless steel block with a temperature controller. The thermocouple used for temperature control was placed on the titania film as close as possible to the sampled area without interfering with the scattering. A GISAXS pattern was collected at room temperature before heat was turned on and again after the final temperature was attained, at which point the sample was realigned. *In-situ* data were collected with a Pilatus 1M pixel array detector using a 1 sec exposure time. Images were corrected for detector nonuniformity and converted to q-space using the GIXSGUI package for Matlab.⁴³¹

To complement the GISAXS measurements, the mesoporous structures of selected titania films were examined using a Hitachi S-900 Scanning electron microscope instrument at 6 kV voltage. The samples were prepared for SEM by cutting a small piece of the titania film-coated substrate and attaching it onto a SEM stub with carbon tape. Coating of colloidal graphite (isopropanol base) was done on the sample edges to increase conductivity by making the top surface in electrical contact with bottom surface.

8.4. Results & Discussion

Figure 8.1 shows the SEM images of P123 templated titania thin films (~60 nm thick as measured by ellipsometry, prepared using 36 g of ethanol) on both an unmodified borosilicate glass substrate and one modified with crosslinked P123 after calcination at 500 °C. For titania films on unmodified substrate, HCP pores were expected to be oriented parallel to the substrate due to preferential interactions of the headgroups of the templating agent with the hydrophilic substrate. Instead, Figure 8.1a shows that some degree of orthogonal orientation of pores was observed on unmodified substrates, indicated by pore openings in the SEM image. Partial orthogonal alignment of HCP titania composite films on unmodified slides was also found in an *in situ* GISAXS study of aging in these films⁴³², and may be a result of decreased segregation between poly(ethylene oxide) [PEO] and poly(propylene oxide) [PPO] blocks during aging at low temperature. The fragments of material on top of the film in Figure 8.1a may be collapsed sections of the top layer of film which were initially oriented parallel to the substrate but whose structure collapsed during heating.⁴²⁷ In contrast, Figure 8.1b shows the 2D HCP pattern of well-ordered pores with perfectly orthogonal orientation on a P123-modified substrate. The unit cell parameter is estimated by the average distance between pores in the SEM images to be approximately 14-15 nm for both types of films, so the only difference between them is the degree of orthogonal orientation of the HCP mesophase.

Figure 8.2 compares the GISAXS patterns of mesostructured titania/P123 composite films on both unmodified and P123-modified substrates at room temperature after aging but before heating. The films were aligned horizontal relative to the incident x-ray beam. Figure 8.2a shows a combination of intense out of plane and in-plane diffraction spots in the GISAXS pattern. Out-of-plane spots were indexed to a distorted 2D HCP mesophase parallel to the substrate, with rectangular symmetry ($C2mm$),^{395, 427} and the in-plane spots were indexed to an orthogonally oriented 2D HCP phase. Unit cell parameter for the rectangular pattern are $a=14$ nm and $b=17.3$ nm. The ratio $b/a=1.4$, which represent 19% contraction normal to the plane of the film compared to an ideal hexagonal structure (which would have $b/a=1.73$). The unit cell parameter for the vertically aligned hexagonal spots is $a= 16.8$ nm. The overall pattern is consistent with a mixed orientation HCP structure. A comparison of calculated and measured d-spacing values based on this structure is shown in *Supporting Information Appendix F*, Figure F.1. In the case of a titania film on P123-modified substrate (Fig. 2b), the presence of only two intense in-plane vertical Bragg rods located on both sides of the beam stop indicates a perfectly orthogonally oriented HCP mesophase that is also consistent with the SEM image in Figure 8.1b obtained upon calcination of this structure.

To determine how the degree of orthogonal alignment affects mesostructure evolution during heating, films on P123-modified and unmodified substrates were subjected to heating. Unfortunately, thermal expansion of the materials made it impossible to collect GISAXS data during the ramp from room temperature to the final temperature, but data collection began as soon as possible after realignment upon reaching the final

temperature. Figure 8.3 shows representative examples of the GISAXS patterns from titania films on both unmodified and modified substrate just after reaching a final calcination temperature of 600 °C and realigning the instrument. For a final calcination temperature below 600 °C, no significant change in the intensity of the diffraction spots was seen after holding the titania films for 90 minutes (data not shown). During the heating of the templated titania films the polymer was oxidized and completely removed at 350 °C⁴²⁷ thus leaving behind porous titania structure. It is evident from Figure 8.3 that both films on unmodified substrate (Figure 8.3a) and on modified substrate (Figure 8.3b) have lost some mesostructural order over the course of ramping to an elevated temperature. In Figure 8.3a, there are no out of plane spots indicating total loss of domains with parallel HCP orientation. Although vertical rods can be seen in Figure 8.3a, they have lost significant intensity and have become broader compared to initial GISAXS pattern at room temperature (Figure 8.2a). All of these features indicate that for titania films on unmodified substrates, the domains of parallel HCP pores are much more susceptible to thermal deterioration than the orthogonally oriented domains. The order of the orthogonally oriented pores in films on unmodified substrates also starts to deteriorate and the pore size distribution may become broader, as indicated by broadening of the vertical rods and the loss of intensity of the vertical rods in Figure 8.3b, compare to the initial condition at room temperature in Figure 8.2b. However, the change is less than for the unmodified substrates (Figure 8.3a). This loss of mesostructural order is caused by diffusion and sintering during crystallization, and

due to anisotropic stress developed due to crystallization of titania in the pore walls, starting above ~ 450 °C,⁴²⁷ and leads to frustrated shrinkage at the substrate surface.

While they have some similarity at the end of the temperature ramp, the GISAXS patterns of P123-templated titania films on unmodified and modified substrates differ dramatically after holding the samples at calcination temperature (600 °C) for 60 min (Figure 8.4). The titania film on unmodified substrate (Figure 8.4a) has a diffuse pattern centered around the Yoneda band with only faint vertical rods, indicating nearly complete loss of long-range mesostructural order. In contrast, titania films on modified substrates not only retained a significant amount of mesostructural order for the initial 60 min, indicated by vertical rods in in Figure 8.4b, but for at least another 30 min during the GISAXS experiment (data not shown). SEM imaging was performed using the same samples as those used for GISAXS experiments to observe the pore structure. As Figure 8.5 shows, the titania film on the unmodified substrate (Figure 8.5a) is partially porous but has lost its long-range mesostructural order completely after 60 min at 600 °C, consistent with GISAXS data (Figure 8.4a). In contrast, the titania film on modified substrate (Figure 8.5b) still retains some long range mesopore order even after 90 min at 600 °C.

To best quantify and compare the stability of the mesostructural order in the films on both unmodified and modified substrates, 2D GISAXS data were taken in 5 min intervals and a slice of each pattern was taken at $q_z = (0.06-0.07) \text{ \AA}^{-1}$ after reaching the final calcination temperature. While it is not in the Yoneda band, this q_z range was chosen

because it is quite sensitive to the presence and intensity of Bragg rods due the o-HCP structure. The area under the vertical rod, the orthogonal (100) peak, was determined after baseline correction and normalized by the peak area just after reaching the final calcination temperature. Figure 8.6 shows the time evolution of the normalized area under the (100) peak after reaching 600 °C for titania films on both unmodified and modified substrates. While both films show deterioration in the intensity of this peak, the film on modified substrate better retains its long range order compared to the film on unmodified substrate. Consistent with the 2D patterns in Figure 8.4, the normalized area for the film on a modified substrate is almost 5 times higher than the area the film on an unmodified substrate after the 60 minutes evolution period used for kinetic analysis.

Insight into the mechanism of the thermal transformation was gained by applying the Avrami equation. The Avrami equation is often used to analyze phase transformation processes involving continuous nucleation and growth or loss of a phase. The Avrami equation is given by:

$$- \ln(1 - \alpha) = (kt)^n \quad (1)$$

where α = the fraction of mesostructural order deteriorated, t = time, k = the rate coefficient of mesostructural deterioration and n = transformation propagation parameter.

The equation 1 can further be linearized as:

$$\ln(-\ln(1 - \alpha)) = n * \ln(t) + n * \ln(k) \quad (2)$$

Isothermal evolution studies of mesostructural deterioration of titania films on both unmodified and modified substrate were done for three different temperatures (600 °C, 625 °C and 650 °C) and the in-situ data were fit by linear regression using eq. 2. Figure 8.7 shows the fitting at each temperature for each sample. The linearized form of the Avrami equation fit all isothermal data reasonably well and can be further used to determine the parameters associated with these mesostructural deterioration processes. The values of n and k at each temperature are summarized in Table 8.1. For all experiments, the value of n associated with mesostructure loss is between 0.63 and 1.1, which is consistent with a one dimensional diffusion controlled mechanism for the thermal transformation of these titania films. This suggests that loss of order occurs due to diffusion along the walls of the material in a preferred direction due to the HCP structure. Increasing rate coefficient (k) values with temperature for films on both unmodified and modified substrates in Table 8.1 indicate an activated process for loss of order.

The effect of orientation on the activation energy for mesostructure loss was \pm determined using the linearized Arrhenius equation (eq. 3):

$$\ln k = \ln A - E_a/(R * T) \quad (3)$$

where, A = a preexponential factor, E_a = activation energy for mesostructural deterioration, T = absolute temperature and R = universal gas constant.

Figure 8.8 shows plots of $\ln(k)$ vs $1/T$ for titania films, which give activation energies of 126 ± 100 kJ/mol for films on unmodified substrates and 155 ± 25 kJ/mol for films on P123-modified substrates. This activation energy is associated with the deterioration of

the orthogonal component of titania films on both unmodified and modified substrate as the parallel domain is already absent above 400 °C.⁴²⁷ These activation energy values are comparable with the activation energy described in the literature for the deterioration of titania films with cubic phase (140 KJ/mol).¹⁶² The large standard error associated with the activation energy for the films on unmodified substrate is due to the large deviation in the measurement at 625 °C compare to other temperatures. We were limited by the beam time available and were unable to replicate this experiment at this temperature or any other temperature, so we are reporting the result here including that measurement. Slightly higher activation energy for films on the modified substrate means that the orthogonally oriented domains of titania films on modified substrate are more thermally stable than the orthogonal domains of films on unmodified substrates. The reason may be that the density of bending defects, or tortuosity associated with the orthogonal component, is higher for films on unmodified substrates (which start with a significant fraction of parallel domains) than the more uniform orthogonal domains on the modified substrate. The heterogeneity of the domains of films on unmodified substrates would be expected to introduce more defects to nucleate loss of order in the orthogonal domains, and would also be less resistant to anisotropic stress than films on modified substrates with more uniform orthogonal domains and a well defined path for diffusion of atoms during crystallization and curing.

The effects of film thickness on the thermal stability of this system were also studied for P123-templated titania films on P123 modified substrates. The film thickness was increased to ~230 nm for this study by using only 6 g of ethanol for the final dilution

step of sol preparation. SEM images and 2D GISAXS pattern of titania films having 230 nm film thickness on P123 modified substrate was already reported in previous work.⁴²⁷ There, it was shown that without sandwiching the films with a second modified slide, only partial orthogonal orientation was obtained. The films exhibited significant mesostructure loss even after calcination at 500 °C. Figure 8.9 shows that similarly, the thicker films on modified substrates lose their long-range order quickly upon heating at elevated temperature (within 5 min at 600 °C). The intensity of the vertical (100) rod is shown in this figure, and all other long-range order was lost by the time that the final calcination temperature was reached. The normalized intensity of the (100) rod from $q_z = (0.06-0.07) \text{ \AA}^{-1}$ was used to generate this plot. As in the previous study,⁴²⁷ more complete orthogonal alignment (in this case in thin films on modified substrates) leads to greater retention of mesostructural order during heating compared with a less completely aligned, thicker film.

The Avrami equation was applied to the mesostructure loss in thick P123-templated films on modified substrates to determine kinetic parameters. Figure 8.10a shows the fitting of avrami equation for three isothermal conditions (400 °C, 500 °C and 600 °C because of the reduced stability of the films) of 230 nm thick P123-templated TiO₂ films on P123 modified substrates. The method of determination the n and k parameters was based on standard linear regression except for the sample at 400 °C, where the n value was adjusted to the average of n values from other two conditions and the value of k was calculated from the slope of $-\ln(1-\alpha)$ vs t^n plot using equation 1. The reason for this adjustment is that the n value that was actually calculated from Figure 8.10 was very

low (0.29) compare to all other isothermal conditions (0.63-1.1). The activation energy for the mesostructural deterioration of these thick films was calculated to be 89 ± 27 kJ/mole using an Arrhenius plot (Figure 8.10b). This activation energy is clearly much lower than for both of the thin films, and lower compare to the reported activation energy of mesostructural loss of TiO_2 films with cubic mesostructures.¹⁶² This lower activation energy suggest that preparing well-oriented, thermally stable o-HCP films by casting films onto a single substrate modified with crosslinked copolymer only works up to a certain thickness. After this critical thickness, the orthogonal orientation of pores does not propagate from the solid substrate all the way to the vapor-film interface, because of which the films form a bilayer structure consisting of orthogonal pores at the substrate-film interface and parallel pores at the vapor-film interface. Due to this mismatch of pore orientation between two layers a high density of mesostructural defects is built into the films, which aids in loss of long-range order. In addition, the mismatch of structures makes these thick films less able to withstand anisotropic stress during heating. As a result of that this thick films deteriorate very quickly during heat treatment.

The above studies show that the thermal evolution of titania films at different isothermal conditions are strongly affected by the temperature history of the film. While *in situ* studies could not be performed during heating from room temperature due to difficulty maintaining alignment during thermal expansion, the effects of the heating rate (a.k.a. the ramp rate) on the mesophase deterioration kinetics of films calcined at 500 ° C were measured for thick films with ramp rates varying from 10

°C/min to 60 °C/min and the data were fitted using the Avrami equation (*Supporting Information Appendix F, Figure F.3*). Table 8.3 shows the Avrami parameter values determined by linear regression for different ramp rates. For higher ramp rate, the rate constant (k) is found to be higher. The reason is most likely that faster heating allows the system to more quickly accumulate nuclei of crystalline material, which leads to uniform growth of titania grains throughout the film thickness. A greater temperature gradient at higher ramp rates may also contribute to accelerated loss of mesostructural order due to non-uniform crystallization across the film. The layer directly attached with the substrate would be expected to reach the final calcination temperature faster than the uppermost layer, resulting in faster growth of titania grains near the substrate than at the vapor-film interface. This kind of uneven growth of grains can introduce an anisotropic thermal stress on the pore walls that ultimately leads to faster deterioration of the mesostructure. More uniform slow heating during calcination may result in uniform growth of titania grains on the pore walls which helps to withstand anisotropic stress better than the higher ramp rates.

8.5. Conclusions

A detailed kinetic study of the thermal transformation mechanism of mesoporous titania thin films with 2D hexagonal close packed (HCP) pores varying only in the degree and uniformity of orthogonally orientation of the pores has been conducted using *in situ* GISAXS complemented by *ex situ* SEM imaging. Thin films (~60 nm thick) templated using Pluronic surfactant P123 were used to obtain films with uniform orthogonal orientation when the substrate was modified with crosslinked P123, and a mix of

orientations (with a significant fraction of parallel oriented pores) on unmodified borosilicate glass slides. Thicker films (~230 nm thick) on modified slides also gave a mix of orientations, and prior studies suggested that they had a bilayer structure with parallel pores at the vapor-film interface and orthogonal pores at the substrate-film interface.

The kinetics of loss of orthogonal mesostructural order was measured by monitoring the decay in intensity of the (100) Bragg rod in the GISAXS patterns. This was the only feature present in all films after reaching their final isothermal calcination temperature. Kinetic parameters were determined by fitting the Avrami equation to all experiments. The activation energy for mesostructural deterioration is greatest for the thin films on modified substrates, which also had nearly perfect orthogonal pore orientation. A slightly smaller activation energy was found for thin films on unmodified substrates (which had a mix of orientations) and a much smaller activation energy for thick films on modified substrates. The thermal stability implied by these activation energies correlates with the degree of orthogonal orientation in the film. The density of bending defects, or the tortuosity of the pores associated with films on unmodified substrate makes them more susceptible to nucleation and growth of disordered regions, and to anisotropic thermal stress and leads to mesostructural loss during high temperature heating. On the other hand films on modified substrate have near perfect pore orientation and that allows them to handle the thermal stress during calcination without excessive mesostructure loss. Consistent with this, the mix of orientations found in thicker films makes films less stable during heating. Finally, the thermal history

or the rate of heating also influences the thermal stability of these films. For thicker films, higher ramp rates were found to cause more rapid mesostructure deterioration during isothermal heating. This is most likely due to nucleation of defects during faster heating, and due to anisotropic stress due to thermal gradients at higher ramp rates.

These detailed kinetic results show that films with orthogonally oriented HCP pores not only have significant transport advantages for photocatalytic and photovoltaic applications, but also that they undergo mesostructure loss by a different mechanism than films with parallel and mixed orientation HCP pores. The continuous pore walls normal to the film provides resistance to stress during heating, and the pore orientation provides a short diffusion path for crystallization within the walls, which both may contribute to enhanced thermal stability. The detailed kinetic results will allow for further refinement of thermal treatment procedures in the future in these orthogonally aligned mesoporous structures, and suggest mechanical and thermal advantages of these types of films for applications requiring accessible pores such as membrane separations, electrochemical sensors, and microfluidic components.

Table 8.1. Avrami parameters n and k determined using the linearized Avrami equation at different isothermal conditions for titania thin films (60 nm thick) on both unmodified and modified borosilicate glass substrates.

Substrate	Temp (°C)	n	k (min ⁻¹)
Unmodified	600	0.7±0.09	0.063±0.02
	625	0.75±0.19	0.054±0.04
	650	1.1±0.05	0.164±0.02
Modified	600	0.81±0.06	0.023±0.004
	625	0.82±0.06	0.049±0.004
	650	0.63±0.22	0.073±0.038

Table 8.2. Avrami parameters n and k determined using the linearized Avrami equation at different isothermal conditions for titania thick films (250 nm thick) on modified substrate.

Temp (°C)	n	k (min ⁻¹)
400	0.89±.09	0.009±0.002
500	0.9±.06	0.178±0.02
600	0.88±1.2	0.322±0.24

Table 8.3. Avrami parameters n and k determined using the linearized Avrami equation for different ramp rates to reach the final calcination temperature of 500 °C for titania thick films (250 nm thick) on modified substrate.

Ramp rate (°C/min)	n	k (min ⁻¹)
10	0.72±0.14	0.233±0.044
25	0.9±0.06	0.178±0.014
30	0.67±0.06	0.243±0.032
40	0.62±0.09	0.64±0.154
60	0.67±0.03	0.444±0.042

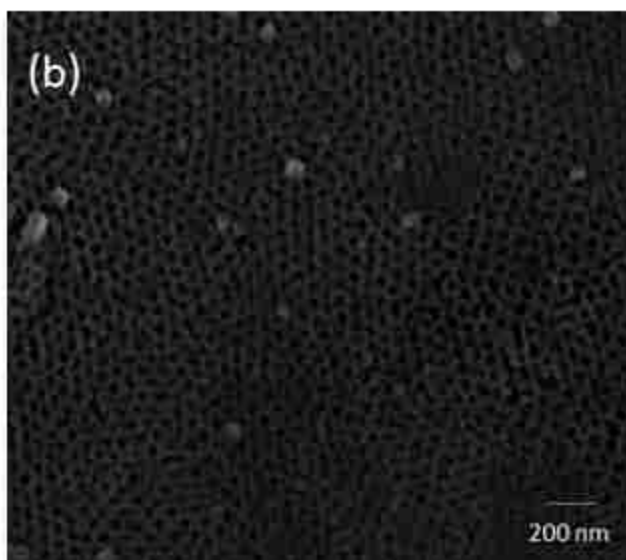
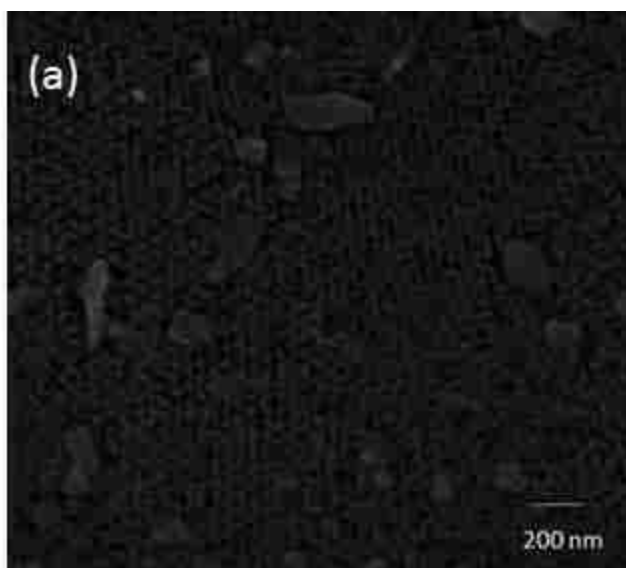


Figure 8.1. SEM images of the top surface of titania films on (a) unmodified (b) modified borosilicate glass slides aged for 2 h at 4 °C and immediately calcined at 500 °C for 60 min after heating at a rate of 40 °C/min.

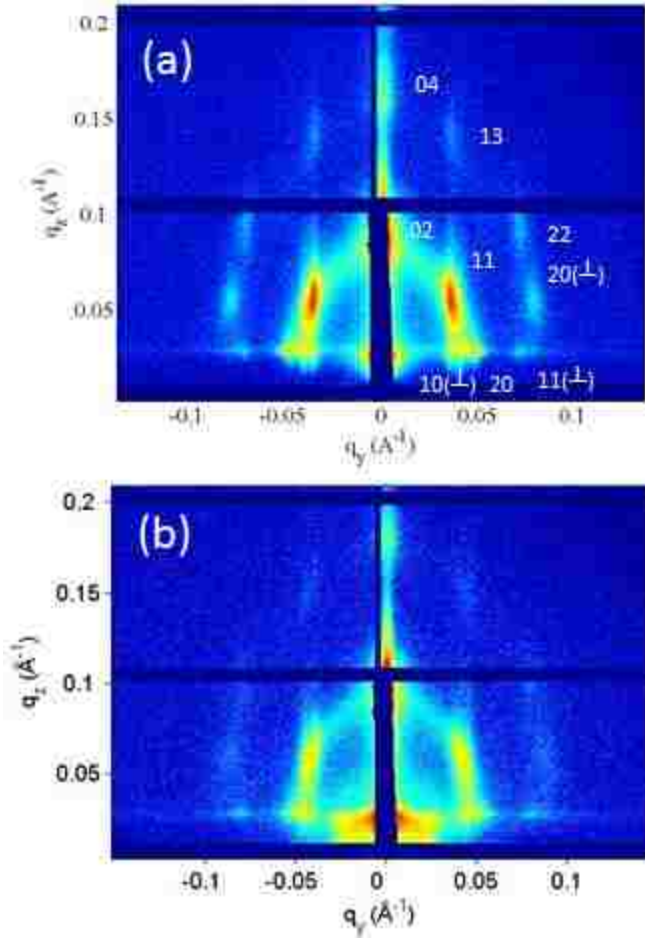


Figure 8.2. GISAXS patterns at room temperature (22.5 °C) of titania thin films (60 nm thick) on (a) unmodified and (b) modified substrate after aging at 4 °C for 2 h but before calcination. The films are oriented horizontally (in the xy plane) relative to the incident beam for this experiment.

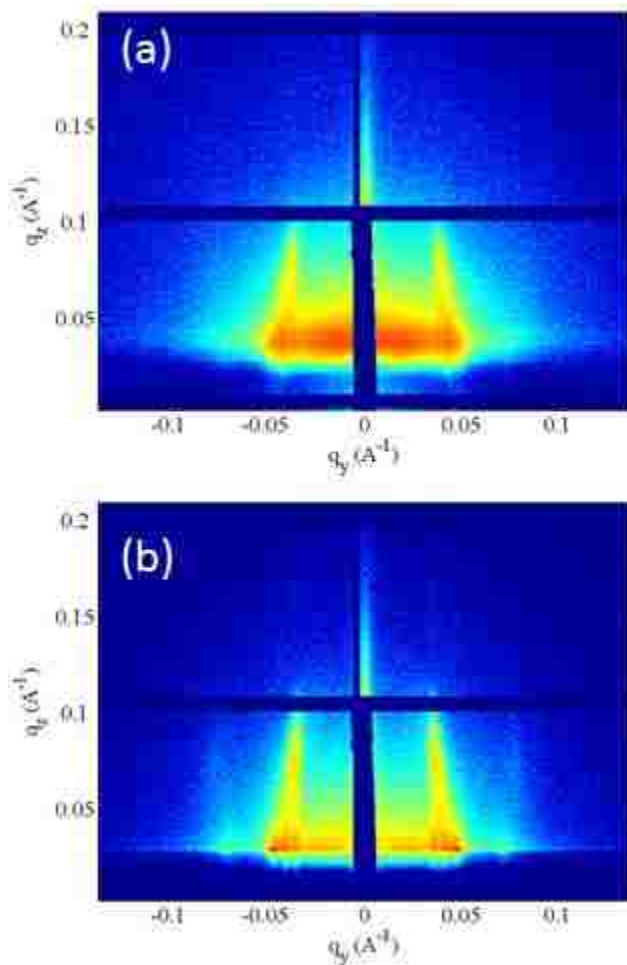


Figure 8.3. GISAXS patterns of titania thin films (60 nm thick) on (a) unmodified and (b) modified substrate after aging at 4 °C for 2 h and just after reaching final calcination temperature 600 °C with a 40 °C/min ramp rate. The films are oriented horizontally (in the xy plane) relative to the incident beam for this experiment.

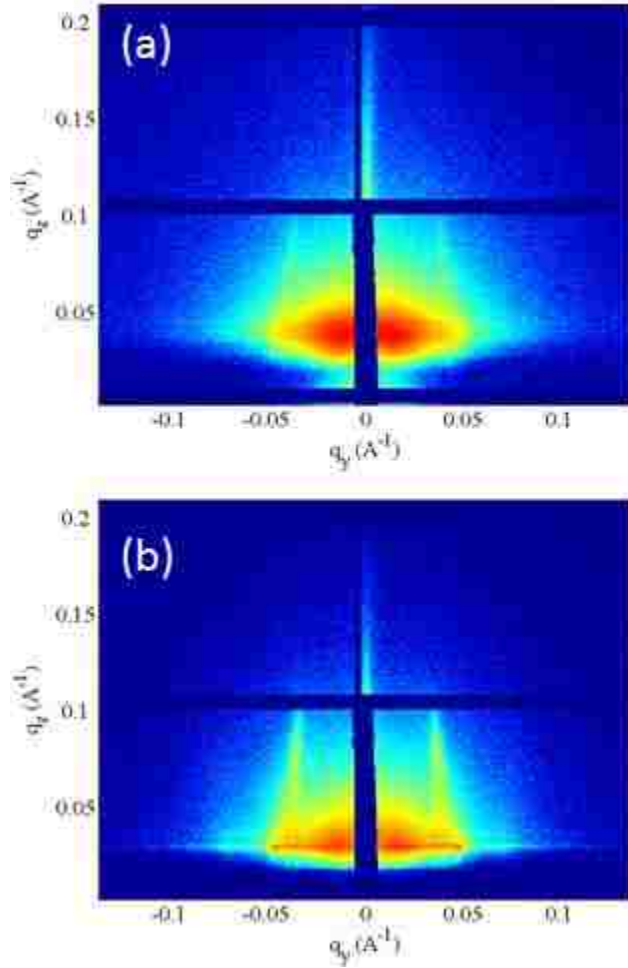


Figure 8.4. GISAXS pattern of titania thin films (60 nm thick) on (a) unmodified and (b) modified substrate after heating at 40 °C/min to 600 °C and holding at that temperature for 60 min. The film is oriented horizontally (in the xy plane) relative to the incident beam for this experiment.

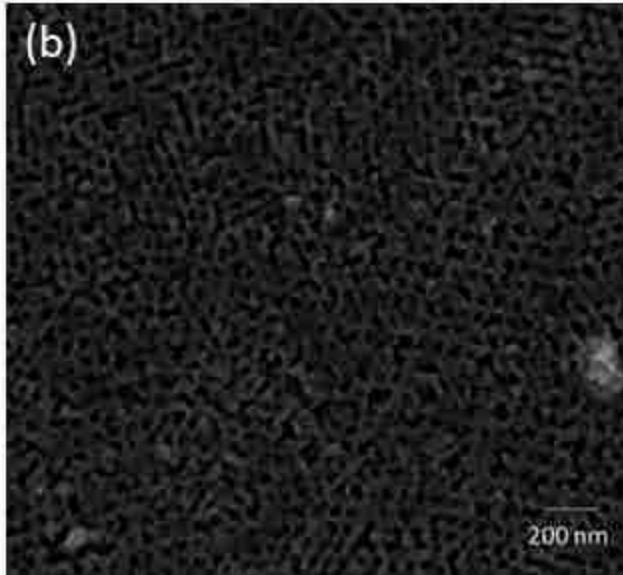
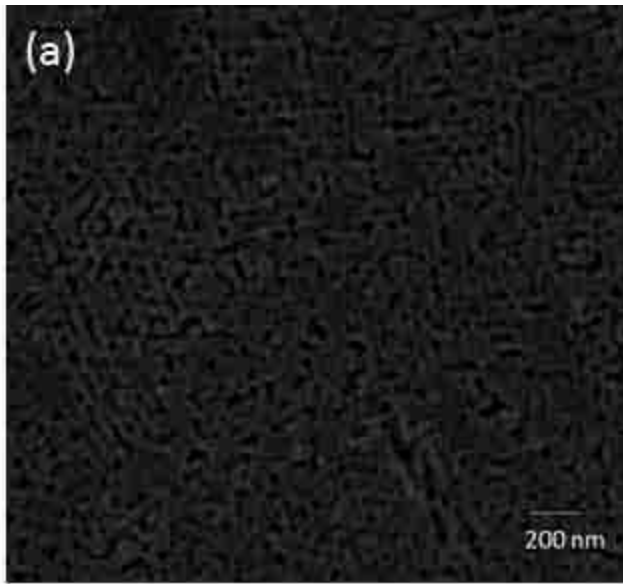


Figure 8.5. SEM images of titania films on (a) unmodified (b) modified substrate titania aged at 4 °C for 2 h and calcined at 600 °C for (a) 60 min and (b) 90 min after heating at a rate of 40 °C/min.

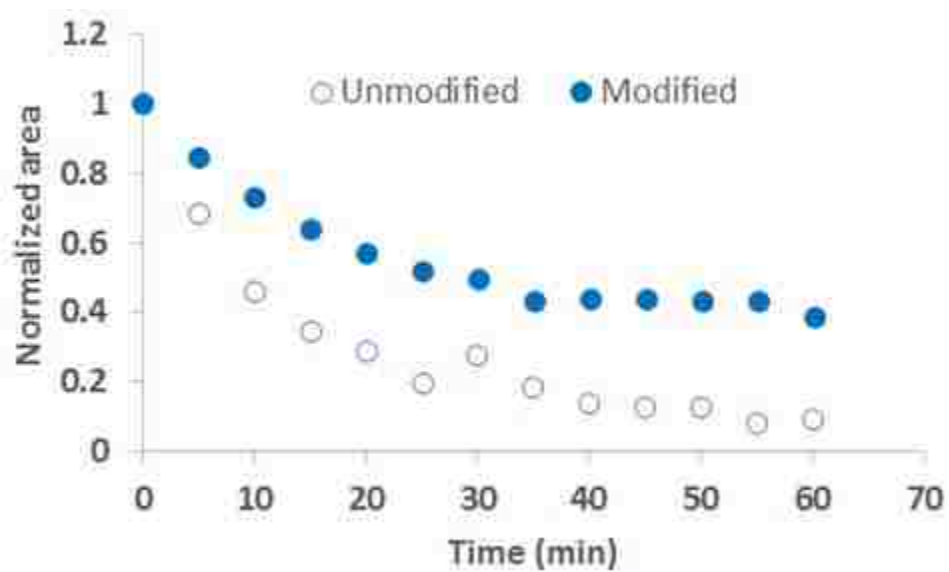


Figure 8.6. Normalized (100) diffraction peak height measured from line cuts over q_z values from 0.06-0.07 \AA^{-1} from *in situ* GISXAS data for titania thin films during isothermal treatment at 600 °C after heating at a ramp of 40 °C/min.

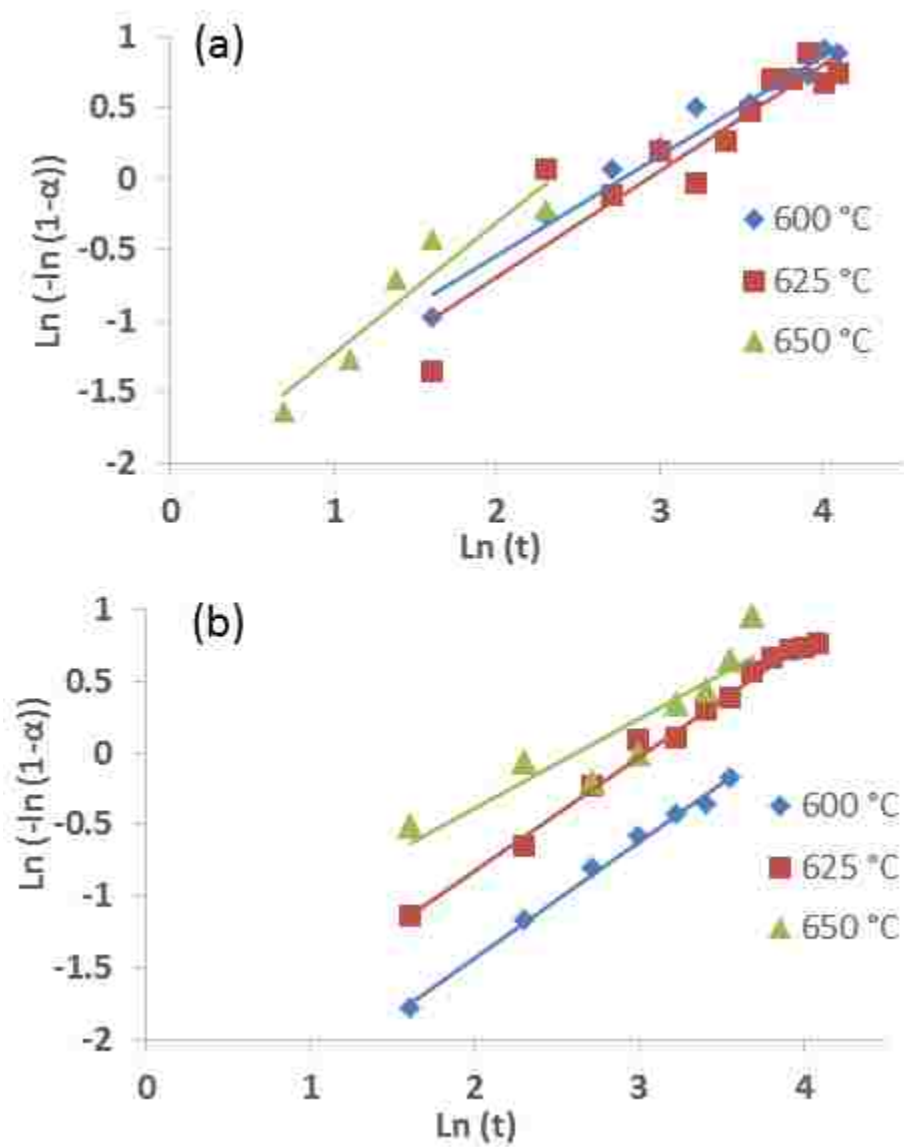


Figure 8.7. Avrami equation plots based on (100) peak height data for thin titania films on (a) unmodified and (b) modified substrate at different isothermal conditions after ramping at 40 °C/min.

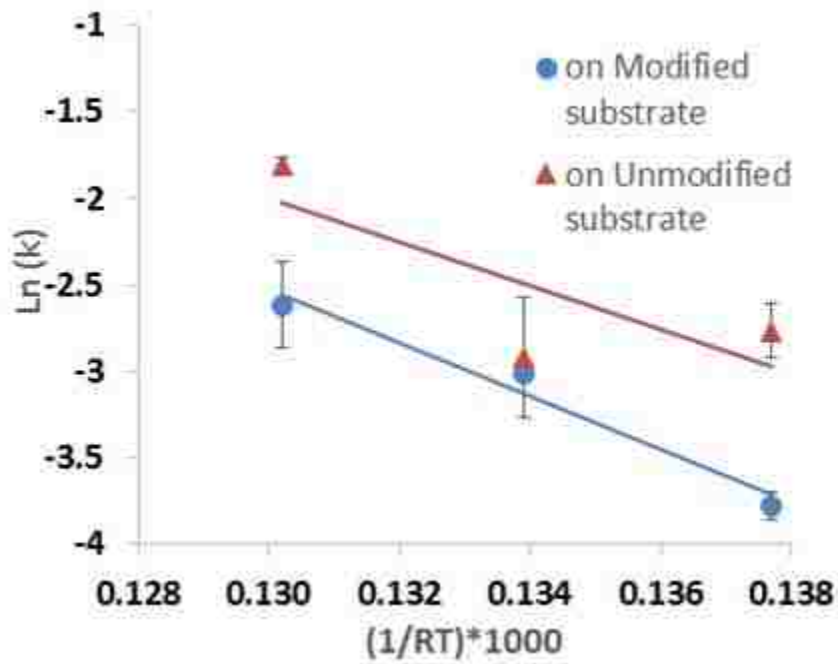


Figure 8.8. Arrhenius plot for HCP mesostructure loss of thin (~60 nm thick) titania films on modified and unmodified borosilicate glass substrates.

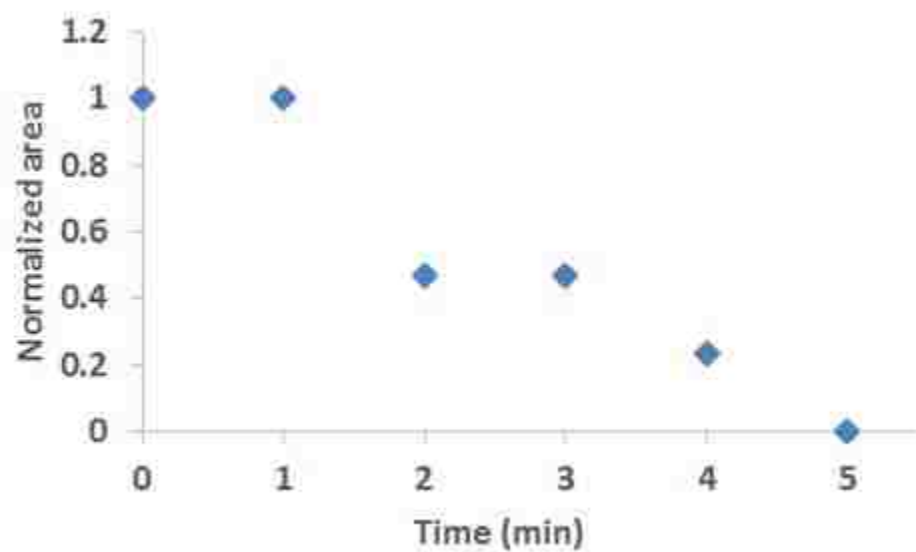


Figure 8.9. Evolution of the normalized (100) diffraction peak height from linecuts taken over q_z from 0.06-0.07 \AA^{-1} from *in situ* GISXAS data of titania thick films on modified borosilicate glass slides during isothermal treatment at 600 °C after heating at 25 °C/min.

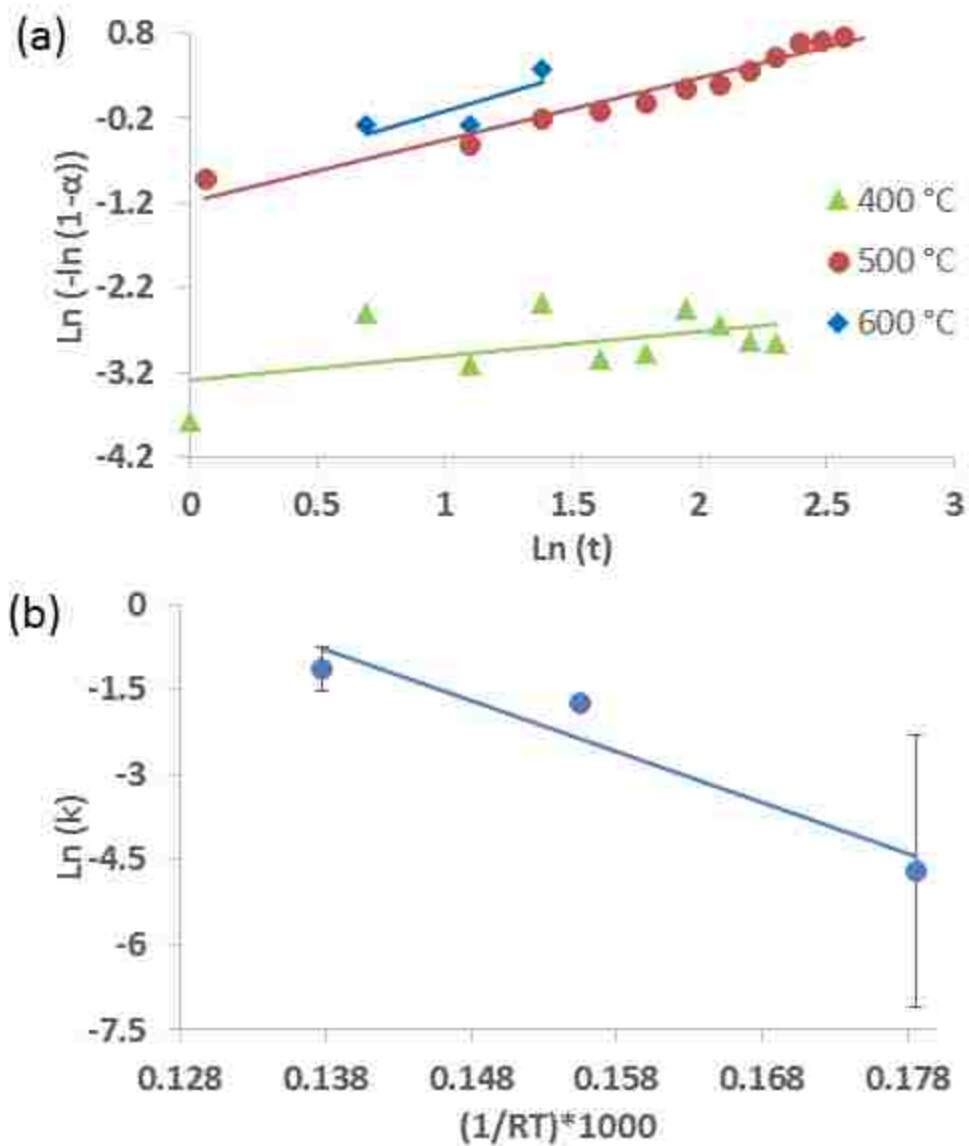


Figure 8.10. Plot of the (a) linearized Avrami equation (b) Arrhenius equation for thick (~250 nm) titania films on modified borosilicate glass slides at different isothermal conditions after heating at a ramp rate of 25 °C/min.

CHAPTER 9

Conclusion & Future work

9.1. Conclusions

In Chapter 3, a detailed study of headgroup interactions in mixed cationic and sugar-based surfactants was performed using fluorescence spectroscopy and Nuclear Magnetic Resonance (NMR) spectroscopy. The NMR results suggest a new type of mixed micelle 3D structure in which the carbohydrate surfactant is inverted with its head towards the core of the micelle in a structure similar to a very small asymmetric vesicle. While it is clear that both octyl glucoside (C8G1) and xyloside (C8X1) surfactants mix favorably with C₁₆TAB as indicated by a negative apparent interaction parameters (β), no protons of the sugar and cationic head groups were located close enough together to induce detectable nuclear Overhauser effect (NOE). Instead of interacting with the cationic head group, sugar head groups were found to interact with other sugars and with the surfactant tails. After ruling out phase separation among headgroups based on relaxation measurements, the most consistent model of these mixed micellar systems has the sugar surfactants in an inverted configuration in the core of the mixed micelles. The hypothesized was further tested using fluorescence quenching experiments where enhanced quenching of a boronic acid fluorescent probe was observed due to the confinement of the sugar heads near the micelle core. This study suggests that the head groups of C8G1 and C8X1 is not directly accessible for molecular imprinting and a new pair of surfactants will be needed where the sugar head is “pushed outside” of the

mixed micelle so that it can better interact with the silica network to create the binding sites.

In Chapter 4, the result suggests that matching of cationic and carbohydrate surfactant chain length is not sufficient to “push out” the carbohydrate head group near the exterior of the micelle. Consistent with the previous study with C₁₆TAB/C8G1 mixture there is no detectable nuclear Overhauser effect (NOE) correlations between the head group of dodecyl glucoside (C12G1) and the head group of C₁₆TAB (with 16 carbon chain length), DTAB (with 12 carbon chain length) and DeTAB (with 10 carbon chain length). Instead of interacting with the cationic head the sugar head is interacting among themselves or with the tails of the surfactants. The reason may be force mismatch between the different surfactant heads and the polar surroundings. As the Coulombic interaction force between the cationic heads with the surrounding water is stronger than the hydrogen bonding forces between the non-ionic sugar head and the surrounding water, the carbohydrate heads prefer to stay near the core of the mixed micelle. We have then hypothesized that an additional interaction force is needed for carbohydrate surfactants to “pull out” the sugar head near the exterior of the mixed micelle. To investigate the hypothesis C₁₆TAB was mixed with n-octyl-β-D-triazolexylopyranoside (C8XT1), a new carbohydrate surfactant with a triazole linker, with prediction that the additional dipolar interaction between the triazole linker with the polar surrounding would “pull out” the sugar head. The results show various interactions between the sugar head with the cationic head of C₁₆TAB which proves the hypothesis. That makes the C₁₆TAB/C8XT1 mixture a perfect candidate for xylose

imprinting. We also expect same result for C₁₆TAB/C8GT1 mixture (C8GT1, n-octyl-β-D-triazole-glucopyranoside) because glucose is more hydrophilic in nature than xylose and that means most likely the glucose head group of C8GT1 will also be accessible for molecular imprinting.

In chapter 5 we describe a simple inexpensive technique to prepare mesoporous silica films with vertically oriented accessible pores. For that we modified the surface of our substrate (glass slides) by using a random-co-polymer (vinyl alcohol-co-ethylene). We hypothesized that the use of this random-co-polymer (58% ethylene w/w %) would provide a uniform distribution of polar hydroxyl and non-polar ethylene functionally on the substrate and would provide similar interactions with both heads and tails of small-molecule surfactants to orient hexagonal mesophase vertically. The XRD and TEM results are consistent with the vertically oriented accessible pores although further future characterization is needed to determine the phase of the mesoporous structure.

In chapter 6 the effect of longtime aging on the mixed surfactant templated silica thin films was discussed. We found that for 10:1 C₁₆TAB/C8G1 templated silica films aged at constant humidity and temperature the structure shrinks and the long range order increases as we increase the time of aging up to 14 days. The internal compressive stress induced by shrinkage of the films during aging may be the reason behind the disordering of the films. Increase in aging temperature at constant humidity for 7 days gives us more disordered structure with shrinkage in the structure. We also see increase in condensation with increase in aging temperature from FT-IR analysis that may be the

reason for shrinking. The loss of long range order due to increase in aging temperature can be explained by the fact that the higher aging temperature introduces a higher number of defects into the long-range structure of the films. Increase in aging humidity at constant temperature for 7 days makes more dis-order structure accompanying with structure expansion. The swelling of the mesostructure due to the absorption of water in the corona region of the micelles, is the reason behind these changes. From results, aging at 20 °C and 45% RH for 2 days was selected for optimum aging time for these templated silica thin films.

Chapter 7 describes the effect of pore orientation on mesostructural stability and crystallization of titania thin films with 2D hexagonal close packed (HCP) columnar nanopores. From the in-situ GISAXS results it is clear that perfect orthogonal pore orientation in sandwiched films has a tremendous impact on mesostructural stability of the films. The SEM and TEM result suggests that this is not only due to differences in how the films respond to stress during crystallization; preferential crystallization at the top surface of the pores also occurs, which most likely leaves the interior of the pores less crystalline and helps to withstand the anisotropic stress that develops due to titania curing and crystallization. In unsandwiched films, the films contain more defects and do not have as many continuous pathways to the top surface of the film, so crystallization occurs in more of a 3D diffusion-limited manner throughout the film. This is the first time that a surface-crystallization phenomenon has been observed in oriented mesoporous films and correlated with enhanced mesostructure stability.

In Chapter 8, to understand the kinetics of thermal transformation mechanism of meso structural titania thin films with different pore orientation in more detailed way, further *in-situ* GISAXS and *ex-situ* SEM imaging was done. This time instead of using sandwiching technique (used in Chapter 7) we reduce the film thickness to get the perfectly orthogonally oriented titania films. From the comparison of activation energy of meso structural deterioration it is clear that near perfect orthogonal pore orientation on modified substrate has better thermal stability than the mixed oriented pores on plain substrate. The degree of bending or tortuosity of pores associated with films on unmodified substrate makes it more susceptible to anisotropic thermal stress and leads to meso structural loss during high temperature heating. On the other hand films on modified substrate have near perfect pore orientation and that makes it a proper candidate to handle the thermal stress during calcination. Effectiveness of this modification technique also have strong correlation with film thickness. For thicker films due to the incomplete propagation of orientation throughout the film, activation energy drops significantly, makes films less stable during heating. Also the thermal history or the rate of heating dictates the thermal stability of these films during isothermal curing. With higher ramp rates the meso structure deteriorates more quickly than the slow heating. All of these detailed kinetic studies of transformation mechanism of titania thin films in this chapter will help us to tune the material properties with optimum condition for the future energy applications.

9.2. Future work

In chapter 3 and 4, extensive research was done to find out the relative position of carbohydrate head group in mixed micelle of cationic-carbohydrate surfactants. From this study for the first time we have presented a new type of mixed micelle 3D structure in which the carbohydrate surfactant is inverted with its head towards the core of the micelle. Although both NMR and Fluorescence spectroscopy data were consistent with the proposed structure, there still exist one possibility where instead of a totally inverted structure, the carbohydrate headgroup is buried well inside the mixed micelle so that the carbohydrate head groups can correlate with the tail protons of surfactants and also are accessible for fluorescent dye partitioning. To check that possibility we need some probe near the ω protons of C₁₆TAB, such as labeling one or more carbons associated with the C₁₆TAB tail after the β position by replacing a hydrogen with fluorine so that the other proton associated with that carbon has a different chemical shift from rest of the tail protons then we can identify the direct interaction of the sugar head with that proton. Doing this would require synthesizing a new surfactant in which only one proton of the tail in C₁₆TAB is replaced with fluorine. This is beyond the scope of the current dissertation but could be pursued in collaboration with a synthetic organic chemist. Molecular dynamics simulations investigating the cationic-carbohydrate mixed micelle structure would also help to understand the relative position of the carbohydrate head group in the mixed micelle and the feasibility and relative energetics of the inverted structure. Our group has already initiated some progress in this field by building the pure C8G1 micelle using Avogadro software⁴³³ and then using AMBER for a

full molecular dynamics simulation⁴³⁴. In future we will get more insights about the mixed micelle 3D structure by using molecular dynamics approach.

In chapter 5 we described a surface modification technique using a random-co-polymer to prepare silica films with orthogonally oriented accessible pores. Although we got very good promising results with XRD and TEM the films still need further characterization. The main problem for characterization these films is the removal of the intermediate polymer layer. We normally calcine the films to remove the polymer but during removal there exist a high possibility that the pores become disordered. Therefore, we need a nondestructive technique to characterize our films. Cross sectional TEM using FIB for sample preparation will be the ideal choice to see the oriented channels in these oriented silica films.

In chapter 6 we described the effect of long time aging on the mixed surfactant templated silica thin films. Here we used FT-IR to understand the degree of condensation by comparing the peak intensity ratio of Si-O-Si peak to Si-OH peak. However, siloxane stretching bands are complex and multiple contributions can come from different bond stretching⁴³⁵. So even if we do not see any change in Si-O-Si/Si-OH ratio, it is possible that change in condensation is still going on. Deconvolution⁴³⁶ of the bands can give us more appropriate estimate about the change in condensation during long time aging.

After combining all results from chapter 3 to 6 we can prepare glucose or xylose imprinted orthogonally oriented silica thin films. The next step is to perform adsorption

experiments on these imprinted silica thin films to show the selective adsorption of targeted carbohydrates. The main challenge of showing the evidence of molecular imprinting from adsorption studies of carbohydrate mixture is the lack of suitable characterization technique. Individual carbohydrate adsorption studies can be done using Fourier transform infrared spectroscopy (FT-IR) and quartz crystal microbalance (QCM) but they are not useful for carbohydrate mixture studies. Mixed carbohydrate adsorption studies can be done using high performance liquid chromatography (HPLC) but this method needs a large amount of materials and can be ambiguous due to the overlapping of peaks. Thus there is a need to establish a proper technique for adsorption studies which requires small amount of materials and can be applied to mixed carbohydrate system. Use of NMR technique for adsorption measurements by using different position labeled (^{13}C labeling) carbohydrates can help us to investigate the selective adsorption of targeted carbohydrate for carbohydrate mixture.

Finally in chapter 7 and 8 we discussed the transformation mechanism of P123 templated titania thin films during high temperature curing. Here we studied the kinetics of mesostructural deterioration with in-situ GISAXS experiments and correlate it with the change in mechanism of crystallization of titania from ex-situ SEM and TEM. Although SEM and TEM can give us some information about crystallization but it fails to give in-detail kinetics of crystallization. The in-situ transformation kinetics of crystallization mechanism of these titania thin films can be thoroughly studied using in-situ Grazing incidence wide angle x-ray scattering (GIWAXS)¹⁶². We already tried some initial experiments at Argonne national lab but was limited by some technical difficulties

during GIWAXS data collection. In future we can perform in-situ GIWAXS to get in-detail information about the crystallization mechanism of these mesoporous titania thin films during high temperature curing.

APPENDIX A

NMR studies of interactions of carbohydrates with molecularly imprinted silica particles

A.1. Summary

The main challenge to showing evidence of molecular imprinting from adsorption studies of carbohydrate mixtures is the lack of suitable characterization techniques. Individual carbohydrate adsorption studies can be done using Fourier transform infrared spectroscopy (FT-IR) and quartz crystal microbalance (QCM) but these approaches are not useful for carbohydrate mixture studies. Mixed carbohydrate adsorption studies can be done using high performance liquid chromatography (HPLC) but the method needs a large amount of material and can be ambiguous due to the overlapping of peaks. Therefore there is a need to establish more techniques that can be used for adsorption studies which requires small amounts of materials and can be applied to mixed carbohydrate system. Here we demonstrate a simple ^{13}C carbon NMR technique for carbohydrate adsorption measurements based on using carbohydrates with ^{13}C labeling at different positions. Such labeled sugars are commercially available for common sugars (such as glucose) and can in principle be synthesized to meet any need. In this case, carbon labeling at different positions of glucose and xylose provides an opportunity to quantify the adsorption of each carbohydrate from a mixed solution onto silica particles.

The second part of this study addresses the application of solid state NMR techniques to identify the nature of the interactions between carbohydrates and silica, with the goal of better understanding molecular imprinting. Although previous studies from our group showed evidence of molecular imprinting using carbohydrate / cationic surfactant mixtures⁴³⁷, the mechanism of molecular imprinting is not thoroughly understood. To gain insight into interactions between carbohydrates and silica associated with molecular imprinting, we initiated a study using solid state NMR. The long-term goal was to study whether there is a difference in binding sites between imprinted and non-imprinted silica or there is a difference in interactions between different carbohydrates. This type of study will show the importance of orientation of hydroxyl group in silica and their preferential interaction with the specific carbons in the carbohydrate structure. For this study we used ^{13}C $\{^1\text{H}\}$ heteronuclear correlation (HETCOR) experiments to seek interaction sites between the adsorbed materials with the surface⁴³⁸. Due to the limited quantity of laboratory synthesized C8XT1, instead of $\text{C}_{16}\text{TAB}/\text{C8XT1}$ templated silica thin films we first try to establish these techniques using another kind of molecular imprinting procedure the Stöber particle approach.

Stöber particles are the mono-dispersed spherical silica particles prepared by precipitation from ethanol-containing aqueous ammonia⁴³⁹. It has already been shown by Joshi et al. using ATR-FT-IR that when these Stöber particles are imprinted by mixed cetyltrimethylammonium bromide (C_{16}TAB) and n-octyl- β -D-glucopyranoside (C8G1) surfactants, these particles show evidence of molecular imprinting⁴³⁷. Our goal was to use these imprinted Stöber particles for the establishment of the NMR techniques for

adsorption studies which are previously described. From these studies it is clear that there is a high affinity for glucose on glucose-imprinted materials compare to non-imprinted materials during adsorption from solutions containing only glucose. High specific adsorption of glucose in the presence of xylose on glucose-imprinted Stöber particles was also seen from this study indicating the evidence of molecular imprinting on these imprinted Stöber particles. From the solid state NMR study we also have found the clear interaction between the carbohydrate and the imprinted silica using 2D ^{13}C $\{^1\text{H}\}$ HETCOR experiments. All of these results will help the further adsorption studies on $\text{C}_{16}\text{TAB}/\text{C8XT1}$ or $\text{C}_{16}\text{TAB}/\text{C8GT1}$ imprinted silica thin films.

A.2. Experimental

Deuterium oxide (D_2O , 100 atom% D, Fischer Scientific) was used as received. All ^{13}C enriched carbohydrates (99% labeled D-[2- ^{13}C] glucose, 99% labeled D-[1- ^{13}C] xylose and 99% D-[all- ^{13}C] Glucose/Xylose) were purchased from Omicron Biochemicals, Inc. Glucose imprinted Stöber particles were synthesized, purified and dried according to the method of Joshi et al⁴³⁷.

For quantitative adsorption experiment using liquid state NMR, 5 mg of non-imprinted or glucose-imprinted Stöber particles were presoaked in a centrifuge tube with 1 ml D_2O overnight. After soaking the particles were centrifuged and effluent D_2O was removed. The required amount of carbohydrate mixture dissolved in 1 ml D_2O was added to the wetted Stöber particles. It was ensured that the total volume (1.5 ml) of the solution with Stöber particles in the centrifuge tube remained constant by adding extra D_2O if required. The sample was then placed in a vortex mixer and stirred for 1 day. After that

the whole sample was placed in an NMR tube. Particle separation was not required because slow tumbling of adsorbed carbohydrates gives a broad signal that provides a negligible contribution to the integrated intensity of carbohydrates in solution. NMR experiments were conducted using a 400 MHz Varian Inova NMR spectrometer at a room temperature (23 ± 1 °C). All of the ^{13}C carbon NMR experiments were done using a standard 1D ^{13}C carbon pulse sequence.

For solid state NMR experiments, 300 mg of glucose imprinted Stöber particles were presoaked in 10 ml of D_2O for 1 day. The sample was centrifuged and the supernatant was removed. 6.5 mg of 99% all ^{13}C carbon labeled glucose was dissolved in 10 ml of D_2O and added to the wetted Stöber particles. The sample was stirred in vortex mixer for 1 day and then the particles were recovered by centrifugation. The required amount of Stöber particles with bound carbohydrate was tightly packed (around 100-120 mg) in a zirconia solid state NMR rotor. Solid state experiments were done with a 600 MHz Varian Inova NMR spectrometer at room temperature (23 ± 1 °C) with 8 kHz MAS rotation. The HETCOR experiments were done using the `hetcorlgcp2d` pulse sequence with cross-polarization contact time of 6 ms and recycling delay of 10 sec.

A.3. Results & Discussion

Figure A.1 shows a representative ^{13}C carbon spectrum of a solution of mixed isotopically labeled glucose and xylose in D_2O . Due to specific carbon labeling at different position of glucose and xylose, the carbon chemical shifts differ and provide the opportunity to quantify the adsorption of each carbohydrate onto silica particles from the mixture. There are two carbon peaks associated with each sugar indicating the

presence of α and β anomers of each carbohydrate^{440, 441}. During the adsorption studies the intensity of the both anomers were integrated after baseline correction to provide a quantitative measure of the carbohydrate concentration in the solution. The linear calibration curves were measured with three carbohydrate concentration varying from 15mM to 45mM (data not shown) for pure individual solutions with $R^2=1$ for both solutions. The amount of carbohydrate adsorption was calculated by depletion measurement where the difference in carbohydrate concentration gives the amount of carbohydrates adsorbed to the silica particle. The amount of carbohydrate adsorbed was calculated per gram of silica and plotted against the final carbohydrate concentration in the solution. The adsorption experiment was done in triplicate for each condition to get the average and standard deviation.

Figure A.2 compares glucose and xylose adsorption from individual solutions onto both non-imprinted and glucose-imprinted Stöber particles. A higher affinity of glucose for glucose imprinted Stöber particles than for non-imprinted particles is evident from the statistically significant difference in adsorption at the highest glucose concentrations in Figure A.2. For xylose the amount of adsorbed carbohydrate is similar on both non-imprinted and glucose imprinted Stöber particles. This result indicates that molecular imprinting is able to create oxide surfaces with greater affinity towards specific carbohydrates, which is also consistent with a previous study by our group using ATR-FTIR⁴³⁷.

To see the specific adsorption of glucose on glucose-imprinted Stöber particle from glucose/xylose mixtures a second adsorption study was performed. Figure A.3 shows the glucose and xylose adsorption from glucose/xylose 1:1 mixtures on both non-imprinted and imprinted Stöber particle. Selective adsorption of glucose on glucose imprinted Stöber particles is seen at the highest saccharide concentration Figure A.3 almost approximately twice as much glucose as xylose adsorbed on glucose imprinted Stöber particles. For adsorption on non-imprinted Stöber particles, no preferential adsorption is observed between glucose and xylose. All of these results show evidence of effectiveness of molecular imprinting towards specific adsorption. Not only do imprinted particles show enhancement in adsorption of the target molecule from a solution containing a single solute, but they also show selective adsorption from mixed solute systems.

To understand the interactions between carbohydrate and the imprinted Stöber particles, solid state NMR experiments were performed. Figure A.4 shows the cross polarization magic angle spinning (CPMAS) spectrum of 99 % uniformly ^{13}C label glucose adsorbed on Stöber particles. 99 % ^{13}C enriched glucose was used to increase the sensitivity of our experiment as the amount of glucose adsorbed to create a monolayer on the Stöber particles was very small compared to the overall sample mass. The peaks associated with different carbons were assigned from literature⁴³⁸. Due to the introduction of ^{13}C enriched glucose the ^{13}C - ^{13}C coupling becomes significant and that leads to poorly resolved carbon peaks. Figure A.5 shows the HETCOR spectrum of 99 % uniformly label glucose adsorbed on glucose imprinted Stöber particle. From Figure A.5,

correlations between the carbons of glucose with and the hydroxyl group of silica (1H, 1.2 ppm) can be observed, although due to the poor resolution the exact binding sites were not identified. More specific information about the interacting carbons can be found using similar NMR studies with a series of glucose molecules labeled with ^{13}C at different positions. These are commercially available but the experiments were not performed due to time constraints.

A.4. Conclusions

Here we establish two uses of NMR spectroscopy to investigate adsorption of carbohydrates onto molecular imprinted silica surfaces. Glucose and xylose with different carbons labeled by ^{13}C were used to allow differentiation in chemical shifts by ^{13}C NMR. This allowed direct measurement of the amount of each carbohydrate adsorbed onto Stöber particles from mixtures using depletion measurement. The results show that the high affinity of glucose for glucose-imprinted materials compare to non-imprinted materials is observed both by comparing separate solutions of glucose vs. xylose, and for selective adsorption from mixtures of the two. Further detailed adsorption studies using this technique with a wider range of carbohydrate concentrations should be done to build competitive Langmuir adsorption isotherms for carbohydrate adsorption to complete this study.

In the second part of these preliminary experiments, solid state NMR techniques including CPMAS and HETCOR were used with ^{13}C enriched glucose to understand the interaction mechanism of carbohydrates with these molecularly imprinted Stöber particles. From this study, a clear indication of interactions between the carbohydrate

and the imprinted silica was found, although further experiments with series of different position labeled (^{13}C) carbohydrates are needed to get more specific information about the sites of strongest interaction between glucose and imprinted silica.

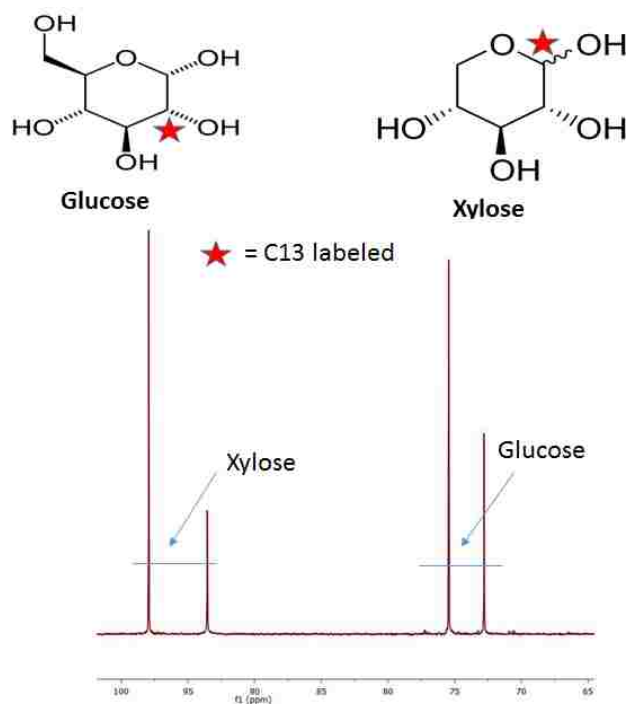


Figure A.1. ^{13}C NMR spectrum of isotopically labeled Glucose and xylose mixture in D_2O . The associated glucose and xylose structures are also shown. The red star on both the structures shows the relative position of the ^{13}C labeling. Two carbon peaks associated with each sugar indicating the presence of α and β anomers of each carbohydrate.

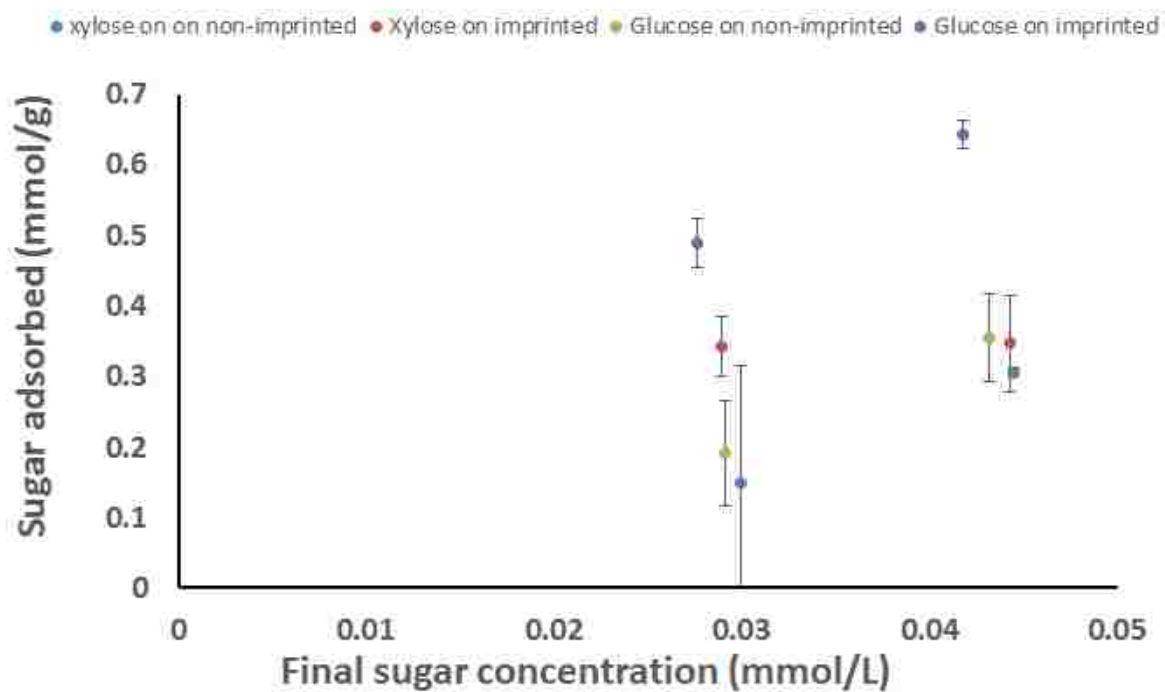


Figure A.2. Comparison of the results of glucose and xylose adsorption from solutions initially containing only individual carbohydrates on both non-imprinted and glucose imprinted Stöber particles. The results show a high degree of affinity of glucose for glucose imprinted Stöber particles compared with non-imprinted particles. In contrast, there is no significant increase in xylose affinity on glucose imprinted Stöber particles compared with non-imprinted particles.

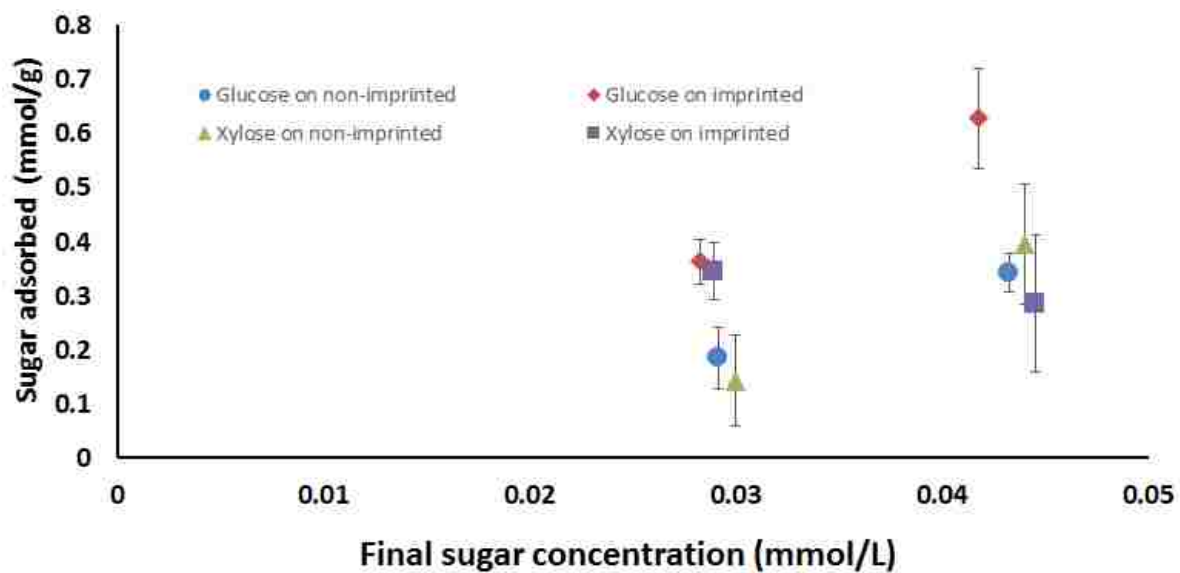


Figure A.3. Comparison of the results of glucose and xylose adsorption from glucose/xylose 1:1 mixtures on both non-imprinted and glucose imprinted Stöber particles. The results show a high degree of affinity of glucose to the glucose imprinted Stöber particles compared with non-imprinted particles, but no significant change in xylose affinity due to glucose imprinting.

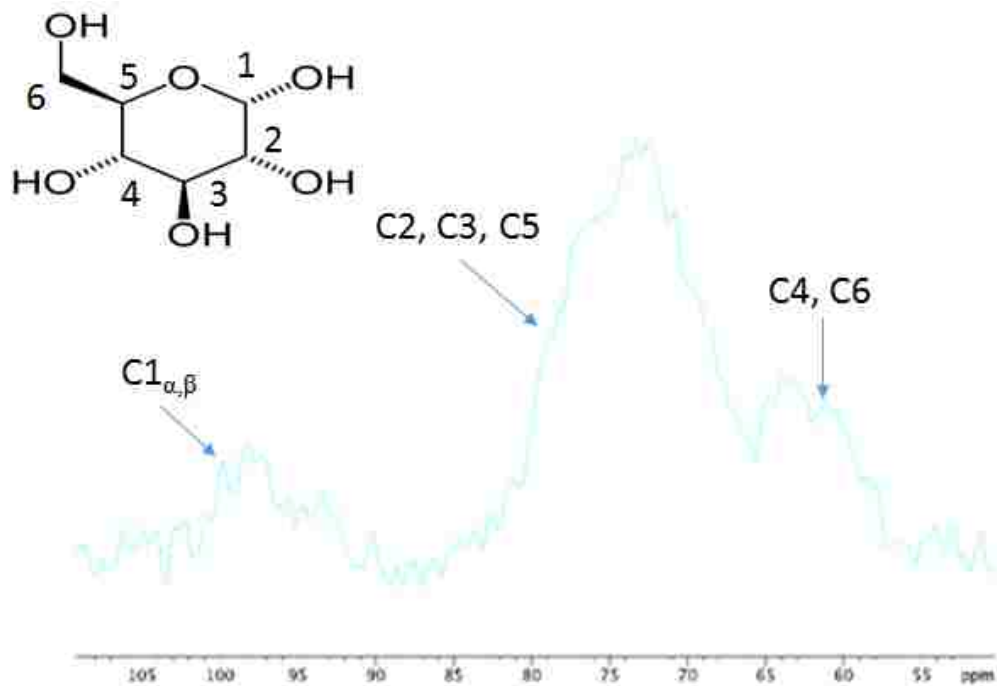


Figure A.4. Solid-state CPMAS NMR spectrum of glucose imprinted stöber particles with 99% all ¹³C labeled glucose adsorbed on the surface. α and β indicate two anomers of glucose.

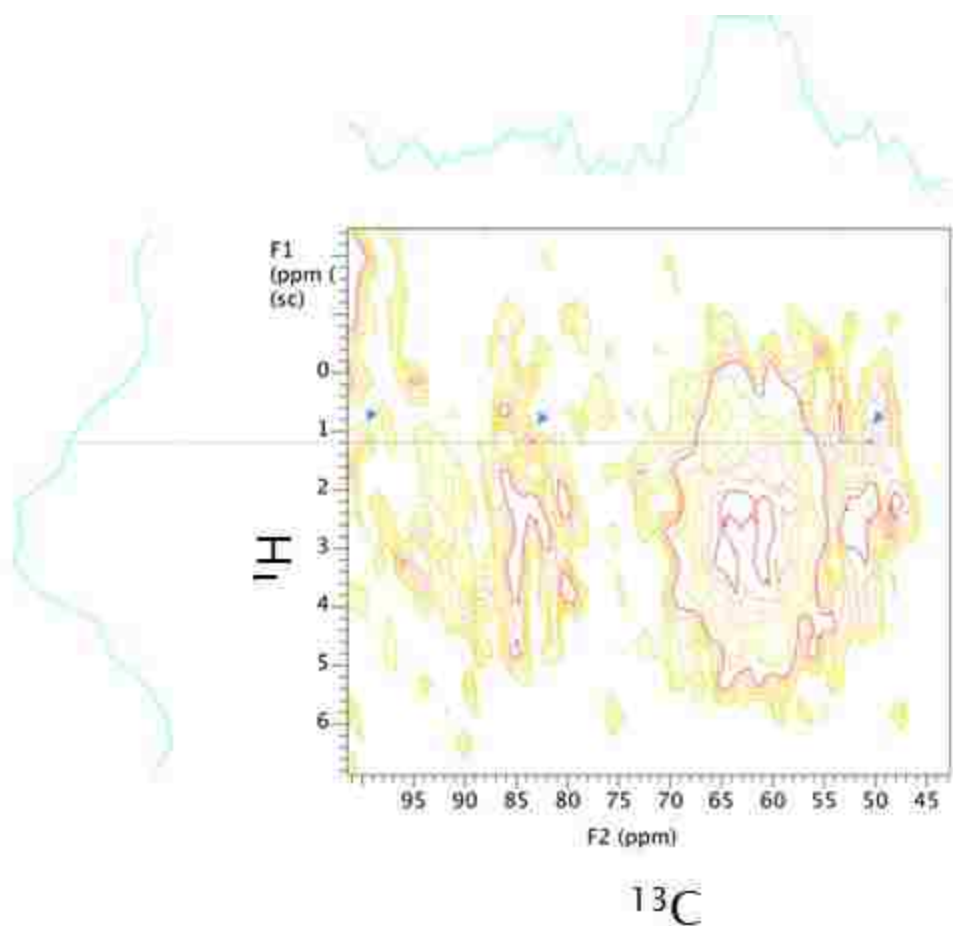


Figure A.5. Solid-state 2D ^{13}C $\{^1\text{H}\}$ HETCOR NMR spectrum of glucose imprinted Stober particles with 99% all ^{13}C labeled glucose adsorbed on the surface. Arrows indicate correlations between the carbons of glucose and the hydroxyl group of silica (at ^1H chemical shift 1.2 ppm).

APPENDIX B

Effect of ammonia pre-treatment & extraction on mesostructural stability of mixed Cationic-carbohydrate surfactant templated silica thin films

B.1. Summary

This study addresses the effectiveness of ammonia vapor pretreatment before aging on the mesostructural stability of surfactant templated silica thin films. Often, conventional curing of templated silica structures in a humid air environment does not facilitate rapid curing to yield a structure stable towards extraction within a desired time interval. This problem was encountered, for example, in C₁₂TAB / C12G1 structures cured at 50 °C at 45% RH for 7 days, at which point extraction led to complete loss of mesostructure. To address this problem we use ammonia pre-treatment before aging to stabilize the films. Our group has already shown the usefulness of mild ammonia pretreatment before aging for C₁₆TAB / C8G1 templated bulk materials to improve the stability of the structure²⁷³. During ammonia treatment, ammonia interacts with micelles to expand the pores (most likely via a Maillard-like reaction with sugar surfactant headgroups) while at the same time ammonia and water adsorb at the silica/surfactant interface to increase the effective pH values to enhance the condensation rate and solidify the network. We use this process for C₁₂TAB / C12G1 10:1 templated thin films and studied the outcome using XRD and FT-IR. The result will show that 15 hours of ammonia vapor

pretreatment before aging of C₁₂TAB/C12G1 templated silica thin films significantly helps the films to retain their mesostructural order during extraction.

The second part of this study addresses the optimum condition for surfactant extraction from templated silica thin films. Removal of templated surfactants from the silica structure without damaging the imprinted sites is a vital part of the whole imprinting process. We can remove the surfactants either by calcination or by extraction. We prefer extraction over calcination because during extraction we are less likely to degrade the quality of imprinted sites due to thermally induced rearrangement of the silica network. During extraction we use a hydrochloric acid / ethanol mixture (1:30 by volume) to extract the surfactants. Previously we used overnight extraction the surfactants from bulk samples. However, excess time spent extracting the surfactant is a waste of time and may allow the structure to reorganize. To avoid this, a study was carried out to find the optimal extraction time to remove all of the surfactant templates without hurting the silica structure. From this study we have found 30 minute as our optimum time for extraction of all surfactants without hampering the imprinted silica structure.

B.2. Experimental

Dodecyltrimethylammonium bromide (C₁₂TAB) (technical grade, Acros Organics), n-dodecyl- β -D-glucopyranoside (C12G1) (99+%, Affymetrix) and tetraethyl orthosilicate (TEOS) (98 % reagent grade, Sigma-Aldrich) were used as received. The surfactant templated silica thin films were prepared by using TEOS as the silica precursor, which was first hydrolyzed by mixing it with water, hydrochloric acid and ethanol (mole ratio

TEOS: ethanol: water: HCl = 1:3.8:1:5×10⁻³) and refluxing the mixture for 90 minutes. After that, more hydrochloric acid and water (mole ratio water: HCl = 1:001) were added and the mixture is stirred vigorously for 30 minutes at 50 °C to hydrolyze the remaining precursor. Subsequently, 24 ml of ethanol was added to the sol to dilute it and the required amount of surfactants (total surfactant mass 1.34 gm) were added to this mixture and it was stirred until all of the surfactants were dissolved. The required amount of surfactants was determined by using the ternary diagram of the mixed surfactants with water and replacing the volume of water in that phase with an equivalent volume of silica. Following sol preparation, clean glass slides and silicon wafers were coated by the spin coating technique using a Laurell spin coater. 100 µl of the sol was placed at the center of the substrate and coating was accomplished by spinning at 2200 rpm for 45 sec. We coated a set of glass slides and silicon wafers with the same 10:1 DTAB / C12G1 templated silica sol and then divided it in to two parts. One part of the samples was not treated with ammonia and instead were simply aged at 50 °C at 45% RH for 7 days. The other part of the sample set was treated for 15 h of ammonia vapor treatment and then was aged at 50 °C at 45% RH for 7 days. FT-IR spectra were measured after certain intervals from the coating of the films during the ammonia pre-treatment and these samples were compared with untreated samples.

To find the optimal extraction time, we used C₁₂TAB / C12G1 (10:1) templated silica thin films, and after aging at 50 °C under 45% RH for 7 days, we used a conventional extraction procedure with a hydrochloric acid / ethanol mixture (1:30 by volume), to extract the surfactants. During extraction we removed the samples after certain

intervals, dried them and collected an FT-IR spectrum to check whether all the surfactants were removed, and then placed them back into the extraction solution.

B.3. Results & Discussion

Figure B.1 shows a time evolution study of C₁₂TAB/C12G1 templated silica thin films on silicon wafers with and without 15 h of ammonia vapor treatment using FT-IR. During ammonia treatment, condensation of the silica structure is enhanced considerably compare to untreated samples. This is indicated in Figure B.1 by the increase in peak intensity of the primary Si-O-Si band ($\sim 1068\text{ cm}^{-1}$), a decrease in the peak intensity of the silanol band ($\sim 960\text{ cm}^{-1}$) and a decrease in peak intensity of the hydroxyl stretching band ($\sim 3500\text{-}3000\text{ cm}^{-1}$)²⁰⁸. This indicates that, as expected, the ammonia treatment accelerates the condensation of silicates to form a solid silica network. Figure B.2 shows the XRD pattern of both ammonia pre-treated and without ammonia pretreated C₁₂TAB/C12G1 templated silica thin films after 7 days of aging followed by surfactant extraction. As we see from Figure B.2(a) the sample without ammonia treatment completely loses its long-range order after extraction (an XRD peak was present prior to extraction) due to the collapse of pores, while the ammonia treated sample retains long-range order shown in Fig. 2(b) after extraction due to enhanced stabilization of the structure by the ammonia treatment. This result indicates that 15 h ammonia vapor pretreatment is an effective strategy to stabilize mesostructural order of templated silica thin films by enhancing the rate of condensation of the silica network.

Figure B.3 shows the time evolution FT-IR study of C₁₂TAB / C12G1 (10:1) templated silica thin films during extraction after aging at 50 °C under 45% RH for 7 days. From

Figure B.3 it is clear that all of the surfactants were totally removed from the films after 30 minutes of extraction, which is indicated by the absence of symmetric and asymmetric CH₂ stretching peaks coming from the surfactants ($\sim 2900\text{ cm}^{-1}$)¹²⁸. Also, we see an indication of evolution of the siloxane network, as a shoulder emerges at the high-wavenumber side of the Si-O-Si peak as extraction time proceeds. This shoulder implies that the silica structure is undergoing condensation to form a more mature siloxane network during extraction. To avoid wasted time and the possibility of unwanted side reactions, 30 minutes is selected as the optimal time for extraction to remove all the surfactants without hurting the silica structure.

B.4. Conclusions

Here we first establish a simple effective technique to stabilize mixed surfactant templated silica thin films using ammonia vapor pretreatment before aging the deposited films. The result shows that for C₁₂TAB/C12G1 10:1 templated silica thin films, 15 hours of ammonia pre-treatment before aging at 50 °C at 45% RH for 7 days help the silica structure to retain its mesostructural stability during the surfactant extraction process. During ammonia treatment, ammonia and water adsorb at the silica/surfactant interface increase the effective pH values to enhance the condensation rate and solidify the network. This technique can be used for any surfactant templated thin films where the conventional aging is not sufficient to stabilize the silica network resulting loss in mesostructural order during extraction. We also established 30 minute as an adequate extraction time for the total removal of surfactants from the templated films by using hydrochloric acid / ethanol mixture (1:30 by volume). This optimum extraction time

minimizes the possibility of altering the silica structure during extraction, and should help to keep the imprinted sites intact. These results will help us to prepare stable molecularly imprinted silica thin films for specific carbohydrate adsorption in future.

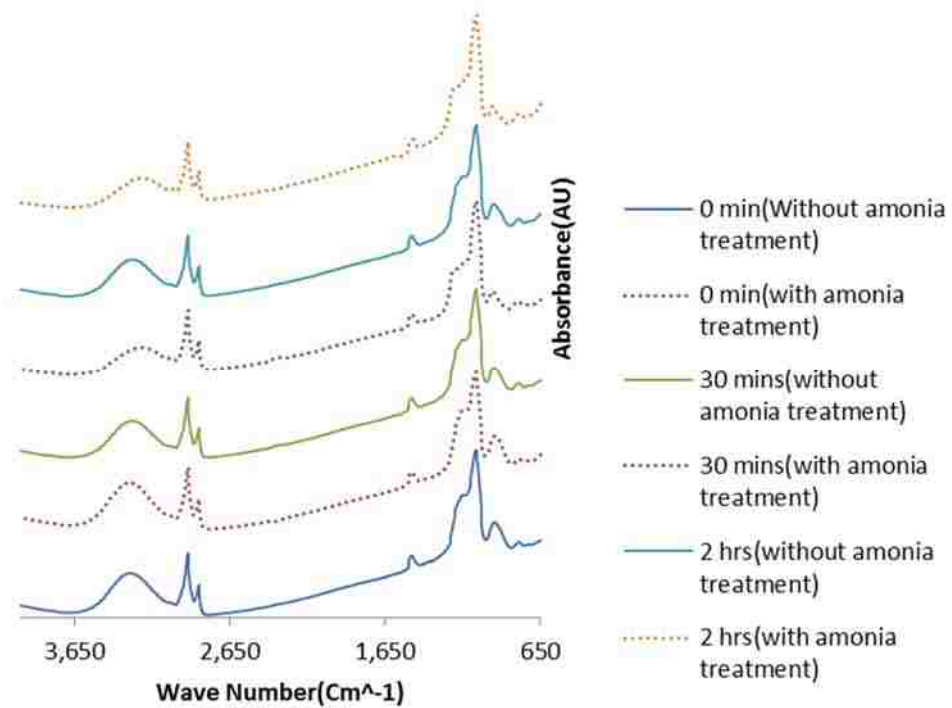


Figure B.1. Evolution of FT-IR absorbance spectra of 10:1 DTAB/ C12G1 templated silica thin films on thin silicon wafers with and without ammonia treatment for 15 h prior to aging at 50° C for 0 min, 30 min, or 2 h.

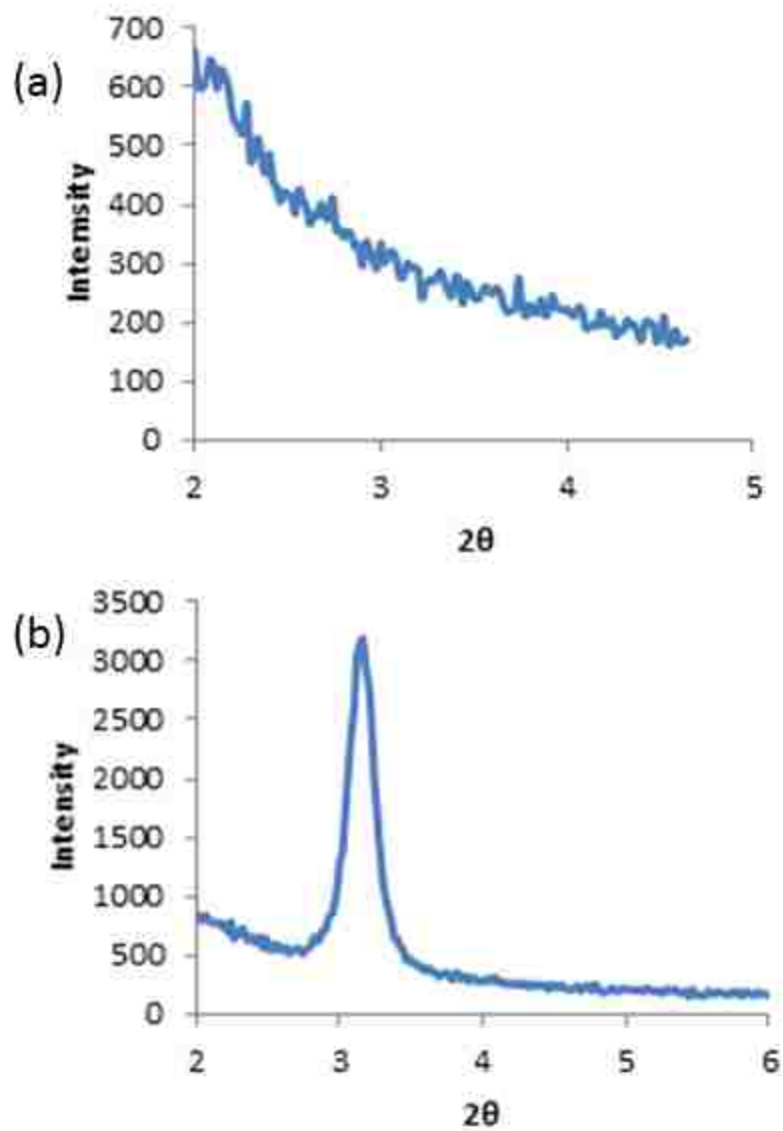


Figure B.2. X-ray diffraction pattern of 10:1 DTAB/C12G1 templated silica thin films after 7 days of aging at 50° C (a) without and (b) with 15 h of ammonia vapor pretreatment.

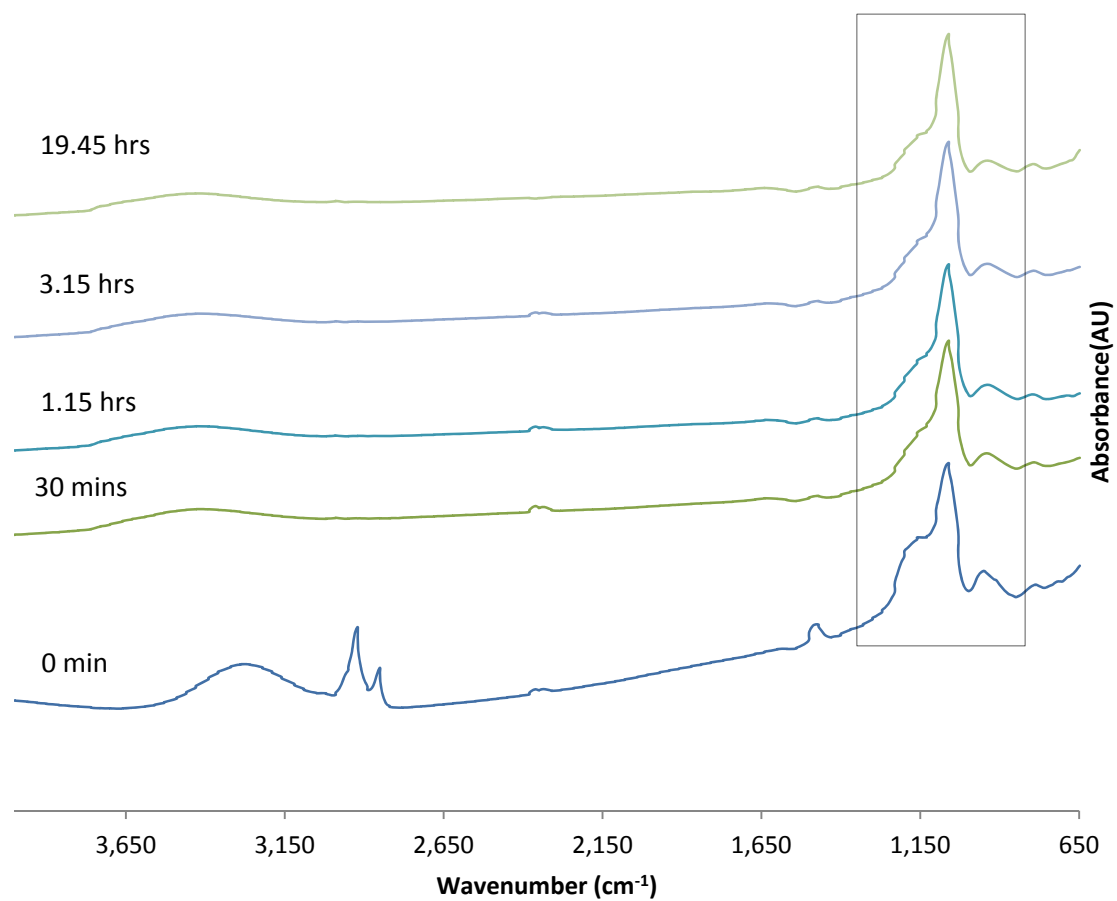


Figure B.3. Evolution of DTAB/C12G1 templated silica thin films during extraction at room temperature (20° C).

APPENDIX C

Supplemental Information of Chapter 3

Methods for Surfactant Structure Determination and NMR

The molecular structures of C₁₆TAB and both carbohydrate surfactants (Figure 3.1 in the chapter 3) were determined by geometry optimization using the PM3 semiempirical molecular orbital method⁴⁴² as implemented in the program Avogadro⁴⁴³.

NMR experiments were conducted using a 400 MHz or 600 MHz Varian Inova NMR spectrometer at a fixed temperature of 50 °C maintained by a variable temperature (VT) controller. One-dimensional ¹H NMR spectra were acquired using the Varian *s2pul* pulse sequence with 32 scans and 3 sec delay (*d*₁) between pulse sequences for each sample. The peaks in the ¹H NMR spectra (Figure 3.1 in the chapter 3) were assigned using gradient double quantum filtered correlation spectroscopy^{444, 445} (gDQFCOSY) (Figures C.1-C.2) and gradient heteronuclear single quantum coherence⁴⁴⁶ (gHSQC) experiments (Figures C.3-C.4). Spin-lattice relaxation (*T*₁) measurements were performed using the INVREC (inversion recovery) pulse sequence with 15 sec delay (*d*₁) between pulse sequences. Spin-spin relaxation (*T*₂) measurements were performed using the CPMGT2 (Carr-Purcell-Meiboom-Gill^{289, 290}) pulse sequence with a 40 sec delay (*d*₁) between pulse sequences. Nuclear Overhauser effect spectroscopy (NOESY) was performed using standard NOESY pulse sequence with 'Z' filter²⁹¹ (to remove artifacts due to through bond magnetization transfer mechanism). Unless otherwise indicated, a mixing time of 600 ms was chosen by matching with the shortest *T*₁ value among all protons and then varied to match the longest *T*₁ value in order to observe every possible NOE correlation.

A delay of 3 sec (d_1) between pulse sequences and, for 2D spectra, a resolution of 512×512 pixels were chosen. Fitting to determine T_2 parameters in some experiments was done using Sigma Plot 11. A 3D NOESY- ^{13}C -H3QC experiment for the C8G1 / C₁₆TAB system was performed using the gnoesyChsqc pulse sequence^{447, 448} with 600 ms mixing time and 2 sec delay (d_1)

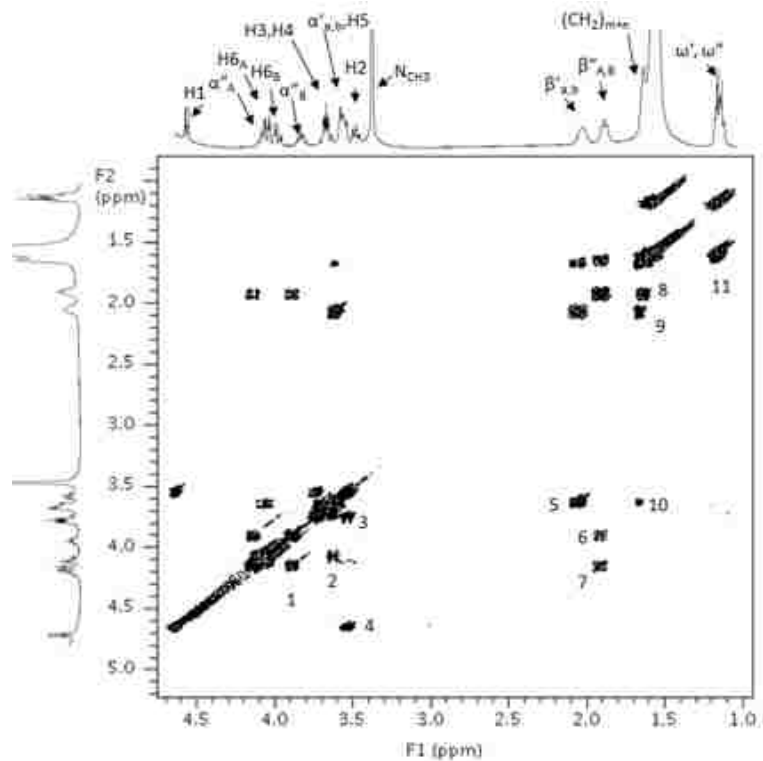


Figure C.1. COSY spectrum of 1:1 $C_{16}TAB/C8G1$ in D_2O at 50 °C (total surfactant concentration 30 mM). The experiment was done using the gDQCOSY (gradient-enhanced double quantum filtered COSY) pulse sequence with a 6 sec relaxation time (d_1) and a resolution of 576×576 pixels. COSY is a homonuclear correlation technique based on magnetization transfer through bonds and correlates protons that are at most 3 to 4 bonds apart. The cross peaks represent the correlations between the associated protons and is symmetric along the diagonal. Several cross peaks (cross peak 1: α''_B and α''_A ; cross peak 2: H3/H4 and H6_B; cross peak 3: H2 and H3/H4; cross peak 4: H2 and H1; cross peak 5: $\alpha'_{a,b}$ and $\beta'_{a,b}$; cross peak 6: α''_B and $\beta''_{A,B}$; cross peak 7: α''_A and $\beta''_{A,B}$; cross peak 8: $\beta''_{A,B}$ and $(CH_2)_m$; cross peak 9: $\beta'_{a,b}$ and $(CH_2)_n$; cross peak 10: $\alpha'_{a,b}$ and $(CH_2)_n$; cross peak 11: ω'/ω'' and $(CH_2)_n/(CH_2)_m$) are present in the spectrum representing the correlated protons, and were used for peak assignment.

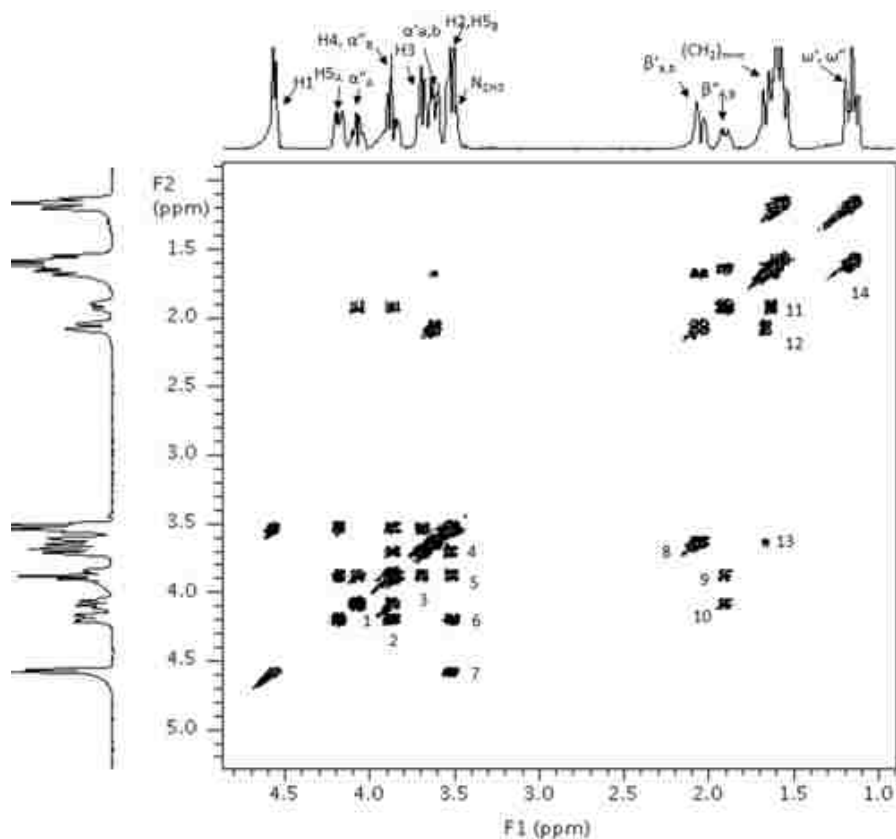


Figure C.2. COSY spectrum of 1:1 $C_{16}TAB/C8X1$ in D_2O at $50\text{ }^\circ C$ (total surfactant concentration 30 mM). The cross peaks represent the correlations between the associated protons and is symmetric along the diagonal. Several cross peaks (cross peak 1: α''_A and α''_B ; cross peak 2: $H4$ and $H5_A$; cross peak 3: $H3$ and $H4$; cross peak 4: $H3$ and $H2/H5_B$; cross peak 5: $H4$ and $H2/H5_B$; cross peak 6: $H5_A$ and $H5_B$; cross peak 7: $H1$ and $H2$; cross peak 8: $\alpha'_{a,b}$ and $\beta'_{a,b}$; cross peak 9: α''_B and $\beta''_{A,B}$; cross peak 10: α''_A and $\beta''_{A,B}$; cross peak 11: $\beta''_{A,B}$ and $(CH_2)_m$; cross peak 12: $\beta'_{a,b}$ and $(CH_2)_n$; cross peak 13: $\alpha'_{a,b}$ and $(CH_2)_n$ and cross peak 14: ω'/ω'' and $(CH_2)_n/(CH_2)_m$) are present in the spectrum representing the correlated protons, and were used for peak assignment.

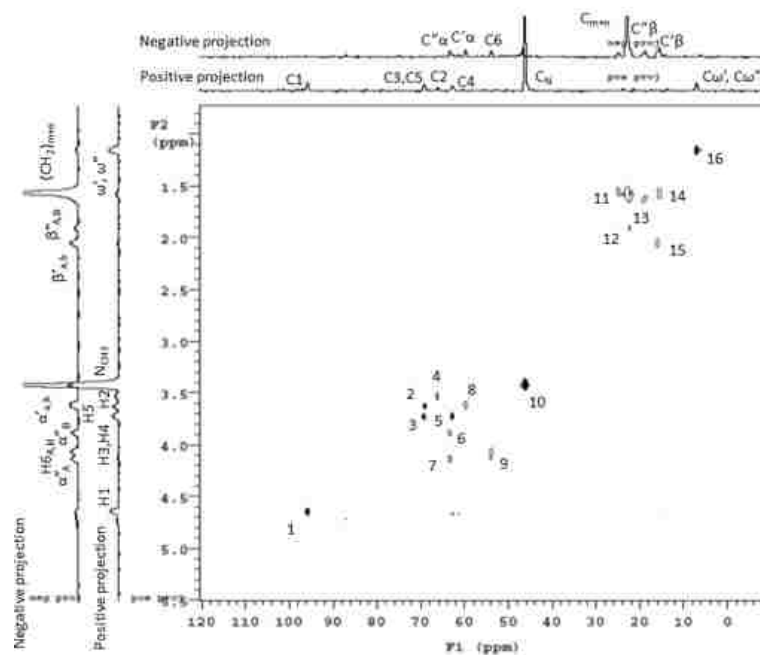


Figure C.3. HSQC spectrum of 1:1 C₁₆TAB/C8G1 in D₂O at 50 °C (total surfactant concentration 30 mM). There are two type of correlations shown in the spectrum. Those with dark spots indicate the correlation of carbon that are directly attached to an odd number of proton(s) (called positive correlation). The other correlation presented by white spots indicates carbons that are directly attached to an even number of protons (i.e. negative correlation). Peaks are assigned based on these correlations and are consistent with the COSY spectrum. There are several correlations (cross peak 1: C₁-H₁; cross peak 2: C₅-H₅; cross peak 3: C₃-H₃; cross peak 4: C₂-H₂; cross peak 5: C₄-H₄; cross peak 6: C''α-α''_B; cross peak 7: C''α-α''_A; cross peak 8: C'α-α'_{a,b}; cross peak 9: C₆-H_{6A,B}; cross peak 10: C_N-N_{CH3}; cross peak 11: C_{m+n}-(CH₂)_{m+n}; cross peak 12: C''β-β''_{A,B}; cross peak 13: C_{m+n}-(CH₂)_{m+n}; cross peak 14: C_{m+n}-(CH₂)_{m+n}; cross peak 15: C'β-β'_{a,b} and cross peak 16: C'ω-ω' and C''ω-ω'') shown in the spectrum helping to allow exact peak assignment.

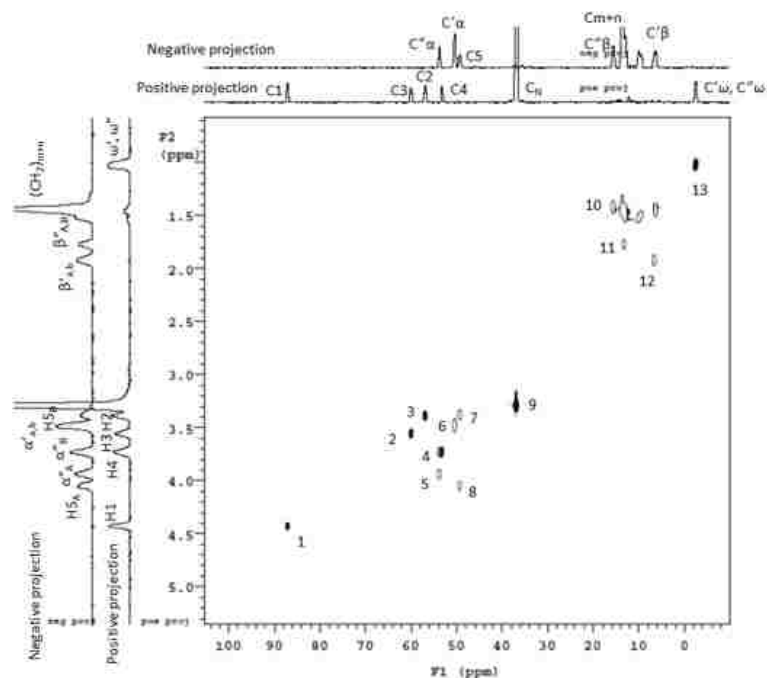


Figure C.4. HSQC spectrum of 1:1 C₁₆TAB/C8X1 in D₂O at 50 °C (total surfactant concentration 30 mM). There are two type of correlations shown in the spectrum. Those with dark spots indicate the correlation of carbon that are directly attached to an odd number of proton(s) (called positive correlation). The other correlation presented by white spots indicates carbons that are directly attached to an even number of protons (i.e. negative correlation). Peaks are assigned based on these correlations and are consistent with the COSY spectrum. There are several correlations (cross peak 1: C1-H1; cross peak 2: C3-H3; cross peak 3: C2-H2; cross peak 4: C4-H4; cross peak and C'' α - α '_B; cross peak 5: C'' α - α '_A; cross peak 6: C' α - α '_{a,b}; cross peak 7: C5-H5_B; cross peak 8: C5-H5_A; cross peak 9: C_N-N_{CH3}; cross peak 10: C_{m+n}-(CH₂)_{m+n}; cross peak 11: C'' β - β '_{A,B}; cross peak 12: C' β - β '_{a,b} and cross peak 13: C' ω - ω ' and C'' ω - ω '') shown in the spectrum helping to exact peak assignment.

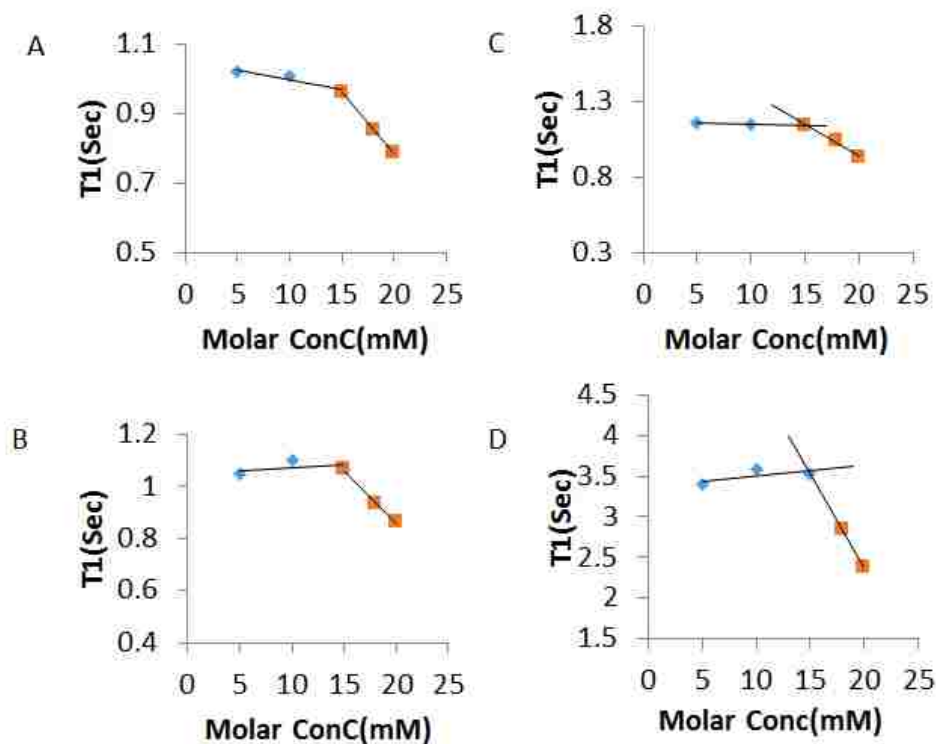


Figure C.5. Determination of critical micelle concentration (cmc) using T_1 (spin-lattice) relaxation time at 50 °C of the (A) H_4/α''_B proton (B) α''_A proton (C) $\beta''_{A,B}$ protons and (D) ω'' proton of C8X1 plotted against the molar concentration of C8X1 (dissolved in D_2O). When the surfactants are dispersed as monomers in the solution they undergo rapid tumbling resulting in longer T_1 values (very fast tumbling has only a relatively small relaxation component at the Larmor frequency resulting in a large T_1) whereas in the micelle the molecules tumble with a longer collective correlation time. The point of inflection in these plots indicates the cmc (critical micelle concentration) value of that surfactant. From the above plots it can be concluded that the cmc value for C8X1 is 15 mM at 50 °C.

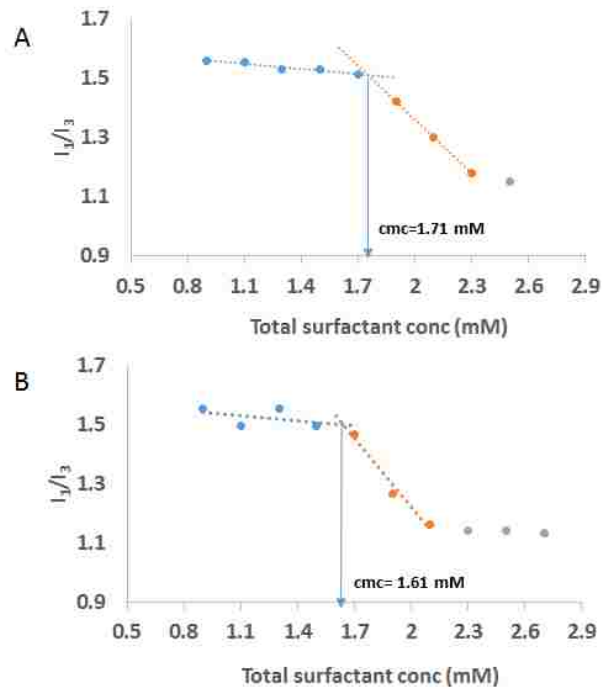


Figure C.6. The ratio of two pyrene fluorescence emission bands appearing at 374 nm (I_2) and 387 nm (I_3) vs. total surfactant concentration for (A) C₁₆TAB/C8G1 and (B) C₁₆TAB/C8X1 at 50 °C. In both cases a 1:1 overall ratio of surfactants was used. Arrows denote the mixed cmc values. This ratio is a measure of polarity near pyrene, where a lower value indicates a less polar microenvironment. The break point in each plot is considered to be the cmc of the mixture, which is 1.71 mM and 1.61 mM for C₁₆TAB/C8G1 and C₁₆TAB/C8X1 respectively.

Analysis of Mixed Micelles based on Regular Solution Theory

At the cmc, the mole fraction of each surfactant in mixed micelles and the interaction parameter (β) can be calculated using Rubingh's implementation of regular solution theory (RST) ⁶⁸. This analysis begins by solving Eq. (C1) for X_1 (the mole fraction of C₁₆TAB in the mixed micelle at the cmc) and then using this value to calculate β using Eq. (C2):

$$\frac{X_1^2 \ln\left(\frac{\alpha_1 cmc}{X_1 cmc_1}\right)}{(1-X_1)^2 \ln\left(\frac{(1-\alpha_1)cmc}{(1-X_1)cmc_2}\right)} = 1 \quad (C1)$$

$$\beta = \frac{\ln\left(\frac{\alpha_1 cmc}{X_1 cmc_1}\right)}{(1-X_1)^2} \quad (C2)$$

where α_1 = mole fraction of C₁₆TAB in overall solution, cmc_1 = critical micelle concentration of C₁₆TAB, cmc_2 = critical micelle concentration of the sugar surfactant and cmc = critical micelle concentration of the C₁₆TAB/sugar surfactant mixture.

The mole fraction of individual surfactants in mixed micelles *above the cmc* can be calculated by solving nonlinear Eq. (C3) based on an expansion of Clint's mixed micelle model using RST ¹²⁸:

$$X_1^2 (e^{(\beta X_1^2)} cmc_2 - e^{(\beta(1-X_1)^2)} cmc_1) + X_1 (c + e^{(\beta(1-X_1)^2)} cmc_1 - e^{(\beta X_1^2)} cmc_2) - \alpha_1 c = 0 \quad (C3)$$

where c = the total surfactant concentration and all other variables are defined above.

Results of this and other analyses are summarized in Table C.1.

Table C.1. Values of mixed critical micelle concentration (cmc) from pyrene solvatochromism, overall mole fraction of C₁₆TAB (α_1) in mixed solution, mole fraction of C₁₆TAB (X_1) in mixed micelle at cmc and at 30 mM total surfactant concentration, interaction parameter (β) and aggregation number (N_{agg}) from pyrene quenching and hydrodynamic radius (R_h) from DLS measurement for C₁₆TAB/C8G1 and C₁₆TAB/C8X1 mixtures with (Mean \pm SD)

Surfactants	cmc (mM)	α_1	X_1 (at cmc)	X_1 (at 30 mM)	β	N_{agg}	R_h (nm)
C ₁₆ TAB/C8G1	1.71	0.5	0.96	0.58	-2.6	42	0.4 \pm 0.07
C ₁₆ TAB/C8X1	1.61	0.5	0.90	0.58	-0.86	48	0.41 \pm 0.11

Aggregation Number Measurements

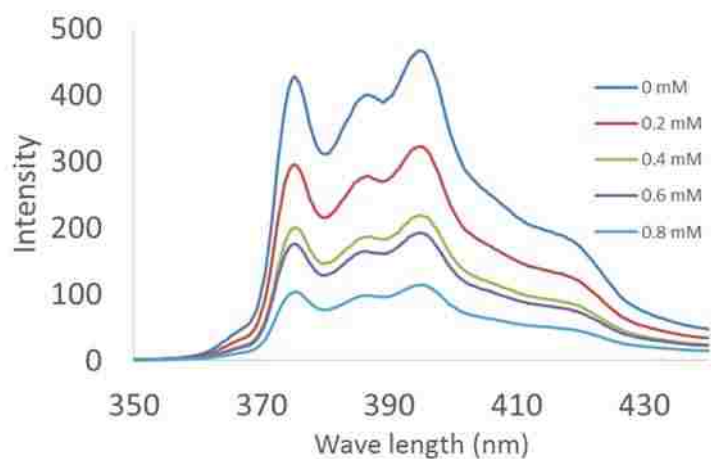


Figure C.7. Fluorescence emission spectra of pyrene in C₁₆TAB/C8X1 1:1 mixture in water at different hexadecylpyridinium chloride quencher concentrations.

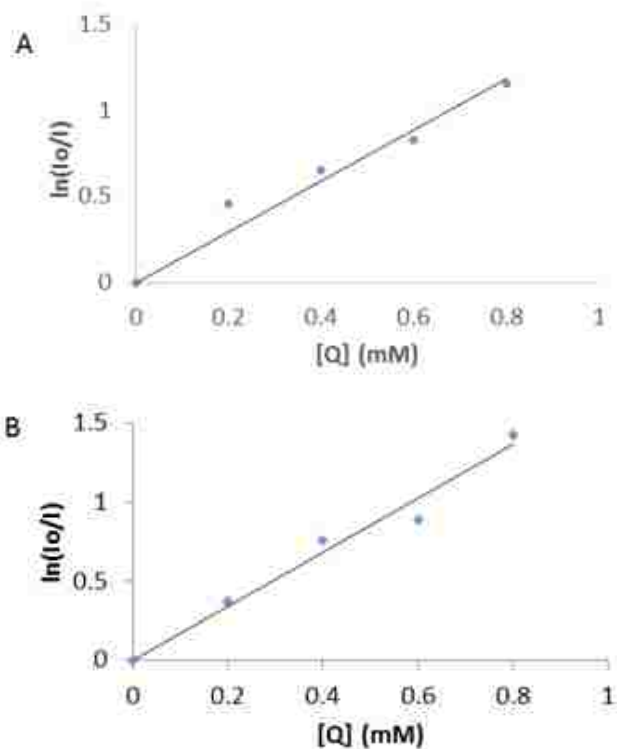


Figure C.8. Determination of aggregation number: Linear fitting of $\ln(I_0/I)$ Vs $[Q]$ for (A) $C_{16}TAB/C8G1$ and (B) $C_{16}TAB/C8X1$ 1:1 mixture at 50 °C. $[Q]$ is the quencher concentration which was varied from 0 mM to 0.8 mM. The R^2 values for linear fitting of $C_{16}TAB/C8G1$ and $C_{16}TAB/C8X1$ were 0.96 and 0.98 respectively. The mean aggregation number was calculated using Eq. (C4) ²⁰⁵:

$$\ln\left(\frac{I}{I_0}\right) = -\frac{(N_{agg}[Q])}{(c-cmc)} \quad (C4)$$

where I = fluorescence intensity in the presence of quencher, I_0 = fluorescence intensity in the absence of quencher, $[Q]$ = concentration of quencher, and c = total surfactant concentration.

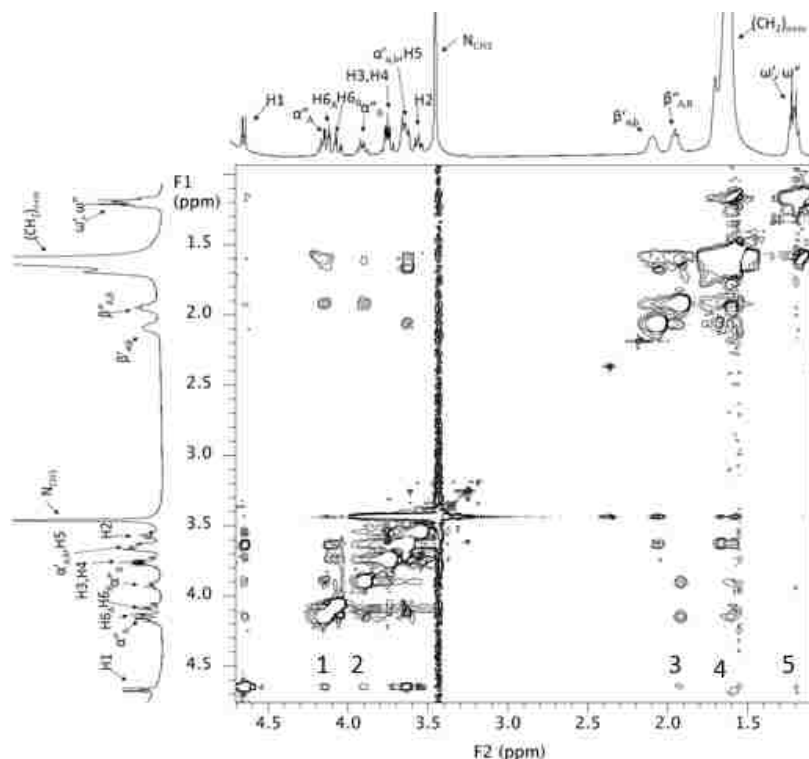


Figure C.9. 2D NOESY spectrum of 1:1 C₁₆TAB/C8G1 in D₂O at 50 °C (total surfactant concentration 30 mM) using 1000 ms mixing time. Here NOE mixing time 1000 ms was used which is in the order of the T₁ relaxation value of H1 proton of C8G1. Here we can observe several extra NOE correlations between the H1 protons of C8G1 and the alkyl tails of C₁₆TAB/C8G1 which were not present in NOESY with 600 ms mixing time. Cross peak 1 correlates H1 & α^A protons of C8G1, cross peak 2 correlates H1 & α^B, cross peak 3 correlates H1 & β protons of C8G1, cross peak 4 correlates H1 & rest of the alkyl chain (after β position) of C₁₆TAB or C8G1 and cross peak 5 correlates H1 & ω protons of C₁₆TAB or C8G1. Other NOESY experiments were also done to accumulate the whole range but did not give other new NOEs apart from those already mentioned. All these cross peaks between the sugar head group protons and the tails indicate the position of the sugar head group near the core of the mixed micelle.

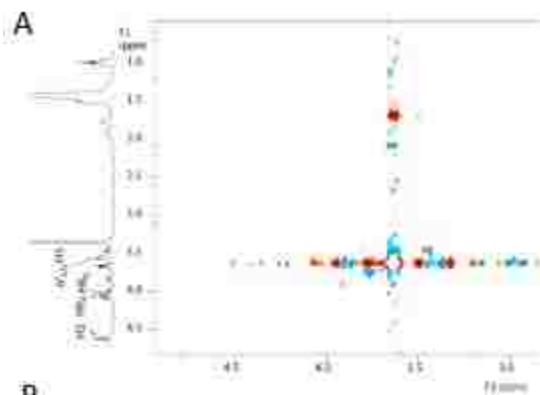


Figure C.10. 3D NOESY-¹³C-HsQc spectrum of 1:1 C₁₆TAB/C8G1 in D₂O at 50 °C (total surfactant concentration 30 mM). Depicted is the ¹H-¹H NOESY plane selected using ¹³C of the α carbon of C₁₆TAB. Besides a strong diagonal peak, no cross peak could be served with confidence below the targeted peak (α' _{a,b} protons of C₁₆TAB, denoted as red peak) indicates no NOE correlations between the α' _{a,b} proton of C₁₆TAB and sugar head group protons.

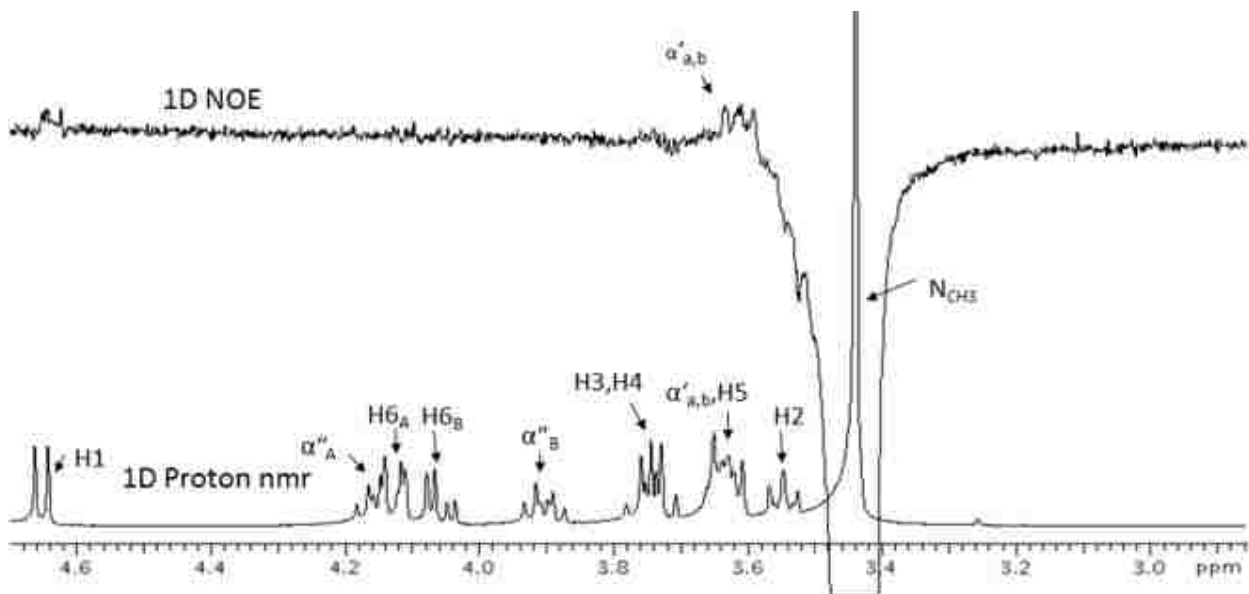


Figure C.11. 1D NOE spectrum of 1:1 C₁₆TAB/C8G1 in D₂O at 50 °C (total surfactant concentration 30 mM). Experiment was done using cyclenoe pluse sequence with the following parameters: d₁ (relaxation delay) = 6 sec; nt (number of transient) = 32; np (number of points) = 8192; satpwr (saturation power)=-16; sattime (saturation time)= 4sec and MixN (mixing time)=600 ms. In this spectrum radiation had been done from N_{CH3} protons of C₁₆TAB head group. The spectrum resulting from off-resonance saturation is subtracted from the one obtained with saturation of N_{CH3} to yield a difference spectrum in which only resonances affected by cross-relaxation with N_{CH3} appear. By comparing the subtracted spectrum (upper part of the figure) with the 1D proton nmr (lower part of the figure) the only correlation that is seen with the N_{CH3} protons is the α protons of C₁₆TAB. There is no correlation with the sugar headgroup protons were found (a small peak like hump pops up at H1 position but this only because of some unavoidable residue after subtraction due to improper baseline).

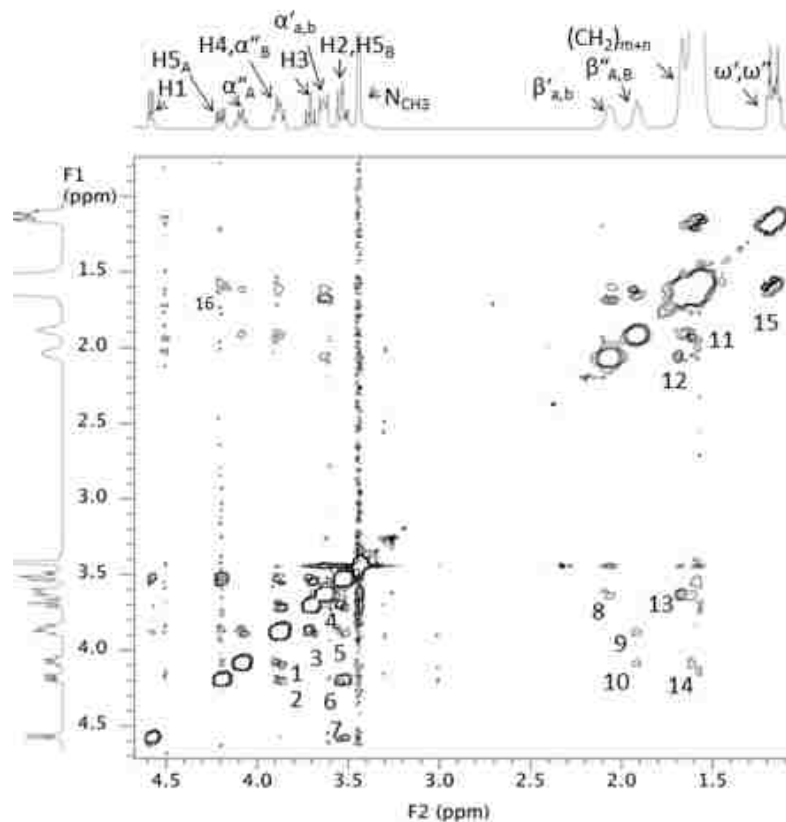


Figure C.12. 2D NOESY spectrum of 1:1 $C_{16}TAB/C8X1$ in D_2O at $50\text{ }^\circ C$ (total surfactant concentration 30 mM). Cross peaks indicate the NOE correlations between the associated protons and are symmetric along the diagonal. The spectrum indicates several sugar-sugar or cationic-cationic surfactant NOE correlations (cross peak 1) $H4/\alpha''_B$ & α''_A proton; 2) $H4/\alpha''_B$ & $H5_A$ proton; 3) $H3$ & $H4/\alpha''_B$ proton; 4) $H2/H5_B$ & $H3$ proton; 5) $H2/H5_B$ & $H4/\alpha''_B$; 6) $H2/H5_B$ & $H5_A$ proton; 7) $H2/H5_B$ & $H1$ proton; 8) $\alpha'_{a,b}$ & $\beta'_{a,b}$; 9) $H4/\alpha''_B$ & $\beta''_{A,B}$; 10) α''_A & $\beta''_{A,B}$; 11) $\beta''_{A,B}$ & $(CH_2)_{m+n}$; 12) $\beta'_{a,b}$ & $(CH_2)_{m+n}$; 13) $\alpha'_{a,b}$ & $(CH_2)_{m+n}$; 14) α''_A & $(CH_2)_{m+n}$; 15) $(CH_2)_{m+n}$ & ω'/ω'' . Cross peak 16 may correlate the $H5_A$ proton of $C8X1$ with alkyl chain of $C_{16}TAB/C8X1$ but is ambiguous due to the absence of symmetry across the diagonal. No specific sugar-cationic correlations are found in this pattern.

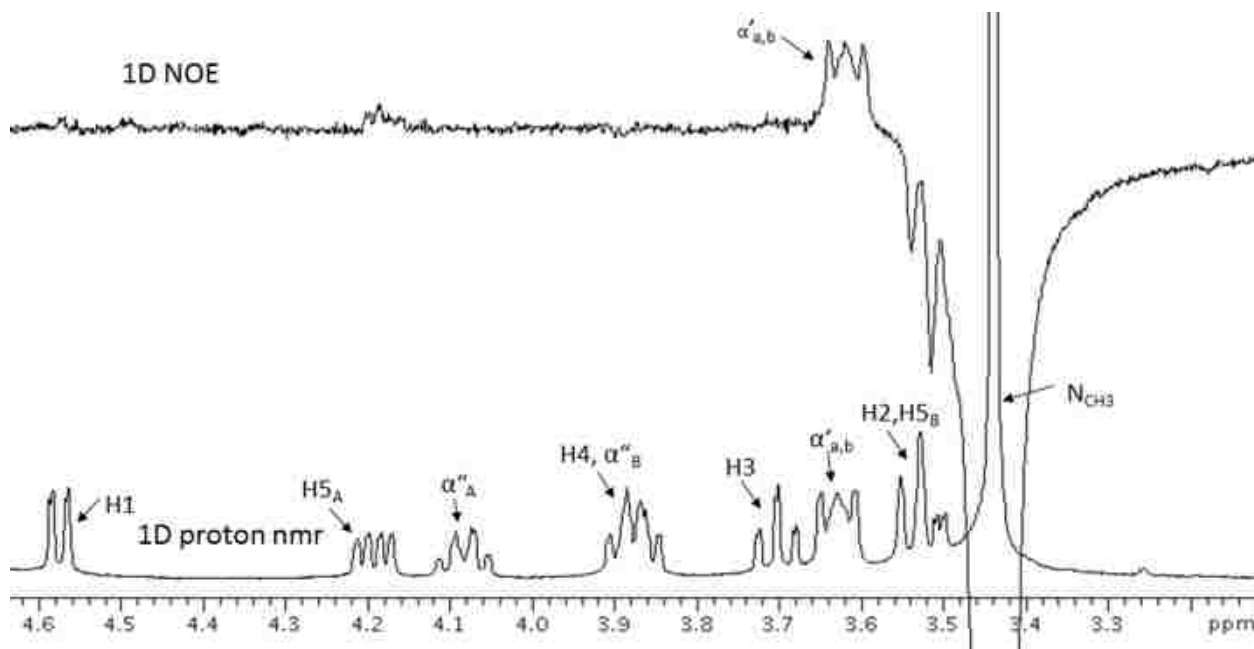


Figure C.13. 1D NOE spectrum of 1:1 C₁₆TAB/C8X1 in D₂O at 50 °C (total surfactant concentration 30 mM). Experiment was done using cyclenoe pulse sequence with the following parameters: d_1 (relaxation delay) = 6 sec; nt (number of transient) = 32; np (number of points) = 8192; $satpwr$ (saturation power) = -16; $sattime$ (saturation time) = 4sec and $MixN$ (mixing time) = 600 ms. In this spectrum radiation had been done from N_{CH₃} protons of C₁₆TAB head group. In cyclenoe every radiated spectrum is subtracted from reference spectrum so that only the peak that has noe correlation with the radiated peak remains and other peaks are subtracted out. By comparing the subtracted spectrum (upper part of the figure) with the 1D proton NMR (lower part of the figure) the only correlation that is seen with the N_{CH₃} protons is the α protons of C₁₆TAB. There is no correlation with the sugar headgroup protons were found (a small peak like hump pops up at H5_A position but this only because of some unavoidable residue after subtraction due to improper baseline).

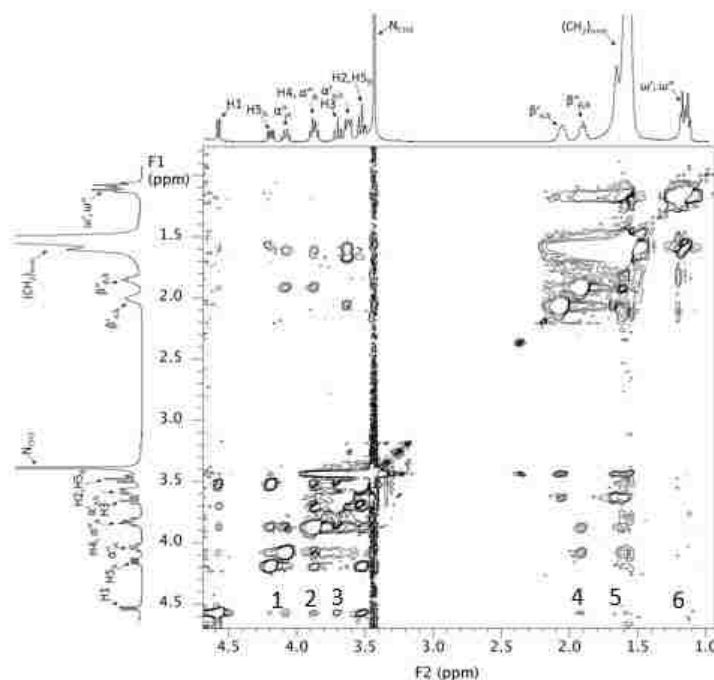


Figure C.14. 2D NOESY spectrum of 1:1 C₁₆TAB/C8X1 in D₂O at 50 °C (total surfactant concentration 30 mM) using 1000 ms mixing time. Here NOE mixing time 1000 ms was used which is in the order of the T₁ relaxation value of H1 proton of C8X1. Here we can observed several extra NOE correlations between the H1 protons of C8X1 and the alkyl tails of C₁₆TAB/C8X1 those were previously not present in NOESY with 600 ms mixing time. Cross peak 1 correlates H1 & α_A protons of C8X1, cross peak 2 correlates H1 & α_B protons of C8X1, cross peak 3 correlates H1 & H3 protons, cross peak 4 correlates H1 & β protons of C8X1, cross peak 5 correlates H1 & rest of the alkyl chain (after β position) of C₁₆TAB or C8X1 and cross peak 6 correlates H1 & ω protons of C₁₆TAB or C8X1. Other NOESY experiments were also done to accumulate the whole range but did not give other new NOEs apart from the already mentioned. All these extra cross peaks between the sugar head group protons and the tails indicate the position of the sugar head group near the core of the mixed micelle.

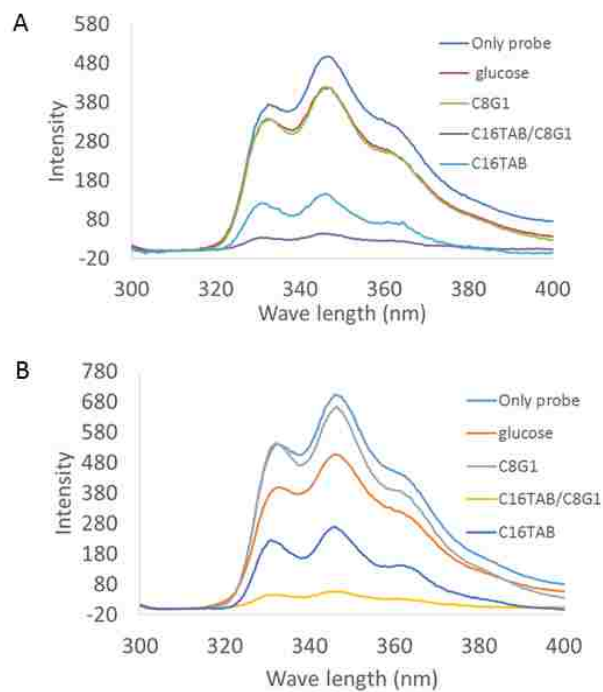


Figure C.15. Fluorescence emission spectra of 2-Naphthylboronic acid (A) probe concentration $6.7 \cdot 10^{-3}$ mM (B) probe concentration $10.05 \cdot 10^{-3}$ mM in glucose and different surfactant solution. Total surfactant or glucose concentration was fixed to 30 mM. For both the cases quenching in $C_{16}TAB/C8G1$ mixture is higher compare to individual $C_{16}TAB$ and $C8G1$ solutions. This enhancement of quenching is due to the inverted carbohydrate micelle configuration where sugar heads groups are near the core of the mixed micelle and able to quench the probe more effectively.

Table C.2. Comparison of T_1 and T_2 values of headgroup protons in C_{16} TAB/C8G1 and C_{16} TAB/C8X1 mixed micellar systems.

Surfactants	Protons	T_1 (ms)*	T_2 (ms)*	T_2/T_1
C_{16} TAB/C8G1	H6 _A	646±8	76±10	0.118±.016
C_{16} TAB/C8X1	H5 _A	695±18	11±4	0.016±.006
C_{16} TAB/C8G1	H1	1010±40	27±6	0.027±.006
C_{16} TAB/C8X1	H1	1110±40	17±4	0.015±.003
C_{16} TAB/C8G1	H3,H4	1590±28	140±22	0.088±.013
C_{16} TAB/C8X1	H3	1730±30	110±20	0.065±.011

*Intervals are ± the 95% confidence interval calculated using the standard error for the parameter.

APPENDIX D

Supplemental Information of Chapter 4

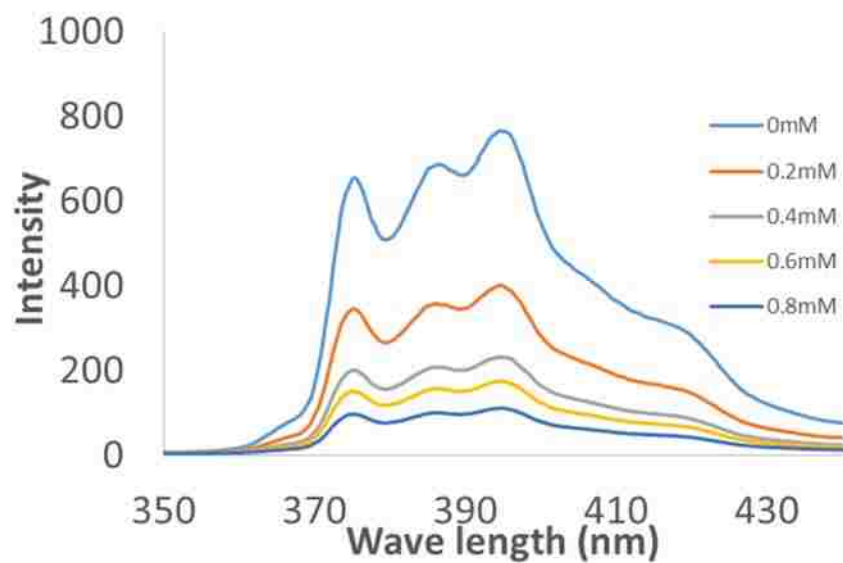


Figure D.1. Fluorescence emission spectra of pyrene in DeTAB/C12G1 1:1 mixture in water at different hexadecylpyridinium chloride quencher concentrations.

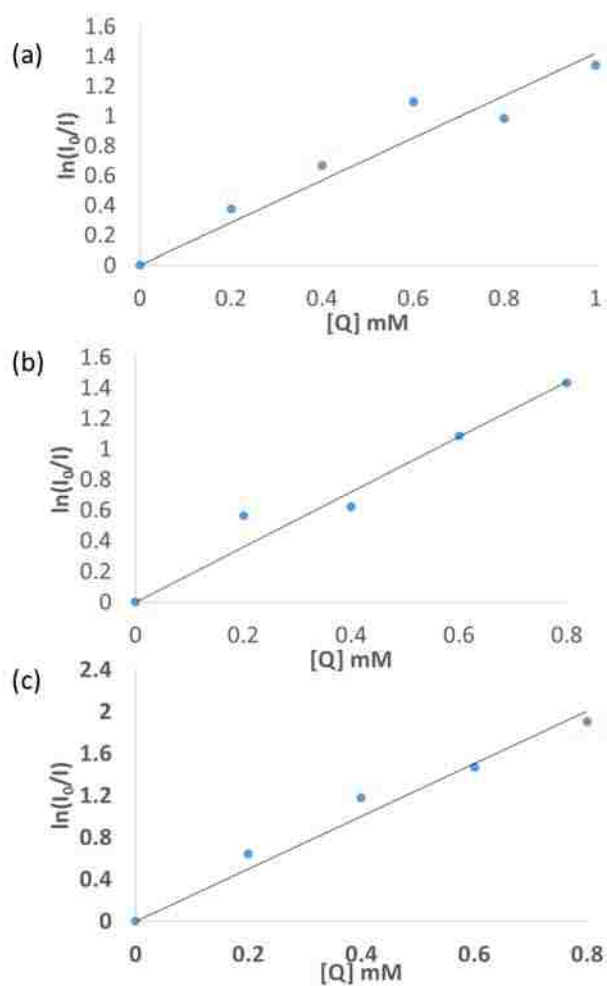


Figure D.2. Determination of aggregation number: Linear fitting of $\ln(I_0/I)$ Vs $[Q]$ for (a) $C_{16}TAB/C12G1$ and (b) $DTAB/C12G1$ and (c) $DeTAB/C12G1$ 1:1 mixture at 50 °C. Where I_0 and I are the fluorescence intensities in the absence and presence of the quencher respectively. $[Q]$ is the quencher concentration which was varied from 0 mM to 0.8 mM. The R_{square} values for linear fitting of $C_{16}TAB/C8G1$, $DTAB/C12G1$ and $DeTAB/C12G1$ were 0.92, 0.96 and 0.97 respectively.

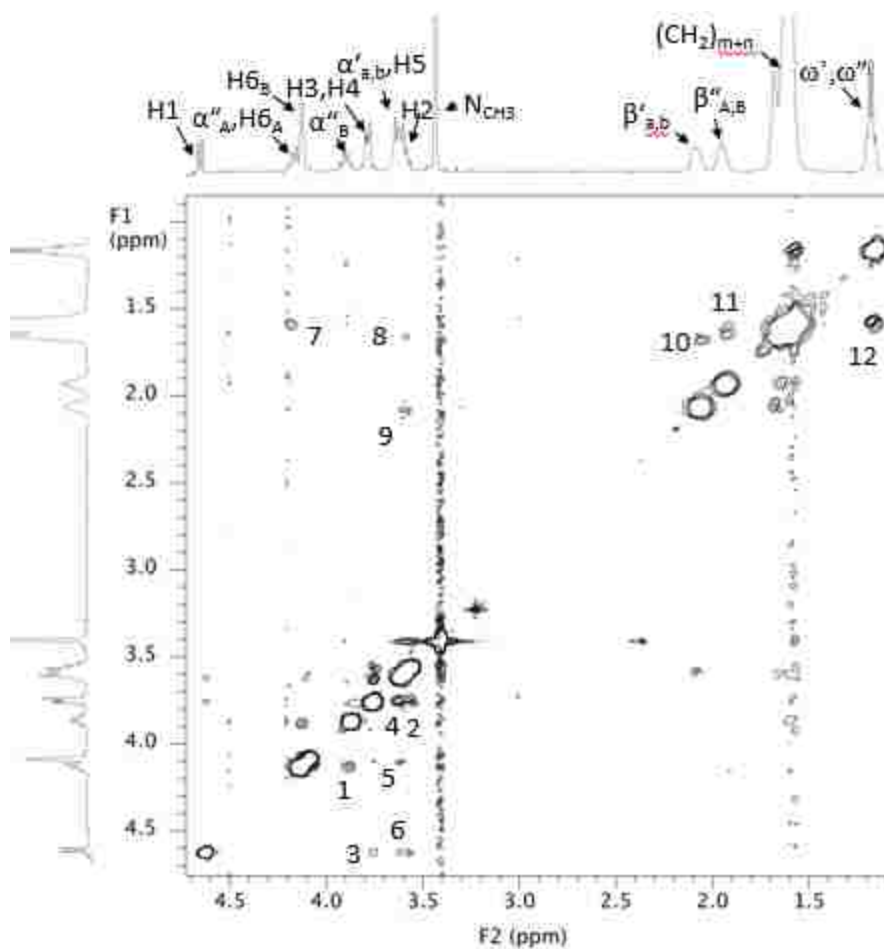


Figure D.3. 2D NOESY spectrum of 1:1 DTAB/C12G1 in D₂O at 50 °C (total surfactant concentration 30 mM). Cross peaks indicate the NOE correlations between the associated protons and are symmetric along the diagonal. The spectrum indicates several sugar-sugar or cationic-cationic surfactant NOE correlations (cross peak 1) $\alpha''_A/H6_A$ & α''_B proton; 2) H2 & H3/H4 proton; 3) H1 & H3/H4 proton; 4) H3/H4 & $\alpha'_{a,b}/H5$ proton; 5) H6_B & $\alpha'_{a,b}/H5$ proton; 6) H1 & $\alpha'_{a,b}/H5$ proton; 7) $\alpha''_A/H6_A$ & (CH₂)_{m+n} proton; 8) $\alpha'_{a,b}/H5$ & (CH₂)_{m+n} proton; 9) $\alpha'_{a,b}/H5$ & $\beta'_{a,b}$ proton; 10) $\beta'_{a,b}$ & (CH₂)_{m+n} proton; 11) $\beta''_{A,B}$ & (CH₂)_{m+n} proton and 12) ω'/ω'' & (CH₂)_{m+n} proton).

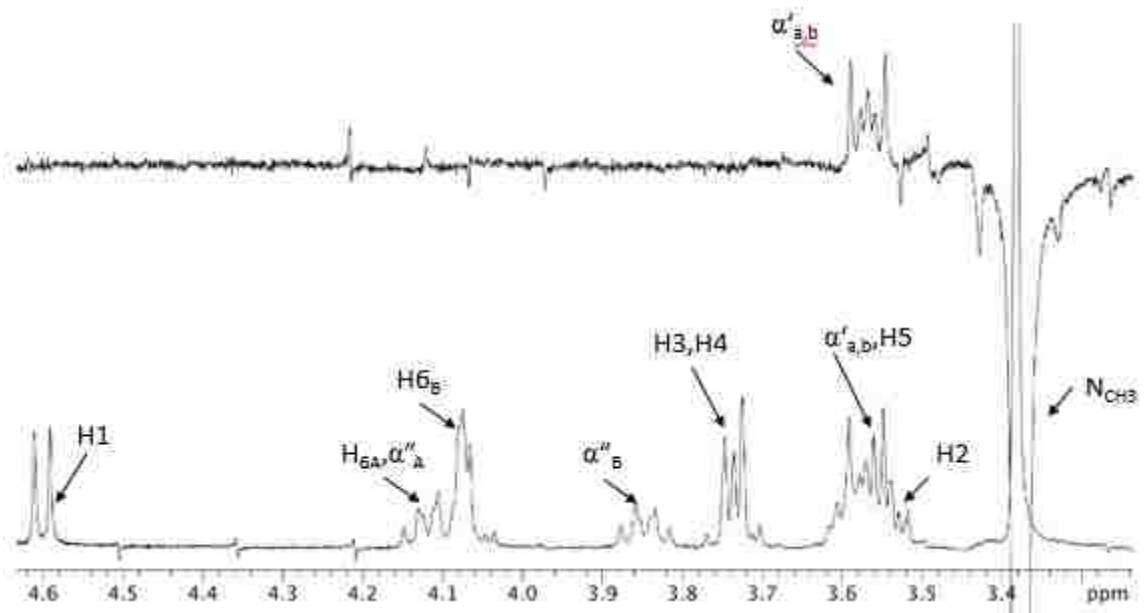


Figure D.4. 1D NOE spectrum of 1:1 DTAB/C12G1 in D₂O at 50 °C (total surfactant concentration 30 mM). Experiment was done using cyclenoe pluse sequence with the following parameters: d_1 (relaxation delay) = 6 sec; nt (number of transient) = 32; np (number of points) = 8192; satpwr (saturation power) = -16; sattime (saturation time) = 4sec and MixN (mixing time) = 600 ms. In this spectrum radiation had been done from N_{CH₃} protons of DTAB head group. In cyclenoe every radiated spectrum is subtracted from reference spectrum so that only the peak that has noe correlation with the radiated peak remains and other peaks are subtracted out. By comparing the subtracted spectrum (upper part of the figure) with the 1D proton nmr (lower part of the figure) the only correlation that is seen with the N_{CH₃} protons is the α protons of DTAB. There is no correlation with the sugar headgroup protons were found.

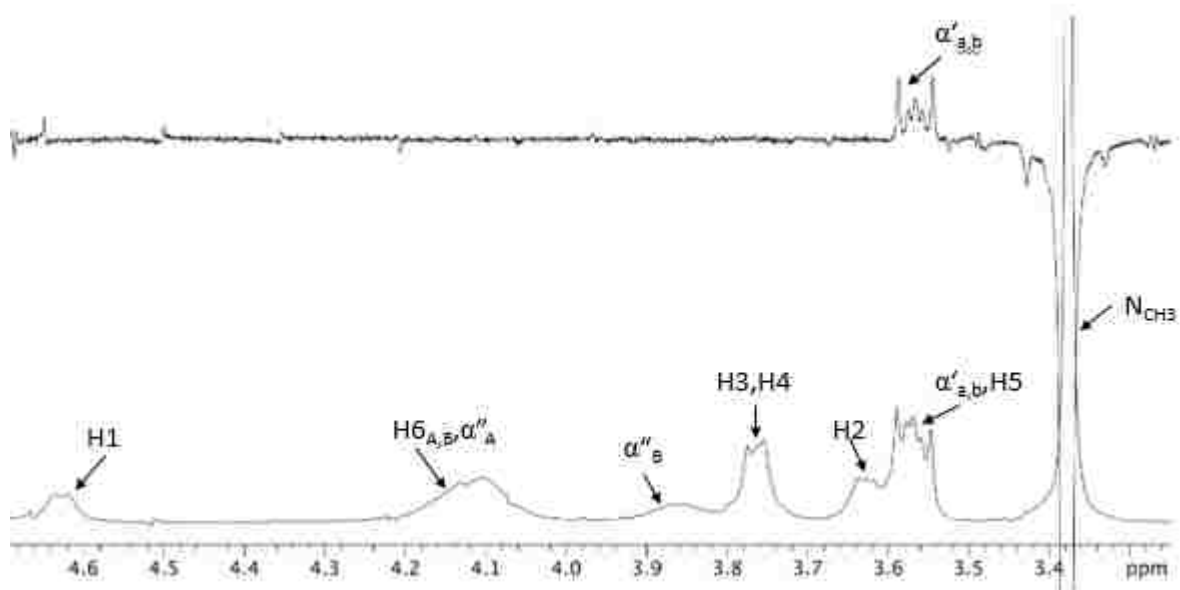


Figure D.5. 1D NOE spectrum of 1:1 DeTAB/C12G1 in D₂O at 50 °C (total surfactant concentration 30 mM). Experiment was done using cyclenoe pluse sequence with the following parameters: d_1 (relaxation delay) = 6 sec; nt (number of transient) = 32; np (number of points) = 8192; satpwr (saturation power) = -16; sattime (saturation time) = 4sec and MixN (mixing time) = 600 ms. In this spectrum radiation had been done from N_{CH₃} protons of DeTAB head group. In cyclenoe every radiated spectrum is subtracted from reference spectrum so that only the peak that has noe correlation with the radiated peak remains and other peaks are subtracted out. By comparing the subtracted spectrum (upper part of the figure) with the 1D proton nmr (lower part of the figure) the only correlation that is seen with the N_{CH₃} protons is the α protons of DeTAB. There is no correlation with the sugar headgroup protons were found.

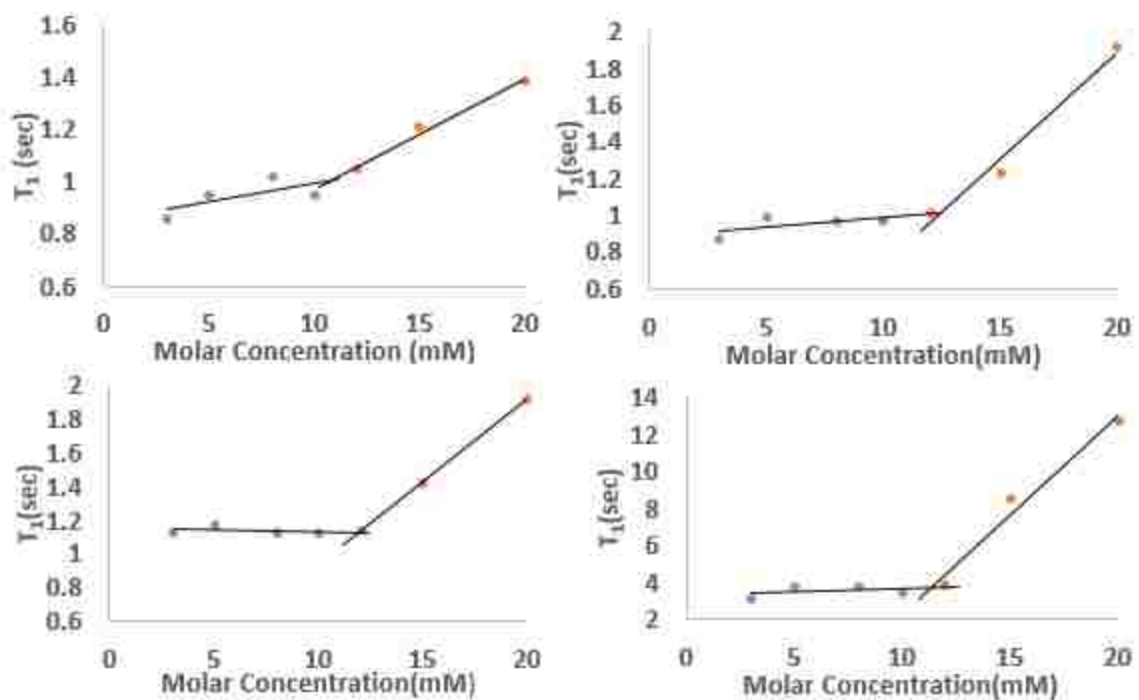


Figure D.6. Determination of cmc: T_1 (Spin-lattice) relaxation time at 50 °C of the (a) H5_A proton (b) H_{N-1} proton (c) $\alpha''_{A,B}$ protons and (d) ω'' proton of C8XT1 plotted against the molar concentration of C8XT1 (dissolved in D₂O). . The point of inflection in these plots indicates the cmc (critical micelle concentration) value of that surfactant. From the above plots it can be concluded that the cmc value for C8X1 is 11 mM at 50 °C.

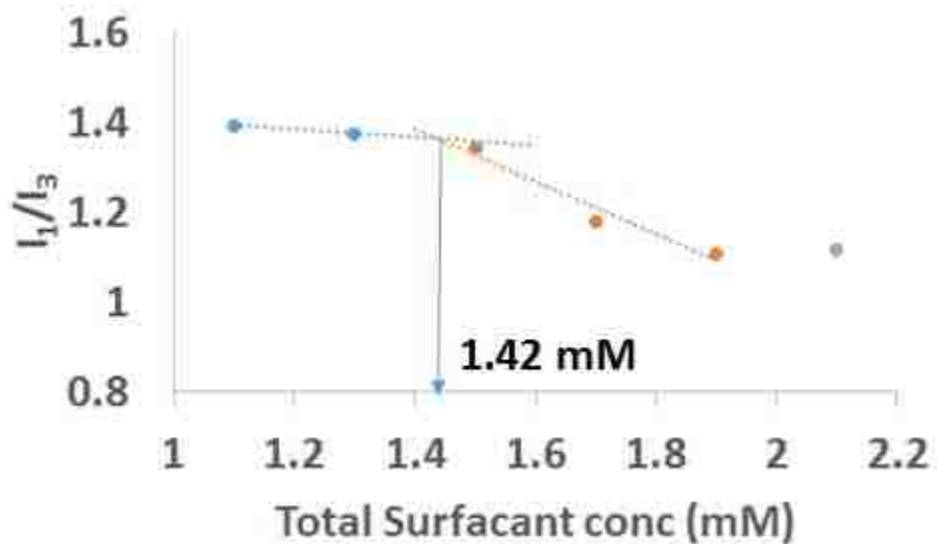


Figure D.7. The ratio of two pyrene fluorescence emission bands appearing at 374 nm (I_1) and 387 nm (I_3) vs. total surfactant concentration for $C_{16}TAB/C8XT1$ mixture at 50 °C. 1:1 overall ratio of surfactants was used. Arrows denote the mixed cmc values. This ratio is a measure of polarity near pyrene, where a lower value indicates a less polar microenvironment. The break point in the plot is considered to be the cmc of the mixture, which is 1.42 mM.

APPENDIX E

Supplemental Information of Chapter 7

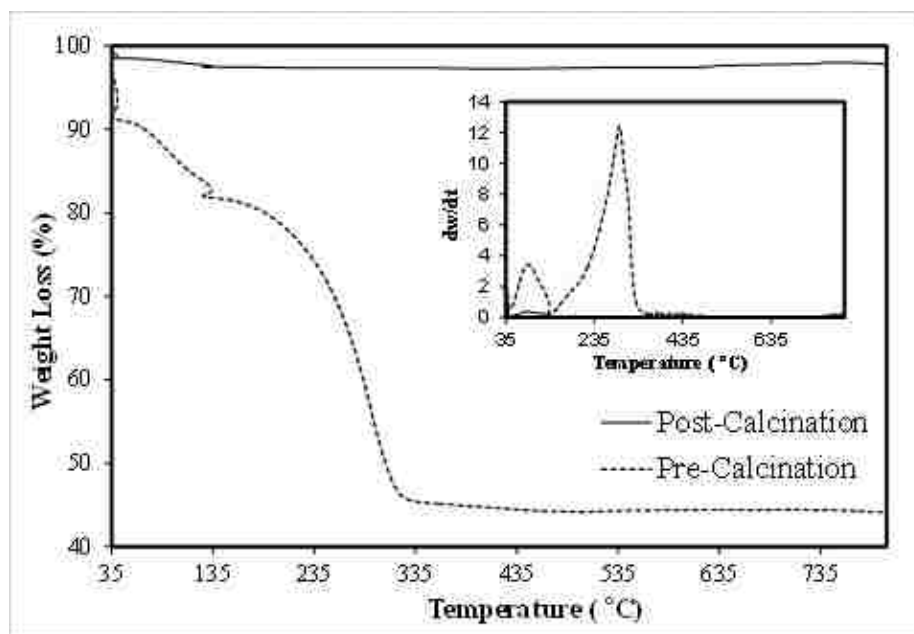


Figure E.1. Thermogravimetric (TGA) results for as-prepared (pre-calcination) and post-calcination (at 500 °C and 40 °C/min) unsandwiched titania films. TGA was performed using a TA Instruments system at 20 °C/min heating rate under nitrogen atmosphere. Two constant-temperature stages for 5 minutes at 35 °C and at 127 °C were also used as part of the ramp to drive off moisture. The samples were prepared by scraping the TiO₂ films from glass slides before and after calcination. Two detectable weight loss steps are observed for the pre-calcination sample: one below 150 °C corresponding to water and solvent evaporation, and one between 150 °C and 335 °C corresponding to P123 decomposition. In the post-calcination sample, the only feature is below 150 °C due to adsorbed water; no measurable weight loss occurs after 150 °C indicating that the template is completely removed by calcination.

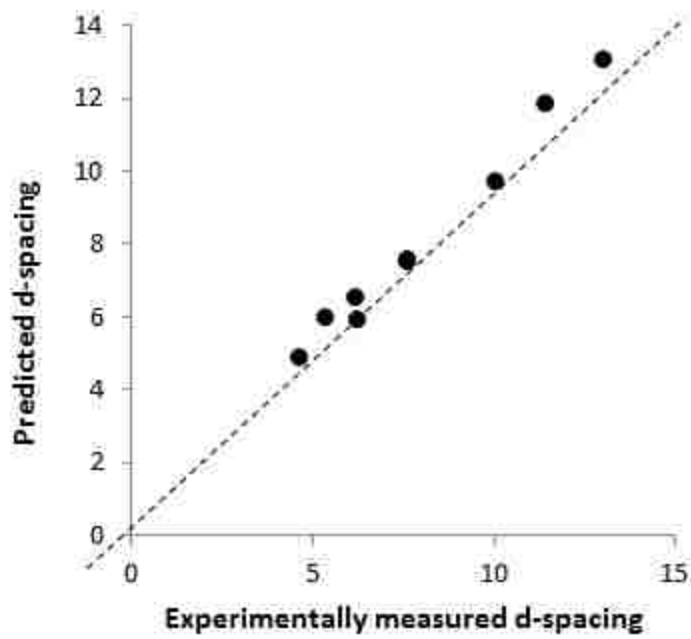


Figure E.2. Comparison between predicted and experimental d-spacing values for the proposed indexing of the unsandwiched film after aging using a combination of parallel rectangular symmetry (c2mm) and orthogonal hexagonal symmetry.

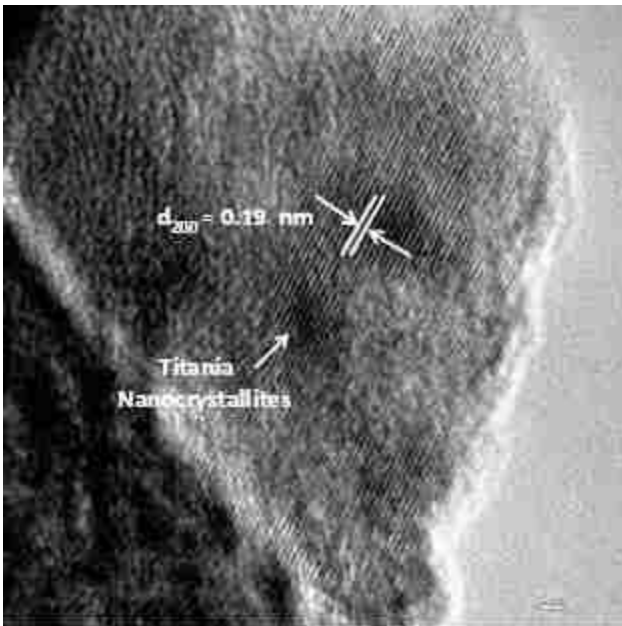


Figure E.3. HRTEM image of a fragment removed from a sandwiched titania thin film prepared using modified glass slides, aged at 4 °C for 2 h, and calcined at 500 °C for 10 min.

Table E.1. Comparison between the d-spacing calculated from the SAED pattern in Fig. 7.9b and d-spacing values reported by Howard et al. for anatase titania.

Calculated d-spacing(nm)	Literature d-spacing(nm)
0.356	0.352
0.237	0.238
0.190	0.189
0.170	0.170
0.148	0.148
0.126	0.126
0.116	0.117

APPENDIX F

Supplemental Information of Chapter 8

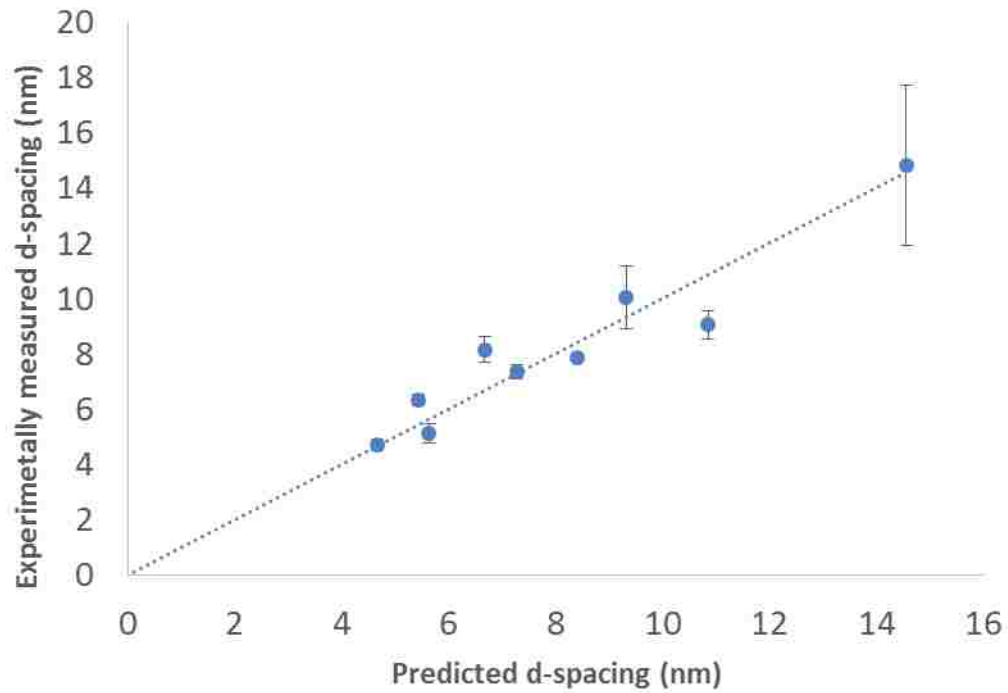


Figure F.1. Comparison between predicted and experimental d-spacing values for the proposed indexing of titania thin films (60 nm thick) on unmodified substrate after aging (Fig. 8.2a) using a combination of parallel rectangular symmetry (C2mm) and orthogonal hexagonal symmetry.

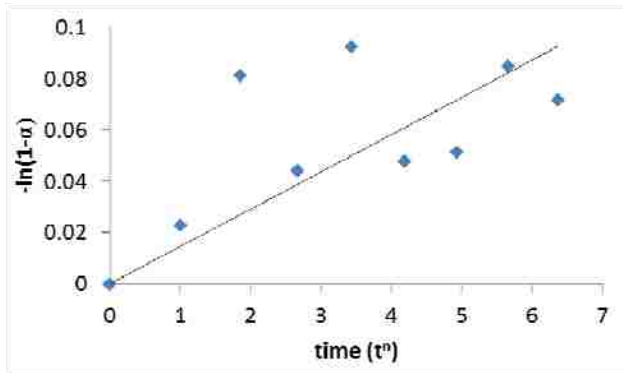


Figure F.2. Plot to determine k parameter using avrami equation for titania thin films (250 nm thick) on P123 modified substrate after calcined at isothermal condition (400 °C).

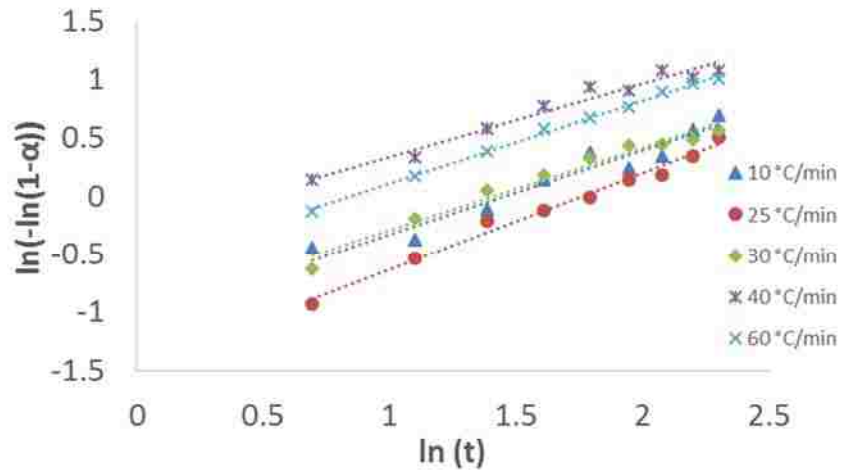


Figure F.3. Plot to determine n & k parameters in avrami equation at different ramp rates to reach final calcination temperature (500 °C). These titania thin films were 250 nm thick films and prepared on P123 modified substrate.

References

1. Saier, M.H., *Mechanisms and regulation of carbohydrate transport in bacteria*. 2014: Academic Press.
2. Alves, M., A. Martins, L. Rato, P. Moreira, S. Socorro, and P. Oliveira, *Molecular mechanisms beyond glucose transport in diabetes-related male infertility*. *Biochimica et Biophysica Acta (BBA)-Molecular Basis of Disease*, 2013. **1832**(5): p. 626-635.
3. Gruber, K., T. Horlacher, R. Castelli, A. Mader, P.H. Seeberger, and B.A. Hermann, *Cantilever Array Sensors Detect Specific Carbohydrate-Protein Interactions with Picomolar Sensitivity*. *ACS nano*, 2011. **5**(5): p. 3670-3678.
4. Klopffleisch, K., N. Phan, K. Augustin, R.S. Bayne, K.S. Booker, J.R. Botella, N.C. Carpita, T. Carr, J.G. Chen, and T.R. Cooke, *Arabidopsis G-protein interactome reveals connections to cell wall carbohydrates and morphogenesis*. *Molecular systems biology*, 2011. **7**(1).
5. Geissner, A., C. Anish, and P.H. Seeberger, *Glycan arrays as tools for infectious disease research*. *Current opinion in chemical biology*, 2014. **18**: p. 38-45.
6. Burkitt, D., *Refined carbohydrate foods and disease*. 2012: Elsevier.
7. Kaminska, I., A. Barras, Y. Coffinier, W. Lisowski, S. Roy, J. Niedziolka-Jonsson, P. Woisel, J. Lyskawa, M. Opallo, and A. Siriwardena, *Preparation of a Responsive Carbohydrate-Coated Biointerface Based on Graphene/Azido-Terminated Tetrathiafulvalene Nanohybrid Material*. *ACS applied materials & interfaces*, 2012. **4**(10): p. 5386-5393.
8. Tellechea, E., K.J. Wilson, E. Bravo, and K. Hamad-Schifferli, *Engineering the interface between glucose oxidase and nanoparticles*. *Langmuir*, 2012. **28**(11): p. 5190-5200.
9. Li, S.-p., D.-t. Wu, G.-p. Lv, and J. Zhao, *Carbohydrates analysis in herbal glycomics*. *TrAC Trends in Analytical Chemistry*, 2013. **52**: p. 155-169.
10. Gao, C., Y. Liu, H. Zhang, Y. Zhang, M.N. Fukuda, A.S. Palma, R.P. Kozak, R.A. Childs, M. Nonaka, and Z. Li, *Carbohydrate sequence of the prostate cancer-associated antigen F77 assigned by a mucin O-glycome designer array*. *Journal of Biological Chemistry*, 2014. **289**(23): p. 16462-16477.
11. Casella, I.G., M. Contursi, and R. Toniolo, *A Non-Enzymatic Carbohydrate Sensor Based on Multiwalled Carbon Nanotubes Modified with Adsorbed Active Gold Particles*. *Electroanalysis*, 2014. **26**(5): p. 988-995.
12. Kristensen, J.S., K. Gregorius, C. Struve, J.M. Frederiksen, and Y. Yu, *Sensor for detection of carbohydrate*. 2014, Google Patents.
13. Gorityala, B.K., Z. Lu, M.L. Leow, J. Ma, and X.-W. Liu, *Design of a "turn-off/turn-on" biosensor: understanding carbohydrate-lectin interactions for use in noncovalent drug delivery*. *Journal of the American Chemical Society*, 2012. **134**(37): p. 15229-15232.
14. Shukla, R.K. and A. Tiwari, *Carbohydrate polymers: Applications and recent advances in delivering drugs to the colon*. *Carbohydrate Polymers*, 2012. **88**(2): p. 399-416.
15. Merino, P., T. Tejero, I. Delso, R. Hurtado-Guerrero, A. Gómez-SanJuan, and D. Sádaba, *Recent Progress on Fucosyltransferase Inhibitors*. *Mini reviews in medicinal chemistry*, 2012. **12**(14): p. 1455-1464.
16. Sansone, F. and A. Casnati, *Multivalent glycolixarenes for recognition of biological macromolecules: glycolyx mimics capable of multitasking*. *Chemical Society Reviews*, 2013. **42**(11): p. 4623-4639.
17. Adsul, M., M. Singhvi, S. Gaikawai, and D. Gokhale, *Development of biocatalysts for production of commodity chemicals from lignocellulosic biomass*. *Bioresource technology*, 2011. **102**(6): p. 4304-4312.

18. Bond, J.Q., A.A. Upadhye, H. Olcay, G.A. Tompsett, J. Jae, R. Xing, D.M. Alonso, D. Wang, T. Zhang, and R. Kumar, *Production of renewable jet fuel range alkanes and commodity chemicals from integrated catalytic processing of biomass*. Energy & Environmental Science, 2014. **7**(4): p. 1500-1523.
19. Cherubini, F. and A.H. Strømman, *Chemicals from lignocellulosic biomass: opportunities, perspectives, and potential of biorefinery systems*. Biofuels, Bioproducts and Biorefining, 2011. **5**(5): p. 548-561.
20. Sheldon, R.A., *Green and sustainable manufacture of chemicals from biomass: state of the art*. Green Chemistry, 2014. **16**(3): p. 950-963.
21. Chen, L., S. Xu, and J. Li, *Recent advances in molecular imprinting technology: current status, challenges and highlighted applications*. Chemical Society Reviews, 2011. **40**(5): p. 2922-2942.
22. Deng, F., Y. Li, X. Luo, L. Yang, and X. Tu, *Preparation of conductive polypyrrole/TiO₂ 2 nanocomposite via surface molecular imprinting technique and its photocatalytic activity under simulated solar light irradiation*. Colloids and Surfaces A: Physicochemical and Engineering Aspects, 2012. **395**: p. 183-189.
23. Kryvshenko, G.A., P.Y. Apel, S.S. Abramchuk, and M.K. Beklemishev, *A highly permeable membrane for separation of quercetin obtained by nickel (II) ion-mediated molecular imprinting*. Separation Science and Technology, 2012. **47**(12): p. 1715-1724.
24. Asliyuce, S., L. Uzun, A.Y. Rad, S. Unal, R. Say, and A. Denizli, *Molecular imprinting based composite cryogel membranes for purification of anti-hepatitis B surface antibody by fast protein liquid chromatography*. Journal of Chromatography B, 2012. **889**: p. 95-102.
25. Li, Y., C. Dong, J. Chu, J. Qi, and X. Li, *Surface molecular imprinting onto fluorescein-coated magnetic nanoparticles via reversible addition fragmentation chain transfer polymerization: a facile three-in-one system for recognition and separation of endocrine disrupting chemicals*. Nanoscale, 2011. **3**(1): p. 280-287.
26. Zheng, C., X.L. Zhang, W. Liu, B. Liu, H.H. Yang, Z.A. Lin, and G.N. Chen, *A Selective Artificial Enzyme Inhibitor Based on Nanoparticle-Enzyme Interactions and Molecular Imprinting*. Advanced Materials, 2013. **25**(41): p. 5922-5927.
27. Fischer, E., *Influence of configuration on the action of enzymes*. Ber. Dtsch. Chem. Ges, 1894. **27**: p. 2985-2993.
28. Wulff, G., *The role of binding-site interactions in the molecular imprinting of polymers*. Trends in biotechnology, 1993. **11**(3): p. 85-87.
29. Wulff, G. and K. Knorr, *Stoichiometric noncovalent interaction in molecular imprinting*. Bioseparation, 2001. **10**(6): p. 257-276.
30. Sellergren, B., M. Lepistö, and K. Mosbach, *Highly enantioselective and substrate-selective polymers obtained by molecular imprinting utilizing noncovalent interactions. NMR and chromatographic studies on the nature of recognition*. Journal of the American Chemical Society, 1988. **110**(17): p. 5853-5860.
31. Schweitz, L., L. Andersson, and S. Nilsson, *Molecular imprinting for chiral separations and drug screening purposes using monolithic stationary phases in CEC*. Chromatographia, 1999. **49**: p. S93-S94.
32. Cheong, W.J., S.H. Yang, and F. Ali, *Molecular imprinted polymers for separation science: A review of reviews*. Journal of separation science, 2013. **36**(3): p. 609-628.
33. Székely, G., E. Fritz, J. Bandarra, W. Heggie, and B. Sellergren, *Removal of potentially genotoxic acetamide and arylsulfonate impurities from crude drugs by molecular imprinting*. Journal of Chromatography A, 2012. **1240**: p. 52-58.

34. Kuriu, Y., A. Kawamura, T. Uragami, and T. Miyata, *Formation of Thin Molecularly Imprinted Hydrogel Layers with Lectin Recognition Sites on SPR Sensor Chips by Atom Transfer Radical Polymerization*. Chemistry Letters, 2014. **43**(6): p. 825-827.
35. Reddy, S.M., Q.T. Phan, H. El-Sharif, L. Govada, D. Stevenson, and N.E. Chayen, *Protein crystallization and biosensor applications of hydrogel-based molecularly imprinted polymers*. Biomacromolecules, 2012. **13**(12): p. 3959-3965.
36. Wulff, G.n. and J. Liu, *Design of biomimetic catalysts by molecular imprinting in synthetic polymers: the role of transition state stabilization*. Accounts of chemical research, 2011. **45**(2): p. 239-247.
37. Li, J., Y. Li, Y. Zhang, and G. Wei, *Highly sensitive molecularly imprinted electrochemical sensor based on the double amplification by an inorganic prussian blue catalytic polymer and the enzymatic effect of glucose oxidase*. Analytical chemistry, 2012. **84**(4): p. 1888-1893.
38. Díaz-Díaz, G., M.C. Blanco-López, M.J. Lobo-Castañón, A.J. Miranda-Ordieres, and P. Tuñón-Blanco, *Hemo-acrylic polymers as catalyst for the oxidative dehalogenation of 2, 4, 6-trichlorophenol. Chloroperoxidase's mimic imprinting effects*. Journal of Molecular Catalysis A: Chemical, 2012. **353**: p. 117-121.
39. Bowen, J.L., P. Manesiotis, and C.J. Allender, *Twenty years since 'antibody mimics' by molecular imprinting were first proposed: A critical perspective*. Molecular Imprinting, 2013. **1**: p. 35-40.
40. Kunath, S., M. Panagiotopoulou, J. Maximilien, N. Marchyk, J. Sängler, and K. Haupt, *Cell and Tissue Imaging with Molecularly Imprinted Polymers as Plastic Antibody Mimics*. Advanced healthcare materials, 2015.
41. Yang, Y.-z., Q. Tang, C.-b. Gong, X.-b. Ma, J.-d. Peng, and M.H.-w. Lam, *Ultrasensitive detection of bisphenol A in aqueous media using photoresponsive surface molecular imprinting polymer microspheres*. New Journal of Chemistry, 2014. **38**(4): p. 1780-1788.
42. Qu, J.R., J.J. Zhang, Y.F. Gao, and H. Yang, *Synthesis and utilisation of molecular imprinting polymer for clean-up of propachlor in food and environmental media*. Food chemistry, 2012. **135**(3): p. 1148-1156.
43. Sharma, P.S., A. Pietrzyk-Le, F. D'Souza, and W. Kutner, *Electrochemically synthesized polymers in molecular imprinting for chemical sensing*. Analytical and bioanalytical chemistry, 2012. **402**(10): p. 3177-3204.
44. Svenson, J. and I.A. Nicholls, *On the thermal and chemical stability of molecularly imprinted polymers*. Analytica Chimica Acta, 2001. **435**(1): p. 19-24.
45. Tada, M. and Y. Iwasawa, *Design of molecular-imprinting metal-complex catalysts*. Journal of Molecular Catalysis A: Chemical, 2003. **199**(1): p. 115-137.
46. Önnby, L., V. Pakade, B. Mattiasson, and H. Kirsebom, *Polymer composite adsorbents using particles of molecularly imprinted polymers or aluminium oxide nanoparticles for treatment of arsenic contaminated waters*. Water research, 2012. **46**(13): p. 4111-4120.
47. Willander, M., K. Khun, and Z.H. Ibupoto, *Metal Oxide Nanosensors Using Polymeric Membranes, Enzymes and Antibody Receptors as Ion and Molecular Recognition Elements*. Sensors, 2014. **14**(5): p. 8605-8632.
48. Saumya, V., K.P. Prathish, and T.P. Rao, *In situ copper oxide modified molecularly imprinted polypyrrole film based voltammetric sensor for selective recognition of tyrosine*. Talanta, 2011. **85**(2): p. 1056-1062.
49. Li, C., M. Lv, J. Zuo, and X. Huang, *SnO₂ Highly Sensitive CO Gas Sensor Based on Quasi-Molecular-Imprinting Mechanism Design*. Sensors, 2015. **15**(2): p. 3789-3800.

50. Wei, S., X. Hu, H. Liu, Q. Wang, and C. He, *Rapid degradation of Congo red by molecularly imprinted polypyrrole-coated magnetic TiO₂ nanoparticles in dark at ambient conditions*. Journal of hazardous materials, 2015. **294**: p. 168-176.
51. Lu, Y., R. Ganguli, C.A. Drewien, M.T. Anderson, C.J. Brinker, W. Gong, Y. Guo, H. Soyez, B. Dunn, and M.H. Huang, *Continuous formation of supported cubic and hexagonal mesoporous films by sol-gel dip-coating*. Nature, 1997. **389**(6649): p. 364-368.
52. Zhao, D., J. Feng, Q. Huo, N. Melosh, G.H. Fredrickson, B.F. Chmelka, and G.D. Stucky, *Triblock copolymer syntheses of mesoporous silica with periodic 50 to 300 angstrom pores*. science, 1998. **279**(5350): p. 548-552.
53. Martin, J.E., M.T. Anderson, J. Odinek, and P. Newcomer, *Synthesis of periodic mesoporous silica thin films*. Langmuir, 1997. **13**(15): p. 4133-4141.
54. Hayward, R.C., P.C. Alberius, E.J. Kramer, and B.F. Chmelka, *Thin films of bicontinuous cubic mesostructured silica templated by a nonionic surfactant*. Langmuir, 2004. **20**(14): p. 5998-6004.
55. Innocenzi, P., A. Martucci, M. Guglielmi, A. Bearzotti, E. Traversa, and J.C. Pivin, *Mesoporous silica thin films for alcohol sensors*. Journal of the European Ceramic Society, 2001. **21**(10): p. 1985-1988.
56. Innocenzi, P., A. Martucci, M. Guglielmi, A. Bearzotti, and E. Traversa, *Electrical and structural characterisation of mesoporous silica thin films as humidity sensors*. Sensors and Actuators B: Chemical, 2001. **76**(1): p. 299-303.
57. Tsai, C.-Y., S.-Y. Tam, Y. Lu, and C.J. Brinker, *Dual-layer asymmetric microporous silica membranes*. Journal of membrane science, 2000. **169**(2): p. 255-268.
58. Xomeritakis, G., C. Braunbarth, B. Smarsly, N. Liu, R. Köhn, Z. Klipowicz, and C. Brinker, *Aerosol-assisted deposition of surfactant-templated mesoporous silica membranes on porous ceramic supports*. Microporous and mesoporous materials, 2003. **66**(1): p. 91-101.
59. Munoz, B., A. Ramila, J. Perez-Pariente, I. Diaz, and M. Vallet-Regi, *MCM-41 organic modification as drug delivery rate regulator*. Chemistry of Materials, 2003. **15**(2): p. 500-503.
60. Lebold, T., C. Jung, J. Michaelis, and C. Bräuchle, *Nanostructured silica materials as drug-delivery systems for doxorubicin: single molecule and cellular studies*. Nano letters, 2009. **9**(8): p. 2877-2883.
61. Díaz-García, M.E. and R.B. Laineño, *Molecular imprinting in sol-gel materials: Recent developments and applications*. Microchimica Acta, 2005. **149**(1-2): p. 19-36.
62. Fireman-Shoresh, S., I. Turyan, D. Mandler, D. Avnir, and S. Marx, *Chiral electrochemical recognition by very thin molecularly imprinted sol-gel films*. Langmuir, 2005. **21**(17): p. 7842-7847.
63. Grosso, D., F. Cagnol, G.d.A. Soler-Illia, E.L. Crepaldi, H. Amenitsch, A. Brunet-Bruneau, A. Bourgeois, and C. Sanchez, *Fundamentals of mesostructuring through evaporation-induced self-assembly*. Advanced Functional Materials, 2004. **14**(4): p. 309-322.
64. Yamaguchi, A., F. Uejo, T. Yoda, T. Uchida, Y. Tanamura, T. Yamashita, and N. Teramae, *Self-assembly of a silica-surfactant nanocomposite in a porous alumina membrane*. Nature materials, 2004. **3**(5): p. 337-341.
65. Stubenrauch, C., *Sugar surfactants—aggregation, interfacial, and adsorption phenomena*. Current opinion in colloid & interface science, 2001. **6**(2): p. 160-170.
66. Richman, E.K., T. Brezesinski, and S.H. Tolbert, *Vertically oriented hexagonal mesoporous films formed through nanometre-scale epitaxy*. Nature materials, 2008. **7**(9): p. 712-717.

67. Xing, R. and S.E. Rankin, *Use of the ternary phase diagram of a mixed cationic/glucopyranoside surfactant system to predict mesostructured silica synthesis*. Journal of Colloid and Interface Science, 2007. **316**(2): p. 930-938.
68. Holland, P. and D. Rubingh, *Nonideal multicomponent mixed micelle model*. The Journal of Physical Chemistry, 1983. **87**(11): p. 1984-1990.
69. Rubingh, D.N., *Mixed micelle solutions*, in *Solution chemistry of surfactants*. 1979, Springer. p. 337-354.
70. Nishiyama, N., D.H. Park, A. Koide, Y. Egashira, and K. Ueyama, *A mesoporous silica (MCM-48) membrane: preparation and characterization*. Journal of Membrane Science, 2001. **182**(1): p. 235-244.
71. Leplan, H., B. Geenen, J. Robic, and Y. Pauleau, *Residual stresses in evaporated silicon dioxide thin films: Correlation with deposition parameters and aging behavior*. Journal of applied physics, 1995. **78**(2): p. 962-968.
72. Hwang, Y.K., K.R. Patil, S.H. Jhung, J.-S. Chang, Y.J. Ko, and S.-E. Park, *Control of pore size and condensation rate of cubic mesoporous silica thin films using a swelling agent*. Microporous and mesoporous materials, 2005. **78**(2): p. 245-253.
73. Lancelle-Beltran, E., P. Prené, C. Boscher, P. Belleville, P. Buvat, S. Lambert, F. Guillet, C. Boissiere, D. Grosso, and C. Sanchez, *Nanostructured hybrid solar cells based on self-assembled mesoporous titania thin films*. Chemistry of materials, 2006. **18**(26): p. 6152-6156.
74. Zúkalová, M., A. Zúkal, L. Kavan, M.K. Nazeeruddin, P. Liska, and M. Grätzel, *Organized mesoporous TiO₂ films exhibiting greatly enhanced performance in dye-sensitized solar cells*. Nano Letters, 2005. **5**(9): p. 1789-1792.
75. Kalyanasundaram, K. and M. Graetzel, *Artificial photosynthesis: biomimetic approaches to solar energy conversion and storage*. Current opinion in Biotechnology, 2010. **21**(3): p. 298-310.
76. Unger, E.L., S.J. Fretz, B. Lim, G.Y. Margulis, M.D. McGehee, and T.D.P. Stack, *Sequential "click" functionalization of mesoporous titania for energy-relay dye enhanced dye-sensitized solar cells*. Physical Chemistry Chemical Physics, 2015. **17**(9): p. 6565-6571.
77. Wu, Q.L. and S.E. Rankin, *Tuning the mesopore size of titania thin films using a polymeric swelling agent*. The Journal of Physical Chemistry C, 2011. **115**(24): p. 11925-11933.
78. Wu, Q.L. and S.E. Rankin, *Tuning the wall thickness and pore orientation in mesoporous titania films prepared with low-temperature aging*. Journal of Sol-Gel Science and Technology, 2011. **60**(1): p. 81-90.
79. Koganti, V.R., D. Dunphy, V. Gowrishankar, M.D. McGehee, X. Li, J. Wang, and S.E. Rankin, *Generalized Coating Route to Silica and Titania Films with Orthogonally Tilted Cylindrical Nanopore Arrays*. Nano Letters, 2006. **6**(11): p. 2567-2570.
80. Koganti, V.R. and S.E. Rankin, *Synthesis of surfactant-templated silica films with orthogonally aligned hexagonal mesophase*. The Journal of Physical Chemistry B, 2005. **109**(8): p. 3279-3283.
81. Yan, M., F. Chen, J. Zhang, and M. Anpo, *Preparation of controllable crystalline titania and study on the photocatalytic properties*. The Journal of Physical Chemistry B, 2005. **109**(18): p. 8673-8678.
82. Kopidakis, N., K.D. Benkstein, J. van de Lagemaat, A.J. Frank, Q. Yuan, and E.A. Schiff, *Temperature dependence of the electron diffusion coefficient in electrolyte-filled TiO₂ nanoparticle films: evidence against multiple trapping in exponential conduction-band tails*. Physical Review B, 2006. **73**(4): p. 045326.

83. Yu, J.-G., H.-G. Yu, B. Cheng, X.-J. Zhao, J.C. Yu, and W.-K. Ho, *The effect of calcination temperature on the surface microstructure and photocatalytic activity of TiO₂ thin films prepared by liquid phase deposition*. The Journal of Physical Chemistry B, 2003. **107**(50): p. 13871-13879.
84. Eastoe, J. and J. Dalton, *Dynamic surface tension and adsorption mechanisms of surfactants at the air–water interface*. Advances in Colloid and Interface Science, 2000. **85**(2): p. 103-144.
85. Zhu, B.Y. and M.J. Rosen, *Synergism in binary mixtures of surfactants: IV. Effectiveness of surface tension reduction*. Journal of colloid and interface science, 1984. **99**(2): p. 435-442.
86. Rosen, M.J., *Relationship of structure to properties in surfactants: II. Efficiency in surface or interfacial tension reduction*. Journal of the American Oil Chemists Society, 1974. **51**(10): p. 461-465.
87. Moulik, S.P., M.E. Haque, P.K. Jana, and A.R. Das, *Micellar properties of cationic surfactants in pure and mixed states*. The Journal of Physical Chemistry, 1996. **100**(2): p. 701-708.
88. van Os, N.M., J.R. Haak, and L.A.M. Rupert, *Physico-chemical properties of selected anionic, cationic and nonionic surfactants*. 2012: Elsevier.
89. Sacripante, G.G., R.D. Patel, M.P. Breton, M.A. Hopper, G.E. Kmieciak-Lawrynowicz, and B.S. Ong, *Combining emulsion of emulsifiable polymer resin in an anionic surfactant medium, a pigment and cationic surfactant, aggregating particles to a desired size, coalescing the particles, adjusting tension and viscosity*. 1997, Google Patents.
90. Derstadt, D.M. and D.W. Moeser, *Anionic surfactant-containing detergent compositions having soil-release properties*. 1978, Google Patents.
91. Scheibel, J.J., *The evolution of anionic surfactant technology to meet the requirements of the laundry detergent industry*. Journal of surfactants and detergents, 2004. **7**(4): p. 319-328.
92. Pancheri, E.J., *Liquid detergent composition containing alkyl sulfate and alkyl ethoxylated sulfate*. 1982, Google Patents.
93. Penfold, J., I. Tucker, R. Thomas, D. Taylor, X. Zhang, C. Bell, C. Breward, and P. Howell, *The interaction between sodium alkyl sulfate surfactants and the oppositely charged polyelectrolyte, polyDMAAC, at the air-water interface: the Role of alkyl chain length and electrolyte and comparison with theoretical predictions*. Langmuir, 2007. **23**(6): p. 3128-3136.
94. Zhu, L. and S. Feng, *Synergistic solubilization of polycyclic aromatic hydrocarbons by mixed anionic–nonionic surfactants*. Chemosphere, 2003. **53**(5): p. 459-467.
95. Sharma, K.S., C. Rodgers, R.M. Palepu, and A. Rakshit, *Studies of mixed surfactant solutions of cationic dimeric (gemini) surfactant with nonionic surfactant C 12 E 6 in aqueous medium*. Journal of colloid and interface science, 2003. **268**(2): p. 482-488.
96. Söderlind, E., M. Wollbratt, and C. von Corswant, *The usefulness of sugar surfactants as solubilizing agents in parenteral formulations*. International journal of pharmaceutics, 2003. **252**(1): p. 61-71.
97. Rico-Lattes, I. and A. Lattes, *Synthesis of new sugar-based surfactants having biological applications: key role of their self-association*. Colloids and Surfaces A: Physicochemical and Engineering Aspects, 1997. **123**: p. 37-48.
98. Li, X., J. Turánek, P. Knötigová, H. Kudláčková, J. Mašek, S. Parkin, S.E. Rankin, B.L. Knutson, and H.-J. Lehmler, *Hydrophobic tail length, degree of fluorination and*

- headgroup stereochemistry are determinants of the biocompatibility of (fluorinated) carbohydrate surfactants.* Colloids and Surfaces B: Biointerfaces, 2009. **73**(1): p. 65-74.
99. Wilhelm, M., C.L. Zhao, Y. Wang, R. Xu, M.A. Winnik, J.L. Mura, G. Riess, and M.D. Croucher, *Poly (styrene-ethylene oxide) block copolymer micelle formation in water: a fluorescence probe study.* Macromolecules, 1991. **24**(5): p. 1033-1040.
 100. Tanford, C., *Theory of micelle formation in aqueous solutions.* The Journal of Physical Chemistry, 1974. **78**(24): p. 2469-2479.
 101. Akhter, M.S. and S.M. Alawi, *The effect of organic additives on critical micelle concentration of non-aqueous micellar solutions.* Colloids and Surfaces A: Physicochemical and Engineering Aspects, 2000. **175**(3): p. 311-320.
 102. Manabe, M. and M. Koda, *The effect of poly (oxyethylene) alkyl ethers, alkanediols, and alkanols on the critical micelle concentration of sodium dodecyl sulfate.* Bulletin of the Chemical Society of Japan, 1978. **51**(6): p. 1599-1601.
 103. Hayase, K. and S. Hayano, *Effect of alcohols on the critical micelle concentration decrease in the aqueous sodium dodecyl sulfate solution.* Journal of Colloid and Interface Science, 1978. **63**(3): p. 446-451.
 104. Hara, K., H. Kuwabara, O. Kajimoto, and K. Bhattacharyya, *Effect of pressure on the critical micelle concentration of neutral surfactant using fluorescence probe method.* Journal of Photochemistry and Photobiology A: Chemistry, 1999. **124**(3): p. 159-162.
 105. Hamann, S.D., *The state of ionic micelles at high pressures.* 1978.
 106. Osugi, J., M. Sato, and N. Ifuku, *Nippon Kagaku Zasshi*, **87**, 329 (1966). Rev. Phys. Chem. Japan, 1965. **35**: p. 32.
 107. Tanaka, M., S. Kaneshina, K. Shin-no, T. Okajima, and T. Tomida, *Partial molal volumes of surfactant and its homologous salts under high pressure.* Journal of Colloid and Interface Science, 1974. **46**(1): p. 132-138.
 108. Mohajeri, E. and G.D. Noudeh, *Effect of temperature on the critical micelle concentration and micellization thermodynamic of nonionic surfactants: polyoxyethylene sorbitan fatty acid esters.* Journal of Chemistry, 2012. **9**(4): p. 2268-2274.
 109. Rico, I. and A. Lattes, *Formamide, a water substitute. 12. Krafft temperature and micelle formation of ionic surfactants in formamide.* The Journal of Physical Chemistry, 1986. **90**(22): p. 5870-5872.
 110. Vautier-Giongo, C. and B.L. Bales, *Estimate of the ionization degree of ionic micelles based on Krafft temperature measurements.* The Journal of Physical Chemistry B, 2003. **107**(23): p. 5398-5403.
 111. Davey, T.W., W.A. Ducker, A.R. Hayman, and J. Simpson, *Krafft temperature depression in quaternary ammonium bromide surfactants.* Langmuir, 1998. **14**(12): p. 3210-3213.
 112. Boyd, B.J., C.J. Drummond, I. Krodkiewska, and F. Grieser, *How chain length, headgroup polymerization, and anomeric configuration govern the thermotropic and lyotropic liquid crystalline phase behavior and the air-water interfacial adsorption of glucose-based surfactants.* Langmuir, 2000. **16**(19): p. 7359-7367.
 113. Danino, D., Y. Talmon, and R. Zana, *Alkanediyl-. alpha.,. omega.-bis (dimethylalkylammonium bromide) surfactants (dimeric surfactants). 5. Aggregation and microstructure in aqueous solutions.* Langmuir, 1995. **11**(5): p. 1448-1456.
 114. Tanford, C., *Micelle shape and size.* The Journal of Physical Chemistry, 1972. **76**(21): p. 3020-3024.
 115. Ogino, K. and M. Abe, *Mixed surfactant systems.* 1992: CRC Press.
 116. Holland, P.M. and D.N. Rubingh, *Mixed surfactant systems.* Vol. 1. 1992: American Chemical Society Washington, DC.

117. Tung, C.-C., Y.-M. Yang, C.-H. Chang, and J.-R. Maa, *Removal of copper ions and dissolved phenol from water using micellar-enhanced ultrafiltration with mixed surfactants*. Waste management, 2002. **22**(7): p. 695-701.
118. Pugh, R.J. and L. Bergstrom, *Surface and colloid chemistry in advanced ceramics processing*. Vol. 51. 1993: CRC Press.
119. Garavito, R.M. and S. Ferguson-Miller, *Detergents as tools in membrane biochemistry*. Journal of Biological Chemistry, 2001. **276**(35): p. 32403-32406.
120. Mukerjee, P. and A.Y. Yang, *Nonideality of mixing of micelles of fluorocarbon and hydrocarbon surfactants and evidence of partial miscibility from differential conductance data*. The Journal of Physical Chemistry, 1976. **80**(12): p. 1388-1390.
121. Scamehorn, J., R. Schechter, and W. Wade, *Micelle Formation in Mixtures of Anionic and Nonionic Surfactants*. JOURNAL OF DISPERSION SCIENCE AND TECHNOLOGY, 1982. **3**(3): p. 261-278.
122. Clint, J.H., *Micellization of mixed nonionic surface active agents*. Journal of the Chemical Society, Faraday Transactions 1: Physical Chemistry in Condensed Phases, 1975. **71**: p. 1327-1334.
123. Clint, J.H., *Surfactant aggregation*. 2012: Springer Science & Business Media.
124. Ruiz, C.C., *Sugar-based surfactants: fundamentals and applications*. Vol. 143. 2008: CRC Press.
125. Azum, N., A.Z. Naqvi, M. Akram, and D. Kabir ud, *Studies of mixed micelle formation between cationic gemini and cationic conventional surfactants*. Journal of Colloid and Interface Science, 2008. **328**(2): p. 429-435.
126. Sierra, M. and M. Svensson, *Mixed micelles containing alkylglycosides: effect of the chain length and the polar head group*. Langmuir, 1999. **15**(7): p. 2301-2306.
127. Wydro, P. and M. Paluch, *Surface properties of cationic–nonionic mixed surfactant systems*. Colloids and Surfaces A: Physicochemical and Engineering Aspects, 2004. **245**(1–3): p. 75-79.
128. Joshi, S., *Mixed Surfactant Systems: Thermodynamics and Applications in Metal Oxide Imprinting*. 2014.
129. Kresge, C., M. Leonowicz, W. Roth, J. Vartuli, and J. Beck, *Ordered mesoporous molecular sieves synthesized by a liquid-crystal template mechanism*. nature, 1992. **359**(6397): p. 710-712.
130. Brinker, C.J., Y. Lu, A. Sellinger, and H. Fan, *Evaporation-induced self-assembly: nanostructures made easy*. Advanced materials, 1999. **11**(7): p. 579-585.
131. Margolese, D. and G. Stucky, *Synthesis of continuous mesoporous silica thin films with three-dimensional accessible pore structures*. Chemical Communications, 1998(22): p. 2499-2500.
132. Baskaran, S., J. Liu, K. Domansky, N. Kohler, X. Li, C. Coyle, G. Fryxell, S. Thevuthasan, and R. Williford, *Low dielectric constant mesoporous silica films through molecularly templated synthesis*. Advanced Materials, 2000. **12**(4): p. 291-294.
133. Hatton, B.D., K. Landskron, W. Whitnall, D.D. Perovic, and G.A. Ozin, *Spin-Coated Periodic Mesoporous Organosilica Thin Films—Towards a New Generation of Low-Dielectric-Constant Materials*. Advanced Functional Materials, 2005. **15**(5): p. 823-829.
134. Davis, M.E., *Ordered porous materials for emerging applications*. Nature, 2002. **417**(6891): p. 813-821.
135. Newalkar, B.L., N.V. Choudary, P. Kumar, S. Komarneni, and T.S. Bhat, *Exploring the potential of mesoporous silica, SBA-15, as an adsorbent for light hydrocarbon separation*. Chemistry of materials, 2002. **14**(1): p. 304-309.

136. Rivera, D. and J.M. Harris, *In situ ATR-FT-IR kinetic studies of molecular transport and surface binding in thin sol-gel films: reactions of chlorosilane reagents in porous silica materials*. Analytical chemistry, 2001. **73**(3): p. 411-423.
137. Grosso, D., A. Balkenende, P. Albouy, A. Ayrat, H. Amenitsch, and F. Babonneau, *Two-dimensional hexagonal mesoporous silica thin films prepared from block copolymers: Detailed characterization and formation mechanism*. Chemistry of Materials, 2001. **13**(5): p. 1848-1856.
138. Alberius, P.C., K.L. Frindell, R.C. Hayward, E.J. Kramer, G.D. Stucky, and B.F. Chmelka, *General Predictive Syntheses of Cubic, Hexagonal, and Lamellar Silica and Titania Mesostructured Thin Films*. Chemistry of Materials, 2002. **14**(8): p. 3284-3294.
139. Doshi, D.A., A. Gibaud, N. Liu, D. Sturmayer, A.P. Malanoski, D.R. Dunphy, H. Chen, S. Narayanan, A. MacPhee, and J. Wang, *In-situ x-ray scattering study of continuous silica-surfactant self-assembly during steady-state dip coating*. The Journal of Physical Chemistry B, 2003. **107**(31): p. 7683-7688.
140. Gibaud, A., D. Grosso, B. Smarsly, A. Baptiste, J. Bardeau, F. Babonneau, D. Doshi, Z. Chen, C.J. Brinker, and C. Sanchez, *Evaporation-controlled self-assembly of silica surfactant mesophases*. The Journal of Physical Chemistry B, 2003. **107**(25): p. 6114-6118.
141. Doshi, D.A., A. Gibaud, V. Goletto, M. Lu, H. Gerung, B. Ocko, S.M. Han, and C.J. Brinker, *Peering into the self-assembly of surfactant templated thin-film silica mesophases*. Journal of the American Chemical Society, 2003. **125**(38): p. 11646-11655.
142. Innocenzi, P., P. Falcaro, D. Grosso, and F. Babonneau, *Order-disorder transitions and evolution of silica structure in self-assembled mesostructured silica films studied through FTIR spectroscopy*. The Journal of Physical Chemistry B, 2003. **107**(20): p. 4711-4717.
143. Alonso, B., A.R. Balkenende, P.-A. Albouy, D. Durand, and F. Babonneau, *Directing role of pH and ethanol vapour on the formation of 2D or 3D mesostructured silica and hybrid organo-silica thin films*. New journal of chemistry, 2002. **26**(10): p. 1270-1272.
144. Grosso, D., F. Babonneau, G.J. de AA Soler-Illia, P.-A. Albouy, and H. Amenitsch, *Phase transformation during cubic mesostructured silica film formation*. Chemical Communications, 2002(7): p. 748-749.
145. Cagnol, F., D. Grosso, G.J. de AA Soler-Illia, E.L. Crepaldi, F. Babonneau, H. Amenitsch, and C. Sanchez, *Humidity-controlled mesostructuration in CTAB-templated silica thin film processing. The existence of a modulable steady state*. Journal of Materials Chemistry, 2003. **13**(1): p. 61-66.
146. Crepaldi, E.L., G.J.d.A. Soler-Illia, D. Grosso, F. Cagnol, F. Ribot, and C. Sanchez, *Controlled formation of highly organized mesoporous titania thin films: from mesostructured hybrids to mesoporous nanoanatase TiO₂*. Journal of the American Chemical Society, 2003. **125**(32): p. 9770-9786.
147. Wang, K., M.A. Morris, and J.D. Holmes, *Preparation of mesoporous titania thin films with remarkably high thermal stability*. Chemistry of materials, 2005. **17**(6): p. 1269-1271.
148. Wang, Z., U. Helmersson, and P.-O. Käll, *Optical properties of anatase TiO₂ thin films prepared by aqueous sol-gel process at low temperature*. Thin Solid Films, 2002. **405**(1): p. 50-54.
149. Hass, G., *Preparation, properties and optical applications of thin films of titanium dioxide*. Vacuum, 1952. **2**(4): p. 331-345.
150. Mo, S.-D. and W. Ching, *Electronic and optical properties of three phases of titanium dioxide: Rutile, anatase, and brookite*. Physical Review B, 1995. **51**(19): p. 13023.

151. Sharma, S.D., K. Saini, C. Kant, C. Sharma, and S. Jain, *Photodegradation of dye pollutant under UV light by nano-catalyst doped titania thin films*. Applied Catalysis B: Environmental, 2008. **84**(1): p. 233-240.
152. Zorn, M.E., D.T. Tompkins, W.A. Zeltner, and M.A. Anderson, *Catalytic and photocatalytic oxidation of ethylene on titania-based thin-films*. Environmental science & technology, 2000. **34**(24): p. 5206-5210.
153. Adachi, M., Y. Murata, J. Takao, J. Jiu, M. Sakamoto, and F. Wang, *Highly efficient dye-sensitized solar cells with a titania thin-film electrode composed of a network structure of single-crystal-like TiO₂ nanowires made by the "oriented attachment" mechanism*. Journal of the American Chemical Society, 2004. **126**(45): p. 14943-14949.
154. Imai, H., Y. Takei, K. Shimizu, M. Matsuda, and H. Hirashima, *Direct preparation of anatase TiO₂ nanotubes in porous alumina membranes*. J. Mater. Chem., 1999. **9**(12): p. 2971-2972.
155. Coakley, K.M., Y. Liu, M.D. McGehee, K.L. Frindell, and G.D. Stucky, *Infiltrating Semiconducting Polymers into Self-assembled Mesoporous Titania Films for Photovoltaic Applications*. Advanced Functional Materials, 2003. **13**(4): p. 301-306.
156. Choi, H., E. Stathatos, and D.D. Dionysiou, *Sol-gel preparation of mesoporous photocatalytic TiO₂ films and TiO₂/Al₂O₃ composite membranes for environmental applications*. Applied Catalysis B: Environmental, 2006. **63**(1): p. 60-67.
157. Lai, C., G. Li, Y. Dou, and X. Gao, *Mesoporous polyaniline or polypyrrole/anatase TiO₂ nanocomposite as anode materials for lithium-ion batteries*. Electrochimica Acta, 2010. **55**(15): p. 4567-4572.
158. Guo, Y.-G., J.-S. Hu, and L.-J. Wan, *Nanostructured materials for electrochemical energy conversion and storage devices*. Adv. Mater, 2008. **20**(15): p. 2878-2887.
159. Ji, L., Z. Lin, M. Alcoutlabi, and X. Zhang, *Recent developments in nanostructured anode materials for rechargeable lithium-ion batteries*. Energy & Environmental Science, 2011. **4**(8): p. 2682-2699.
160. Hu, Y., H.L. Tsai, and C.L. Huang, *Phase transformation of precipitated TiO₂ nanoparticles*. Materials Science and Engineering: A, 2003. **344**(1-2): p. 209-214.
161. Zhang, H. and J.F. Banfield, *Kinetics of Crystallization and Crystal Growth of Nanocrystalline Anatase in Nanometer-Sized Amorphous Titania*. Chemistry of Materials, 2002. **14**(10): p. 4145-4154.
162. Kirsch, B.L., E.K. Richman, A.E. Riley, and S.H. Tolbert, *In-situ X-ray diffraction study of the crystallization kinetics of mesoporous titania films*. The Journal of Physical Chemistry B, 2004. **108**(34): p. 12698-12706.
163. Lorenzo, A.T., M.L. Arnal, J. Albuérne, and A.J. Müller, *DSC isothermal polymer crystallization kinetics measurements and the use of the Avrami equation to fit the data: Guidelines to avoid common problems*. Polymer testing, 2007. **26**(2): p. 222-231.
164. Khanna, Y. and T. Taylor, *Comments and recommendations on the use of the Avrami equation for physico-chemical kinetics*. Polymer Engineering & Science, 1988. **28**(16): p. 1042-1045.
165. Cebe, P. and S.-D. Hong, *Crystallization behaviour of poly (ether-ether-ketone)*. Polymer, 1986. **27**(8): p. 1183-1192.
166. Emsley, J.W., J. Feeney, and L.H. Sutcliffe, *High resolution nuclear magnetic resonance spectroscopy*. Vol. 2. 2013: Elsevier.
167. Jackman, L.M. and S. Sternhell, *Application of Nuclear Magnetic Resonance Spectroscopy in Organic Chemistry: International Series in Organic Chemistry*. 2013: Elsevier.
168. Harris, R.K., *Nuclear magnetic resonance spectroscopy*. 1986.

169. Hore, P., *Nuclear magnetic resonance*. 2015: Oxford University Press.
170. Levitt, M.H., *Spin dynamics: basics of nuclear magnetic resonance*. 2001: John Wiley & Sons.
171. Ruchatz, D. and G. Fink, *Ethene-norbornene copolymerization using homogenous metallocene and half-sandwich catalysts: Kinetics and relationships between catalyst structure and polymer structure. 2. Comparative study of different metallocene-and half-sandwich/methylaluminumoxane catalysts and analysis of the copolymers by ¹³C nuclear magnetic resonance spectroscopy*. *Macromolecules*, 1998. **31**(15): p. 4674-4680.
172. Billeter, M., W. Braun, and K. Wüthrich, *Sequential resonance assignments in protein 1 H nuclear magnetic resonance spectra: computation of sterically allowed proton-proton distances and statistical analysis of proton-proton distances in single crystal protein conformations*. *Journal of molecular biology*, 1982. **155**(3): p. 321-346.
173. Jones, R.A. and A. Katritzky, *Phosphorus nuclear magnetic resonance spectroscopy*. *Angewandte Chemie International Edition in English*, 1962. **1**(1): p. 32-41.
174. Urenjak, J., S.R. Williams, D.G. Gadian, and M. Noble, *Proton nuclear magnetic resonance spectroscopy unambiguously identifies different neural cell types*. *The Journal of neuroscience*, 1993. **13**(3): p. 981-989.
175. Ackerstaff, E., B.R. Pflug, J.B. Nelson, and Z.M. Bhujwala, *Detection of increased choline compounds with proton nuclear magnetic resonance spectroscopy subsequent to malignant transformation of human prostatic epithelial cells*. *Cancer research*, 2001. **61**(9): p. 3599-3603.
176. Burdett, J.L. and M.T. Rogers, *Keto-enol tautomerism in β-dicarbonyls studied by nuclear magnetic resonance spectroscopy. 1 I. Proton chemical shifts and equilibrium constants of pure compounds*. *Journal of the American Chemical Society*, 1964. **86**(11): p. 2105-2109.
177. Moliner, N., A.B. Gaspar, M.C. Muñoz, V. Niel, J. Cano, and J.A. Real, *Light-and Thermal-Induced Spin Crossover in {Fe(abpt)₂[N(CN)₂]₂}. Synthesis, Structure, Magnetic Properties, and High-Spin↔ Low-Spin Relaxation Studies*. *Inorganic chemistry*, 2001. **40**(16): p. 3986-3991.
178. Kohlmann, O., W.E. Steinmetz, X.-A. Mao, W.P. Wuelfing, A.C. Templeton, R.W. Murray, and C.S. Johnson, *NMR diffusion, relaxation, and spectroscopic studies of water soluble, monolayer-protected gold nanoclusters*. *The Journal of Physical Chemistry B*, 2001. **105**(37): p. 8801-8809.
179. Mariette, F., *NMR relaxation of dairy products*, in *Modern Magnetic Resonance*. 2006, Springer. p. 1697-1701.
180. Papanikolaou, N., E. Papadaki, S. Karampekios, M. Spilioti, T. Maris, P. Prassopoulos, and N. Gourtsoyiannis, *T2 relaxation time analysis in patients with multiple sclerosis: correlation with magnetization transfer ratio*. *European radiology*, 2004. **14**(1): p. 115-122.
181. Wagner, G., *NMR relaxation and protein mobility*. *Current Opinion in Structural Biology*, 1993. **3**(5): p. 748-754.
182. Kay, L., P. Keifer, and T. Saarinen, *Pure absorption gradient enhanced heteronuclear single quantum correlation spectroscopy with improved sensitivity*. *Journal of the American Chemical Society*, 1992. **114**(26): p. 10663-10665.
183. Ernst, R.R., G. Bodenhausen, and A. Wokaun, *Principles of nuclear magnetic resonance in one and two dimensions*. Vol. 14. 1987: Clarendon Press Oxford.
184. Marion, D., *Reprint of "Application of phase sensitive two-dimensional correlated spectroscopy (COSY) for measurements of 1 H-1 H spin-spin coupling constants in*

- proteins*". Biochemical and biophysical research communications, 2012. **425**(3): p. 519-526.
185. Viguera, A.R., F.J. Blanco, and L. Serrano, *The order of secondary structure elements does not determine the structure of a protein but does affect its folding kinetics*. Journal of molecular biology, 1995. **247**(4): p. 670-681.
 186. NEUHAUS, D., G. WAGNER, M. VAŠÁK, J.H. KÄGI, and K. WÜTHRICH, *Systematic application of high-resolution, phase-sensitive two-dimensional 1H-NMR techniques for the identification of the amino-acid-proton spin systems in proteins*. European Journal of Biochemistry, 1985. **151**(2): p. 257-273.
 187. Buchanan, G.W., E. Munteanu, B.A. Dawson, and D. Hodgson, *Concerning the origin of 19F-19F NMR COSY and NOESY connections in the spectra of perfluorooctanoic acid, RF-palmitic acid-F13 and diethyl perfluorosuberate*. Magnetic Resonance in Chemistry, 2005. **43**(7): p. 528-534.
 188. Takasaki, M., K. Kimura, K. Kawaguchi, A. Abe, and G. Katagiri, *Structural analysis of a perfluorosulfonate ionomer in solution by 19F and 13C NMR*. Macromolecules, 2005. **38**(14): p. 6031-6037.
 189. Majumdar, A., Y. Sun, M. Shah, and C.L. Freel Meyers, *Versatile 1H- 31P- 31P COSY 2D NMR Techniques for the Characterization of Polyphosphorylated Small Molecules*. The Journal of organic chemistry, 2010. **75**(10): p. 3214-3223.
 190. Goodreau, B.H. and J.T. Spencer, *Small heteroborane cluster systems. 5. Factors affecting the 2D 11B-11B (boron-11) COSY NMR spectra of terminal-and bridge-substituted pentaborane cluster systems*. Inorganic Chemistry, 1992. **31**(12): p. 2612-2621.
 191. Friebolin, H. and J.K. Becconsall, *Basic one-and two-dimensional NMR spectroscopy*. 1993: VCH Weinheim.
 192. Zhang, L. and G. Gellerstedt, *Quantitative 2D HSQC NMR determination of polymer structures by selecting suitable internal standard references*. Magnetic Resonance in Chemistry, 2007. **45**(1): p. 37-45.
 193. Yuan, T.-Q., S.-N. Sun, F. Xu, and R.-C. Sun, *Characterization of lignin structures and lignin-carbohydrate complex (LCC) linkages by quantitative 13C and 2D HSQC NMR spectroscopy*. Journal of agricultural and food chemistry, 2011. **59**(19): p. 10604-10614.
 194. Gjerde, M.I., W. Nerdal, and H. Høiland, *A NOESY NMR study of the interaction between sodium dodecyl sulfate and poly (ethylene oxide)*. Journal of colloid and interface science, 1996. **183**(1): p. 285-288.
 195. Davis, D.G. and A. Bax, *Separation of chemical exchange and cross-relaxation effects in two-dimensional NMR spectroscopy*. Journal of Magnetic Resonance (1969), 1985. **64**(3): p. 533-535.
 196. Dominguez, A., A. Fernandez, N. Gonzalez, E. Iglesias, and L. Montenegro, *Determination of critical micelle concentration of some surfactants by three techniques*. Journal of Chemical Education, 1997. **74**(10): p. 1227.
 197. Khan, A.M. and S.S. Shah, *Determination of critical micelle concentration (Cmc) of sodium dodecyl sulfate (SDS) and the effect of low concentration of pyrene on its Cmc using ORIGIN software*. JOURNAL-CHEMICAL SOCIETY OF PAKISTAN, 2008. **30**(2): p. 186.
 198. Yekta, A., B. Xu, J. Duhamel, H. Adiwidjaja, and M.A. Winnik, *Fluorescence studies of associating polymers in water: determination of the chain end aggregation number and a model for the association process*. Macromolecules, 1995. **28**(4): p. 956-966.
 199. Infelta, P.P., *Fluorescence quenching in micellar solutions and its application to the determination of aggregation numbers*. Chemical physics letters, 1979. **61**(1): p. 88-91.

200. Lakowicz, J.R., *Principles of fluorescence spectroscopy*. 2007: Springer Science & Business Media.
201. Lakowicz, J.R., *Topics in Fluorescence Spectroscopy: Volume 1: Techniques*. Vol. 1. 1991: Springer Science & Business Media.
202. Ray, G.B., I. Chakraborty, and S.P. Moulik, *Pyrene absorption can be a convenient method for probing critical micellar concentration (cmc) and indexing micellar polarity*. *Journal of colloid and interface science*, 2006. **294**(1): p. 248-254.
203. Zhao, C.L., M.A. Winnik, G. Riess, and M.D. Croucher, *Fluorescence probe techniques used to study micelle formation in water-soluble block copolymers*. *Langmuir*, 1990. **6**(2): p. 514-516.
204. Lianos, P. and R. Zana, *Use of pyrene excimer formation to study the effect of sodium chloride on the structure of sodium dodecyl sulfate micelles*. *The Journal of Physical Chemistry*, 1980. **84**(25): p. 3339-3341.
205. van Stam, J., S. Depaemelaere, and F.C. De Schryver, *Micellar aggregation numbers-A fluorescence study*. *Journal of chemical education*, 1998. **75**(1): p. 93.
206. Smith, B.C., *Fundamentals of Fourier transform infrared spectroscopy*. 2011: CRC press.
207. Schmitt, J. and H.-C. Flemming, *FTIR-spectroscopy in microbial and material analysis*. *International Biodeterioration & Biodegradation*, 1998. **41**(1): p. 1-11.
208. Koganti, V.R., S. Das, and S.E. Rankin, *In Situ FTIR Investigation of the Kinetics of Silica Polycondensation in Surfactant Templated, Mesostuctured Thin Films*. *The Journal of Physical Chemistry C*, 2014. **118**(33): p. 19450-19461.
209. Warren, B.E., *X-ray Diffraction*. 1969: Courier Corporation.
210. Cullity, B.D. and S.R. Stock, *Elements of X-ray Diffraction*. 2001: Pearson.
211. Klug, H.P. and L.E. Alexander, *X-ray diffraction procedures*. Vol. 2. 1954: Wiley New York.
212. Pitschke, W., H. Hermann, and N. Mattern, *The influence of surface roughness on diffracted X-ray intensities in Bragg-Brentano geometry and its effect on the structure determination by means of Rietveld analysis*. *Powder Diffraction*, 1993. **8**(02): p. 74-83.
213. Drenth, J., *X-Ray Crystallography*. 2007: Wiley Online Library.
214. Parrill, J.L., P. Georgopoulos, Y.-W. Chung, and J. Cohen, *GISAXS-Glancing incidence small angle X-ray scattering*. *Le Journal de Physique IV*, 1993. **3**(C8): p. C8-411-C8-417.
215. Ezquerra, T.A., A. Nogales, and M. Gomez, *Applications of synchrotron light to scattering and diffraction in materials and life sciences*. Vol. 776. 2009: Springer Science & Business Media.
216. Ruiz, C.C., ed. *Sugar-Based Surfactants. Fundamentals and applications*. *Surfactant Science Series*, ed. A.T. Hubbard. Vol. 143. 2009, CRC Press: Boca Raton, FL.
217. Stubenrauch, C., *Sugar surfactants - aggregation, interfacial, and adsorption phenomena*. *Current Opinion in Colloid & Interface Science*, 2001. **6**(2): p. 160-170.
218. Martel, F., B. Estrine, R. Plantier-Royon, N. Hoffmann, and C. Portella, *Development of Agriculture Left-Overs: Fine Organic Chemicals from Wheat Hemicellulose-Derived Pentoses*. *Carbohydrates in Sustainable Development I: Renewable Resources for Chemistry and Biotechnology*, 2010. **294**: p. 79-115.
219. Molina-Bolivar, J.A. and C.C. Ruiz, *Self-Assembly and Micellar Structure of Sugar-Based Surfactants: Effect of Temperature and Salt Addition*, in *Sugar-Based Surfactants*, C.C. Ruiz, Editor. 2009, CRC Press: Boca Raton, FL. p. 61-104.
220. Bogusz, S., R.M. Venable, and R.W. Pastor, *Molecular dynamics simulations of octyl glucoside micelles: Structural properties*. *Journal of Physical Chemistry B*, 2000. **104**(23): p. 5462-5470.

221. Bonicelli, M.G., G.F. Ceccaroni, and C. La Mesa, *Lyotropic and thermotropic behavior of alkylglucosides and related compounds*. Colloid and Polymer Science, 1998. **276**(2): p. 109-116.
222. Ruiz, C.C., *Micellar Properties and Molecular Interactions in Binary Surfactant Systems Containing a Sugar-Based Surfactant*, in *Sugar-Based Surfactants*, C.C. Ruiz, Editor. 2009, CRC Press: Boca Raton, FL. p. 413-499.
223. Štangar, U. and N. Hüsing, *Alkyl-glycoside surfactants in the synthesis of mesoporous silica films*. Silicon Chemistry, 2003. **2**(3-4): p. 157-165.
224. Bakshi, M.S. and G. Kaur, *Mixed micelles of series of monomeric and dimeric cationic, zwitterionic, and unequal twin-tail cationic surfactants with sugar surfactants: A fluorescence study*. Journal of Colloid and Interface Science, 2005. **289**(2): p. 551-559.
225. Yang, Q., Q. Zhou, and P. Somasundaran, *Mixed micelles of octane-1, 8 bis (dodecyl dimethyl ammonium chloride) and n -dodecyl- β -D-maltoside by ^1H NMR study*. Colloids and Surfaces A: Physicochemical and Engineering Aspects, 2007. **305**(1): p. 22-28.
226. Yang, Q., Q. Zhou, and P. Somasundaran, *NMR study of micellar microstructures of cationic single-chain and gemini surfactants and their mixtures with nonionic surfactant n -dodecyl- β -D-maltoside*. Colloids and Surfaces A: Physicochemical and Engineering Aspects, 2008. **322**(1): p. 40-46.
227. Xua, W., G. Osei-Prempeh, C. Lema, E.D. Oldham, R.J. Aguilera, S. Parkin, S.E. Rankin, B.L. Knutson, and H.-J. Lehmler, *Synthesis, thermal properties, and cytotoxicity evaluation of hydrocarbon and fluorocarbon alkyl β -D-xylopyranoside surfactants*. Carbohydrate Research, 2012. **349**: p. 12-23.
228. Talagala, S.L., *NMR STUDIES OF MICELLE FORMING*. 1982, UNIVERSITY;-OF BRITISH COLUMBIA.
229. Ulmius, J., B.r. Lindman, G.r. Lindblom, and T.r. Drakenberg, *^1H , ^{13}C , ^{35}Cl , and ^{81}Br NMR of aqueous hexadecyltrimethylammonium salt solutions: solubilization, viscoelasticity, and counterion specificity*. Journal of Colloid and Interface Science, 1978. **65**(1): p. 88-97.
230. Modaressi, A., H. Sifaoui, B. Grzesiak, R. Solimando, U. Domanska, and M. Rogalski, *CTAB aggregation in aqueous solutions of ammonium based ionic liquids; conductimetric studies*. Colloids and Surfaces A: Physicochemical and Engineering Aspects, 2007. **296**(1): p. 104-108.
231. Kameyama, K. and T. Takagi, *Micellar properties of octylglucoside in aqueous solutions*. Journal of colloid and interface science, 1990. **137**(1): p. 1-10.
232. Goyal, P.S., B.A. Dasannacharya, V.K. Kelkar, C. Manohar, K. Srinivasa Rao, and B.S. Valaulikar, *Shapes and sizes of micelles in CTAB solutions*. Physica B: Condensed Matter, 1991. **174**(1-4): p. 196-199.
233. Lorber, B., J.B. Bishop, and L.J. DeLucas, *Purification of octyl β -D-glucopyranoside and re-estimation of its micellar size*. Biochimica et Biophysica Acta (BBA)-Biomembranes, 1990. **1023**(2): p. 254-265.
234. Das, N.C., H. Cao, H. Kaiser, G.T. Warren, J.R. Gladden, and P.E. Sokol, *Shape and Size of Highly Concentrated Micelles in CTAB/NaSal Solutions by Small Angle Neutron Scattering (SANS)*. Langmuir, 2012. **28**(33): p. 11962-11968.
235. Aswal, V.K., P.S. Goyal, and P. Thiyagarajan, *Small-Angle Neutron-Scattering and Viscosity Studies of CTAB/NaSal Viscoelastic Micellar Solutions*. The Journal of Physical Chemistry B, 1998. **102**(14): p. 2469-2473.

236. Suenaga, H., M. Mikami, K. Sandanayake, and S. Shinkai, *Screening of fluorescent boronic acids for sugar sensing which show a large fluorescence change*. Tetrahedron letters, 1995. **36**(27): p. 4825-4828.
237. Bloembergen, N., E.M. Purcell, and R.V. Pound, *RELAXATION EFFECTS IN NUCLEAR MAGNETIC RESONANCE ABSORPTION*. Physical Review, 1948. **73**(7): p. 679-712.
238. Warner, K.S., S.K. Li, N. He, T.M. Suhonen, D. Chantasart, D. Bolikal, and W.I. Higuchi, *Structure-activity relationship for chemical skin permeation enhancers: Probing the chemical microenvironment of the site of action*. Journal of Pharmaceutical Sciences, 2003. **92**(6): p. 1305-1322.
239. Wenk, M.R., T. Alt, A. Seelig, and J. Seelig, *Octyl-beta-D-glucopyranoside partitioning into lipid bilayers: Thermodynamics of binding and structural changes of the bilayer*. Biophysical Journal, 1997. **72**(4): p. 1719-1731.
240. Heerklotz, H. and J. Seelig, *Titration calorimetry of surfactant-membrane partitioning and membrane solubilization*. Biochimica Et Biophysica Acta-Biomembranes, 2000. **1508**(1-2): p. 69-85.
241. Angelov, B., M. Ollivon, and A. Angelova, *X-ray diffraction study of the effect of the detergent octyl glucoside on the structure of lamellar and nonlamellar lipid/water phases of use for membrane protein reconstitution*. Langmuir, 1999. **15**(23): p. 8225-8234.
242. Israelachvili, J.N., *Intermolecular and Surface Forces*. 2011, Waltham, MA: Academic Press.
243. Misran, O., B.A. Timimi, T. Heidelberg, A. Sugimura, and R. Hashim, *Deuterium NMR Investigation of the Lyotropic Phases of Alkyl beta-Glycoside/D2O Systems*. Journal of Physical Chemistry B, 2013. **117**(24): p. 7335-7344.
244. Pautot, S., B.J. Frisken, and D.A. Weitz, *Engineering asymmetric vesicles*. Proceedings of the National Academy of Sciences of the United States of America, 2003. **100**(19): p. 10718-10721.
245. Lin, Q. and E. London, *Preparation of Artificial Plasma Membrane Mimicking Vesicles with Lipid Asymmetry*. Plos One, 2014. **9**(1).
246. Zaldivar, M. and R.G. Larson, *Lattice Monte Carlo simulations of dilute mixed micelles*. Langmuir, 2003. **19**(24): p. 10434-10442.
247. Sheng, Y.P., X.P. Yang, N. Yan, and Y.T. Zhu, *Janus-like spheres, disks, rings, cylinders, and vesicles from the self-assembly of mixture of AB and BC diblock copolymers in A- and C-selective solvents*. Soft Matter, 2013. **9**(27): p. 6254-6262.
248. Cui, J., Y. Han, and W. Jiang, *Asymmetric Vesicle Constructed by AB/CB Diblock Copolymer Mixture and Its Behavior: A Monte Carlo Study*. Langmuir, 2014. **30**(30): p. 9219-9227.
249. Zhuang, Y., J. Lin, L. Wang, and L. Zhang, *Self-Assembly Behavior of AB/AC Diblock Copolymer Mixtures in Dilute Solution*. Journal of Physical Chemistry B, 2009. **113**(7): p. 1906-1913.
250. Spence, K., R. Venditti, and O.J. Rojas, *Sugar surfactants in paper recycling*. NORDIC PULP & PAPER RESEARCH JOURNAL, 2009. **24**(1): p. 107-111.
251. Belgacem, M.N. and A. Gandini, *Monomers, polymers and composites from renewable resources*. 2011: Elsevier.
252. Maneerat, S., *Production of biosurfactants using substrates from renewable-resources*. Songklanakarin J Sci Technol, 2005. **27**(3): p. 675-683.
253. Kaplan, D.L., *Introduction to biopolymers from renewable resources*. 1998: Springer.

254. Khiew, P., N. Huang, S. Radiman, and S. Ahmad, *Synthesis of NiS nanoparticles using a sugar-ester nonionic water-in-oil microemulsion*. *Materials Letters*, 2004. **58**(5): p. 762-767.
255. Hill, K. and O. Rhode, *Sugar-based surfactants for consumer products and technical applications*. *Fett-Lipid*, 1999. **101**(1): p. 25-33.
256. Xu, W., G. Osei-Prempeh, C. Lema, E.D. Oldham, R.J. Aguilera, S. Parkin, S.E. Rankin, B.L. Knutson, and H.-J. Lehmler, *Synthesis, thermal properties, and cytotoxicity evaluation of hydrocarbon and fluorocarbon alkyl β -D-xylopyranoside surfactants*. *Carbohydrate research*, 2012. **349**: p. 12-23.
257. Yoshimura, T., K. Ishihara, and K. Esumi, *Sugar-based gemini surfactants with peptide bonds synthesis, adsorption, micellization, and biodegradability*. *Langmuir*, 2005. **21**(23): p. 10409-10415.
258. Miao, S., N. Callow, S.S. Dashtbozorg, J.-L. Salager, and L.-K. Ju, *Ethylation of Di-rhamnolipids: A Green Route to Produce Novel Sugar Fatty Acid Nonionic Surfactants*. *Journal of Surfactants and Detergents*, 2014. **17**(6): p. 1069-1080.
259. Nakayama, S., Y. Kimura, M. Sayuri, J. Oshitani, T. Kobayashi, S. Adachi, T. Matsuura, H. Imanaka, N. Ishida, and H. Tada, *Influence of Sugar Surfactant Structure on the Encapsulation of Oil Droplets in an Amorphous Sugar Matrix during Freeze-drying*. *Food Research International*, 2015.
260. Kanan, K., M. Fanun, S. Wadaah, and I. Kayali, *Formulation of Microemulsions Based on Sugar Surfactant as an Alternative Fuel*. *Journal of Dispersion Science and Technology*, 2014(just-accepted).
261. Carvalho, L., J.C. Morales, J.M. Pérez-Victoria, and I. Pérez-Victoria, *Hemolytic activity and solubilizing capacity of raffinose and melezitose fatty acid monoesters prepared by enzymatic synthesis*. *European Journal of Pharmaceutics and Biopharmaceutics*, 2015.
262. Bogusz, S., R.M. Venable, and R.W. Pastor, *Molecular dynamics simulations of octyl glucoside micelles: dynamic properties*. *The Journal of Physical Chemistry B*, 2001. **105**(35): p. 8312-8321.
263. Söderman, O., P. Stilbs, and W.S. Price, *NMR studies of surfactants*. *Concepts in Magnetic Resonance Part A*, 2004. **23**(2): p. 121-135.
264. Bonicelli, M., G. Ceccaroni, and C. La Mesa, *Lyotropic and thermotropic behavior of alkylglucosides and related compounds*. *Colloid and Polymer Science*, 1998. **276**(2): p. 109-116.
265. Goloub, T., R. Pugh, and B. Zhmud, *Micellar interactions in nonionic/ionic mixed surfactant systems*. *Journal of colloid and interface science*, 2000. **229**(1): p. 72-81.
266. Ahuja, E.S., K.R. Nielsen, J.P. Foley, and E.L. Little, *Infinite elution range in micellar electrokinetic capillary chromatography using a nonionic/anionic mixed micellar system*. *Analytical Chemistry*, 1995. **67**(1): p. 26-33.
267. Saini, R.K., N. Tonmukayakul, T.D. Welton, J.E. Bryant, and S.G. Gaskins, *Degradable Surfactants, Including Degradable Gemini Surfactants, and Associated Methods*. 2009, Google Patents.
268. Van Zanten, R. and D.J. Harrison, *Viscoelastic surfactants and methods of making and using same*. 2009, Google Patents.
269. Balzer, D., *Anionic, betainic, and nonionic surfactants, electrolytes, water soluble polymer, and further constituent in given weights so the shear modulus is between 50 and 500 pa between 20-40 degrees celcius and ph of 4-8; optimum flow behaviour*. 1999, Google Patents.

270. Botella, P., A. Corma, and M. Quesada, *Synthesis of ordered mesoporous silica templated with biocompatible surfactants and applications in controlled release of drugs*. Journal of Materials Chemistry, 2012. **22**(13): p. 6394-6401.
271. Fan, H., E.W. Leve, C. Scullin, J. Gabaldon, D. Tallant, S. Bunge, T. Boyle, M.C. Wilson, and C.J. Brinker, *Surfactant-assisted synthesis of water-soluble and biocompatible semiconductor quantum dot micelles*. Nano Letters, 2005. **5**(4): p. 645-648.
272. Štangar, U.L. and N. Hüsing, *Alkyl-glycoside surfactants in the synthesis of mesoporous silica films*. Silicon Chemistry, 2003. **2**(3-4): p. 157-165.
273. Xing, R. and S.E. Rankin, *Reactive pore expansion during ammonia vapor post-treatment of ordered mesoporous silica prepared with mixed glucopyranoside and cationic surfactants*. Microporous and Mesoporous Materials, 2008. **108**(1): p. 65-76.
274. Sellergren, B., *Imprinted dispersion polymers: a new class of easily accessible affinity stationary phases*. Journal of chromatography A, 1994. **673**(1): p. 133-141.
275. Katz, A. and M.E. Davis, *Molecular imprinting of bulk, microporous silica*. Nature, 2000. **403**(6767): p. 286-289.
276. Sellergren, B., *Molecular imprinting by noncovalent interactions. Enantioselectivity and binding capacity of polymers prepared under conditions favoring the formation of template complexes*. Die Makromolekulare Chemie, 1989. **190**(11): p. 2703-2711.
277. Madhuri, R., E. Roy, K. Gupta, and P.K. Sharma, *Combination of Molecular Imprinting and Nanotechnology: Beginning of a New Horizon*. Biosensors Nanotechnology, 2014: p. 375-432.
278. Taguchi, H., H. Sunayama, E. Takano, Y. Kitayama, and T. Takeuchi, *Preparation of molecularly imprinted polymers for the recognition of proteins via the generation of peptide-fragment binding sites by semi-covalent imprinting and enzymatic digestion*. Analyst, 2015. **140**(5): p. 1448-1452.
279. Rosen, M.J., *Selection of surfactant pairs for optimization of interfacial properties*. Journal of the American Oil Chemists' Society, 1989. **66**(12): p. 1840-1843.
280. Zhou, Q. and M.J. Rosen, *Molecular interactions of surfactants in mixed monolayers at the air/aqueous solution interface and in mixed micelles in aqueous media: the regular solution approach*. Langmuir, 2003. **19**(11): p. 4555-4562.
281. Penfold, J., E. Staples, L. Thompson, I. Tucker, J. Hines, R. Thomas, and J. Lu, *Solution and adsorption behavior of the mixed surfactant system sodium dodecyl sulfate/n-hexaethylene glycol monododecyl ether*. Langmuir, 1995. **11**(7): p. 2496-2503.
282. Sharma, R., S. Mahajan, and R.K. Mahajan, *Surface adsorption and mixed micelle formation of surface active ionic liquid in cationic surfactants: Conductivity, surface tension, fluorescence and NMR studies*. Colloids and Surfaces A: Physicochemical and Engineering Aspects, 2013. **427**: p. 62-75.
283. Small, D., S. Penkett, and D. Chapman, *Studies on simple and mixed bile salt micelles by nuclear magnetic resonance spectroscopy*. Biochimica et Biophysica Acta (BBA)-Lipids and Lipid Metabolism, 1969. **176**(1): p. 178-189.
284. Sasmal, D.K., A.K. Mandal, T. Mondal, and K. Bhattacharyya, *Diffusion of organic dyes in ionic liquid and giant micron sized ionic liquid mixed micelle: Fluorescence correlation spectroscopy*. The Journal of Physical Chemistry B, 2011. **115**(24): p. 7781-7787.
285. Zhang, R., L. Zhang, and P. Somasundaran, *Study of mixtures of n-dodecyl-β-D-maltoside with anionic, cationic, and nonionic surfactant in aqueous solutions using surface tension and fluorescence techniques*. Journal of colloid and interface science, 2004. **278**(2): p. 453-460.

286. Yang, Q., Q. Zhou, and P. Somasundaran, *NMR study of micellar microstructures of cationic single-chain and gemini surfactants and their mixtures with nonionic surfactant n-dodecyl- β -D-maltoside*. *Colloids and Surfaces A: Physicochemical and Engineering Aspects*, 2008. **322**(1): p. 40-46.
287. Yang, Q., Q. Zhou, and P. Somasundaran, *Mixed micelles of octane-1, 8 bis (dodecyl dimethyl ammonium chloride) and n-dodecyl- β -D-maltoside by ^1H NMR study*. *Colloids and Surfaces A: Physicochemical and Engineering Aspects*, 2007. **305**(1): p. 22-28.
288. Oldham, E.D., S. Seelam, C. Lema, R.J. Aguilera, J. Fiegel, S.E. Rankin, B.L. Knutson, and H.-J. Lehmler, *Synthesis, surface properties, and biocompatibility of 1, 2, 3-triazole-containing alkyl β -D-xylopyranoside surfactants*. *Carbohydrate research*, 2013. **379**: p. 68-77.
289. Carr, H.Y. and E.M. Purcell, *EFFECTS OF DIFFUSION ON FREE PRECESSION IN NUCLEAR MAGNETIC RESONANCE EXPERIMENTS*. *Physical Review*, 1954. **94**(3): p. 630-638.
290. Meiboom, S. and D. Gill, *MODIFIED SPIN-ECHO METHOD FOR MEASURING NUCLEAR RELAXATION TIMES*. *Review of Scientific Instruments*, 1958. **29**(8): p. 688-691.
291. Keeler, J., *Understanding NMR Spectroscopy*. 2010, Singapore: Wiley.
292. Garcia-Mateos, I., M. Mercedes Velazquez, and L.J. Rodriguez, *Critical micelle concentration determination in binary mixtures of ionic surfactants by deconvolution of conductivity/concentration curves*. *Langmuir*, 1990. **6**(6): p. 1078-1083.
293. Das, S., W. Xu, H.-J. Lehmler, A.-F. Miller, B.L. Knutson, and S.E. Rankin, *NMR Studies Suggest an Inverted Micelle-in-Micelle Configuration in Simple Mixed Cationic/Carbohydrate Surfactant Systems*. *Proc. Nat. Acad. Sci.*, 2015. **submitted**.
294. Bergstrom, M., P. Jonsson, M. Persson, and J.C. Eriksson, *A model-independent evaluation of experimental data, and comparison with theory, of synergistic effects in mixtures of an ionic and a nonionic surfactant*. *Langmuir*, 2003. **19**(26): p. 10719-10725.
295. Neidig, K.P. and H.R. Kalbitzer, *Improvement of 2D NMR spectra by matching symmetry-related spectral features*. *Magnetic resonance in chemistry*, 1988. **26**(10): p. 848-851.
296. Oldham, E.D., L.M. Nunes, A. Varela-Ramirez, S.E. Rankin, B.L. Knutson, R.J. Aguilera, and H.-J. Lehmler, *Cytotoxic activity of triazole-containing alkyl β -D-glucopyranosides on a human T-cell leukemia cell line*. *Chemistry Central Journal*, 2015. **9**(1): p. 3.
297. Kim, J.M., Y. Sakamoto, Y.K. Hwang, Y.-U. Kwon, O. Terasaki, S.-E. Park, and G.D. Stucky, *Structural design of mesoporous silica by micelle-packing control using blends of amphiphilic block copolymers*. *The Journal of Physical Chemistry B*, 2002. **106**(10): p. 2552-2558.
298. Rahman, M.S. and S.E. Rankin, *Predictive synthesis of ordered mesoporous silica with maltoside and cationic surfactants based on aqueous lyotropic phase behavior*. *Journal of colloid and interface science*, 2010. **342**(1): p. 33-42.
299. Song, M.-G., J.-Y. Kim, S.-H. Cho, and J.-D. Kim, *Mixed cationic-nonionic surfactant templating approach for the synthesis of mesoporous silica*. *Langmuir*, 2002. **18**(16): p. 6110-6115.
300. Zhai, S.-R., J.-L. Zheng, J. Zou, D. Wu, and Y.-H. Sun, *Mixed cationic-nonionic surfactants route to MCM-48: Effect of the nonionic surfactant on the structural properties*. *Journal of sol-gel science and technology*, 2004. **30**(3): p. 149-155.
301. Zhao, W., Q. Li, L. Wang, J. Chu, J. Qu, S. Li, and T. Qi, *Synthesis of High Quality MCM-48 with Binary Cationic–Nonionic Surfactants*. *Langmuir*, 2010. **26**(10): p. 6982-6988.
302. Chandra, D. and A. Bhaumik, *Highly active 2D hexagonal mesoporous titanium silicate synthesized using a cationic-anionic mixed-surfactant assembly*. *Industrial & engineering chemistry research*, 2006. **45**(14): p. 4879-4883.

303. Rankin, S.E., B. Tan, H.-J. Lehmler, K.P. Hindman, and B.L. Knutson, *Well-ordered mesoporous silica prepared by cationic fluorinated surfactant templating*. Microporous and mesoporous materials, 2004. **73**(3): p. 197-202.
304. Li, Y., T. Sasaki, Y. Shimizu, and N. Koshizaki, *Hexagonal-close-packed, hierarchical amorphous TiO₂ nanocolumn arrays: transferability, enhanced photocatalytic activity, and superamphiphilicity without UV irradiation*. Journal of the American Chemical Society, 2008. **130**(44): p. 14755-14762.
305. Goux, A., J. Ghanbaja, and A. Walcarius, *Prussian Blue electrodeposition within an oriented mesoporous silica film: preliminary observations*. Journal of materials science, 2009. **44**(24): p. 6601-6607.
306. Yamauchi, Y., M. Sawada, M. Komatsu, A. Sugiyama, T. Osaka, N. Hirota, Y. Sakka, and K. Kuroda, *Magnetically induced orientation of mesochannels in mesoporous silica films at 30 Tesla*. Chemistry—An Asian Journal, 2007. **2**(12): p. 1505-1512.
307. Lu, Q., F. Gao, S. Komarneni, and T.E. Mallouk, *Ordered SBA-15 nanorod arrays inside a porous alumina membrane*. Journal of the American Chemical Society, 2004. **126**(28): p. 8650-8651.
308. Platschek, B., R. Köhn, M. Döblinger, and T. Bein, *In situ GISAXS study of the formation of mesostructured phases within the pores of anodic alumina membranes*. Langmuir, 2008. **24**(9): p. 5018-5023.
309. Tan, B. and S.E. Rankin, *Interfacial alignment mechanism of forming spherical silica with radially oriented nanopores*. The Journal of Physical Chemistry B, 2004. **108**(52): p. 20122-20129.
310. Goux, A., M. Etienne, E. Aubert, C. Lecomte, J. Ghanbaja, and A. Walcarius, *Oriented mesoporous silica films obtained by electro-assisted self-assembly (EASA)*. Chemistry of Materials, 2009. **21**(4): p. 731-741.
311. Joshi, S., A. Rao, H.-J. Lehmler, B.L. Knutson, and S.E. Rankin, *Interfacial molecular imprinting of Stober particle surfaces: A simple approach to targeted saccharide adsorption*. Journal of Colloid and Interface Science, 2014. **428**: p. 101-110.
312. Rahman, M.S., J. Ambati, S. Joshi, and S.E. Rankin, *Incorporation of isolated Ti sites into mesoporous silica thin films by sugar surfactant complexation*. Microporous and Mesoporous Materials, 2014. **190**: p. 74-83.
313. Hillhouse, H., J. Van Egmond, M. Tsapatsis, J. Hanson, and J. Larese, *The interpretation of X-ray diffraction data for the determination of channel orientation in mesoporous films*. Microporous and mesoporous materials, 2001. **44**: p. 639-643.
314. Nisticò, R., D. Scalarone, and G. Magnacca, *Preparation and physico-chemical characterization of large-mesopore silica thin films templated by block copolymers for membrane technology*. Microporous and Mesoporous Materials, 2014. **190**: p. 208-214.
315. Guillemin, Y., J. Ghanbaja, E. Aubert, M. Etienne, and A. Walcarius, *Electro-assisted self-assembly of cetyltrimethylammonium-templated silica films in aqueous media: critical effect of counteranions on the morphology and mesostructure type*. Chemistry of Materials, 2014. **26**(5): p. 1848-1858.
316. Kao, K.-C., C.-H. Lin, T.-Y. Chen, Y.-H. Liu, and C.-Y. Mou, *A General Method of Growing Large Area Mesoporous Silica Thin Film on Flat Substrates with Perpendicular Nanochannels*. Journal of the American Chemical Society, 2015.
317. Dunphy, D.R., P.H. Sheth, F.L. Garcia, and C.J. Brinker, *Enlarged Pore Size in Mesoporous Silica Films Templated by Pluronic F127: Use of Poloxamer Mixtures and Increased Template/SiO₂ Ratios in Materials Synthesized by Evaporation-Induced Self-Assembly*. Chemistry of Materials, 2014.

318. Qu, F., H. Sun, Y. Zhang, H. Lu, and M. Yang, *Electrochemically deposited Pd nanorod array/sol-gel silica thin film for the fabrication of electrochemical sensors*. *Sensors and Actuators B: Chemical*, 2012. **166**: p. 837-841.
319. Han, B.-H., I. Manners, and M.A. Winnik, *Oxygen sensors based on mesoporous silica particles on layer-by-layer self-assembled films*. *Chemistry of materials*, 2005. **17**(12): p. 3160-3171.
320. Wang, Z., M. Etienne, F. Quilès, G.-W. Kohring, and A. Walcarius, *Durable cofactor immobilization in sol-gel bio-composite thin films for reagentless biosensors and bioreactors using dehydrogenases*. *Biosensors and Bioelectronics*, 2012. **32**(1): p. 111-117.
321. Elbert, J., F. Krohm, C. Rüttiger, S. Kienle, H. Didzoleit, B.N. Balzer, T. Hugel, B. Stühn, M. Gallei, and A. Brunsen, *Polymer-Modified Mesoporous Silica Thin Films for Redox-Mediated Selective Membrane Gating*. *Advanced Functional Materials*, 2014. **24**(11): p. 1591-1601.
322. Wooten, M.K., *Nanofiltration Membranes from Oriented Mesoporous Silica Thin Films*. 2014.
323. Wohl, B.M. and J.F. Engbersen, *Responsive layer-by-layer materials for drug delivery*. *Journal of controlled release*, 2012. **158**(1): p. 2-14.
324. Lai, N., C. Lin, P. Ku, L. Chang, K. Liao, W. Lin, and C. Yang, *Hollow mesoporous 1a3d silica nanospheres with singleunit-cell-thick shell: Spontaneous formation and drug delivery application*. *Nano Research*, 2014. **7**(10): p. 1439-1448.
325. Choudhari, Y., H. Hoefler, C. Libanati, F. Monsuur, and W. McCarthy, *Mesoporous Silica Drug Delivery Systems*, in *Amorphous Solid Dispersions*. 2014, Springer. p. 665-693.
326. Rutkowska, I.A., J.P. Sek, B.L. Mehdi, P.J. Kulesza, and J.A. Cox, *Assembly of crosslinked oxo-cyanoruthenate and zirconium oxide bilayers: Application in electrocatalytic films based on organically modified silica with templated pores*. *Electrochimica acta*, 2014. **122**: p. 197-203.
327. Etienne, M., Y. Guillemin, D. Grosso, and A. Walcarius, *Electrochemical approaches for the fabrication and/or characterization of pure and hybrid templated mesoporous oxide thin films: a review*. *Analytical and bioanalytical chemistry*, 2013. **405**(5): p. 1497-1512.
328. Sen, D., J. Bahadur, S. Mazumder, G. Verma, P. Hassan, S. Bhattacharya, K. Vijai, and P. Doshi, *Nanocomposite silica surfactant microcapsules by evaporation induced self assembly: tuning the morphological buckling by modifying viscosity and surface charge*. *Soft Matter*, 2012. **8**(6): p. 1955-1963.
329. Bahadur, J., D. Sen, S. Mazumder, P. Sastry, B. Paul, H. Bhatt, and S. Singh, *One-step fabrication of thermally stable TiO₂/SiO₂ nanocomposite microspheres by evaporation-induced self-assembly*. *Langmuir*, 2012. **28**(31): p. 11343-11353.
330. Teng, Z., G. Zheng, Y. Dou, W. Li, C.Y. Mou, X. Zhang, A.M. Asiri, and D. Zhao, *Highly Ordered Mesoporous Silica Films with Perpendicular Mesochannels by a Simple Stöber-Solution Growth Approach*. *Angewandte Chemie International Edition*, 2012. **51**(9): p. 2173-2177.
331. Ogawa, M. and N. Masukawa, *Preparation of transparent thin films of lamellar, hexagonal and cubic silica-surfactant mesostructured materials by rapid solvent evaporation methods*. *Microporous and mesoporous materials*, 2000. **38**(1): p. 35-41.
332. Feng, P., X. Bu, G.D. Stucky, and D.J. Pine, *Monolithic mesoporous silica templated by microemulsion liquid crystals*. *Journal of the American Chemical Society*, 2000. **122**(5): p. 994-995.

333. Huo, Q., D.I. Margolese, and G.D. Stucky, *Surfactant control of phases in the synthesis of mesoporous silica-based materials*. Chemistry of Materials, 1996. **8**(5): p. 1147-1160.
334. Patarin, J., B. Lebeau, and R. Zana, *Recent advances in the formation mechanisms of organized mesoporous materials*. Current opinion in colloid & interface science, 2002. **7**(1): p. 107-115.
335. Grosso, D., F. Babonneau, P.-A. Albouy, H. Amenitsch, A. Balkenende, A. Brunet-Bruneau, and J. Rivory, *An in situ study of mesostructured CTAB-silica film formation during dip coating using time-resolved SAXS and interferometry measurements*. Chemistry of Materials, 2002. **14**(2): p. 931-939.
336. Anderson, M.T., J.E. Martin, J.G. Odinek, and P.P. Newcomer, *Effect of methanol concentration on CTAB micellization and on the formation of surfactant-templated silica (STS)*. Chemistry of materials, 1998. **10**(6): p. 1490-1500.
337. Huang, M.H., B.S. Dunn, and J.I. Zink, *In situ luminescence probing of the chemical and structural changes during formation of dip-coated lamellar phase sodium dodecyl sulfate sol-gel thin films*. Journal of the American Chemical Society, 2000. **122**(15): p. 3739-3745.
338. Baccile, N., G. Laurent, C. Bonhomme, P. Innocenzi, and F. Babonneau, *Solid-state NMR characterization of the surfactant-silica interface in templated silicas: acidic versus basic conditions*. Chemistry of materials, 2007. **19**(6): p. 1343-1354.
339. Nicole, L., C. Boissière, D. Grosso, A. Quach, and C. Sanchez, *Mesostructured hybrid organic-inorganic thin films*. Journal of Materials Chemistry, 2005. **15**(35-36): p. 3598-3627.
340. Klotz, M., A. Ayrál, C. Guizard, and L. Cot, *Synthesis conditions for hexagonal mesoporous silica layers* Supplementary data available: calculation of the wall density and calculation of the surfactant volume fraction from the surfactant weight percentage. For direct electronic access see <http://www.rsc.org/suppdata/jm/a9/a906181i>. Journal of Materials Chemistry, 2000. **10**(3): p. 663-669.
341. Adachi, M., T. Harada, and M. Harada, *Formation processes of silica nanotubes through a surfactant-assisted templating mechanism in laurylamine hydrochloride/tetraethoxysilane system*. Langmuir, 2000. **16**(5): p. 2376-2384.
342. Innocenzi, P., T. Kidchob, J.M. Bertolo, M. Piccinini, M.C. Guidi, and C. Marcelli, *Time-resolved infrared spectroscopy as an in situ tool to study the kinetics during self-assembly of mesostructured films*. The Journal of Physical Chemistry B, 2006. **110**(22): p. 10837-10841.
343. Hillhouse, H.W., J.W. van Egmond, M. Tsapatsis, J.C. Hanson, and J.Z. Larese, *The interpretation of X-ray diffraction data for the determination of channel orientation in mesoporous films*. Microporous and Mesoporous Materials, 2001. **44**: p. 639-643.
344. Chatterjee, P. and S. Hazra, *The hydrophilic/hydrophobic nature of a Cl-terminated Si surface*. Soft Matter, 2013. **9**(41): p. 9799-9806.
345. Cortes, A.B. and M. Valiente, *The effect of a minimum amount of octyl-beta-D-glucoside on micellar, nematic, and hexagonal phases of the CTAB/glycerol/water system*. Colloid and Polymer Science, 2003. **281**(4): p. 319-324.
346. Besson, S., T. Gacoin, C. Ricolleau, C. Jacquiod, and J.-P. Boilot, *Phase diagram for mesoporous CTAB-silica films prepared under dynamic conditions*. J. Mater. Chem., 2003. **13**: p. 404-409.
347. Liu, Y.-C., Y.-F. Lu, Y.-Z. Zeng, C.-H. Liao, J.-C. Chung, and T.-Y. Wei, *Nanostructured Mesoporous Titanium Dioxide Thin Film Prepared by Sol-Gel Method for Dye-Sensitized Solar Cell*. International Journal of Photoenergy, 2011. **2011**.

348. Vivero-Escoto, J.L., Y.D. Chiang, K. C-Wwu, and Y. Yamauchi, *Recent progress in mesoporous titania materials: adjusting morphology for innovative applications*. Science and Technology of Advanced Materials, 2012. **13**(1).
349. Soni, S.S., M.J. Henderson, J.-F. Bardeau, and A. Gibaud, *Visible-Light Photocatalysis in Titania-Based Mesoporous Thin Films*. Advanced Materials, 2008. **20**(8): p. 1493-1498.
350. Ismail, A.A. and D.W. Bahnemann, *Mesoporous titania photocatalysts: preparation, characterization and reaction mechanisms*. Journal of Materials Chemistry, 2011. **21**(32): p. 11686-11707.
351. Nakata, K. and A. Fujishima, *TiO₂ photocatalysis: Design and applications*. Journal of Photochemistry and Photobiology C-Photochemistry Reviews, 2012. **13**(3): p. 169-189.
352. Pan, J.H., X.S. Zhao, and W.I. Lee, *Block copolymer-templated synthesis of highly organized mesoporous TiO₂-based films and their photoelectrochemical applications*. Chemical Engineering Journal, 2011. **170**(2-3): p. 363-380.
353. Zhou, W. and H.G. Fu, *Mesoporous TiO₂: Preparation, Doping, and as a Composite for Photocatalysis*. Chemcatchem, 2013. **5**(4): p. 885-894.
354. Hazra, S. and S. Basu, *High sensitivity and fast response hydrogen sensors based on electrochemically etched porous titania thin films*. Sensors and Actuators B: Chemical, 2006. **115**(1): p. 403-411.
355. Devi, G.S., T. Hyodo, Y. Shimizu, and M. Egashira, *Synthesis of mesoporous TiO₂-based powders and their gas-sensing properties*. Sensors and Actuators B-Chemical, 2002. **87**(1): p. 122-129.
356. Hagfeldt, A. and M. Gratzel, *Light-induced redox reactions in nanocrystalline systems*. Chemical Reviews, 1995. **95**(1): p. 49-68.
357. Hanley, T.L., V. Luca, I. Pickering, and R.F. Howe, *Structure of Titania Sol-Gel Films: A Study by X-Ray Absorption Spectroscopy*. The Journal of Physical Chemistry B, 2002. **106**(6): p. 1153-1160.
358. Brinker, C.J., Y.F. Lu, A. Sellinger, and H.Y. Fan, *Evaporation-induced self-assembly: Nanostructures made easy*. Advanced Materials, 1999. **11**(7): p. 579-+.
359. Soler-Illia, G.J.d.A.A., A. Louis, and C. Sanchez, *Synthesis and Characterization of Mesostructured Titania-Based Materials through Evaporation-Induced Self-Assembly*. Chemistry of Materials, 2002. **14**(2): p. 750-759.
360. Bosc, F., A. Ayral, P.A. Albouy, and C. Guizard, *A simple route for low-temperature synthesis of mesoporous and nanocrystalline anatase thin films*. Chemistry of Materials, 2003. **15**(12): p. 2463-2468.
361. Lin, C., A. Nakaruk, and C. Sorrell, *Mn-doped titania thin films prepared by spin coating*. Progress in Organic Coatings, 2012.
362. Rawolle, M., M.A. Ruderer, S.M. Prams, Q. Zhong, D. Magerl, J. Perlich, S.V. Roth, P. Lellig, J.S. Gutmann, and P. Müller-Buschbaum, *Nanostructuring of Titania Thin Films by a Combination of Microfluidics and Block-Copolymer-Based Sol-Gel Templating*. Small, 2011. **7**(7): p. 884-891.
363. Wang, C.T. and C.F. Yen, *Titania nanocomposite thin films with enhanced photovoltaic efficiency: Effects of Ti-alkoxide sol and compact layer*. Surface and Coatings Technology, 2011.
364. Manurung, P., Y. Putri, W. Simanjuntak, and I.M. Low, *Synthesis and characterisation of chemical bath deposited TiO₂ thin-films*. Ceramics International, 2013. **39**(1): p. 255-259.
365. Zhang, R.Y., A.A. Elzatahry, S.S. Al-Deyab, and D.Y. Zhao, *Mesoporous titania: From synthesis to application*. Nano Today, 2012. **7**(4): p. 344-366.

366. Wu, Q.L. and S.E. Rankin, *Tuning the Mesopore Size of Titania Thin Films Using a Polymeric Swelling Agent*. Journal of Physical Chemistry C, 2011. **115**(24): p. 11925-11933.
367. Wu, Q.L., N. Subramanian, and S.E. Rankin, *Hierarchically Porous Titania Thin Film Prepared by Controlled Phase Separation and Surfactant Templating*. Langmuir, 2011. **27**(15): p. 9557-9566.
368. Wu, Q.L., N. Subramanian, J. Strzalka, Z. Jiang, and S.E. Rankin, *Tuning the mesopore structure of 3D hexagonal thin films using butanol as a co-solvent*. Thin Solid Films, 2012. **520**(9): p. 3558-3566.
369. Alberius, P.C.A., K.L. Frindell, R.C. Hayward, E.J. Kramer, G.D. Stucky, and B.F. Chmelka, *General predictive syntheses of cubic, hexagonal, and lamellar silica and titania mesostructured thin films*. Chemistry of Materials, 2002. **14**(8): p. 3284-3294.
370. Crepaldi, E.L., G. Soler-Illia, D. Grosso, F. Cagnol, F. Ribot, and C. Sanchez, *Controlled formation of highly organized mesoporous titania thin films: From mesostructured hybrids to mesoporous nanoanatase TiO₂*. Journal of the American Chemical Society, 2003. **125**(32): p. 9770-9786.
371. Malfatti, L., M.G. Bellino, P. Innocenzi, and G. Soler-Illia, *One-Pot Route to Produce Hierarchically Porous Titania Thin Films by Controlled Self-Assembly, Swelling, and Phase Separation*. Chemistry of Materials, 2009. **21**(13): p. 2763-2769.
372. Zhao, L.L., Y. Yu, L.X. Song, M.L. Ruan, X.F. Hu, and A. Larbot, *Preparation of mesoporous titania film using nonionic triblock copolymer as surfactant template*. Applied Catalysis a-General, 2004. **263**(2): p. 171-177.
373. Choi, S.Y., M. Mamak, N. Coombs, N. Chopra, and G.A. Ozin, *Thermally stable two-dimensional hexagonal mesoporous nanocrystalline anatase, meso-nc-TiO₂: Bulk and crack-free thin film morphologies*. Advanced Functional Materials, 2004. **14**(4): p. 335-344.
374. Grosso, D., G. Soler-Illia, F. Babonneau, C. Sanchez, P.A. Albouy, A. Brunet-Bruneau, and A.R. Balkenende, *Highly organized mesoporous titania thin films showing mono-oriented 2D hexagonal channels*. Advanced Materials, 2001. **13**(14): p. 1085-+.
375. Lu, R.G., C.A. Drewlen, M.T. Anderson, C.J. Brinker, W. Gong, Y. Guo, H. Soyez, B. Dunn, M.H. Huang, J.I. Zink, Nature, 1997. **389**: p. 364.
376. Guldin, S., S. Hüttner, P. Tiwana, M.C. Orilall, B. Ülgüt, M. Stefik, P. Docampo, M. Kolle, G. Divitini, and C. Ducati, *Improved conductivity in dye-sensitised solar cells through block-copolymer confined TiO₂ crystallisation*. Energy Environ. Sci., 2010. **4**(1): p. 225-233.
377. Guldin, S., S. Huttner, P. Tiwana, M.C. Orilall, B. Ulgut, M. Stefik, P. Docampo, M. Kolle, G. Divitini, C. Ducati, S.A.T. Redfern, H.J. Snaith, U. Wiesner, D. Eder, and U. Steiner, *Improved conductivity in dye-sensitised solar cells through block-copolymer confined TiO₂ crystallisation*. Energy & Environmental Science, 2011. **4**(1): p. 225-233.
378. Docampo, P., S. Guldin, M. Stefik, P. Tiwana, M.C. Orilall, S. Huttner, H. Sai, U. Wiesner, U. Steiner, and H.J. Snaith, *Control of Solid-State Dye-Sensitized Solar Cell Performance by Block-Copolymer-Directed TiO₂ Synthesis*. Advanced Functional Materials, 2010. **20**(11): p. 1787-1796.
379. Beyers, E., P. Cool, and E.F. Vansant, *Anatase formation during the synthesis of mesoporous titania and its photocatalytic effect*. Journal of Physical Chemistry B, 2005. **109**(20): p. 10081-10086.
380. Angelome, P.C., L. Andrini, M.E. Calvo, F.G. Requejo, S.A. Bilmes, and G. Soler-Illia, *Mesoporous anatase TiO₂ films: Use of TiK XANES for the quantification of the*

- nanocrystalline character and substrate effects in the photocatalysis behavior.* Journal of Physical Chemistry C, 2007. **111**(29): p. 10886-10893.
381. Cassiers, K., T. Linssen, M. Mathieu, Y.Q. Bai, H.Y. Zhu, P. Cool, and E.F. Vansant, *Surfactant-directed synthesis of mesoporous titania with nanocrystalline anatase walls and remarkable thermal stability.* Journal of Physical Chemistry B, 2004. **108**(12): p. 3713-3721.
382. Grosso, D., G. Soler-Illia, E.L. Crepaldi, F. Cagnol, C. Sinturel, A. Bourgeois, A. Brunet-Bruneau, H. Amenitsch, P.A. Albouy, and C. Sanchez, *Highly porous TiO₂ anatase optical thin films with cubic mesostructure stabilized at 700 degrees C.* Chemistry of Materials, 2003. **15**(24): p. 4562-4570.
383. Bass, J.D., D. Grosso, C. Boissiere, and C. Sanchez, *Pyrolysis, crystallization, and sintering of mesostructured titania thin films assessed by in situ thermal ellipsometry.* Journal of the American Chemical Society, 2008. **130**(25): p. 7882-7897.
384. Choi, S.Y., M. Mamak, S. Speakman, N. Chopra, and G.A. Ozin, *Evolution of nanocrystallinity in periodic mesoporous anatase thin films.* Small, 2005. **1**(2): p. 226-232.
385. Dewalque, J., R. Cloots, O. Dubreuil, N. Krins, B. Vertruyen, and C. Henrist, *Microstructural evolution of a TiO₂ mesoporous single layer film under calcination: Effect of stabilization and repeated thermal treatments on the film crystallization and surface area.* Thin Solid Films, 2012. **520**(16): p. 5272-5276.
386. Herregods, S.J.F., M. Mertens, K. Van Havenbergh, G. Van Tendeloo, P. Cool, A. Buekenhoudt, and V. Meynen, *Controlling pore size and uniformity of mesoporous titania by early stage low temperature stabilization.* Journal of Colloid and Interface Science, 2013. **391**: p. 36-44.
387. Innocenzi, P., L. Malfatti, T. Kidchob, S. Enzo, G. Della Ventura, U. Schade, and A. Marcelli, *Correlative Analysis of the Crystallization of Sol-Gel Dense and Mesoporous Anatase Titania Films.* Journal of Physical Chemistry C, 2010. **114**(51): p. 22385-22391.
388. Carreon, M.A., S.Y. Choi, M. Mamak, N. Chopra, and G.A. Ozin, *Pore architecture affects photocatalytic activity of periodic mesoporous nanocrystalline anatase thin films.* Journal of Materials Chemistry, 2007. **17**(1): p. 82-89.
389. Fukuda, K., Y. Ebina, T. Shibata, T. Aizawa, I. Nakai, and T. Sasaki, *Unusual Crystallization Behaviors of Anatase Nanocrystallites from a Molecularly Thin Titania Nanosheet and Its Stacked Forms: Increase in Nucleation Temperature and Oriented Growth.* Journal of the American Chemical Society, 2006. **129**(1): p. 202-209.
390. Jiang, Z., X. Li, J. Strzalka, M. Sprung, T. Sun, A.R. Sandy, S. Narayanan, D.R. Lee, and J. Wang, *The dedicated high-resolution grazing-incidence X-ray scattering beamline 8-ID-E at the Advanced Photon Source.* J. Synchrotron Rad., 2012. **19**: p. 627-636.
391. Jiang, Z., *GIXSGUI, a Matlab-based software for visualization and reduction of Grazing Incidence X-ray Scattering data.*
<http://www.aps.anl.gov/Sectors/Sector8/Operations/GIXSGUI.html>.
392. Grosso, D., G.J.d.A. Soler-Illia, E.L. Crepaldi, F. Cagnol, C. Sinturel, A. Bourgeois, A. Brunet-Bruneau, H. Amenitsch, P.A. Albouy, and C. Sanchez, *Highly porous TiO₂ anatase optical thin films with cubic mesostructure stabilized at 700 C.* Chemistry of Materials, 2003. **15**(24): p. 4562-4570.
393. Choi, S.Y., B. Lee, D.B. Carew, M. Mamak, F.C. Peiris, S. Speakman, N. Chopra, and G.A. Ozin, *3D Hexagonal (R-3m) Mesostructured Nanocrystalline Titania Thin Films: Synthesis and Characterization.* Advanced Functional Materials, 2006. **16**(13): p. 1731-1738.

394. Soler-Illia, G.J., P.C. Angelomé, M.C. Fuertes, D. Grosso, and C. Boissiere, *Critical aspects in the production of periodically ordered mesoporous titania thin films*. *Nanoscale*, 2012. **4**(8): p. 2549-2566.
395. Klotz, M., P.-A. Albouy, A. Ayrat, C. Ménager, D. Grosso, A. Van der Lee, V. Cabuil, F. Babonneau, and C. Guizard, *The true structure of hexagonal mesophase-templated silica films as revealed by X-ray scattering: Effects of thermal treatments and of nanoparticle seeding*. *Chemistry of materials*, 2000. **12**(6): p. 1721-1728.
396. Smarsly, B., A. Gibaud, W. Ruland, D. Sturmayr, and C.J. Brinker, *Quantitative SAXS Analysis of Oriented 2D Hexagonal Cylindrical Silica Mesostructures in Thin Films Obtained from Nonionic Surfactants*. *Langmuir*, 2005. **21**(9): p. 3858-3866.
397. Matej, Z., R. Kuzel, and L. Nichtova, *XRD total pattern fitting applied to study of microstructure of TiO₂ films*. *Powder Diffraction*, 2010. **25**(2): p. 125-131.
398. Klotz, M., P.A. Albouy, A. Ayrat, C. Menager, D. Grosso, A. Van der Lee, V. Cabuil, F. Babonneau, and C. Guizard, *The true structure of hexagonal mesophase-templated silica films as revealed by X-ray scattering: Effects of thermal treatments and of nanoparticle seeding*. *Chemistry of Materials*, 2000. **12**(6): p. 1721-1728.
399. Chatterjee, P., S. Hazra, and H. Amenitsch, *Substrate and drying effect in shape and ordering of micelles inside CTAB-silica mesostructured films*. *Soft Matter*, 2012. **8**(10): p. 2956-2964.
400. Williford, R.E., R.S. Addleman, X.S. Li, T.S. Zemanian, J.C. Birnbaum, and G.E. Fryxell, *Pore shape evolution in mesoporous silica thin films: From circular to elliptical to rectangular*. *Journal of Non-Crystalline Solids*, 2005. **351**(27-29): p. 2217-2223.
401. Howard, C., T. Sabine, and F. Dickson, *Structural and thermal parameters for rutile and anatase*. *Acta Crystallographica Section B: Structural Science*, 1991. **47**(4): p. 462-468.
402. Kirsch, B.L., E.K. Richman, A.E. Riley, and S.H. Tolbert, *In-situ X-ray diffraction study of the crystallization kinetics of mesoporous titania films*. *Journal of Physical Chemistry B*, 2004. **108**(34): p. 12698-12706.
403. Soler-Illia, G.d.A., A. Louis, and C. Sanchez, *Synthesis and characterization of mesostructured titania-based materials through evaporation-induced self-assembly*. *Chemistry of Materials*, 2002. **14**(2): p. 750-759.
404. Liu, K., M. Zhang, K. Shi, and H. Fu, *Large-pore mesoporous nanocrystalline titania thin films synthesized through evaporation-induced self-assembly*. *Materials Letters*, 2005. **59**(26): p. 3308-3310.
405. Wang, C.-T. and C.-F. Yen, *Titania nanocomposite thin films with enhanced photovoltaic efficiency: Effects of Ti-alkoxide sol and compact layer*. *Surface and Coatings Technology*, 2012. **206**(8): p. 2622-2627.
406. Rawolle, M., M.A. Niedermeier, G. Kaune, J. Perlich, P. Lellig, M. Memesa, Y.-J. Cheng, J.S. Gutmann, and P. Müller-Buschbaum, *Fabrication and characterization of nanostructured titania films with integrated function from inorganic-organic hybrid materials*. *Chemical Society Reviews*, 2012. **41**(15): p. 5131-5142.
407. Krüger, R.A., T.J. Gordon, T. Baumgartner, and T.C. Sutherland, *End-Group Functionalization of Poly (3-hexylthiophene) as an Efficient Route to Photosensitize Nanocrystalline TiO₂ Films for Photovoltaic Applications*. *ACS applied materials & interfaces*, 2011. **3**(6): p. 2031-2041.
408. Agarwala, S., M. Kevin, A. Wong, C. Peh, V. Thavasi, and G. Ho, *Mesophase ordering of TiO₂ film with high surface area and strong light harvesting for dye-sensitized solar cell*. *ACS applied materials & interfaces*, 2010. **2**(7): p. 1844-1850.

409. Uchida, H., M.N. Patel, R.A. May, G. Gupta, K.J. Stevenson, and K.P. Johnston, *Highly-ordered mesoporous titania thin films prepared via surfactant assembly on conductive indium–tin-oxide/glass substrate and its optical properties*. *Thin Solid Films*, 2010. **518**(12): p. 3169-3176.
410. Pan, J.H., X. Zhao, and W.I. Lee, *Block copolymer-templated synthesis of highly organized mesoporous TiO₂-based films and their photoelectrochemical applications*. *Chemical Engineering Journal*, 2011. **170**(2): p. 363-380.
411. Si, P., S. Ding, J. Yuan, X.W. Lou, and D.-H. Kim, *Hierarchically structured one-dimensional TiO₂ for protein immobilization, direct electrochemistry, and mediator-free glucose sensing*. *ACS nano*, 2011. **5**(9): p. 7617-7626.
412. Gajjela, S.R., K. Ananthanarayanan, C. Yap, M. Grätzel, and P. Balaya, *Synthesis of mesoporous titanium dioxide by soft template based approach: characterization and application in dye-sensitized solar cells*. *Energy & Environmental Science*, 2010. **3**(6): p. 838-845.
413. Smarsly, B., D. Grosso, T. Brezesinski, N. Pinna, C. Boissiere, M. Antonietti, and C. Sanchez, *Highly crystalline cubic mesoporous TiO₂ with 10-nm pore diameter made with a new block copolymer template*. *Chemistry of materials*, 2004. **16**(15): p. 2948-2952.
414. Rampaul, A., I.P. Parkin, S.A. O'Neill, J. DeSouza, A. Mills, and N. Elliott, *Titania and tungsten doped titania thin films on glass; active photocatalysts*. *Polyhedron*, 2003. **22**(1): p. 35-44.
415. Zhang, R., A.A. Elzatahry, S.S. Al-Deyab, and D. Zhao, *Mesoporous titania: from synthesis to application*. *Nano Today*, 2012. **7**(4): p. 344-366.
416. Grosso, D., G. de AA Soler-Illia, F. Babonneau, C. Sanchez, P.A. Albouy, A. Brunet-Bruneau, and A.R. Balkenende, *Highly Organized Mesoporous Titania Thin Films Showing Mono-Oriented 2D Hexagonal Channels*. *Advanced Materials*, 2001. **13**(14): p. 1085-1090.
417. Choi, S.Y., M. Mamak, N. Coombs, N. Chopra, and G.A. Ozin, *Thermally Stable Two-Dimensional Hexagonal Mesoporous Nanocrystalline Anatase, Meso-nc-TiO₂: Bulk and Crack-Free Thin Film Morphologies*. *Advanced Functional Materials*, 2004. **14**(4): p. 335-344.
418. Stein, A., S.G. Rudisill, and N.D. Petkovich, *Perspective on the Influence of Interactions Between Hard and Soft Templates and Precursors on Morphology of Hierarchically Structured Porous Materials*. *Chemistry of Materials*, 2014. **26**(1): p. 259-276.
419. Haring, A., A. Morris, and M. Hu, *Controlling Morphological Parameters of Anodized Titania Nanotubes for Optimized Solar Energy Applications*. *Materials*, 2012. **5**(10): p. 1890-1909.
420. Huo, K.F., B. Gao, J.J. Fu, L.Z. Zhao, and P.K. Chu, *Fabrication, modification, and biomedical applications of anodized TiO₂ nanotube arrays*. *Rsc Advances*, 2014. **4**(33): p. 17300-17324.
421. Regonini, D., C.R. Bowen, A. Jaroenworarluck, and R. Stevens, *A review of growth mechanism, structure and crystallinity of anodized TiO₂ nanotubes*. *Materials Science & Engineering R-Reports*, 2013. **74**(12): p. 377-406.
422. Maeda, M. and T. Watanabe, *Effects of crystallinity and grain size on photocatalytic activity of titania films*. *Surface and Coatings Technology*, 2007. **201**(22): p. 9309-9312.
423. Malfatti, L., P. Falcaro, H. Amenitsch, S. Caramori, R. Argazzi, C.A. Bignozzi, S. Enzo, M. Maggini, and P. Innocenzi, *Mesostructured self-assembled titania films for photovoltaic applications*. *Microporous and mesoporous materials*, 2006. **88**(1): p. 304-311.

424. Alem, A., H. Sarpoolaky, and M. Keshmiri, *Sol-gel preparation of titania multilayer membrane for photocatalytic applications*. *Ceramics International*, 2009. **35**(5): p. 1837-1843.
425. Yang, P., D. Zhao, D.I. Margolese, B.F. Chmelka, and G.D. Stucky, *Generalized syntheses of large-pore mesoporous metal oxides with semicrystalline frameworks*. *Nature*, 1998. **396**(6707): p. 152-155.
426. Cassiers, K., T. Linssen, M. Mathieu, Y.Q. Bai, H.Y. Zhu, P. Cool, and E.F. Vansant, *Surfactant-directed synthesis of mesoporous titania with nanocrystalline anatase walls and remarkable thermal stability*. *The Journal of Physical Chemistry B*, 2004. **108**(12): p. 3713-3721.
427. Das, S., Q. Wu, R.K. Garlapalli, S. Nagpure, J. Strzalka, Z. Jiang, and S.E. Rankin, *In-Situ GISAXS Investigation of Pore Orientation Effects on the Thermal Transformation Mechanism in Mesoporous Titania Thin Films*. *The Journal of Physical Chemistry C*, 2014. **118**(2): p. 968-976.
428. Arabatzis, I., T. Stergiopoulos, M. Bernard, D. Labou, S. Neophytides, and P. Falaras, *Silver-modified titanium dioxide thin films for efficient photodegradation of methyl orange*. *Applied Catalysis B: Environmental*, 2003. **42**(2): p. 187-201.
429. Chang, W.-L., H.-W. Su, and W.-C. Chen, *Synthesis and properties of photosensitive polyimide-nanocrystalline titania optical thin films*. *European Polymer Journal*, 2009. **45**(10): p. 2749-2759.
430. Jiang, Z., X. Li, J. Strzalka, M. Sprung, T. Sun, A.R. Sandy, S. Narayanan, D. Lee, and J. Wang, *The dedicated high-resolution grazing-incidence X-ray scattering beamline 8-ID-E at the Advanced Photon Source*. *Journal of synchrotron radiation*, 2012. **19**(4): p. 627-636.
431. Jiang, Z., *GIXSGUI is available for download: <http://www.aps.anl.gov/Sectors/Sector8/Operations/GIXSGUI.html>*. There is no corresponding record for this reference.
432. Nagpure, S., S. Das, R.K. Garlapalli, J. Strzalka, and S.E. Rankin, *In Situ GISAXS Investigation of Low-Temperature Aging in Oriented Surfactant-Mesostructured Titania Thin Films*. *The Journal of Physical Chemistry C*, 2015. **Submitted**.
433. Hanwell, M.D., D.E. Curtis, D.C. Lonie, T. Vandermeersch, E. Zurek, and G.R. Hutchison, *Avogadro: An advanced semantic chemical editor, visualization, and analysis platform*. *J. Cheminformatics*, 2012. **4**(1): p. 17.
434. Salomon-Ferrer, R., D.A. Case, and R.C. Walker, *An overview of the Amber biomolecular simulation package*. *Wiley Interdisciplinary Reviews: Computational Molecular Science*, 2013. **3**(2): p. 198-210.
435. Innocenzi, P., *Infrared spectroscopy of sol-gel derived silica-based films: a spectra-microstructure overview*. *Journal of Non-Crystalline Solids*, 2003. **316**(2): p. 309-319.
436. Mittlefehldt, E.R., J.A. Gardella, and L. Salvati, *Fourier transform-based deconvolution techniques for resolution of overlapping bands in x-ray photoelectron and fourier-transform infrared spectra of bisphenol-a-polycarbonate/dimethyl siloxane block copolymers*. *Analytica Chimica Acta*, 1986. **191**: p. 227-241.
437. Joshi, S., A. Rao, H.-J. Lehmler, B.L. Knutson, and S.E. Rankin, *Interfacial molecular imprinting of Stöber particle surfaces: A simple approach to targeted saccharide adsorption*. *Journal of colloid and interface science*, 2014. **428**: p. 101-110.
438. Smith, B.J., A. Rawal, G.P. Funkhouser, L.R. Roberts, V. Gupta, J.N. Israelachvili, and B.F. Chmelka, *Origins of saccharide-dependent hydration at aluminate, silicate, and*

- aluminosilicate surfaces*. Proceedings of the National Academy of Sciences, 2011. **108**(22): p. 8949-8954.
439. Stöber, W., A. Fink, and E. Bohn, *Controlled growth of monodisperse silica spheres in the micron size range*. Journal of colloid and interface science, 1968. **26**(1): p. 62-69.
440. Koch, H. and A. Perlin, *Synthesis and ¹³C NMR spectrum of D-glucose-3-d. bond-polarization differences between the anomers of D-glucose*. Carbohydrate Research, 1970. **15**(3): p. 403-410.
441. Perlin, A.S., B. Casu, and H. Koch, *Configurational and conformational influences on the carbon-13 chemical shifts of some carbohydrates*. Canadian Journal of Chemistry, 1970. **48**(16): p. 2596-2606.
442. Stewart, J.J., *Optimization of parameters for semiempirical methods I. Method*. Journal of Computational Chemistry, 1989. **10**(2): p. 209-220.
443. Hanwell, M.D., D.E. Curtis, D.C. Lonie, T. Vandermeersch, E. Zurek, and G.R. Hutchison, *Avogadro: an advanced semantic chemical editor, visualization, and analysis platform*. Journal of cheminformatics, 2012. **4**(1): p. 1-17.
444. Hurd, R.E., *GRADIENT-ENHANCED SPECTROSCOPY*. Journal of Magnetic Resonance, 1990. **87**(2): p. 422-428.
445. Rance, M., O.W. Sorensen, G. Bodenhausen, G. Wagner, R.R. Ernst, and K. Wuthrich, *IMPROVED SPECTRAL RESOLUTION IN COSY H-1-NMR SPECTRA OF PROTEINS VIA DOUBLE QUANTUM FILTERING*. Biochemical and Biophysical Research Communications, 1983. **117**(2): p. 479-485.
446. Kay, L.E., P. Keifer, and T. Saarinen, *PURE ABSORPTION GRADIENT ENHANCED HETERONUCLEAR SINGLE QUANTUM CORRELATION SPECTROSCOPY WITH IMPROVED SENSITIVITY*. Journal of the American Chemical Society, 1992. **114**(26): p. 10663-10665.
447. Bose-Basu, B., E.F. DeRose, T.W. Kirby, G.A. Mueller, W.A. Beard, S.H. Wilson, and R.E. London, *Dynamic characterization of a DNA repair enzyme: NMR studies of [methyl-¹³C] methionine-labeled DNA polymerase β*. Biochemistry, 2004. **43**(28): p. 8911-8922.
448. Julien, O., P. Mercier, L. Spyropoulos, J.E. Corrie, and B.D. Sykes, *NMR studies of the dynamics of a bifunctional rhodamine probe attached to troponin C*. Journal of the American Chemical Society, 2008. **130**(8): p. 2602-2609.

CURRICULUM VITAE

PLACE OF BIRTH:

Kolkata, India

EDUCATION:

Bachelor of Chemical Engineering, Jadavpur University, Kolkata, India, 2010

PUBLICATIONS:

Das, S.; Wu, Q.; Garlapalli, R.; Nagpure, S.; Strzalka, J.; Jiang, Z.; Rankin, S. "In-Situ GISAXS studies of Orientation Effects on the Transformation Mechanisms in Mesoporous Titania Thin Films". **Journal of Physical Chemistry C**, 2014, **118**, 968-976.

Koganti, V.; Das, S.; Rankin, S. "In Situ FTIR Investigation of the Kinetics of Silica Polycondensation in Surfactant Templated, Mesostructured Thin Films". **Journal of Physical Chemistry C**, 2014, **118(33)**, 19450-19461.

Sen, D.; Sarkar, A.; Das, S.; Chowdhury, R.; Bhattacharjee, C. "Batch Hydrolysis and Rotating Disk Membrane Bioreactor for the Production of Galacto-oligosaccharides: A Comparative Study". **Industrial and Engineering Chemistry Research**, 2012, **51**, 10671-10681.

PRESENTATIONS:

"In-Situ GISAXS Studies of the Transformation Mechanisms in Oriented Mesoporous Titania Thin Films". **12th International Conference of Surface X-ray and Neutron Scattering (SXNS) 2012**.

"NMR Investigation of Surfactant Structure Effects on Mixing in Cationic/Carbohydrate Surfactants". **American Institute of Chemical Engineers (AIChE) Conference 2012**.

“Synthesis of cationic-carbohydrate mixed small molecule surfactant templated silica thin films with orthogonally oriented pores by tuning the surface chemistry of the substrate”. **Materials Research Society (MRS) conference 2013.**

“In-Situ GISAXS Investigation of Pore Orientation Effects on the Thermal Transformation Mechanism in Mesoporous Titania Thin Films”. **APS/CNM/EMC user meeting 2013.**

“Effect of surfactant structure on relative position of surfactant head groups in mixed micelle of cationic-carbohydrate surfactants micelles”. **American Chemical Society (ACS) Colloids and Surfaces 2013.**

“Interaction of Carbohydrates with the Molecularly Imprinted Silica Particles”. **American Institute of Chemical Engineers (AIChE) Conference 2013.**

“In-Situ GISAXS Kinetic Studies of Surfactant Templated Mesoporous Titania Thin Films: Orientation Effect on formation and transformation mechanism”. **American Crystallographic Association (ACA) Annual Meeting 2014.**

“Effects of Surfactant Structural Parameters on the Relative Position of Surfactant Head Groups in Mixed Cationic-Carbohydrate Surfactants Micelles”. **American Institute of Chemical Engineers (AIChE) Conference 2014.**

“In-Situ Gisaxs Study of Pore Orientation Effect on Thermal Transformation Mechanism of Surfactant Templated Mesoporous Titania Thin Films”. **American Institute of Chemical Engineers (AIChE) Conference 2014.**